To the Graduate Council:

I am submitting herewith a dissertation written by Georgi Metodiev Daskalov entitled "Propagation of Ultrasonic Pulses in Flawed Media: Applications to Nondestructive Testing and Evaluation". I have examined the final copy of this dissertation for form and content and recommend that it be accepted in partial fulfillment of the requirements for the degree of Doctor of Philosophy with a major in Nuclear Engineering.

Rafael B. Perez, Major Professor

We have read this dissertation
and recommend its acceptance:

Accepted for the Council

Associate Vice Chancellor and
Dean of the Graduate School

Propagation of Ultrasonic Pulses in Flawed Media: Applications to Nondestructive Testing and Evaluation

A Dissertation

Presented for the

Doctor of Philosophy Degree

The University of Tennessee, Knoxville

Georgi Metodiev Daskalov

May 1996

To my wife Galina,

and my daughters Juliana and Nadia,

for their love and patience

ACKNOWLEDGMENTS

The work presented in this dissertation was sponsored by the Nuclear Engineering Department of The University of Tennessee and the Fulbright Board of the United States Information Agency. The author wishes to recognize the continuous support and encouragement of the Department head Dr. Thomas W. Kerlin.

The author also wishes to acknowledge the many contributions, both professional and personal, of Dr. Rafael B. Perez (my Advisor), to whom I am forever indebted.

The author also wishes to recognize the faculty of the Nuclear Engineering Department for years of support and encouragement. The author also wishes to acknowledge the contributions, both professional and personal, of the committee members: Dr. L. F. Miller, Dr. B. R. Upadhyaya and Dr. P. K. Liaw.

Finally, the author wishes to recognize the staff of the Institute for International Education - Southern Region in Houston, for their encouragement and assistance from my first day at The University of Tennessee, in Knoxville.

ABSTRACT

A detailed analysis of the propagation of elastic waves in flawed materials is presented in this dissertation.

After a thorough review of various analytical and numerical procedures, a computer code, **JUNA**, has been developed for the computation of wave propagation and interaction in two-dimensional closed systems with flaws. Care has been exercised to validate the code by comparison with analytical and experimental results. Upon performance of these tests, the code was found to be stable, robust and consistent with the expected features associated with elastic wave propagation. In particular, excellent results were obtained in the detection of cracks.

The code validation step also led to the conclusion that its output does in fact provide a convenient way for the visualization and analysis of wave propagation in flawed systems.

One of the first applications of the code **JUNA**, has been the modeling of finite-size transducers.

Parallel to the above development, new, modern signal analysis methods, of immediate application to Nondestructive Evaluation (NDE) techniques, were implemented for the evaluation and understanding of the **JUNA** output, by means of the Gabor Short Time Fourier Transform (STFT) and Continuous Wavelet Transform (CWT). Based on these methods, a procedure for the measurement of the dispersion law for ultrasonic pulses was developed and applied to specific measurements.

This particular development was made possible by the introduction of wavelet-like pulses as excitation sources, containing a wide spectrum of input frequencies.

The combination of the **JUNA** code, the Gabor STFT and CWT allowed the study of Lamb waves in thin plates.

The basis for the extension of the code to cylindrical geometry was developed; however, both its numerical implementation and that of the propagation of elastic waves along interfaces, await future developments.

Table of Contents

List of Figures

List of Tables

List of Symbols

A list of the symbols most frequently used throughout this dissertation and their meaning is given below

$\vec{U}$ - three-dimensional displacement vector field;
u - X-component of the displacement vector field;
v - Y-component of the displacement vector field;
w - Z-component of the displacement vector field;
Φ - the scalar wave potential;
$\vec{H}$ - the vector wave potential;
$\psi(t)$ - basic (or "mother") wavelet;
$\psi_\theta(x,y,t)$ - Z-component of the vector wave potential;
λ,μ - Lamé elastic constants for isotropic media;
c_{ijkl} - elements of the elastic stiffness matrix;
θ - angle between the wave normal and the X-axis;
$\vec{n}$ - wave normal;
f - frequency (in Hz);
ω - circular frequency (in s^{-1});
h - stepsize with respect to the spatial variables;
ρ - material density
ν - Poisson ratio;
E - Young modulus;
S_{ij} - strain matrix components;
σ_{ij} - components of the stress matrix;
$\delta(x)$ - Dirac delta-function;
δ_{ij} - 0 if $i \neq j$, 1 otherwise;
$g(r|r')$ - scalar wave Green function;
$G_{ij}(r|r')$ - Green tensor components;
$\Sigma_{ijk}(r|r')$ - stress Green tensor components;
Γ_{ij} - components of the Christoffel tensor;
k - wavenumber;
λ_l, λ_s - wave length of compression and shear waves, respectively.
p - magnitude of the longitudinal velocity for isotropic medium $\left(=\sqrt{\dfrac{\lambda+2\mu}{\rho}}\right)$;
s - magnitude of the shear velocity for isotropic medium $\left(=\sqrt{\dfrac{\mu}{\rho}}\right)$;
α - compression wave dimensionless velocity;
β - shear wave dimensionless velocity;

$q = \dfrac{p^2 - 2s^2}{2p^2}$;

$\left(G_b^{\alpha} f\right)(\omega)$ - Gabor STFT of a function f(t);

$\left(W_{\psi} f\right)(b, a)$ - CWT of a function f(t);

b - time shift;

a - time scale in CWT (μs); crack length (mm);

$\hat{f}$ - Fourier transform of the function f;

$\bar{f}$ - complex conjugate of the function f;

$u_{n,x} = \dfrac{\partial u_n}{\partial x}$;

u^{in}, v^{in} - displacement components of the incident field;

u^{t}, v^{t} - displacement components of the total field.

CHAPTER 1

Introduction

The propagation of elastic waves is an important phenomenon in engineering and in many branches of the physical sciences. In the last few decades this fact has been increasingly recognized, which has led to a considerable growth of both interest and research activity in this field.

Elastic waves propagate in solids, liquids and gases, and so the whole range of technological materials are assessable. In recent decades, several important technological and scientific developments have motivated a renewed interest in this field. In engineering applications there is a continually growing need for information on the performance of structures subjected to high rates of loading. In seismology more accurate information on earthquake phenomena and improved prospecting techniques are needed. Studies on surface waves and waves in waveguides have stimulated the development of electrical devices. This wide range of applications is because the elastic wave propagation phenomenon, in its various forms, occurs in a wide range of wavelengths - from 40 km (seismology) to 0.05 mm and below (electronics). As it will be seen in the next chapters, for relatively rigid materials the stiffness constants are of the order of 10^{11} newtons/m^2. For a typical mass density ρ in the neighborhood of 4,000 kg/m^3, the shear wave velocity is therefore of the order of 5,000 m/s. The typical wavelength is then $\lambda_s \approx 5 \times 10^{-5}$ meters, or 50 microns, at a frequency of 100 MHz. These values are approximately 5 orders of magnitude smaller than the equivalent quantities for electromagnetic waves, and it is just this property of elastic waves that makes them so attractive for many technological applications. Analytical work on the diffraction of ultrasonic waves by flaws began to play an important role in methods of nondestructive evaluation of structural elements. In non-destructive testing and evaluation (NDE), the interaction of pulses of ultrasound waves with the material surface and volume features should provide a good means of characterizing those features and determining important parameters like crack depth and size as well as its position. In recent years the aim of the ultrasonic nondestructive inspection has shifted from merely to detect defects which may lead to a failure of the system, towards identification of what is seen by nondestructive techniques, although the impossibility of a complete analytical treatment of the interaction of the elastic waves greatly hinders interpretation of the experimental results. On the other hand, in many industries the integrity of structures such as pressure vessels and pipes is of vital importance, and elastic waves are commonly used to test them. In the nuclear power industry in particular, in recent years there has been a continually growing need to estimate the current state of the aging structural components of nuclear plants in order to predict the service life and provide a reliable and safe operation of the plants. Many different factors contribute to the degradation of structural materials such as **(i)** irradiation effects; **(ii)** operation at high temperature; **(iii)** corrosive environment; **(iv)** loading conditions (fatigue and wear), etc. Along with the degradation the appearance of cracks can vastly reduce the strength of the components material and may cause serious faults in the related systems. Therefore, it is of crucial importance to develop reliable and relatively non-expensive on-line and off-line methods for evaluation of the current status and changes in the properties and integrity of the structural components materials directly which closely relates to their reliable and continuous operation. NDE can serve those purposes as well as many other cases when the material integrity is required to be estimated (e.g. in weld inspection after manufacture or repair).

1.1. Implementation of Ultrasonic Elastic Waves for NDE Purposes

In recent years ultrasonic wave interactions with elastic media found increasing implementation to evaluate material properties. This application has proven to be efficient, fast, reliable and inexpensive [1, 3]. The basic quantities to be measured are the attenuation $\alpha(\omega)$ and the wave phase velocity dispersion curve $v(\omega)$. A sample of the material under investigation is usually immersed in an elastic liquid (in most cases water) and either the transmitted signal or reflected from the sample (pulse-echo experiment) is measured, and the result is compared with the reference signal (without a sample). Essentially three different scan modes are used for measurements:

A-scan mode, representing the amplitude of the signal (usually voltage) versus the time;

B-scan mode, representing a 2D plot of the color coded amplitude versus position and time;

C-scan mode, representing the amplitude or time-of-flight (usually color coded) versus 2D position.

For the analysis of the obtained data, frequency spectral techniques are used (most often Fourier transform). The material properties and defect parameters may be extracted from $\alpha(\omega)$ and $v(\omega)$. An important step in the evaluation is the development of a model relating the measured quantities with the quantities of interest. For instance, in the case of composite materials' measurements, various models have been developed for the purpose of gauging the composite layered media [108, 109] or to evaluate the elastic stiffness constants [110, 111]. Since the B- and C-scans produce a huge amount of data, representing in general non-stationary signals, the Gabor Short Time Fourier Transform (STFT) and the Continuous Wavelet Transform (CWT) can play important role for simplification and speedup of data analysis and may increase the resolution of the measurements.

In the light of the discussion above, the ultrasonic applications for NDE purposes may be stated as follows:

(i) - thickness gauging - based on the known velocity and measured time-of-flight;

(ii) - material properties' characterization, e.g. measurement of the elastic stiffness constants;

(iii) - flaw detection and classification. The flaw types include voids, cracks, delamination regions (vacations or other defects in crystals, delamination regions of porosity in composite materials, etc.).

1.2. Numerical Modeling of the Wave Propagation and NDE

In all cases where the ultrasonic techniques are used, the modeling studies play an important role by providing:

a) physical insight into the nature of ultrasound wave interactions;

b) design data for planned ultrasonic tests;

c) simulation results for ultrasonic testing situations too difficult or expensive to replicate in the laboratory;

d) benchmark studies for the validation of defect characterization and property evaluation schemes.

Unfortunately, most NDE situations of practical interest preclude the use of classical analysis techniques based on plane wave considerations and scattering from idealized defect shapes. The modeling of ultrasonic NDE systems must include the ability to account for finite transducers apertures and complex defect geometries. These goals can be achieved only through properly applied numerical methods. Moreover, with the recent development in the field of Artificial Intelligence (AI), in particular Artificial Neural Networks, the modeling studies can provide necessary data, which may be used as a foundation of the automatic ultrasonic signal analyses with a very wide range of applications.

To achieve all these goals NDE requires further development in order to increase the efficiency and reliability of experimental data examination and to provide additional opportunities for data acquisition and interpretation. Though the wave propagation in homogeneous isotropic and anisotropy materials is well understood analytically [1, 3, 7-10, 13], the accurate analytical treatment of the wave propagation in many cases of practical interest is essentially impossible and development of numerical models becomes important for further NDE progress and for the computerization of data acquisition and analysis.

1.3. Objectives of the Present Work, Contributions and Structure of the Dissertation

Motivated by the wide opportunities for ultrasonic applications, in particular for crack and delamination detection and for evaluation of material properties together with the substantial advances in signal processing techniques, we established the objective of this dissertation to be as follows:

1) To develop an accurate numerical treatment of ultrasonic wave propagation in flawed media with finite sizes in two dimensions by using the finite-difference approach for solution of the wave equations and modeling the material boundaries.

2) To develop a realistic representation of the ultrasonic pulses used in practice and to study the model behavior when interaction of these pulses with material flaws and boundaries is modeled.

3) To apply time-frequency and wavelet techniques for the analysis of ultrasonic measurements.

The main contributions of the present work may be stated as follows:

1) Based on the finite difference approach, an algorithm was developed for solution of the wave equations in two-dimensional Cartesian geometry, and a computer code **JUNA** was developed for computation of the solution, representing propagating waves in the medium. The numerical scheme was tested up to 30,000 time steps and does not give rise to any instability.

2) A model for representing infinitesimally thin cracks and delaminations in the medium

was developed and implemented in the code **JUNA**. This scheme also was checked and does not cause any instability.

3) Analytical expressions for three-dimensional wavelet pulse, representing an exact analytical solution of the wave equations, was developed and implemented. Both plane wave excitation and surface source waves excitation of compression and shear wave modes, developed in the code **JUNA**, were analyzed in detail.

4) A set of dimensionless variables was introduced in the model in an effort to keep the roundoff error small and to provide an opportunity for computation in a wide range of parameter values.

5) The Gabor STFT was applied for analysis of the signal generated due to tangential stresses on the face of parallel to the free surface of a solid crack and allowed us to verify the analytically predicted peaks in the frequency distribution of the displacement component tangential to the crack face, which were found to be a function of the ratio d/a, where d is the crack depth and a is the length of the crack.

6) The angular distribution of the amplitudes of a compression elastic waves diffracted from a crack tip was calculated and compared with the analytical predictions and experimental measurements.

7. A method was developed based on the Gabor STFT and CWT for calculations of the dependence of the elastic wave velocity by the frequency and wave mode characterization in two cases: on the generated by **JUNA** Lamb waves and on experimental data from through-sample transmission ultrasonic measurements, when the sample is a SiC/SiC composite material.

This dissertation is organized as follows:

Chapter 2 contains a review of the existing, most commonly used theoretical and numerical methods of solving wave propagation problems with a short description of the mathematical foundation of each method. It also gives the mathematical foundation and explicit formulation of the methods used in this dissertation, mainly STFT and CWT.

Chapter 3 gives the details on the finite-difference method developed in this dissertation and a discussion of the conditions for accuracy and stability of the numerical algorithm. The explicit expressions for the finite-difference approximation of the wave equations and the boundary conditions in Cartesian and cylindrical two-dimensional geometries are given.

Chapter 4 gives a detailed analysis of the methods developed for the study of the elastic wave excitation and propagation which have been implemented in the computer code **JUNA**. Cases of parallel to the surface cracks, surface breaking cracks and Lamb wave modeling are presented. These, as well as a set of experimental data are analyzed by using the Gabor Short Time Fourier Transform (STFT) and Continuous Wavelet Transform (CWT) and the corresponding conclusions are made for the applicability of the numerical model and the use of the STFT and CWT methods for signal analysis.

Chapter 5 describes the original features of the present work and contains the main conclusions reached. Future research and applications of the present work are also discussed.

Appendixes provide additional information used in the dissertation. **Appendix A** gives the finite difference approximations used in the development of the finite difference model in Chapter 3. **Appendix B** gives detailed description of some types of guided waves such as Rayleigh waves, Lamb waves and Stoneley waves. **Appendix C** describes the input - output features of the code **JUNA**.

CHAPTER 2

Theory of Elasticity. Fundamentals of Short Time Fourier Transform and Continuous Wavelet Transform

In the first section of the present chapter the mathematical foundations of the theory of elastic waves propagation as it is considered by the acoustics theory will be presented and the basic mathematical terms and equations, used further for elastic waves propagation and interaction modeling, will be discussed. In the second section the mathematical theory of the Short Time Fourier Transform (STFT) and the Continuous Wavelet Transform (CWT) will be established in a way to clarify their further use for ultrasonic signal analyses.

2.1. Theory of elasticity

All material substances are composed of atoms, which may be forced into vibrations about their equilibrium positions. Many different patterns of vibrational motion may exist at this atomic level. However, in the present work we will be concerned only with material particles that are small but yet contain many atoms, moving in unison. Therefore, we will deal only with macroscopic phenomena, which is the topic of the acoustics, and is formulated as if matter were a continuum*.

---

* Structure at the microscopic level is of interest only insofar as it affects the medium's macroscopic properties.

2.1.1. Gradient Matrix and Strain

When the particles of the medium are displaced from their equilibrium positions, internal restoring forces arise. It is the elastic restoring forces between particles, combined with inertia of the particles, which lead to oscillatory motions of the medium. The particle motions at each position and time may be characterized by particle displacement at a given point at given time instant *t*. Thus, the elastic motion of the medium can be described mathematically by a continuous vector variable $\vec{\mathbf{U}}$ - the displacement vector field.

Let assign to each particle an equilibrium position vector $\vec{\mathbf{L}}$ and a displaced position vector $\vec{l}\,(\vec{\mathbf{L}},t)$, measured from some point of origin O, as shown in fig. 2-1.

The vector $\vec{l}$ is, in general, a time varying quantity and is also shown as a function of $\vec{\mathbf{L}}$. Both $\vec{\mathbf{L}}$ and $\vec{l}$ are continuous variables. The displacement of the particle located at $\vec{\mathbf{L}}$ is therefore

$$\vec{\mathbf{U}}(\vec{\mathbf{L}},t) = \vec{l}\,(\vec{\mathbf{L}},t) - \vec{\mathbf{L}}. \tag{2.1}$$

Since the term "material deformation" is understood to apply only when particles of a medium are displaced relative to each other, it is necessary to eliminate the rigid translations and rotations, where all particles of the body maintain their relative positions. Therefore $\vec{\mathbf{U}}$ in its form (2.1) does not itself provide a measurement of the material deformation. The rigid translational displacements may be eliminated [1, 3, 7-11, 13] by considering the differential form of (2.1) at constant *t*

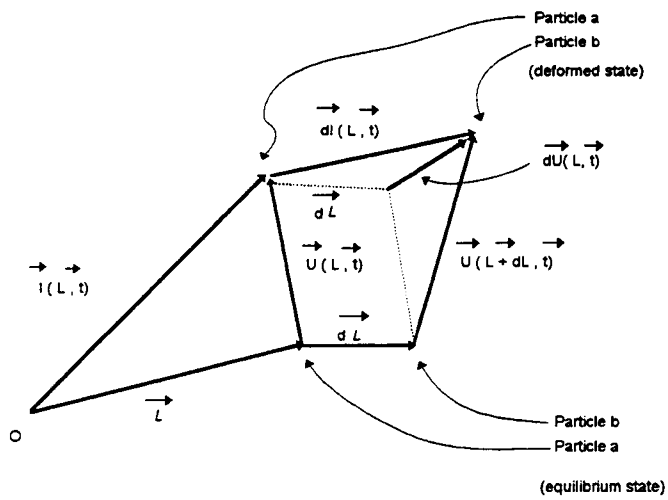

Figure 2-1. The displacement field between two neighboring points in a particular time instant inside the medium.

$$d\vec{\mathbf{U}}(\vec{\mathbf{L}},t) = d\vec{l}\,(\vec{\mathbf{L}},t) - d\vec{\mathbf{L}}\,. \tag{2.2}$$

Fig. 2-1 shows the displaced particle positions at a particular instant of time for two neighboring particles a and b. It is seen that for rigid translations since $\vec{\mathbf{U}}(\vec{\mathbf{L}},t)$ and $\vec{\mathbf{U}}(\vec{\mathbf{L}}+d\vec{\mathbf{L}},t)$ are equal, $d\vec{\mathbf{U}}(\vec{\mathbf{L}},t)$ is zero. Eq. (2.2) can be written in the form

$$d\vec{\mathbf{U}}(\vec{\mathbf{L}},t) = \frac{\partial}{\partial L_1}\ \vec{\mathbf{U}}(\vec{\mathbf{L}},t)dL_1 + \frac{\partial}{\partial L_2}\ \vec{\mathbf{U}}(\vec{\mathbf{L}},t)dL_2 + \frac{\partial}{\partial L_3}\ \vec{\mathbf{U}}(\vec{\mathbf{L}},t)dL_3, \tag{2.3}$$

where dL_1 , dL_2 , dL_3 are components of $d\vec{\mathbf{L}}$ with respect to some orthogonal coordinate system, and $\frac{\partial}{\partial t}\vec{\mathbf{U}}(\vec{\mathbf{L}},t) = 0$. In rectangular Cartesian coordinates we use the notation

$$\vec{\mathbf{U}}(\vec{\mathbf{L}},t) = \hat{x}U_1(\vec{\mathbf{L}},t) + \hat{y}U_2(\vec{\mathbf{L}},t) + \hat{z}U_3(\vec{\mathbf{L}},t),$$

where subscript i (i=1, 2, 3) denotes the corresponding vector components with respect to X-, Y-, and Z- axes respectively. Since $\hat{x}, \hat{y}$, and $\hat{z}$ are constant *, (2.2) in a matrix form becomes

$$\begin{bmatrix} dU_1(\vec{\mathbf{L}},t) \\ dU_2(\vec{\mathbf{L}},t) \\ dU_3(\vec{\mathbf{L}},t) \end{bmatrix} = \varepsilon(\vec{\mathbf{L}},t) \begin{bmatrix} dL_1 \\ dL_2 \\ dL_3 \end{bmatrix}, \tag{2.3}$$

where

$$\varepsilon(\vec{\mathbf{L}},t) = \begin{bmatrix} \frac{\partial U_1(\vec{\mathbf{L}},t)}{\partial x} & \frac{\partial U_1(\vec{\mathbf{L}},t)}{\partial y} & \frac{\partial U_1(\vec{\mathbf{L}},t)}{\partial z} \\ \frac{\partial U_2(\vec{\mathbf{L}},t)}{\partial x} & \frac{\partial U_2(\vec{\mathbf{L}},t)}{\partial y} & \frac{\partial U_2(\vec{\mathbf{L}},t)}{\partial z} \\ \frac{\partial U_3(\vec{\mathbf{L}},t)}{\partial x} & \frac{\partial U_3(\vec{\mathbf{L}},t)}{\partial y} & \frac{\partial U_3(\vec{\mathbf{L}},t)}{\partial z} \end{bmatrix}. \tag{2.4}$$

Equation (2.4) defines the displacement gradient matrix. Using (2.3), $d\vec{\mathbf{U}}(\vec{\mathbf{L}},t)$ may be calculated for any two neighboring particles from their equilibrium spacing $d\vec{\mathbf{L}}$ (fig.2-1).

As a measure of material deformation, $\varepsilon(\vec{\mathbf{L}},t)$, given by (2.4), is deficient in one respect. It does not go to zero for rigid rotations [1, 3, 7-11, 13]. A quantity that meets this requirement is the scalar quantity $\Delta = d\vec{l}(\vec{\mathbf{L}},t) - d\vec{\mathbf{L}}$, or a more convenient one

---

* A case of cylindrical coordinate system, when they are not constant, will be considered separately below.

$$\Delta = d\vec{l}^{\,2}(\vec{\mathbf{L}},t) - (d\vec{\mathbf{L}})^2,$$

and this is customarily defined as deformation.

In rectangular Cartesian coordinates

$$dl_1 = dL_1 + dU_1 = dL_1 + \frac{\partial U_1}{\partial x}dL_1 + \frac{\partial U_1}{\partial y}dL_2 + \frac{\partial U_1}{\partial z}dL_3, \tag{2.5a}$$

$$dl_2 = dL_2 + dU_2 = dL_2 + \frac{\partial U_2}{\partial x}dL_1 + \frac{\partial U_2}{\partial y}dL_2 + \frac{\partial U_2}{\partial z}dL_3, \tag{2.5b}$$

$$dl_3 = dL_3 + dU_3 = dL_3 + \frac{\partial U_3}{\partial x}dL_1 + \frac{\partial U_3}{\partial y}dL_2 + \frac{\partial U_3}{\partial z}dL_3. \tag{2.5c}$$

Therefore, we get

$$dl_1^2 = dL_1^2 + \left(\frac{\partial U_1}{\partial L_1}\right)^2 dL_1^2 + \left(\frac{\partial U_1}{\partial L_2}\right)^2 dL_2^2 + \left(\frac{\partial U_1}{\partial L_3}\right)^2 dL_3^2 + 2\frac{\partial U_1}{\partial L_1}dL_1^2 + 2\frac{\partial U_1}{\partial L_2}dL_1dL_2$$
$$+2\frac{\partial U_1}{\partial L_3}dL_1dL_3 + 2\frac{\partial U_1}{\partial L_1}\frac{\partial U_1}{\partial L_2}dL_1dL_2 + 2\frac{\partial U_1}{\partial L_1}\frac{\partial U_1}{\partial L_3}dL_1dL_3 + 2\frac{\partial U_1}{\partial L_2}\frac{\partial U_1}{\partial L_3}dL_2dL_3$$

Similar expressions are obtained for the other components dl_i. Finally, for the quantity Δ we get

$$\Delta = (dl)^2 - dL^2 = (dl_1)^2 + (dl_2)^2 + (dl_3)^2 - dL_1^2 - dL_2^2 - dL_3^2$$
$$= \left[\left(\frac{\partial U_1}{\partial L_1}\right)^2 + \left(\frac{\partial U_2}{\partial L_1}\right)^2 + \left(\frac{\partial U_3}{\partial L_1}\right)^2 + 2\frac{\partial U_1}{\partial L_1}\right]dL_1^2 + \left[\left(\frac{\partial U_1}{\partial L_2}\right)^2 + \left(\frac{\partial U_2}{\partial L_2}\right)^2 + \left(\frac{\partial U_3}{\partial L_2}\right)^2 + 2\frac{\partial U_2}{\partial L_2}\right]dL_2^2$$
$$+\left[\left(\frac{\partial U_1}{\partial L_3}\right)^2 + \left(\frac{\partial U_2}{\partial L_3}\right)^2 + \left(\frac{\partial U_3}{\partial L_3}\right)^2 + 2\frac{\partial U_3}{\partial L_3}\right]dL_3^2 + 2\left[\frac{\partial U_1}{\partial L_2} + \frac{\partial U_2}{\partial L_1} + \frac{\partial U_1}{\partial L_1}\frac{\partial U_1}{\partial L_2} + \frac{\partial U_2}{\partial L_1}\frac{\partial U_2}{\partial L_2}\right]dL_1dL_2$$

$$+2\left[\frac{\partial U_1}{\partial L_3}+\frac{\partial U_3}{\partial L_1}+\frac{\partial U_1}{\partial L_1}\frac{\partial U_1}{\partial L_3}+\frac{\partial U_3}{\partial L_1}\frac{\partial U_3}{\partial L_2}\right]dL_1dL_3+2\left[\frac{\partial U_3}{\partial L_2}+\frac{\partial U_2}{\partial L_3}+\frac{\partial U_3}{\partial L_2}\frac{\partial U_3}{\partial L_3}+\frac{\partial U_2}{\partial L_2}\frac{\partial U_2}{\partial L_3}\right]dL_2dL_3$$

which, in matrix form, can be written

$$\Delta = 2\left(\left[dL_1, dL_2, dL_3\right]\begin{bmatrix} S_{11} & S_{12} & S_{13} \\ S_{21} & S_{22} & S_{23} \\ S_{31} & S_{32} & S_{33}\end{bmatrix}\begin{bmatrix} dL_1 \\ dL_2 \\ dL_3\end{bmatrix}\right)$$

$$= 2S_{11}dL_1^2 + 2S_{22}dL_2^2 + 2S_{33}dL_3^2 + 2(S_{12}+S_{21})dL_1dL_2 + 2(S_{13}+S_{31})dL_1dL_3 \,. \qquad (2.6)$$
$$+2(S_{32}+S_{23})dL_2dL_3$$

Since only sum of the off-diagonal elements appears in (2.6), the matrix **S** may be chosen to be symmetric without loss of generality [1, 2, 7, 10], i. e.

$$S_{ij}(\bar{\mathbf{L}},t) = \frac{1}{2}\left(\frac{\partial U_i}{\partial L_j}+\frac{\partial U_j}{\partial L_i}+\sum_{k=1}^{3}\frac{\partial U_k}{\partial L_i}\frac{\partial U_k}{\partial L_j}\right),\ i,j=1,2,3. \qquad (2.7)$$

The Eq. (2.7) determines the strain matrix **S**, and it is seen that

$$\Delta = 2\sum_{i,j=1}^{3} S_{ij}(\bar{\mathbf{L}},t)dL_i dL_j\,, \qquad (2.8)$$

i.e. the strain field determines the deformation Δ in terms of the particle displacements $\bar{\mathbf{U}}(\bar{\mathbf{L}},t)$, and reduces to zero for all rigid motions [1, 2, 3, 7-11].

Despite of the fact that for some materials, like rubber, displacement gradients greater than unity are easily to reach, with more rigid materials, however, the displacement gradient must be kept below the range 10^{-4} to 10^{-3} if permanent deformation or fracture is to be avoided [1, 3, 7-11]. For displacement derivatives much smaller than this range, the quadratic terms in (2.4) are negligible and the linearized strain-displacement relation

$$S_{ij}(\vec{\mathbf{L}},t) = \frac{1}{2}\left(\frac{\partial U_i}{\partial L_j} + \frac{\partial U_j}{\partial L_i}\right), \text{ i,j} = 1, 2, 3. \tag{2.9}$$

can usually be used*. Moreover, since $dL_i = dl_i - dU_i$, the partial derivative of U_i with respect to L_j in (2.9) differs from $\frac{\partial U_i}{\partial l_j}$ only by quadratic and higher order terms [1, 7-11]

$$\frac{\partial U_i}{\partial L_j} = \frac{\partial U_i}{\partial l_j}\left(1 - \frac{\partial U_i}{\partial l_j}\right)^{-1}.$$

For linearized theory there is therefore no need to distinguish between components of the deformed position vector $\vec{l}$ and those of equilibrium position vector $\vec{\mathbf{L}}$. That is

$$\vec{\mathbf{L}} \cong \vec{l} = \hat{x}x + \hat{y}y + \hat{z}z = \vec{r}$$

in rectangular Cartesian coordinates. The linearized strain-displacement relation therefore becomes

$$S_{ij} = \frac{1}{2}\left(\frac{\partial U_i}{\partial r_j} + \frac{\partial U_j}{\partial r_i}\right), \text{ i, j} = 1, 2, 3. \tag{2.10}$$

In the same approximation the displacement gradient matrix (2.4) becomes

$$\varepsilon_{ij}(\vec{r},t) = \frac{\partial U_i}{\partial r_j}. \tag{2.11}$$

---

* In nonlinear acoustics, it is often necessary to use (2.4) instead of (2.9), as it is in [4, 5, 6].

As it can be shown [1, 2, 7, 10], further analysis of the transformation properties of the quantities **S** and $\mathcal{E}$ proves that both **S** and $\mathcal{E}$ are second rank tensors. The analysis of the equations (2.10) and (2.11) [1-3, 7-11] shows that **S** represents the symmetric part of $\mathcal{E}$. More precisely

$$\mathcal{E} = \mathbf{S} + \boldsymbol{\omega} ,$$

where

$$\omega_{ij} = \frac{1}{2}\left(\frac{\partial U_i}{\partial r_j} - \frac{\partial U_j}{\partial r_i}\right), \ \omega_{ij} = -\omega_{ji} . \qquad (2.11a)$$

As the way introducing the material deformation shows, the antisymmetric matrix $\boldsymbol{\omega}$ does not affect the medium deformation, and represents the equivoluminal part of the propagating elastic wave* .

2.1.2. Stresses.

There are essentially two different methods of exciting acoustic vibrations in a material body: **(a)** by applying long-range body forces acting directly upon particles in the interior of a body; and **(b)** by applying a surface forces at its boundary. The last case is commonly used for NDE purposes and will be considered below.

In the case of traction (or surface) forces the applied excitation does not act directly on particles within the body but is transmitted to them by means of the elastic forces (or stresses) acting between neighboring particles. Like the traction forces applied

---

* This part of the wave, related to the shear wave, does not exists in liquids and gases.

at the boundary, the stresses between particles act upon a surface rather than a volume and may therefore be described as internal traction forces.

In order to define the stresses acting on an arbitrary oriented surface, let consider the tetrahedral volume element in figure 2-2. Three of the faces are normal to the rectangular coordinate axes and the fourth face has its outward-directed normal $\vec{n} = (n_1, n_2, n_3)$ in an arbitrary direction. The fourth face, of area δS_n, may be an arbitrary oriented area within the body or may lie in the boundary surface.

Forces acting on the volume element δV include traction forces on the surfaces δS_x, δS_y, δS_z, δS_n and a body force density $\rho \vec{F} \delta V$, which may include both applied and internal force terms. Let σ_{in} (i=1, 2, 3) denotes the stress components of the stress σ_n, acting on a surface normal to $\vec{n}$ (fig. 2-2). Considering the forces all to be in balance, we obtain along X-axis

$$\sigma_{1n}\delta S_n - \sigma_{11}\delta S_x - \sigma_{12}\delta S_y - \sigma_{13}\delta S_z + \rho F_1 \delta V = 0. \tag{2.12}$$

Here and below σ_{ij} (i,j = x,y,z) are the stress components of a stress applied at a point. In a vibrating medium, these are always functions of spatial position. According to the definition, $\sigma_{ij}(\vec{r}, t)$ is the i^{th} component of the force density acting on the +j face of the infinitesimal volume element at position $\vec{r}$. This convention for the index order is the same as in references [1, 7, 8 and 9]* . If the volume element is allowed to approach zero, the body force term drops out because δV goes to zero faster than the δS's. Since δS_x is the

* However, the opposite convention is also used as in [10, 11].

projection of δS_n on the YZ-plane (fig.2-2)

$\delta S_x = n_1\, \delta S_n$

Similarly

$\delta S_y = n_2\, \delta S_n$, $\delta S_z = n_3\, \delta S_n$

and then (2.12) becomes

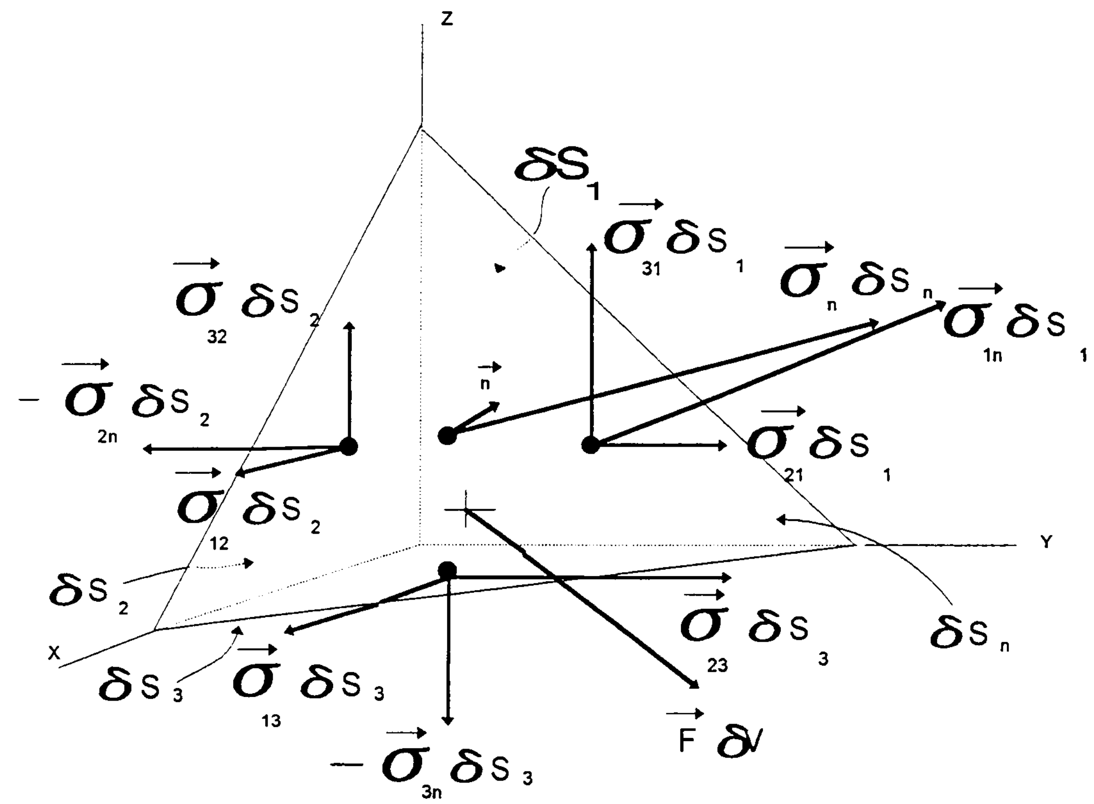

Figure 2-2. The stress acting on an arbitrary surface δS in the interior of a body.

$$\sigma_{1n} = \sigma_{11}n_1 + \sigma_{12}n_2 + \sigma_{13}n_3. \tag{2.13}$$

Repeating this calculation for Y- and Z-directions yields

$$\sigma_{2n} = \sigma_{21}n_1 + \sigma_{22}n_2 + \sigma_{23}n_3. \tag{2.14a}$$

$$\sigma_{3n} = \sigma_{31}n_1 + \sigma_{32}n_2 + \sigma_{33}n_3. \tag{2.14b}$$

In matrix form (2.13)-(2.14) become

$$\begin{bmatrix} t_1 \\ t_2 \\ t_3 \end{bmatrix} = \begin{bmatrix} \sigma_{11} & \sigma_{12} & \sigma_{13} \\ \sigma_{21} & \sigma_{22} & \sigma_{23} \\ \sigma_{31} & \sigma_{32} & \sigma_{33} \end{bmatrix} \begin{bmatrix} n_1 \\ n_2 \\ n_3 \end{bmatrix}. \tag{2.15}$$

Equation (2.15) may be written in a form

$$\vec{t} = \sigma.\vec{n}$$

where $\vec{t}$ is the traction force acting on a surface with normal $\vec{n}$ and σ is the stress-matrix. The last equation represents the well known Cauchy formula for the stress-traction relation.

The analysis of the transformation properties of the stress-component matrix σ [1, 7-11] shows that it is a true second-rank tensor.

2.1.3. Translational Equation of Motion.

Consider a vibrating material particle of arbitrary shape, with volume δV and surface area δS. The forces associated with its vibration are a body force density $\rho \vec{F} \delta V$ and traction forces applied to its surface by the neighboring particles. Using (2.15) and the

Newton's Law, we have

$$\int_{\delta S} \sigma.\vec{n}dS + \int_{\delta V} \rho\vec{F}dV = \int_{\delta V} \rho\frac{\partial^2\vec{U}}{\partial t^2}, \tag{2.16}$$

where ρ is the equilibrium mass density of the medium*. If the particle volume is sufficiently small, the integrands of the volume integral in (2.16) are essentially constant, and

$$\frac{\int_{\delta S} \sigma.\vec{n}ds}{\delta V} = \rho\frac{\partial^2\vec{U}}{\partial t^2} - \rho\vec{F}. \tag{2.17}$$

The limit of the left side when $\delta V \to 0$ is defined as the divergence of the stress [1, 2], i.e.

$$\vec{\nabla}.\sigma = lim_{\delta V \to 0}\frac{\int_{\delta S} \sigma.\vec{n}dS}{\delta V}$$

and (2.17) becomes

$$\vec{\nabla}.\sigma + \rho\vec{F} = \rho\frac{\partial^2\vec{U}}{\partial t^2}. \tag{2.18}$$

Equations (2.18) represent the translational equations of motion for a vibrating medium, and it is independent of the coordinate system used.

2.1.4. Rotational Equations of Motion .

Let consider a body torque acting on a particle, together with the torques arising

---

* Changes in the particle volume due to deformation lead to first order changes in the mass density, which can be ignored in linearized analysis [1, 7-11].

from traction forces acting on the particle surface. Figure 2-3 shows the Z-component of these torques for a rectangular particle. The net traction force is $(\sigma_{21} - \sigma_{12})\delta x \delta y \delta z$ and the rotational equation of motion is therefore

$$(\sigma_{21} - \sigma_{12} + G_z)\delta x \delta y \delta z = I_z \frac{\partial^2}{\partial t^2} \theta_z,$$

where G_z is the Z-component of the body torque density, θ_z is the rotational angle about Z, and $I_z = \rho \delta x \delta y \delta z (\delta x^2 + \delta y^2)_{average}$ is the moment of inertia about the Z-axis. As $\delta x, \delta y, \delta z \to 0$, I_z goes to zero faster than the volume of the element, and the equation of motion reduces to

$$\sigma_{21} - \sigma_{12} + G_z = 0.$$

Analogous results are obtained for rotation about the X- and Y- axes, giving the general rotational equation of motion

$$\sigma_{ij} - \sigma_{ji} + G_k = 0, \tag{2.19}$$

where subscripts occur in the cyclic patterns as shown in Table 2.1.

Table 2.1. Index rotation in Equation (2.19).

i	*j*	*k*
1	2	3
2	3	1
3	1	2

The rotational equation of motion (2.19) shows, first of all, that there are no inertial effects associated with particle rotation. This paradoxical result cames about because the inertial forces decrease faster than the torques when the elementary volume approaches zero. Another consequence from (2.19) is that the stress matrix is not symmetric ($\sigma_{ij} \neq \sigma_{ji}$) only when body torques are present. Such torques occur in media with permanent electric or magnetic polarization (ferroelectric or ferromagnetic materials). However, even in strongly polarized materials the body torques G_k are going to be of negligible importance in linearized vibration theory, and they will be neglected. Under these conditions the stress matrix is always symmetric, and particle rotation plays no part in the dynamics of the vibration.

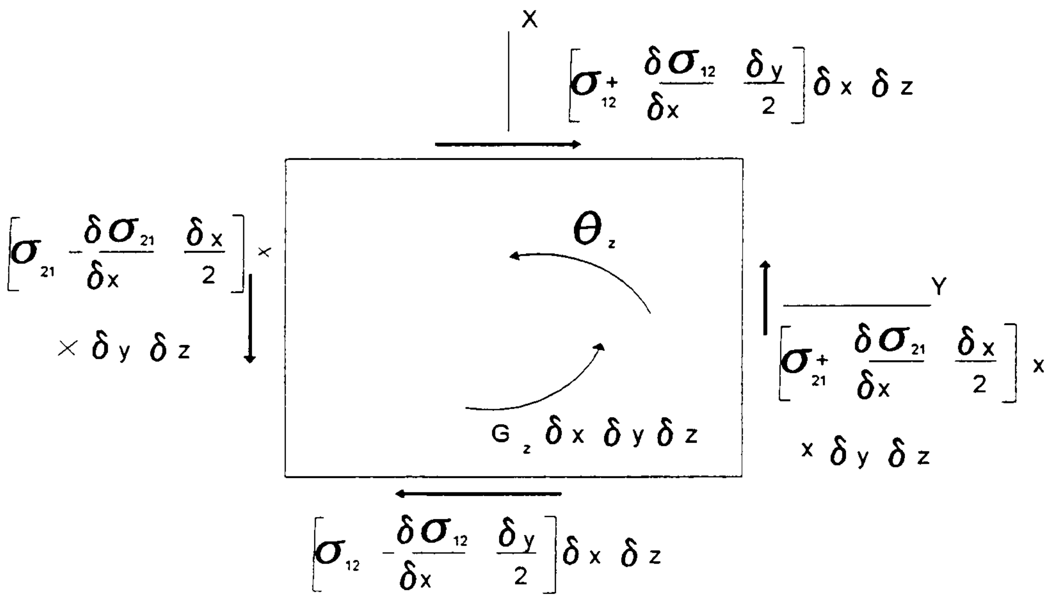

Figure 2-3. Torques along Z-axis for derivation of rotational equation of motion.

2.1.5. Hooke's Law

For small deformations it is an experimentally observed fact that the strain in a deformed body is linearly proportional to the applied stresses (Hooke's Law). As increasing deformations are imposed, the relationship between strain and stress becomes increasingly nonlinear, but the body still returns to its original state when the stress is removed. This is the region of linear and nonlinear deformation (fig. 2-4). If, however, the strain is increased past a certain limit, typically in the range 10^{-4} to 10^{-3} for relatively rigid materials, the deformation becomes permanent (plastic deformation) and the body ultimately fractures. Of interest for the acoustics is the region of the linear elastic deformation, where the Hooke's Law states that the strain is linearly proportional to the stress, or conversely, that the strain is linearly proportional to the strain. In general

$$\sigma_{ij} = \sum_{k,l=1}^{3} c_{ijkl} S_{kl}\,,\ i, j, k, l = 1,2,3. \tag{2.20}$$

The quantities c_{ijkl} are the elastic stiffness constants. They have small values for easily deformed materials and large values for very rigid materials.

Conversely to (2.20)

$$S_{kl} = \sum_{i,j=1}^{3} s_{klij} \sigma_{ij}\,,\ i, j, k, l = 1,2,3. \tag{2.21}$$

In this case s_{ijkl} are the compliance constants. The analysis of the transformation properties of **S** and **C** shows [1, 2, 7, 10] that both matrices are fourth rank tensors. It is seen from (2.20) and (2.21) that

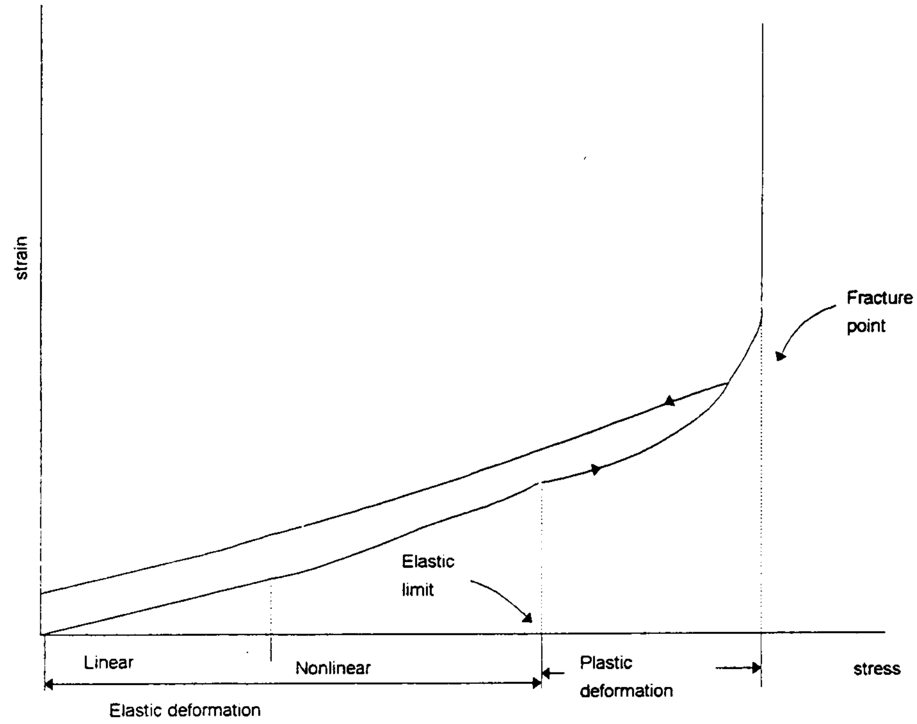

Figure 2-4. Typical strain-stress dependence for a rigid body with the regions of linear and nonlinear stress-strain relation and the region of plastic deformation.

$\mathbf{S} = \mathbf{C}^{-1}$,

i.e. the compliance matrix is simply the inverse of the stiffness matrix. Both matrices contain 81 constants each. However, they are not all independent. When the symmetry conditions are satisfied, $\sigma_{ij} = \sigma_{ji}$, and $S_{ij}=S_{ji}$, which due to the Hooke's Law leads to

$c_{ijkl} = c_{jikl} = c_{ijlk}$.

Similar argument shows that

$s_{ijkl} = s_{jikl} = s_{ijlk}$.

These conditions reduce the number of independent constants to 36. It can be also shown [1, 7-11] that

$c_{ijkl} = c_{klij}$, $s_{ijkl} = s_{klij}$,

which reduces the number of independent constants to 21. This is the maximum number of constants for any medium [1, 7-11]. Table 2-2 shows the number of constants for some anisotropic structure systems.

Table 2-2. Number of independent constants for some structure systems.

system	*Number of constants*
Triclinic	21
Monoclinic	13
Orthorhombic	9
Tetragonal	7
Trigonal	6
Hexagonal	5
Cubic	3
Isotropic	2

The symmetry of the stress and strain matrices together with the compliance and stiffness matrices' symmetry implies that two and correspondingly four matrix indices may be reduced to one and two respectively, according to the rule shown in table 2-3 [1, 7].

The general relations (2.20) and (2.21) then become

$$\sigma_I = \sum_{J=1}^{6} c_{IJ} S_J , \quad S_I = \sum_{J=1}^{6} s_{IJ} \sigma_J , \; I = 1,..,6, \quad s_{IJ} = \begin{cases} 1 \text{ if } I,J = 1,2,3 \\ 2 \text{ if or } J = 4,5,6 \\ 4 \text{ if } I \text{ and } J = 4,5,6 \end{cases} . \tag{2.22}$$

Table 2-3. The relation between the full and abbreviated subscripts.

I	*ij*
1	11
2	22
3	33
4	23, 32
5	13, 31
6	12, 21

In order to distinguish between abbreviated and regular subscripts, we shall further denote the abbreviated subscripts with capital letters such as I, J etc. = 1, ..., 6. The regular subscripts will be denoted with lower case letters, as i, j etc. = 1, 2, 3. The introduction of abbreviated subscripts is widely used in the literature and certainly provides economy of space and facilitates the algebraic manipulations. The matrices c_{IJ} (s_{IJ} correspondingly), however, do not represent true second rank tensors. In order to avoid additional efforts in performing coordinate transformations, W. L. Bond [12] has developed an efficient matrix technique for transformation of c_{IJ} , s_{IJ} , σ_I and S_I without necessity of the full subscript restoration.

Christoffel Equations and Christoffel Matrix

Introducing the wave velocity by

$$\vec{V} = \frac{\partial \vec{U}}{\partial t},$$

we obtain after differentiation with respect to t (2.20) and substituting the result in differentiated with respect to t (2.18)

$$\sum_{j=1}^{3}\sum_{k,l=1}^{3} \frac{1}{2} c_{ijkl}\left(\frac{\partial V_k}{\partial r_l}+\frac{\partial V_l}{\partial r_k}\right)=\rho\frac{\partial^2 V_i}{\partial t^2}-\frac{\partial F_i}{\partial t}. \tag{2.24}$$

In a force free region ($F_i = 0$), a uniform plane wave propagating along the direction $\vec{l} = \hat{x}l_1 + \hat{y}l_2 + \hat{z}l_3$ has field proportional to $e^{i(\omega t - k\vec{l}.\vec{r})}$, where $i^2 = -1$. In this case the differentiation with respect to r_i reduces to multiplication by $-ikl_i$ correspondingly. The derivation with respect to t reduces to multiplication by $-i\omega$. Substituting these results in (2.24), we obtain

$$\sum_{j,k,l} \frac{1}{2} c_{ijkl}(-k^2)(l_l V_k l_j + l_k V_l l_j) = -\rho\omega^2 V_i .$$

Introducing the matrix

$$l_{Lj} = l_{jL}^{T} = \begin{bmatrix} l_1 & 0 & 0 \\ 0 & l_2 & 0 \\ 0 & 0 & l_3 \\ 0 & l_3 & l_2 \\ l_3 & 0 & l_1 \\ l_2 & l_1 & 0 \end{bmatrix}, \tag{2.25}$$

where superscript T denotes transpose operation, and using the abbreviated subscripts, we obtain [1, 3, 7-11]

$$k^2\,(l_{iK}\, c_{KL}\, l_{Lj})V_j = k^2\,\Gamma_{ij}\,V_j = \rho\,\omega^2\,V_i\,. \tag{2.26}$$

Equation (2.26) represents the Christoffel equation. The matrix

$$\Gamma_{ij} = l_{iK}\, c_{KL}\, l_{Lj} \tag{2.27}$$

is the Christoffel matrix. Its elements are function only of the plane wave propagation direction and the stuffiness constants of the medium.

2.1.6. Problem Statement in Dynamic Elasticity. Uniqueness of the solution

We consider a body B occupying a regular region V in space, which may be bounded or unbounded, with interior V, closure $\overline{V}$ and boundary S. The system of equations governing the motion of a linearly elastic body consists of the stress equations of motion (2.18), Hooke's Law (2.20), and the strain-displacement relations (2.10). If the strain-displacement relations are substituted into Hooke's Law and the expressions for the stresses are subsequently substituted in the stress equations of motion, we obtain the displacement equations of motion

$$\frac{\partial}{\partial r_j}\left[c_{ijkl}\frac{\partial U_k}{\partial r_l}\right] + \rho F_i = \rho\frac{\partial^2 U_i}{\partial t^2}, \tag{2.28}$$

where it is assumed summation over repeated indices.

In general, we require

$$U_i(\bar{r},t) \in \mathcal{L}^2(\mathrm{VxT}) \cap \mathcal{L}^1(\overline{\mathrm{V}}\mathrm{xT}) \tag{2.29}$$

$$F_i(\bar{r},t) \in \mathcal{L}(\overline{\mathrm{V}}\mathrm{xT}), \tag{2.30}$$

where T is an arbitrary interval of time. The class of functions defined by $\mathcal{L}$ (R) consists of all tensor-valued functions of any order that are defined and continuous on a subset defined by R. For a positive integer n, $\mathcal{L}^n$ (R) consists of all functions in $\mathcal{L}$ (R) whose partial derivatives of order up to and including n exist on the interior of R, and there coincide with functions belonging to $\mathcal{L}$ (R) . If the displacement does not satisfy the smoothness requirements (2.29), separate relations must be satisfied by the discontinuities.

On the surface S of the undeformed body, the following boundary conditions are most common:

(i)-*displacement boundary conditions* - the three components u, v and w are prescribed on S;

(ii)-*traction boundary conditions* - the three traction components t_i are prescribed on S with unit normal **n**. Through Cauchy's formula (2.15) $t_i = \sigma_{ij} n_j$ it is seen that this case actually corresponds to conditions on three components of the stress tensor; in particular, in order to describe cracks in the medium it is necessary to apply zero-stress boundary conditions when the normal and tangential components of the stress tensor are zero;

(iii)-*mixed boundary conditions*-(i) is applied on part S_1 of S and (ii) on the remaining part $S-S_1$.

Other boundary conditions are also possible [13]. However, as it will be shown below, for the NDE purposes it is enough to deal with the conditions described above.

To complete the problem statement, we define initial conditions; in V we have at time $t = 0$

$$\vec{U}(\vec{r},0) = \vec{U}_0(\vec{r}), \quad \frac{\partial \vec{U}(\vec{r},0)}{\partial t} = \vec{U}_1(\vec{r}). \tag{2.31}$$

It is not difficult to show that the solution of the problem stated above satisfies the criterion of uniqueness for an appropriate set of boundary conditions. For a discussion of the uniqueness theorem we refer to the proof due to von Neumann, which is based on energy considerations [13, 17]. For a discussion of the uniqueness theorem for an unbounded domain we refer to the paper by Wheeler and Sternberg [18].

In addition to the conditions stated above, we shall deal with interfaces between media with different elastic properties. The mathematical representation of the interfaces is provided by the requirements that the displacement components together with their first spatial derivatives are continuous along the interfaces. In terms of the elasticity theory the last condition is provided by the continuity of the corresponding stress components in the media at the both sides of the interface at each interface point. The explicit expressions for the interface in 2-dimensional Cartesian and cylindrical geometry will be stated in sections 2.1.7 and 2.1.8 respectively.

2.1.7. Elastic Wave Equations in 3- and 2- Dimensional Cartesian Geometry in Isotropy Medium

Combining the linearized stress-strain relations (2.10), the translational equations of motion (2.18) and the Hooke's Law (2.20), one may obtain the following system of second order partial differential equations for the displacement components

$$c_{ijkl}U_{k,lj} + \rho f_i = \rho \ddot{U}_i, \quad U_{k,lj} = \frac{\partial^2 U_k}{\partial r_l \partial r_j}, \tag{2.32}$$

where it is assumed that c_{ijkl} is homogeneous. In fact, in the case of linearly elastic medium it can be shown [1, 7-11, 13] that the stress-strain matrix **C** becomes

$$c_{ijkl} = \lambda\delta_{ij}\delta_{kl} + \mu(\delta_{ik}\delta_{jl} + \delta_{il}\delta_{jk}),\ \delta_{ij} = \begin{cases} 0 & i \neq j \\ 1 & i = j \end{cases},\ i, j, k, l = 1, 2, 3, \tag{2.33}$$

and a summation over the repeated indices is assumed.

Using the abbreviation indices notation, it is seen that in that case there are only two independent constants, mainly $c_{12} = \lambda$, $c_{44}=\mu$, and the relation $c_{12}=c_{11} - 2c_{44}$ is proven [1, 7] to be the general elastic isotropy condition. The stiffness matrix for isotropy medium in abbreviated notation therefore becomes

$$\mathbf{C} = \begin{bmatrix} \lambda+2\mu & \lambda & \lambda & 0 & 0 & 0 \\ \lambda & \lambda+2\mu & \lambda & 0 & 0 & 0 \\ \lambda & \lambda & \lambda+2\mu & 0 & 0 & 0 \\ 0 & 0 & 0 & \mu & 0 & 0 \\ 0 & 0 & 0 & 0 & \mu & 0 \\ 0 & 0 & 0 & 0 & 0 & \mu \end{bmatrix}. \tag{2.34}$$

The Hooke's law then assumes the well-known form

$$\sigma_{ij} = \lambda\varepsilon_{kk}\delta_{ij} + \mu\varepsilon_{ij}. \tag{2.35}$$

Equation (2.35) contains two elastic constants λ and μ, which are known as Lamé's elastic constants. The relations between λ and μ, and the commonly used in engineering practice Young modulus E, bulk modulus B and Poisson ratio ν, are shown in table 2-4. Using (2.33) and (2.35), the system (2.32) can be rewritten in vector form

$$\mu\vec{\nabla}^2\vec{U} + (\mu+\lambda)\vec{\nabla}\vec{\nabla}.\vec{U} + \rho\vec{F} = \rho\frac{\partial^2\vec{U}}{\partial t^2}. \tag{2.36}$$

Equation (2.36) shows the highly complex nature of the displacement wave equations. In fact, (2.36) represents a system of 3 coupled second order linear differential equation s of hyperbolic type for the three displacement components. However, it is possible to obtain a simpler set of equations by introducing the scalar and vector potentials Φ and $\vec{H}$ such that

$$\vec{U} = \vec{\nabla}\Phi + \vec{\nabla}x\vec{H}\,,\ \vec{\nabla}.\vec{H} = 0\,. \tag{2.37}$$

Table 2-4. Relationships among isotropic elastic constants

	E, ν	E, μ	λ, μ
λ	$\frac{E\nu}{(1+\nu)(1-2\nu)}$	$\frac{\mu(E-2\mu)}{3\mu-E}$	λ
μ	$\frac{E}{2(1+\nu)}$	μ	μ
E	E	E	$\frac{\mu(3\lambda+2\mu)}{\lambda+\mu}$
B	$\frac{E}{3(1-2\nu)}$	$\frac{\mu E}{3(3\mu-E)}$	$\lambda+\frac{2}{3}\mu$
ν	ν	$\frac{E-2\mu}{2\mu}$	$\frac{\lambda}{2(\lambda+\mu)}$

The resolution of a vector field into the gradient of a scalar and the curl of a zero-divergence vector is due to a theorem by Helmholtz [2]. The condition $\vec{\nabla}.\vec{H} = 0$ provides the necessary additional conditions to uniquely determine the three components of $\vec{U}$ from the four components of Φ, $\vec{H}$. We also express

$$\vec{F} = \vec{\nabla}f + \vec{\nabla}x\vec{B}, \ \vec{\nabla}.\vec{B} = 0. \tag{2.38}$$

Substituting (2.37) and (2.38) in (2.36) gives

$$(\lambda + \mu)\vec{\nabla}\vec{\nabla}(\vec{\nabla}\Phi + \vec{\nabla}x\vec{H}) + \mu\vec{\nabla}^2(\vec{\nabla}\Phi + \vec{\nabla}x\vec{H}) + \rho(\vec{\nabla}f + \vec{\nabla}x\vec{B}) = \rho\left(\vec{\nabla}\frac{\partial^2\Phi}{\partial t^2} + \vec{\nabla}x\frac{\partial^2\vec{H}}{\partial t^2}\right)$$

These regroup to*

$$\vec{\nabla}\left\{(\lambda + 2\mu)\vec{\nabla}^2\Phi + \rho f - \rho\frac{\partial^2\Phi}{\partial t^2}\right\} + \vec{\nabla}x\left\{\mu\vec{\nabla}^2\vec{H} + \rho\vec{B} - \rho\frac{\partial^2\vec{H}}{\partial t^2}\right\} = 0. \tag{2.39}$$

This equation will be satisfied if each bracketed term vanishes, thus giving

$$(\lambda + 2\mu)\vec{\nabla}^2\Phi + \rho f = \rho\frac{\partial^2\Phi}{\partial t^2}, \tag{2.40}$$

$$\mu\vec{\nabla}^2\vec{H} + \rho\vec{B} = \rho\frac{\partial^2\vec{H}}{\partial t^2}. \tag{2.41}$$

While it is evident that (2.39) will be satisfied if equations (2.40) and (2.41) hold, it would also appear that values of Φ and $\vec{H}$ not satisfying these equations might still cause the

---

* We use $\vec{\nabla}.\vec{\nabla}\Phi = \vec{\nabla}^2\Phi$, the fact that $\vec{\nabla}^2(\vec{\nabla}\Phi) = \vec{\nabla}(\vec{\nabla}^2\Phi)$ and the fact that $\vec{\nabla}.\vec{\nabla}x\vec{H} = 0$.

original equation (2.39) to be satisfied. This aspect, in fact, has been investigated by Sternberg and Gintin [14-16], and it has been established that the complete solution is given by the solution of (2.40) and (2.41).

Introducing the notation

$$p^2 = \frac{\lambda + 2\mu}{\rho}; s^2 = \frac{\mu}{\rho}, \tag{2.42}$$

and assuming that f=0, $\vec{B} = 0$ (force free medium), we obtain for (2.36), (2.40) and (2.41)

$$s^2\vec{\nabla}^2\vec{U} + (p^2 - s^2)\vec{\nabla}\vec{\nabla}.\vec{U} = \frac{\partial^2\vec{U}}{\partial t^2}, \tag{2.43}$$

$$p^2\vec{\nabla}^2\Phi = \frac{\partial^2\Phi}{\partial t^2}, \tag{2.44}$$

$$s^2\vec{\nabla}^2\vec{H} = \frac{\partial^2\vec{H}}{\partial t^2}. \tag{2.45}$$

Equations (2.44) and (2.45) represent a wave motion of a scalar field Φ, propagating with a velocity p, and a vector field $\vec{H}$, propagating with a velocity s. These waves can exist independent - or uncoupled - from one another, and propagate with different velocities.

Defining the dilatation of the material as [3]

$$\Delta = \vec{\nabla}\vec{U} = \sum_{i=1}^{3} S_{ii} \tag{2.46}$$

and performing a divergence operation on equation (2.43), we obtain the dilatational (or irrotational) equation of motion

$$p^2\vec{\nabla}^2\Delta = \frac{\partial^2\Delta}{\partial t^2}. \tag{2.47}$$

Comparing (2.44) and (2.47), we see [3] that the scalar potential Φ is associated with the dilatational part of the propagating disturbance, customarily called compression wave. Further defining the rotational vector $\vec{\omega}$ as

$$\vec{\omega} = \frac{1}{2}\operatorname{curl}\bar{U} \tag{2.48}$$

and performing the operation of curl on (2.43), we obtain

$$s^2\vec{\nabla}^2\vec{\omega} = \frac{\partial^2\vec{\omega}}{\partial t^2}. \tag{2.49}$$

Thus, the rotational (or equivoluminal) waves propagate with velocity *s*. Comparing (2.49) with (2.45), it is seen that the vector potential $\vec{H}$ is associated with the rotational part of the propagating disturbance, customarily called shear wave.

Let us denote the three components of $\bar{U}$ by u, v and w. In 2D Cartesian geometry (2.43) splits in two uncorrelated subsets of equations: one set of two coupled equations for u and v and one equation for w, i.e.

$$\left|\begin{array}{l}(p^2 - s^2)(u_{xx} + v_{xy}) + s^2(u_{xx} + u_{yy}) + f_1 = u_{tt} \\ (p^2 - s^2)(u_{xy} + v_{yy}) + s^2(v_{xx} + v_{yy}) + f_2 = v_{tt}\end{array}\right. \tag{2.50}$$

and

$$s^2(w_{xx} + w_{yy}) + f_3 = w_{tt} \tag{2.51}$$

where it is introduced the notation $u_{xx} = \frac{\partial^2 u}{\partial x^2}, u_{xy} = \frac{\partial^2 u}{\partial x \partial y}, u_{tt} = \frac{\partial^2 u}{\partial t^2}$ etc. The corresponding stress-tensor components in XY geometry by using (2.35) and the notation introduced above are

$$\sigma_{xx} = \lambda(u_x + v_y) + 2\mu u_x$$

$$\sigma_{yy} = \lambda(u_x + v_y) + 2\mu v_y \tag{2.52}$$

$$\sigma_{xy} = \mu\,(u_y + v_x)$$

The equation (2.51) represents the antiplane equation of motion in 2D geometry. In fact, its solution is a wave polarized along Z-direction* . It is seen that this wave propagates independently with the same velocity as in Y-direction polarized wave, which is a solution of (2.50). Shear waves that propagate along the same direction with same velocity are called degenerate. This is an important characteristic because, in any linear system, degenerate waves may be combined in any manner to produce wave solutions with a wide variety of polarizations. This is a physical phenomenon of fundamental importance.

The equations (2.50)-(2.51) play fundamental role in 2D NDE modeling of the wave propagation, where they are subject of initial and boundary conditions.

The initial conditions are stated as in (2.31). The zero-displacement boundary conditions do not represent any difficulty and will not be discussed further. The traction-free boundary conditions represent the important for NDE case of free surfaces. Due to the Cauchy's formula (2.15), for a free surface parallel to X-axis we obtain in the case of

---

* In the monograph by Brekhovskikh [19] it is called a wave with vertical polarization.

the system (2.50)

$$\begin{vmatrix}\sigma_{xy} = \mu(u_y + v_x) = 0 \\ \sigma_{yy} = \lambda(u_x + v_y) + 2\mu v_y = 0\end{vmatrix}, \tag{2.53}$$

where (2.52) is used. Both equations in (2.53) must be satisfied simultaneously.

For a free surface parallel to Y-axis, we obtain, again using (2.15) and (2.52)

$$\begin{vmatrix}\sigma_{xy} = \mu(u_y + v_x) = 0 \\ \sigma_{xx} = \lambda(u_x + v_y) + 2\mu u_x = 0\end{vmatrix}. \tag{2.54}$$

Equations (2.54) again must be satisfied simultaneously.

In the case of equation (2.51), the only non-trivial stress component to be considered is

$$\sigma_{xy} = \mu(w_x + w_y) = 0. \tag{2.55}$$

Let now consider an interface between two elastic media with different elastic properties. Using the superscripts (1) and (2) to denote variables corresponding to the media 1 and 2 at the both sides of the interface, in two dimensions for an interface parallel to the X-axis we have

$$\sigma_{xy}^{(1)} = \sigma_{xy}^{(2)}, \; \sigma_{yy}^{(1)} = \sigma_{yy}^{(2)},$$

or, using (2.52)

$$\lambda^{(1)}(u_x^{(1)} + v_y^{(1)}) + 2\mu^{(1)}v_y^{(1)} = \lambda^{(2)}(u_x^{(2)} + v_y^{(2)}) + 2\mu^{(2)}v_y^{(2)}, \tag{2.56}$$

$$\mu^{(1)}(u_y^{(1)} + v_x^{(1)}) = \mu^{(2)}(u_y^{(2)} + v_x^{(2)}).$$

Similarly, for an interface parallel to Y-axis we have

$$\sigma_{xx}^{(1)} = \sigma_{xx}^{(2)}, \ \sigma_{xy}^{(1)} = \sigma_{xy}^{(2)},$$

which, using (2.52), gives

$$\lambda^{(1)}(u_x^{(1)} + v_y^{(1)}) + 2\mu^{(1)}u_x^{(1)} = \lambda^{(2)}(u_x^{(2)} + v_y^{(2)}) + 2\mu^{(2)}u_x^{(2)}, \tag{2.57}$$

$$\mu^{(1)}(u_y^{(1)} + v_x^{(1)}) = \mu^{(2)}(u_y^{(2)} + v_x^{(2)}).$$

These equations, together with the requirements for displacement continuity along the interfaces, given by

$$\vec{U}^{(1)} = \vec{U}^{(2)} \tag{2.58}$$

give the set of conditions along the interface between two media with different elastic properties.

2.1.8. Elastic Waves in 3- and 2- Dimensional Cylindrical Coordinates in Isotropy Medium

To obtain the displacement equations in cylindrical coordinates for isotropy medium, we need explicit expressions for the displacement spatial derivatives and for the stiffness matrix **C**. For this purpose we shall use (2.3), taking into account that the coordinate vectors in this case are no longer constants.

In this case, the components of $d\bar{\mathbf{L}}$ are $dL_1 = dr$, $dL_2 = rd\varphi$, $dL_3 = dz$, and the unit vectors are denoted by $\hat{r}$, $\hat{\varphi}$ and $\hat{z}$. Equation (2.3) then takes the form

$$d\vec{\mathbf{U}} = \frac{\partial \vec{\mathbf{U}}}{\partial r}(dr) + \frac{1}{r}\frac{\partial \vec{\mathbf{U}}}{\partial \varphi}(rd\varphi) + \frac{\partial \vec{\mathbf{U}}}{\partial z}dz. \tag{2.59}$$

By small increments in *r*, *φ* and *z*, one can show [1, 2, 7, 10] that

$$\begin{array}{lll} \frac{\partial}{\partial r}\hat{r} = 0 & \frac{\partial}{\partial r}\hat{\varphi} = 0 & \frac{\partial}{\partial r}\hat{z} = 0 \\ \frac{\partial}{\partial \varphi}\hat{r} = -\hat{\varphi} & \frac{\partial}{\partial \varphi}\hat{\varphi} = -\hat{r} & \frac{\partial}{\partial \varphi}\hat{z} = 0. \\ \frac{\partial}{\partial z}\hat{r} = 0 & \frac{\partial}{\partial z}\hat{\varphi} = 0 & \frac{\partial}{\partial z}\hat{z} = 0 \end{array} \tag{2.60}$$

Let denote with *u*, *v* and *w* the corresponding displacement components with respect to *r*, *φ* and *z*. Substitution of $\vec{\mathbf{U}} = \hat{r}u + \hat{\varphi}v + \hat{z}w$ in (2.59) then gives

$$d\vec{\mathbf{U}} = \left(\frac{\partial u}{\partial r}\hat{r} + \frac{\partial v}{\partial r}\hat{\varphi} + \frac{\partial w}{\partial r}\hat{z}\right)dr + \frac{1}{r}\left[\left(\frac{\partial u}{\partial \varphi} - v\right)\hat{r} + \left(\frac{\partial v}{\partial \varphi} + u\right)\hat{\varphi} + \frac{\partial w}{\partial \varphi}\hat{z}\right]rd\varphi \\ + \left(\frac{\partial u}{\partial z}\hat{r} + \frac{\partial v}{\partial z}\hat{\varphi} + \frac{\partial w}{\partial z}\hat{z}\right)dz ,$$

and the gradient therefore has the matrix representation

$$\vec{\nabla}\vec{\mathbf{U}} \to \begin{bmatrix} \frac{\partial u}{\partial r} & \frac{1}{r}\frac{\partial u}{\partial \varphi} - \frac{v}{r} & \frac{\partial u}{\partial z} \\ \frac{\partial v}{\partial r} & \frac{1}{r}\frac{\partial v}{\partial \varphi} + \frac{u}{r} & \frac{\partial v}{\partial z} \\ \frac{\partial w}{\partial r} & \frac{1}{r}\frac{\partial w}{\partial \varphi} & \frac{\partial w}{\partial z} \end{bmatrix}. \tag{2.61}$$

The strain matrix then becomes

$$\mathbf{S}=\frac{1}{2}(\vec{\nabla}\vec{\mathbf{U}}+\vec{\nabla}\vec{\mathbf{U}}^T)=\begin{bmatrix} \frac{\partial u}{\partial r} & \frac{1}{2}\left(\frac{\partial v}{\partial r}+\frac{1}{r}\frac{\partial u}{\partial \varphi}-\frac{v}{r}\right) & \frac{1}{2}\left(\frac{\partial u}{\partial z}+\frac{\partial w}{\partial r}\right) \\ \frac{1}{2}\left(\frac{\partial v}{\partial r}+\frac{1}{r}\frac{\partial u}{\partial \varphi}-\frac{v}{r}\right) & \frac{1}{r}\frac{\partial v}{\partial \varphi}+\frac{u}{r} & \frac{1}{2}\left(\frac{\partial v}{\partial z}+\frac{1}{r}\frac{\partial w}{\partial \varphi}\right) \\ \frac{1}{2}\left(\frac{\partial u}{\partial z}+\frac{\partial w}{\partial r}\right) & \frac{1}{2}\left(\frac{\partial v}{\partial z}+\frac{1}{r}\frac{\partial w}{\partial \varphi}\right) & \frac{\partial w}{\partial z} \end{bmatrix}. \tag{2.62}$$

In abbreviated subscript notation the strain is represented by a six-element column vector

$$\begin{aligned} S_1 &= S_{rr} \quad S_4 = 2S_{\varphi z} \\ S_2 &= S_{\varphi\varphi} \quad S_5 = 2S_{rz} \,. \\ S_3 &= S_{zz} \quad S_6 = 2S_{r\varphi} \end{aligned} \tag{2.63}$$

Coordinate transformation laws for stiffness can be used to obtain the stiffness matrix in cylindrical coordinates. The orthogonal transformation matrix from Cartesian to cylindrical coordinates is given by [1, 2, 7, 10]

$$\mathbf{a}=\begin{bmatrix} \cos\varphi & \sin\varphi & 0 \\ -\sin\varphi & \cos\varphi & 0 \\ 0 & 0 & 1 \end{bmatrix}. \tag{2.64}$$

Since for isotropy medium $\left(\frac{c_{11}-c_{12}}{2}-c_{44}\right)=0$, for the stiffness matrix we obtain exactly the form (2.34). Then, using the Hooke's Law (2.20), we obtain

$$\sigma_1=\sigma_{rr}=c_{11}S_1+c_{12}S_2+c_{13}S_3=(\lambda+2\mu)\frac{\partial u}{\partial r}+\lambda\left(\frac{1}{r}\frac{\partial v}{\partial \varphi}+\frac{u}{r}+\frac{\partial w}{\partial z}\right), \tag{2.65a}$$

$$\sigma_2=\sigma_{\varphi\varphi}=c_{21}S_1+c_{22}S_2+c_{23}S_3=(\lambda+2\mu)\left(\frac{1}{r}\frac{\partial v}{\partial \varphi}+\frac{u}{r}\right)+\lambda\left(\frac{\partial u}{\partial r}+\frac{\partial w}{\partial z}\right), \tag{2.65b}$$

$$\sigma_3 = \sigma_{zz} = c_{31}S_1 + c_{32}S_2 + c_{33}S_3 = (\lambda + 2\mu)\frac{\partial w}{\partial z} + \lambda\left(\frac{\partial u}{\partial r} + \frac{1}{r}\frac{\partial v}{\partial \varphi} + \frac{u}{r}\right), \tag{2.65c}$$

$$\sigma_4 = \sigma_{\varphi z} = c_{44}S_4 = \mu\left(\frac{\partial v}{\partial z} + \frac{1}{r}\frac{\partial w}{\partial \varphi}\right), \tag{2.65d}$$

$$\sigma_5 = \sigma_{rz} = c_{55}S_5 = \mu\left(\frac{\partial u}{\partial z} + \frac{\partial w}{\partial r}\right), \tag{2.65e}$$

$$\sigma_6 = \sigma_{r\varphi} = c_{66}S_6 = \mu\left(\frac{1}{r}\frac{\partial u}{\partial \varphi} - \frac{u}{r} + \frac{\partial v}{\partial r}\right). \tag{2.65f}$$

Using (2.65) and the equations of motion (2.18), we obtain

$$\left|\begin{array}{l} \left(\dfrac{\partial}{\partial r} + \dfrac{1}{r}\right)\sigma_1 - \dfrac{1}{r}\sigma_2 + \dfrac{\partial}{\partial z}\sigma_5 + \dfrac{1}{r}\dfrac{\partial}{\partial \varphi}\sigma_6 = \rho\dfrac{\partial^2 u}{\partial t^2} \\ \dfrac{1}{r}\dfrac{\partial}{\partial \varphi}\sigma_2 + \dfrac{\partial}{\partial z}\sigma_4 + \left(\dfrac{\partial}{\partial r} + \dfrac{2}{r}\right)\sigma_6 = \rho\dfrac{\partial^2 v}{\partial t^2} \\ \dfrac{\partial}{\partial z}\sigma_3 + \dfrac{1}{r}\dfrac{\partial}{\partial \varphi}\sigma_4 + \left(\dfrac{\partial}{\partial r} + \dfrac{1}{r}\right)\sigma_5 = \rho\dfrac{\partial^2 w}{\partial t^2} \end{array}\right. \tag{2.66}$$

Equations (2.65) together with the system (2.66) represent the equations of motion in general 3-dimensional cylindrical geometry. Assuming that all variables depend on *r* and *z* and the derivatives with respect to φ are zero, we obtain for the case of 2-dimensional R-Z geometry*

* The same procedure can be used to obtain the equations of motion in the case of 2-dimensional R-φ geometry.

$$\sigma_1 = \sigma_{rr} = (\lambda + 2\mu)\frac{\partial u}{\partial r} + \lambda\left(\frac{u}{r} + \frac{\partial w}{\partial z}\right), \ \sigma_2 = \sigma_{\varphi\varphi} = (\lambda + 2\mu)\frac{u}{r} + \lambda\left(\frac{\partial u}{\partial r} + \frac{\partial w}{\partial z}\right), \tag{2.67a}$$

$$\sigma_3 = \sigma_{zz} = (\lambda + 2\mu)\frac{\partial w}{\partial z} + \lambda\left(\frac{\partial u}{\partial r} + \frac{u}{r}\right), \ \sigma_4 = \sigma_{\varphi z} = \mu\frac{\partial v}{\partial z}, \tag{2.67b}$$

$$\sigma_5 = \sigma_{rz} = \mu\left(\frac{\partial u}{\partial z} + \frac{\partial w}{\partial r}\right), \ \sigma_6 = \sigma_{r\varphi} = \mu\left(\frac{\partial v}{\partial r} - \frac{u}{r}\right), \tag{2.67c}$$

and the equations of motion for u, w are

$$\left|\begin{aligned} &p^2\left(\frac{\partial^2 u}{\partial r^2} + \frac{1}{r}\frac{\partial u}{\partial r} + \frac{\partial^2 w}{\partial r \partial z} - \frac{u}{r^2}\right) + s^2\left(\frac{\partial^2 u}{\partial z^2} - \frac{\partial^2 w}{\partial r \partial z}\right) = \frac{\partial^2 u}{\partial t^2} \\ &p^2\left(\frac{\partial^2 w}{\partial z^2} + \frac{1}{r}\frac{\partial u}{\partial z} + \frac{\partial^2 u}{\partial r \partial z}\right) + s^2\left(\frac{\partial^2 w}{\partial r^2} + \frac{1}{r}\frac{\partial w}{\partial r} - \frac{1}{r}\frac{\partial u}{\partial z} - \frac{\partial^2 u}{\partial r \partial z}\right) = \frac{\partial^2 w}{\partial t^2} \end{aligned}\right., \tag{2.68}$$

where p and s are defined with (2.49). The equation for v in this case is

$$\frac{p^2}{r}\frac{\partial u}{\partial r} + (p^2 - 2s^2)\left(\frac{\partial^2 u}{\partial r \partial z} + \frac{\partial^2 w}{\partial z^2}\right) + s^2\left(\frac{\partial^2 v}{\partial r^2} + \frac{1}{r}\frac{\partial v}{\partial r} - \frac{v}{r^2}\right) = \frac{\partial^2 v}{\partial t^2}. \tag{2.69}$$

As it is seen from (2.69), a "pure" antiplane motion in the sense as it is in Cartesian coordinates does not exist since (2.69) depends on derivatives of u and w. In other words, a polarized along $\hat{\varphi}$-direction independent shear wave in R-Z cylindrical geometry does not exist.

On a free surface at $r = r_o$ = constant, we have the boundary conditions

$$\sigma_{rr} = (\lambda+2\mu)\frac{\partial u}{\partial r} + \lambda\left(\frac{u}{r_0} + \frac{\partial w}{\partial z}\right) = 0$$
$$\sigma_{rz} = \mu\left(\frac{\partial u}{\partial z} + \frac{\partial w}{\partial r}\right) = 0 \qquad (2.70)$$

On a free surface at Z=const.

$$\sigma_{zz} = (\lambda+2\mu)\frac{\partial w}{\partial z} + \lambda\left(\frac{\partial u}{\partial r} + \frac{u}{r}\right) = 0$$
$$\sigma_{rz} = \mu\left(\frac{\partial u}{\partial z} + \frac{\partial w}{\partial r}\right) = 0 \qquad (2.71)$$

Equations (2.70) ((2.71) respectively) must be satisfied simultaneously.

The conditions on an interface at $r = r_o$ between the two media (1) and (2) with different elastic properties become

$$\sigma_{rr}^{(1)} = \sigma_{rr}^{(2)}, \quad u^{(1)} = u^{(2)}$$
$$\sigma_{rz}^{(1)} = \sigma_{rz}^{(2)}, \quad v^{(1)} = v^{(2)} \qquad (2.72)$$

On an interface at $z=z_o$ we have

$$\sigma_{zz}^{(1)} = \sigma_{zz}^{(2)}, \quad u^{(1)} = u^{(2)}$$
$$\sigma_{rz}^{(1)} = \sigma_{rz}^{(2)}, \quad v^{(1)} = v^{(2)} \qquad (2.73)$$

The Helmholtz expansion (2.40) and (2.41) in cylindrical coordinates becomes, using the notation (2.42) in a force-free region

$$\frac{\partial^2\Phi}{\partial r^2} + \frac{1}{r}\frac{\partial\Phi}{\partial r} + \frac{1}{r^2}\frac{\partial^2\Phi}{\partial\varphi^2} + \frac{\partial^2\Phi}{\partial z^2} = \frac{1}{p^2}\frac{\partial^2\Phi}{\partial t^2}, \qquad (2.74)$$

$$\left(\nabla^2 H_r - \frac{H_r}{r^2} - \frac{2}{r^2}\frac{\partial H_\varphi}{\partial \varphi}\right)\hat{r} + \left(\nabla^2 H_\varphi - \frac{H_\varphi}{r^2} + \frac{2}{r^2}\frac{\partial H_r}{\partial \varphi}\right)\hat{\varphi} + \nabla^2 H_z \hat{z} = \frac{1}{s^2}\frac{\partial^2 \bar{H}}{\partial t^2}, \tag{2.75}$$

where $\hat{r}$, $\hat{\varphi}$ and $\hat{z}$ are the unit vectors in cylindrical coordinates.

2.1.9. Propagating Waves in Liquids and Gases

As it is mentioned above, only longitudinal waves can propagate through liquids and gases. Instead of material deformation it is a pressure disturbance that propagates through the medium [19]. The solution of the wave propagation problem is given then entirely by the solution of the equation for the scalar potential (2.44), and this solution is determined completely by the scalar field distribution Φ. This greatly simplifies the theoretical analysis [19]. For the purposes of the present work, however, in order to provide a simple representations of the liquid-solids interfaces, we shall consider different approach. In the liquid medium we set the shear speed $s = 0$. That is, the liquids and gases will be considered as linearly isotropic media, which have the Lamé constant $\mu = 0$ [19]. The equations of motion for the displacement field then become

$$p^2 \nabla\nabla \bar{U} = \frac{\partial^2 \bar{U}}{\partial t^2}. \tag{2.76}$$

The last equation represents the propagation of a longitudinal wave through the medium.

In 2-dimensional Cartesian geometry the corresponding system for the displacement components becomes

$$\left|\begin{array}{l} p^2(u_{xx}+v_{xy}) = u_{tt}, \\ p^2(v_{xx}+u_{xy}) = v_{tt} \quad . \end{array}\right. \tag{2.77}$$

Correspondingly, the equation similar to (2.51) does not exists, and (2.77) describes all possible wave motions in the medium, where shear waves do not exist. Using (2.52) and putting $\mu = 0$, we obtain for the interface parallel to X-axis

$$\sigma_{xy}^{(1)} = 0, \quad \sigma_{yy}^{(1)} = \sigma_{yy}^{(2)}, \tag{2.78}$$

where (1) represents the variables corresponding to the solid medium, and (2) to the liquid. These relations on the interface must be used together with the requirements (2.58) for the displacement continuity.

2.2 A Review of the Methods of Solution

For the nondestructive testing applications, we are interesting in the entire process of elastic wave generation, propagation, scattering and detection. There are basically two approaches for the solution of the equations (2.18). The theoretical approach is concerned by both the exact solutions and the development of approximate approaches to derive the solution. The elastic waves in most cases are considered to be harmonic, and more general solution is derived by using Fourier inverse theorem. Numerical methods are concerned by finding an approximate solution, when the equations are somehow transformed and numerical models for approximate representation of the boundary and interface conditions are applied [20]. Some of these methods are considered below.

2.2.1. Green Functions

The wave equations may be recast as an integral equations. This is a purely formal re-expression of the same mathematics, but it has some advantages when approximate methods of solution are sought. The basic idea is that if one knows the response of the elastic material to local forces with specified time dependencies, the principle of superposition allows us that we can build models of more complicated cases by combining these elementary solutions. The elementary forces are usually taken to be single-frequency simple harmonic waves, step functions, or delta functions. The response to unit local forces define the Green tensor.

For steady-state excitation with angular frequency ω, the integral equations have been derived, among the others, in [21,22]. Morse and Freshbach [2] also give the result.

Consider two sets of displacements $\bar{U}=(u_1 , u_2 , u_3)^T$ and $\bar{U}'=(u'_1 , u'_2 , u'_3)^T$, corresponding to body forces $\bar{F}$ and $\bar{F}'$, respectively. The reciprocity principle [23] states that the total of the work done by the first set of forces acting on the second set of displacements is equal to the work done by the second set of forces acting on the first set of displacements. From the divergence theorem, inside a body volume V with surface S we obtain

$$\int_V [\nabla_i(c_{ijkl}\nabla_l u_k)u_j' - \nabla_i(c_{ijkl}\nabla_l u'_k)u_j]dV = \int_S [c_{ijkl}\nabla_l u_k u_j' - c_{ijkl}\nabla_l u'_k u_j]dS_i , \qquad (2.79)$$

where we assume the integrals converge. Vector $d\bar{S}$ points out of the volume V. In a case of unbounded V, a radiation conditions [24] must be invoked* . If $\vec{U}$ and $\vec{U}'$ satisfy the equations of motion

$$\nabla_i(c_{ijkl}\nabla_l u_k) = \rho(u_{j,tt} - F_j), \tag{2.80}$$

and similar for $\vec{U}'$, then, using the symmetry properties of c_{ijkl}, we obtain

$$\int_V \rho[(\vec{U}_{tt} - \vec{F}).\vec{U}' - (\vec{U}'_{tt} - \vec{F}').\vec{U}]dV = \int_S [\vec{U}'.\sigma - \vec{U}.\sigma'].d\vec{S}. \tag{2.81}$$

In the equations above we use the same notation for the derivatives as in (2.50), (2.51) etc. The terms of the left-hand side represent the difference between the work done in increasing of the kinetic energy and the work done by the body forces. The right-hand side represents the work done by the tractions on the surface. Let assume, that

$$\rho F'_i = \delta_{ij}\delta(t)\delta(\vec{r} - \vec{r}'). \tag{2.82}$$

The response to this force is the Green function for the problem.

If we consider a single frequency time variation, when the time derivatives in (2.82) give equal and opposite terms, we obtain an integral involving the single-frequency Green tensor $G(\vec{r}|\vec{r}')$. If both the stress and the displacement are regular within V and on S, then

$$\int_S \left\{\sigma_{ij}G_{ik}(\vec{r}|\vec{r}')\hat{n}_j - u_i(\vec{r}')\hat{n}_j\Sigma_{ijk}(\vec{r}|\vec{r}')\right\}dS' + \int_V \rho F_j(\vec{r}')G_{jk}(\vec{r}|\vec{r}')dV' = \begin{cases} u_k(\vec{r}), \ \vec{r} \in V \\ 0, \ \vec{r} \notin V \end{cases}, \tag{2.83}$$

---

* Radiation condition essentially means that only outgoing waves are considered.

where $\hat{\mathbf{n}}$ is the unit vector normal to S and pointing out of V, and $\Sigma_{ijk}(\vec{r}|\vec{r}')$ is the stress Green tensor, related to G_{ik} by

$$\Sigma_{ijk}(\vec{r}|\vec{r}') = c_{ijkl}\frac{\partial}{\partial r_m}G_{ml}(\vec{r}|\vec{r}'), \tag{2.84}$$

or, for isotropic materials

$$\Sigma_{ijk}(\vec{r}|\vec{r}') = \lambda\delta_{ij}\frac{\partial}{\partial r_m}G_{ml}(\vec{r}|\vec{r}') + \mu\left[\frac{\partial}{\partial r_i}G_{jk}(\vec{r}|\vec{r}') + \frac{\partial}{\partial r_j}G_{ik}(\vec{r}|\vec{r}')\right]. \tag{2.85}$$

Equation (2.83) represents, in principle, the solution of any elastodynamic problem. The Green tensor $G_{ik}(\vec{r}|\vec{r}')$ represents the displacement in the direction k of $\vec{r}$ caused by a unit force at $\vec{r}$' directed in the direction *i*. It may, as shown in [2], be built up from the Green function for scalar waves $g(\vec{r}|\vec{r}')$, which has the form [2]

$$g(\vec{r}|\vec{r}') = \frac{e^{i\omega|\vec{r}-\vec{r}'|/c}}{|\vec{r}-\vec{r}'|}. \tag{2.86}$$

Following [2, 24], we use the Fourier transform $\hat{f}(\vec{k},\omega)$ of the function $f(\vec{r},t)$

$$\hat{f}(\vec{k},\omega) = \int\int\int\int f(\vec{r},t)e^{i(\omega t-\vec{k}.\vec{r})}d\vec{r}dt, \tag{2.87}$$

with the corresponding inversion expression

$$(2\pi)^4 f(\vec{r},t) = \int\int\int\int \hat{f}(\vec{r},t)e^{-i(\omega t-\vec{k}.\vec{r})}d\vec{k}d\omega\,. \tag{2.88}$$

We assume that f is such that the conditions of the Fourier inversion theorem are met: the detail may be found in [25].

Substituting in the elastodynamic equation with a delta-force function, satisfied by the Green tensor

$$c_{ijkl}\frac{\partial^2}{\partial r_j \partial r_l}G_{km}(\bar{r}|\bar{r}') - \rho\frac{\partial^2}{\partial t^2}G_{im}(\bar{r}|\bar{r}') = \delta_{im}\delta(t)\delta(\bar{r}-\bar{r}'),$$

we obtain

$$c_{ijkl}k_j k_l \hat{G}_{km}(\vec{k}|\bar{r}') - \rho\omega^2\hat{G}_{im}(\vec{k}|\bar{r}') = \delta_{im}e^{-i\vec{k}.\bar{r}'}. \tag{2.89}$$

The presence of the exponential on the right-hand side ensures that when the inversion theorem is applied G will depends on only the difference $|\bar{r}-\bar{r}'|$. The solution of (2.89) is complicated except for isotropic medium, when [2]

$$\hat{G}_{ij}(\vec{k}|\bar{r}') = -\frac{(\lambda+2\mu)(k_p^2-k^2)\delta_{ij} + (\lambda+\mu)k_i k_j}{\mu(k_s^2-k^2)(\lambda+2\mu)(k_p^2-k^2)}e^{-i\vec{k}.\bar{r}'}, \tag{2.90}$$

where $k_p = \frac{\omega}{p}$, $k_s = \frac{\omega}{s}$ are the compression and shear wavenumbers. Equation (2.90) may be rewritten as [2,24]

$$\hat{G}_{ij}(\vec{k}|\bar{r}') = -\frac{\delta_{ij}}{\mu(k_s^2-k^2)}e^{-i\vec{k}.\bar{r}'} - \frac{1}{\rho\omega^2}\left[\frac{k_i k_j}{k_p^2-k^2} - \frac{k_i k_j}{k_s^2-k^2}\right]e^{-i\vec{k}.\bar{r}}.$$

The basic Fourier inversion integral now has the form

$$I(R) = \frac{1}{(2\pi)^4}\int\frac{e^{i\vec{k}.\vec{R}}}{q^2-k^2}d\vec{k}. \tag{2.92}$$

In order to evaluate this integral we have to assume that q has a small imaginary part, so as to move the poles of the integrand away from the path of integration along the real axis. In physical terms this is usually justified on the grounds that no material is totally losless, and the imaginary part represents dissipation in the medium. In fact, only a positive imaginary part represents dissipation: a negative imaginary part would lead to exponential growth of an outgoing spherical wave. In the limit as $\mathrm{Im}(q)\to 0^+$, we obtain [2]

$$I(R) = -\frac{1}{4\pi}\frac{e^{ik_pR}}{R}. \tag{2.93}$$

Then (2.91) becomes

$$\hat{G}_{ij}(\bar{r}|\bar{r}') = -\frac{1}{4\pi\rho\omega^2}\left\{\delta_{ij}k_s^2\frac{e^{ik_sR}}{R} - \frac{\partial}{\partial r_i}\frac{\partial}{\partial r_j}\left[\frac{e^{ik_pR}}{R} - \frac{e^{ik_sR}}{R}\right]\right\},\ R=|\bar{r}-\bar{r}'|. \tag{2.94}$$

Despite of the fact that (2.83) represents, in principle, each possible situation, it is still an integral equation for the field $\bar{U}$, and there is no reason to expect it to be easier to solve than the differential form of the wave equation. It is, however, an important starting point for systematic approximations to the solutions of scattering problems, as it is described below. It is quite straightforward to derive asymptotic fields using the Green function, and this allows total scattering cross-section to be investigated.

2.2.2. Exact Solutions

Unfortunately, there are very few problems in scalar wave theory which are exactly soluble, and the solutions for the elastodynamic equations are slightly harder. There are two difficulties which may be described in terms of the solution in the form of an eigenfunction expansion. In general, we take the three curvilinear coordinates ξ with a set of scale factors **h**, so that the length scale is defined by

$$ds^2 = dr_i \, dr_j = h_{ij} \, \xi_j \, h_{ik} \, \xi_k \,. \tag{2.95}$$

In an orthogonal curvilinear system $h_{ij} = h_i \, \delta_{ij}$, and the scale factors are computed from the coordinate transformation

$$h_i^2 = \sum_{j=1}^{3}\left(\frac{\partial r_j}{\partial \xi_i}\right)^2 \left[\sum_{k=1}^{3}\left(\frac{\partial \xi_k}{\partial r_i}\right)^2\right]^{-1} . \tag{2.96}$$

Now there are only eleven coordinate systems* for which the scalar wave equation is separable [2], i.e. the solution can be represented in the form

$$f(\xi) = \Xi_1(\xi_1)\Xi_2(\xi_2)\Xi_3(\xi_3), \tag{2.97}$$

when the differential equation separates into three terms, each of which is a function of only one of the components ξ_i . Solutions to the scalar equation are possible when the surfaces on which the boundary conditions are specified coincide with constant-coordinate surfaces.

One way of proceeding is to expand each of Ξ_i in terms of the eigenfunctions Λ_n of the three ordinary differentials. Λ_n are generally special functions whose properties are well known. The boundary conditions then reduce to simple relationships between the

---

* We refer to [2], Chapter 5, to specify the types of these eleven coordinate systems of general ellipsoidal type or their various degenerate forms.

coefficients in the expansions, and the problem may be solved to any desired accuracy by continuing the expansion to sufficiently high order n.

For the vector equation, a more restricted set of coordinate systems allows exact solutions. The problem concerns the resolution into potentials, where the vector potentials will only be determined by wave equations if at least one of the scale factors h_i is unity and the ratio of the other two is independent of ξ_i. Only six of the eleven coordinate systems have this property [2]. Further complications for the elastodynamic equation are the boundary conditions, since they can cause mixing between eigenfunctions of compression and shear waves. Similarly, they cause mixing between eigenfunctions in all coordinate systems except rectangular, circular cylindrical and spherical. The coefficients for different orders of n are coupled together, and an infinite set of simultaneous equations must be solved to find the solution.

Examples of the expansion method are the cases of scattering in spherical and cylindrical coordinates, from a sphere or cylinder, respectively. We refer to [3, 13, 20] for details of the solution. More details of analytical methods and eigenfunction expansions in particular are given by Pao and Mow in [26].

2.2.3. Scattering in the Integral Equation Formalism. General Properties of Elastic Wave Scattering. t-matrix Approach and Geometric Ray Theory in Elastodynamics

The integral form of the wave equation is given by (2.83). For simplicity, we treat waves of single frequency ω. However, if the scattering of a pulse is required, an additional integral, inverting the Fourier transform, will be required, i.e. the integral equation must be solved for all values of ω.

When the volume V in (2.83) contains a defect, the elastic properties of the material vary inside V. The variation may be described by defining V to be the volume outside the flaw, V' the volume inside, when

$$c_{ijkl} \rightarrow c_{ijkl} + \delta c_{ijkl} H(\bar{r}) \tag{2.98}$$

and

$$\rho \rightarrow \rho + \delta\rho H(\bar{r}), \tag{2.99}$$

where $H(\bar{r})$ is defined to be unity inside V' and zero outside, and the differences in material properties inside and outside the flaw are

$$\delta c_{ijkl} = c'_{ijkl} - c_{ijkl}, \quad \delta\rho = \rho' - \rho, \tag{2.100}$$

the primed values being those of the material in the flaw. The elastic equation may then be written as

$$c_{ijkl} u_{k,lj} + \rho\omega^2 u_i = -(\delta\rho\omega^2 u_i H + \delta c_{ijkl} u_{k,lj} H + c_{ijkl} u_{k,l} H_{,j}), \tag{2.101}$$

where H_j is the derivative of the step function H with respect to r_j, which may be written as

$$H_{,j}(\bar{r}) = -\hat{n}_j \delta(\bar{r} - \bar{r}^{S'}), \tag{2.102}$$

$\bar{r}^{S'}$ being on the surface of the flaw, $\hat{\mathbf{n}}$ being the unit vector normal to S' pointing out of

V'. The right-hand side of (2.102) may be treated as the body force F_i in (2.83), and inside the entire region of interest V-V' we may write the wavefield $\vec{U}$ as a sum of the incident and scattered fields

$$\vec{U} = \vec{U}^i + \vec{U}^s, \tag{2.103}$$

so the scattering equation becomes

$$u_k(\vec{r}) = u_k^i(\vec{r}) + \int_{V'} (\delta\rho\omega^2 G_{ki}(\vec{r}|\vec{r}')u_i(\vec{r}') - \delta c_{ijkl} u_{m,n}(\vec{r}') G_{ki,j}(\vec{r}|\vec{r}'))dV'. \tag{2.104}$$

This is an integral equation representing the scattering of the incident wave $\vec{U}^i$. It includes a notional incident field inside the scatterer, which is equal to the field that would have been present if the scatterer were absent.

Let confine the integral in (2.83) to the region outside the scatterer. We also assume that the scattered field is zero on the enclosing surface at infinity. It then follows [20] that the scattered wave outside S' is given by

$$u_k^s(\vec{r}) = \int_{S'} (u_i(\vec{r}')\Sigma_{ijk}(\vec{r}|\vec{r}')\hat{n}_j - \sigma_{ij}(\vec{r}')G_{ki,j}(\vec{r}|\vec{r}')\hat{n}_j)dS'. \tag{2.105}$$

Since $\vec{U}^i$ satisfies the homogeneous ($F_i = 0$) wave equation, the equation (2.105) may be written as

$$u_k^s(\vec{r}) = \int_{S'} (u_i^s(\vec{r}')\Sigma_{ijk}(\vec{r}|\vec{r}')\hat{n}_j - \sigma_{ij}(\vec{r}')G_{ki,j}(\vec{r}|\vec{r}')\hat{n}_j)dS'. \tag{2.106}$$

This equation is not an integral equation for the scattered field since the boundary conditions on the surface S' cannot be included in (2.106), as the integral involves only part of the integral field: they can be included in (2.105), which involves the total wavefield. Equation (2.106) represents the basic equation of the Kirchhoff approximation in the elastodynamic theory. It has been quite extensively applied to the scattering of ultrasound (for example, see [27-29]). The method is not restricted to cracks, and the basic assumptions for arbitrary scatterer shape is that the scattered field and its gradients at the surface are equal to those of the incident field, multiplied by a reflection coefficient [19], in the region which is reached by the incident wave, and that the total field is zero in the shadow zone.

The basic assumptions for the Kirchhoff approximation can be modified so that the outgoing wave from the scatterer is assumed to be the incident signal at each point multiplied by an appropriate plane-wave reflection coefficient [30,31]. Since for elastic waves the outgoing wave may be of compression or shear types, the mode conversion can be included [32]. This version of the Kirchhoff approximation, called physical elastodynamic approximation [32], is the most commonly used. The Kirchhoff approximation gives good results for scattering from cracks, for scatterer a few wavelengths in size and close to the specular direction* . It also been observed that away from the specular direction the Kirchhoff approximation to the crack-opening displacement** is less accurate.

---

* i.e. direction in which the scatterer coincide with some of the coordinate surfaces.
** It means that the scattered field is expressed in terms of jumps in the wavefield across the crack.

Approximate solutions to the integral equations may be sought in several other ways, but most commonly used are the **Born and Quasistatic approximations**. The Born approximation [1, 2, 20] is suited to weak scattering, and consists of approximating the displacement in the interior of the flaw by the incident field $\vec{U}^i$ (i.e. the first term in the perturbation expansion [1, 2, 20]). It is limited to small changes in material properties and to small scatterers for which k^i a <<1. It should be noted [2] that the Born approximation does not conserve energy. Better approximation could be obtained by substituting the resulting total field back into the integral; in practice the expansion is usually halted at the first term. For stronger scatterers, a better estimate of the field inside the flaw is obtained by using solutions of the corresponding static problem: this technique is suitable when the wavelength of the elastic wave is large compared with the flaw and constitutes the Quasistatic approximation.

Direct solutions of the integral equation (2.83) has been attempted by three methods: finite difference, finite element and moments [24, 35-41]. The problem to be handled in the first two methods is that the Green function has a singularity at r = r', and the contribution from the singularity often dominates the solution. Another problem of the integral equation method, when formulated as a boundary integral (equation (2.105)), is that the solution is not unique at wavevectors corresponding to eigenstates of the scattering region. Various methods exist [36, 37, 42] to overcome this difficulty.

In general, in cases where the analytic form of the Green function is known, as in a homogeneous region, the boundary integral equation method can be applied. Essentially, the Green function is used to describe how an element of the boundary will interact with another element of the boundary. The method only requires the boundary to be discretized, as the wavefield at other points can be obtained from the Green function. The method appears attractive the dimensionality of the boundary is one less than that of the region it encloses. However, each point of the boundary is linked through the Green function to every other point, whereas in a finite-element model each volume element is linked only to its immediate neighbors. It can be shown [20] that the boundary element method only becomes advantageous for n ≥ 20, where n is the number of elements. In addition, the integrals involved are singular where they contain $G_{ij}(\bar{r}|\bar{r}')$ for r = r'. A further problem arises if numerical values of the field are required at many point remote from the boundary, as the values must be obtained by numerical integration using the boundary values and the Green function.

General Properties of Elastic Wave Scattering.

Some important new effects, which occur in the elastic wave scattering when compared with scalar (acoustic) waves were derived in [43] within the context of the integral formalism. First, one may define [20] the total cross-section of a particular flaw as the ratio of the average power scattered in all directions to the average incident density

$$\sigma(\omega) = \frac{\langle P^s \rangle}{\langle F^i \rangle}, \tag{2.107}$$

where < > denotes average over time. Superscripts s and i refer to the incident and scattered wave. If S is the scatterer surface, then

$$P^s = \int_S \vec{U}^s_{,t}\sigma^s.d\vec{S}. \tag{2.108}$$

The differential cross-section $\frac{d\sigma}{d\Omega}$, where $d\Omega$ is the solid angle element, gives the distribution of the scattered power into different directions. At a distance r from the scatterer in the direction $\hat{\mathbf{r}}$

$$d\vec{S} = r^2 d\Omega\hat{\mathbf{r}}, \tag{2.109}$$

so that

$$\frac{d\sigma}{d\Omega} = \frac{\left\langle r^2\,\vec{U}^s_{,t}.\sigma^s.\hat{r}\right\rangle}{\left\langle F^i\right\rangle}. \tag{2.110}$$

In principle, (2.110) is to be evaluated in the limit $r \to \infty$. To calculate $\frac{d\sigma}{d\Omega}$, it is necessary to evaluate $\vec{U}^s$ far away from the flaw. Since $G_{ij}(\bar{r}|\bar{r}')$ depends only on $\vec{R} = \bar{r} - \bar{r}'$, where $\bar{r}$ is the vector to the point of observation and $\bar{r}'$ is a point inside the scatterer, as shown in (2.94), one can immediately derive the limits for large r

$$R^{-1} \approx r^{-1},\ R \approx r - \bar{r}'.\bar{r},\ \frac{\partial}{\partial r_j}\frac{e^{ikR}}{R} \approx ik\hat{r}_j e^{-i\bar{k}.\bar{r}'}\frac{e^{ikr}}{r}, \tag{2.111}$$

with higher derivatives giving expressions similar to (2.111), including factor $(ik)\hat{r}_i$ for each derivative. The far-field scattered wave than has a displacement [20]

$$u_i^s \approx \hat{r}_i\hat{r}_j f_i(k_p\vec{r})\frac{e^{ik_pr}}{k_pr} + (\delta_{ij} - \hat{r}_i\hat{r}_j)f_j(k_s\vec{r})\frac{e^{ik_sr}}{k_sr}, \tag{2.112}$$

where the scattering vector $\vec{f}(\vec{k})$ is defined by

$$f_i(\vec{k}) = \frac{k^3}{4\pi\rho\omega^2}\left\{\delta\rho\omega^2\int_{V'} u_i e^{-i\vec{k}.\vec{r}'}dV' + ik\hat{r}_j\delta c_{ijkl}\int_{V'} u_{k,l}e^{-i\vec{k}.\vec{r}'}dV'\right\}, \tag{2.113}$$

which differs from that in [43] since they have used $\frac{e^{ikr}}{r}$ instead of $\frac{e^{ikr}}{kr}$. In (2.112) f_i has a dimension of length.

The scattered field can obviously be separated into longitudinal and transverse components,

$$u_i^s \approx P_i\frac{e^{ik_pr}}{k_pr} + S_i\frac{e^{ik_sr}}{k_sr}, \tag{2.114}$$

with the compression and shear wave scattering amplitudes

$$P_i(\theta,\varphi) = \hat{r}_i\hat{r}_j f_j(k_p\vec{r}),\quad S_i(\theta,\varphi) = (\delta_{ij} - \hat{r}_i\hat{r}_j)f_j(k_s\vec{r}). \tag{2.115}$$

Considering an isotropy medium, one can express the stress arising from the scattering wave in terms of usual constants λ and μ [20, 43]

$$\sigma_{ij}^s \approx i\lambda k_p P_k\hat{r}_k\delta_{ij}\frac{e^{ik_pr}}{k_pr} + i\mu k_p(P_i\hat{r}_j + P_j\hat{r}_i)\frac{e^{ik_pr}}{k_pr} + i\mu k_s(S_i\hat{r}_j + S_j\hat{r}_i)\frac{e^{ik_sr}}{k_sr}. \tag{2.116}$$

If the incident wave is a mixture of compression and shear waves traveling parallel to the Z-axis,

$$u_i^i = p_i e^{i(k_p z - \omega t)} + s_i e^{i(k_s z - \omega t)}, \tag{2.117}$$

which has amplitudes $|\vec{p}|$ for the compression and $|\vec{s}|$ for the shear component, the incident density is

$$F = \frac{1}{2}\omega[k_p(\lambda + 2\mu)|\vec{p}|^2 + k_s\mu|\vec{s}|^2] \tag{2.118}$$

and the limiting value of the scattered power as $r \to \infty$ is [20, 43]

$$\left\langle r^2 \hat{r}_i \sigma_{ij} u_{,t}^s \right\rangle \approx \frac{1}{2}\omega^2\left[k_p(\lambda + 2\mu)|P|^2 + k_s\mu|S|^2\right]. \tag{2.119}$$

The differential cross-section is then

$$\frac{d\sigma(\omega)}{d\Omega} = \frac{\frac{1}{2}\omega^2\left[k_p(\lambda + 2\mu)|\vec{P}|^2 + k_s\mu|\vec{S}|^2\right]}{k_p(\lambda + 2\mu)|\vec{p}|^2 + k_s\mu|\vec{s}|^2}. \tag{2.120}$$

If the incident wave is purely compressional ($\vec{s} = 0,\ |\vec{p}| = 1$)

$$\frac{d\sigma(\omega)}{d\Omega} = |\vec{P}|^2 + \frac{k_p}{k_s}|\vec{S}|^2, \tag{2.121}$$

whereas, if the incident wave is purely transverse and of unit amplitude ($\vec{p} = 0,\ |\vec{s}| = 1$)

$$\frac{d\sigma(\omega)}{d\Omega} = |\vec{S}|^2 + \frac{k_s}{k_p}|\vec{P}|^2. \tag{2.122}$$

This clearly shows that the form of the cross-section depends on the type of the incident wave, but always contains contribution from both types of scattered wave.

Another important result, derived in [43], is the elastodynamic equivalent of the optical theorem. In the scalar wave theory

$$\sigma(\omega) = 4\pi f(\theta = 0), \tag{2.123}$$

where $f(\theta = 0)$ is the forward scattering amplitude. For elastic waves, the total incident intensity is [20, 43]

$$F_i = \sigma^i_{ij} u^i_{j,t} + (\sigma^i_{ij} u^s_{j,t} + \sigma^s_{ij} u^i_{j,t}) + \sigma^s_{ij} u^s_{j,t}, \tag{2.124}$$

where superscripts i,s denote the incident and scattered wave, respectively. Equation (2.124) may be written as the sum of incident, interference and scattered intensity

$$F_i = F^i_i + F^{\mathbf{int}}_i + F^s_i. \tag{2.125}$$

Since $\vec{F}^i$ is related to the power being put into the system, from the conservation of energy law, if S represents a closed surface, we obtain

$$\int_S dS_i F^s_i = -\int_S dS_i F^{\mathbf{int}}_i, \tag{2.126}$$

i.e. the intervals of interference and scattered intensities must cancel. If S is taken to be the limit of a large sphere with $r \to \infty$,

$$\lim_{r\to\infty} \int d\Omega \hat{r}_i F^s_i = -\lim_{r\to\infty} r^2 \int d\Omega \hat{r}_i F^{\mathbf{int}}_i, \tag{2.127}$$

in which the true average of the left hand side is proportional to the total cross-section. Thus, $\sigma(\omega)$ is related to the interference of the incident power traveling parallel to the Z-axis with the scattered power traveling radially from the flaw. The key difference between

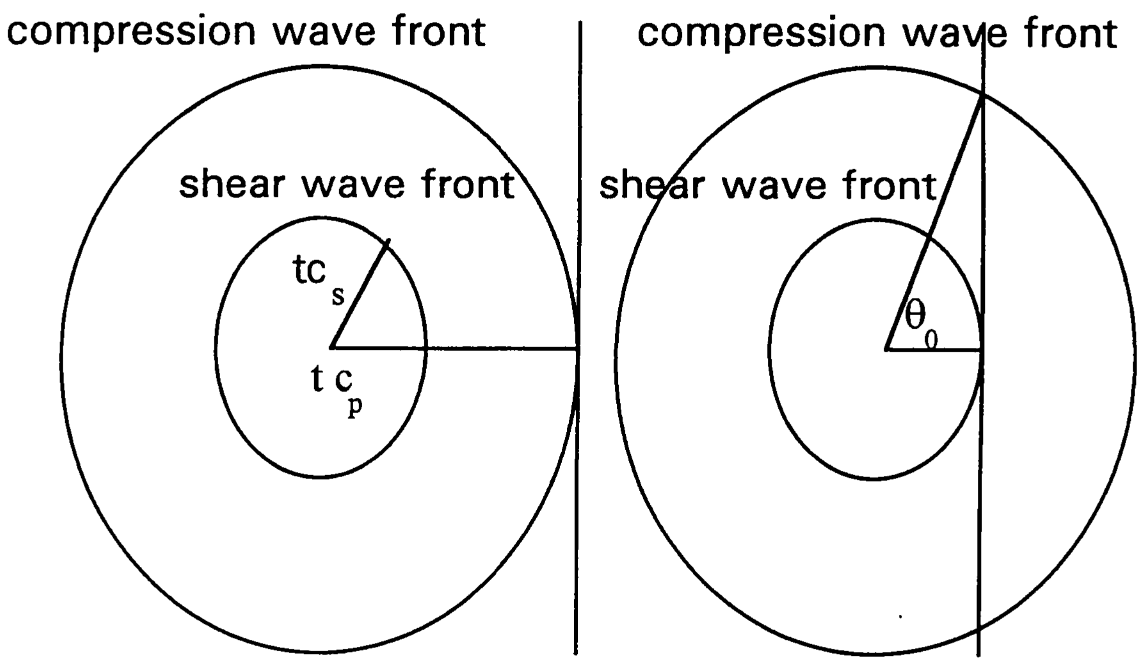

Figure 2-5. The interference in the forward direction only of scattered waves from incident compression waves (left) and from incident shear waves (right). θ_0 is the critical angle.

the acoustic and elastodynamic cases arises from the existence of two elastodynamic wave speeds. Fig. 2-5 shows how this affects compression and shear wave scattering differently. The explicit expression for the total cross-section is [43]

$$\sigma(\omega) = \frac{4\pi}{k_s} Im \frac{(\lambda + 2\mu) k_s \widetilde{P}_i(0) P_i^* + \mu k_s \widetilde{S}_i(0) S_i^* + (\lambda + 2\mu) k_p \widetilde{P}_i(\theta_0) S_i^*}{(\lambda + 2\mu) k_p p_i p_i^* + \mu k_s s_i s_i^*}, \tag{2.128}$$

where the quantities denoted by tilda are the asimutal averages of the scattered amplitudes

$$\widetilde{\mathbf{A}}(\theta) = \frac{1}{2\pi} \int_0^{2\pi} \mathbf{A}(\theta, \varphi) d\varphi . \tag{2.129}$$

In the equation (2.128) the existence of additional interference at the critical angle $\theta_0 = \cos^{-1}\left(\frac{c_s}{c_p}\right)$ is quite clearly shown. Note that this critical angle is observed when initial shear wave scatters.

The discussion above is concerned by harmonic wave and cases when the scatterer properties are constant in time. de Hoop [44] has extended that work to derive theorems of the scattering and absorption of plane waves of arbitrary shape,. He considered time variations of the scatterer properties and concluded that his theorems applied in such cases as well as in cases of non-linear behavior in the scatterer.

An important approach, using the integral equation formulation, is the so-called t-matrix approach, which came from analogy with the general scattering theory, which is described in terms of channels and matrices. The terminology comes from elementary particle and high energy physics, where most of the information about the particles is obtained from scattering cross-sections. Well before and well after the scattering event, the particles are described in terms of similar to waves functions, related by the scattering operator Θ. If the waves are expanded in, for example, plane waves, then the coefficients before and after the scattering are related by the matrix **S**. In general, the scattering is weak, and so the major part of Θ describes the particles which pass through unscattered. It is then useful to separate out the part of Θ which corresponds to a change of state, and this contribution is the transition operator **Q**, giving rise to the matrix **T**. The scattering and transition matrices are frequently referred to as s-matrix and the t-matrix.

For elastic waves, t-matrix theory was derived by Waterman [46] and

Varatharajulu and Pao [47]. They define vector-basis functions **L** and **M** for the compression and shear waves. In two dimensions, in planes perpendicular to Z-axis

$$\mathbf{L}_\sigma(\vec{r}) = \vec{\nabla}\psi_\sigma(k_p\vec{r}) \\ \mathbf{M}_\sigma(\vec{r}) = \vec{\nabla}[\psi_\sigma(k_s\vec{r})\hat{r}_3], \tag{2.130}$$

where ψ_σ are some expansion functions, $\hat{r}_3$ is the unit vector in Z-direction. The **L** and **M** functions have orthogonality relations, tabulated in [46]. The incident and scattered waves are expanded as

$$\vec{u}^i = \sum_\sigma \left\{a_\sigma \mathrm{Re}\left[\mathbf{L}_\sigma(\vec{r})\right] + b_\sigma \mathrm{Re}\left[\mathbf{M}_\sigma(\vec{r})\right]\right\}, \tag{2.131}$$

and

$$\vec{u}^s = \sum_\sigma \left\{f_\sigma \mathbf{L}_\sigma(\vec{r}) + g_\sigma \mathbf{M}_\sigma(\vec{r})\right\}. \tag{2.132}$$

Here a_σ , b_σ are known, f_σ and g_σ are to be found. The Green tensor can also be expanded in terms of **L** and **M** functions,

$$G_{ij} = \frac{\pi}{\rho\omega^2}\sum_\sigma \left\{\mathbf{L}_{\sigma i}(\vec{r}_>)\mathrm{Re}\left[\mathbf{L}_{\sigma j}(\vec{r}_<)\right] + \mathbf{M}_{\sigma i}(\vec{r}_>)\mathrm{Re}\left[\mathbf{M}_{\sigma j}(\vec{r}_<)\right]\right\}, \tag{2.133}$$

where $\vec{r}_>$ denotes r > r', and $\vec{r}_<$ denotes r < r'. Inside the scatterer, where r < r', the integral equation gives

$$\sum_\sigma \left\{a_\sigma \mathrm{Re}\left[\mathbf{L}_\sigma(\vec{r})\right] + b_\sigma \mathrm{Re}\left[\mathbf{M}_\sigma(\vec{r})\right]\right\} = -\sum_\sigma \sum_{i,j} \int_S \left\{\Sigma_{ijk}(\vec{r}|\vec{r}\,')u_j(\vec{r}\,') - G_{ij}(\vec{r}|\vec{r}\,')\sigma_{jk}(\vec{r}\,')\right\} dS'_k . \tag{2.134}$$

Outside the scatterer we have instead

$$\sum_{\sigma}\left\{f_\sigma \mathrm{Re}\left[\mathbf{L}_\sigma(\vec{r})\right] + g_\sigma \mathrm{Re}\left[\mathbf{M}_\sigma(\vec{r})\right]\right\} = -\sum_{\sigma}\sum_{i,j}\int_{S}\left\{\Sigma_{ijk}(\vec{r}'|\vec{r})u_j(\vec{r}') - G_{ij}(\vec{r}'|\vec{r})\sigma_{jk}(\vec{r}')\right\}dS'_k \;.(2.135)$$

The change from $(\vec{r}|\vec{r}')$ to $(\vec{r}'|\vec{r})$ between (2.134) and (2.135) indicates that, whereas in the first equation $\vec{r}$ was the argument of Re(**L**) and Re(**M**), in the second equation $\vec{r}$ is the argument of **L** and **M**. In both equations the displacement u_j and the surface traction $\sigma_{jk}\, dS'_k$ remain unspecified. If we take the scatterer is an empty cavity, the traction will be zero. The displacement u_j will still be unknown, so we expand them

$$\vec{u}(\vec{r}') = \sum_{\sigma}\left\{\alpha_\sigma \mathrm{Re}\left[\mathbf{L}_\sigma(\vec{r})\right] + \beta_\sigma \mathrm{Re}\left[\mathbf{M}_\sigma(\vec{r})\right]\right\}. \tag{2.136}$$

Using the orthogonality of **L** and **M**, we find

$$\begin{pmatrix} a_\sigma \\ b_\sigma \end{pmatrix} = -i\begin{pmatrix} Q^{LL}_{\sigma\tau} & Q^{LM}_{\sigma\tau} \\ Q^{ML}_{\sigma\tau} & Q^{MM}_{\sigma\tau} \end{pmatrix}\begin{pmatrix} \alpha_\tau \\ \beta_\tau \end{pmatrix} \tag{2.137}$$

and, for outside the scatterer

$$\begin{pmatrix} f_\sigma \\ g_\sigma \end{pmatrix} = i\mathrm{Re}\begin{pmatrix} Q^{LL}_{\sigma\tau} & Q^{LM}_{\sigma\tau} \\ Q^{ML}_{\sigma\tau} & Q^{MM}_{\sigma\tau} \end{pmatrix}\begin{pmatrix} \alpha_\tau \\ \beta_\tau \end{pmatrix}. \tag{2.138}$$

The matrices **Q** contain all the information about the scattering. For the cavity, the elements of **Q** matrices may be expressed as

$$Q^{LL}_{\sigma\tau} = \frac{\pi}{\rho\omega^2}\int_{S}\sum_{i,j}\mathrm{Re}\left[L_{\tau i}(\vec{r}')\right]\left\{\lambda\delta_{ij}\sum_{k}\frac{\partial}{\partial r_k}L_{\sigma k}(\vec{r}') + \mu\frac{\partial}{\partial r'_i}L_{\sigma j}(\vec{r}') + \mu\frac{\partial}{\partial r'_j}L_{\sigma i}(\vec{r}')\right\}dS'_j \;,(2.139)$$

and

$$Q_{\sigma\tau}^{ML} = \frac{\pi\mu}{\rho\omega^2}\int_S \sum_{i,j} \mathrm{Re}\left[L_{\tau i}(\bar{r}')\right]\left\{\frac{\partial}{\partial r'_i}M_{\sigma j}(\bar{r}') + \frac{\partial}{\partial r'_j}M_{\sigma i}(\bar{r}')\right\}dS'_j, \tag{2.140}$$

$$Q_{\sigma\tau}^{LM} = \frac{\pi}{\rho\omega^2}\int_S \sum_{i,j} \mathrm{Re}\left[M_{\tau i}(\bar{r}')\right]\left\{\lambda\delta_{ij}\sum_k \frac{\partial}{\partial r_k}L_{\sigma k}(\bar{r}') + \mu\frac{\partial}{\partial r'_i}L_{\sigma j}(\bar{r}') + \mu\frac{\partial}{\partial r'_j}L_{\sigma i}(\bar{r}')\right\}dS'_j, \tag{2.141}$$

$$Q_{\sigma\tau}^{MM} = \frac{\pi}{\rho\omega^2}\int_S \sum_{i,j} \mathrm{Re}\left[M_{\tau i}(\bar{r}')\right]\left\{\frac{\partial}{\partial r'_i}M_{\sigma j}(\bar{r}') + \frac{\partial}{\partial r'_j}M_{\sigma i}(\bar{r}')\right\}dS'_j. \tag{2.142}$$

Then, a simple elimination of (α, β) yields the solution

$$\sum_\sigma T_{\tau\sigma}Q_{\sigma\eta} = \mathrm{Re}\left[Q_{\tau\eta}\right]. \tag{2.143}$$

In three dimensions principles are exactly the same. The summation over σ above is up to infinity, so (2.143) is a formal solution. The convergence of the expansion, in a formal sense, has been confirmed in [45, 48-50]. In any real calculation we have to use a finite set of functions **L** and **M**, and in general the integrals involved in **Q** will have to be taken numerically. As it was pointed out [45], one advantage of the t-matrix theories is that the surface integrals needed involve non-singular kernels. General approaches to the construction of t-matrix theories have been given in [51, 52], where also the method of optimal truncation (MOOT) has been developed, and it is based on the minimization of the difference between the required and actual solution.

As currently formulated, the t-matrix theory is directly applicable to problems with a periodic time variation. To treat pulses, the problem must be solved for many frequencies and the pulse synthesized by Fourier methods. In [53] it has been suggested that it might be possible to use a complete set of time-dependent functions for the expansion, and to solve general time-varying problems in that way, but this does not seen to have been attempted yet.

Other approaches for solving the wave equations have also been attempted. Such is the geometric acoustics, which is the acoustic analogue of geometric optics. The problem is to relate the simple laws of reflection and refraction, which were derived for infinite wave fronts, to the more complicated wavefronts, encountered in practice. Geometrical acoustics make the generalization by treating every point on a wavefront as part of a plane wave. It assumes that rays and wavefronts are always perpendicular to each other, even in complicated cases where the material properties vary from point to point, so the rays are not straight.

The formalism of ray theory can be traced back to Hamilton's work in early 19th century. The disturbance is assumed to travel along curves called rays, and at the interface between two media rays are bent according to Snell's law, giving reflected and refracted waves. Keller [56] made an important extension to geometric ray theory by introducing rays originating at edges of scattering bodies, and propagating into shadow zones - diffracted waves.

The geometric theory of diffraction for elastic waves was derived by Karal and Keller [57]. Starting with the wave equation (2.36), a time harmonic solution is sought in the form

$$\bar{\mathbf{U}} = \vec{\mathbf{A}}\, e^{i\omega(S-t)}, \tag{2.144}$$

where $\vec{A}$ and S are both functions of position, to be determined. It is further assumed that S is independent of the frequency ω, and

$$\vec{A} = \sum_{n=0}^{\infty} (i\omega)^n \vec{A}^{(n)} . \tag{2.145}$$

The vectors $\vec{A}^{(n)}$ are functions of positions to be determined. Involving only integer powers of ω makes clear that ray theory in this form cannot treat diffraction effects* . Substituting (2.145) in (2.144) and solving separately for each power of ω, one can obtain [57] for each $n \geq 0$

$$\begin{aligned} &-\rho A_i^{(n)} + (\lambda+\mu)(A_j^{(n)}\nabla_j S)\nabla_i S + \mu(\nabla_j S)(\nabla_j S)A_i^{(n)} + (\lambda+\mu)\nabla_i(A_j^{(n)}\nabla_j S) \\ &+(\lambda+\mu)(\nabla_j A_j^{(n-1)})\nabla_i S + 2\mu(\nabla_j S)\nabla_j A_i^{(n-1)} + \mu(\nabla_j\nabla_j S)A_i^{(n-1)} \\ &+(\lambda+\mu)\nabla_i(\nabla_j A_j^{(n-2)}) + \mu\nabla_j\nabla_j A_i^{(n-2)} = 0 \end{aligned} \tag{2.146}$$

For n=0 (2.146) may be simplified by taking the scalar product of (2.146) with gradS,

$$[-\rho + (\lambda+2\mu)(\vec{\nabla}S)^2]\vec{A}^{(0)}\vec{\nabla}S = 0, \tag{2.147}$$

or vector cross product with gradS

$$[-\rho + \mu(\vec{\nabla}S)^2]\vec{A}^{(0)} x \vec{\nabla}S = 0 . \tag{2.148}$$

These two equations have two possible solutions. Either

$$\vec{A}^{(0)}.\mathrm{grad}S = 0 \text{ and } (\vec{\nabla}S)^2 = \frac{\rho}{\mu}, \tag{2.149}$$

---

* The exact theory of diffraction introduces half-integer powers of ω.

or

$$\vec{A}^{(0)} x \vec{\nabla} S = 0 \text{ and } (\vec{\nabla} S)^2 = \frac{\rho}{\lambda + 2\mu}. \tag{2.150}$$

The equations for $\vec{\nabla} S$ are eikonal equations, which determine the phase S in terms of the phase on the initial surface, which may be the initial wavefront. The perpendiculars to the surfaces of constant phase are the rays, and in the case above they are straight lines. It is clear that (2.147) and (2.148) describe compression and shear waves respectively. Also S is a linear function of distance along a ray, s: for shear waves

$$S = S_0 + \sqrt{\frac{\rho}{\mu}}(s - s_0) = S_0 + \frac{(s - s_0)}{c_s}, \tag{2.151}$$

where c_s is the shear wave velocity. For compression wave

$$S = S_0 + \sqrt{\frac{\rho}{\lambda + 2\mu}}(s - s_0) = S_0 + \frac{(s - s_0)}{c_p}.$$

Further, substituting (2.148) in (2.146), for n=1 gives

$$(\lambda + \mu)(A_j^{(1)} \nabla_j S)\nabla_i S + (\lambda + \mu)(\nabla_j A_j^{(0)})\nabla_i S + 2\mu(\nabla_j S)\nabla_j A_i^{(0)} + \mu A_i^{(0)}(\nabla_j \nabla_j S) = 0. \tag{2.152}$$

The scalar product of (2.152) with gradS yields

$$\vec{A}^{(1)}.\vec{\nabla} S = -\vec{\nabla}.\vec{A}^{(0)}, \tag{2.153}$$

which may be substituted back to give

$$2\nabla_j S \nabla_j A_i^{(0)} + A_i^{(0)}(\nabla_j \nabla_j S) = 0, \tag{2.154}$$

a first order equation for $A_i^{(0)}$. In terms of distances along rays, and note that $\vec{\nabla}S.\vec{\nabla}$ is a derivative taken along a ray, (2.154) becomes

$$\frac{d}{dS}\vec{A}^{(0)} = c_s(\nabla^2 S)\vec{A}^{(0)} \tag{2.155}$$

with the solution

$$\vec{A}^{(0)}(s) = \vec{A}^{(0)}(s_0)e^{-\frac{1}{2}c_s\int_{s_0}^{s}\nabla^2 S dS} \quad . \tag{2.156}$$

The procedure described above is repeated for any n = 1, 2, ... until the required n is achieved. Then the solution of the problem is obtained according to (2.145) and (2.144).

The geometric ray theory may be extended to inhomogeneous media [57], where it provides significant insights. It was able to solve the important canonical problem for diffraction of semi-infinite crack.

The theory of the reflection and diffraction of ultrasounds at oblique incidence on crack-like discontinuities has been reviewed by Achenbach *et al.* [32]. The approach commonly involves the conversion of dynamic elasticity problem into a form amenable to a solution using Wigner-Hopf method [13], and leaves one relatively simple one-dimensional integral to be performed numerically.

Achenbach and Gautesen [58] considered arbitrary angles of incidence. In general case, an incident wave will produce two cones of diffracted bulk rays. The semiangle of one cone is equal to the angle between the incident wave and the tangent to the crack edge, and the semiangle of the mode-converted cone is given by the Snell's law. The theory has been extended [59] to include the surface waves which will be generated on the crack faces. These are important because strong resonance effects can be seen on finite cracks as a result of surface waves which are multiply reflected from the crack edges, shedding some energy into bulk waves at each reflection. The bulk waves arising in this way are known as secondary diffraction, as opposed to the primary diffraction of a bulk waves at the crack edge and producing further bulk waves.

Geometric ray theory has been applied to surface breaking cracks as well [60], where the scattering of surface waves was considered. The authors difficulties centered on computing the reflection and transmission coefficients of surface waves from the 90° corner at the root of the crack, where it brakes the open surface. No simple solution exists for this problem, so they relied on numerical results from [61], supplemented by finite-difference and experimental results from Bond [62]. Similar problems will arise in scattering of bulk waves from surface breaking defects, suggesting that it might be advantageous to adopt a purely numerical method from the start of the problem for such cases.

2.3.4. Numerical Methods for Solution. Historical Review of Finite-Difference Method Development and Applications

In the study of the scattering of elastic waves, in practical applications such as nondestructive testing, one frequently wants to treat complicated geometrical situations, which are not amenable to analytic treatment. Even expert practitioners of analytic methods recognize this [63-65].

Rather than face both tedious analysis and lengthy numerical work, one can opt for a completely numerical approach. The commonest methods are based on finite differences and finite elements. There are distinctions between the approaches and the solution techniques used in these two methods, but they are quite closely related and the equivalencies between the two schemes can be drawn up [66]. Historically, finite difference methods have precedence. They were introduced by Euler [67] for one-dimensional problems, and the extension to two-dimensions was made by Runge [68]. Finite element methods, on the other hand, were not introduced until electronic digital computers became available. The term *finite element method* was first used by Clough [69], although the foundations of the method were laid by Turner *et al.* [70] and Argyris [71].

Although finite-difference methods for elastic wave problems have been in use for some time [72, 73], their application to nondestructive testing did not begin until about 1973. At about that time Harumi, Suzuki and Saito [74] modeled the near field of a transducer, and Rose and Meyer [75] used a numerical model to confirm the results of their model calculations of transducer field. Calculations of scattering have been undertaken since about 1976, and the first published works were [76-79]. A review is given by Bond [62] and Harker [20]. A consistent finite difference model with applications to scattering by cracks with infinitesimally small width was developed by Harker [80], and a comparison of the finite-difference modeled results of the ray tracing technique [57] was modeled in [81] for austenitic steels.

Below the basic approach of the finite element method as it is most commonly introduced in practice will be given. The method is characterized by the following three features:

(1). The domain of the problem is represented by a collection of simple subdomains, called finite elements, which constitute the finite element mesh.

(2). Over each finite element, the physical process is approximated by functions of desired type (polynomials or otherwise), and algebraic equations relating physical quantities at selective points (nodes) of the element are developed.

(3). The element equations are assembled using continuity and/or 'balance" of physical quantities.

The discretization of equation (2.28) is most easily achieved through the weak formulation of the equations using the principle of the virtual work [82, 83]. An alternative approach relies on a direct, weighted residual method [84]. This method employs the formation of an inner product between the governing equation (2.28) and a weight w_i, such that

$$\begin{aligned}&\left\langle w_i;\sigma_{ij,j}+\rho F_i-\rho\frac{\partial^2 u_i}{\partial t^2}\right\rangle\\&=-\left\langle w_{i,j};\sigma_{ij}\right\rangle+\left\langle w_{i,j};\rho F_i\right\rangle-\left\langle w_i;\rho\frac{\partial^2 u_i}{\partial t^2}\right\rangle+\int_S w_i\sigma_{ij}n_j dS=0\end{aligned}, \tag{2.157}$$

where the notation < ; > indicates integration over the solution domain Ω. Besides volume terms, the integration by parts yields a surface integral as part of implicit traction boundary conditions.

As a next step, the field region Ω is subdivided into finite elements. Within each element displacement field and weight are approximated by interpolation polynomials or shape functions $N(x_1, x_2, x_3)$ weighted by function values $U_T^i(t)$ and $W_T^i(t)$ at the elementary nodes I (P= total number of nodes per element)

$$
\begin{aligned}
u_i &\approx \sum_{I=1}^{P} N_I(x_1,x_2,x_3)U_I^i(t) \\
w_i &\approx \sum_{I=1}^{P} N_I(x_1,x_2,x_3)W_I^i(t)
\end{aligned}
\tag{2.158}
$$

Substituting (2.158) in (2.157) and utilizing the constitutive relations (2.20) yields an elemental matrix equation for losless material

$$
\left[K_{IJ}^e\right]\left\{U_J^e\right\}+\left[M_{IJ}\right]\left\{\ddot{U}_J^e\right\}+\left\{F_I^e\right\}=\left\{R_I^e\right\},
\tag{2.159}
$$

where

$$
\begin{aligned}
K_{IJ}^e &= \int_{V^e} \frac{\partial N_I}{\partial x_i} c_{ijkl} \frac{\partial N_J}{\partial x_j} dV^e, \quad M_{IJ}^e = \int_{V^e} N_I \rho(x,y,z) N_J dV^e, \\
F_I^e &= \int_{V^e} N_I f_i dV^e, \quad f_i = \rho(x,y,z)F_i, \qquad , \\
R_I^e &= \int_{V^e} N_I \sigma_{ij} n_j dV^e
\end{aligned}
\tag{2.160}
$$

The quantities $\left\{U_J^e\right\}$, $\left\{\ddot{U}_J^e\right\}$ refer to the nodal displacement and its second time derivative, respectively. The notation also implies that each of the elemental nodes J (=1,..,P) either contains three displacement components (i=1,2,3) for three-dimensional case, or two components for two-dimensional case.

Equation (2.159) is subsequently assembled into a global matrix form encompassing all individual element contributions

$$[K]\{U\}+[M]\{\ddot{U}\}+\{F\}=\{R\}, \tag{2.161}$$

where the matrices are of positive, semidefinite bounded structure. The second time-derivative is approximated by center-differences, as it is described in the following chapter. The mass matrix [M] is diagonalized in order to eliminate matrix inversion at each time step [82-84]. This diagonalization, or lumping, is achieved on an elemental level according to

$$M_{IJ}^{diag}=\begin{cases} M_{IJ}^{e}\dfrac{\sum\limits_{K=1}^{P}\sum\limits_{L=1}^{P}M_{KL}^{e}}{\sum\limits_{L=1}^{P}M_{LL}^{e}}, & I=J, \\ 0, & I\neq J. \end{cases} \tag{2.162}$$

With these transformations, equation (2.161) is the base for finite-element analysis. For static stress problems, finite element methods is generally the preferred technique [20]. To date, however, there seem to have been no finite-element calculations on elastic wave scattering problems which exploit what is usually claimed to be the major advantage of finite elements over finite differences method, namely the ease with which complicated geometries can be treated (see also [20, 82-84]).

2.3 Gabor Short Time Fourier Transform (STFT) and Wavelet Transform

It is seen from the above discussion, the non-destructive testing analyses frequently have to deal with nonstationary signals, and their timely distributed spectral behavior. In order to study the spectral behavior of an analog signal from its Fourier transform, full knowledge of the signal in the time domain must be acquired . In addition, if a signal is altered in a small neighborhood of some time instant, then the entire spectrum is altered. In the extreme case, the Fourier transform of a delta distribution $\delta(t-t_0)$ is $e^{-it_0\omega}$, which certainly covers the whole frequency domain. Hence, in many applications such as analysis of non-stationary signals and real time signal processing, the formula of Fourier transform is quite inadequate.

The deficiency of the Fourier transform in time-frequency analysis was already observed by D. Gabor [85], who introduced a time-localization "window" function g(t-b), where the parameter b is used to translate the window in order to cover the whole time domain, for extracting local information of the Fourier transform of the signal. In fact, Gabor has used a Gaussian function for the window function:

$$g(t) = \frac{1}{2\sqrt{\pi\alpha}} e^{-\frac{t^2}{4\alpha}}, \tag{2.163}$$

where $\alpha>0$ is fixed. The "Gabor Transform" of a function f is defined as

$$(G_b^\alpha f)(\omega) = \int_{-\infty}^{\infty} (e^{-it\omega} f(t)) g_\alpha(t-b) dt \tag{2.164}$$

that is, $(G^\alpha_b f)(\omega)$ localizes the Fourier transform of f around t=b. The "width" of the window is determined by the (fixed) $\alpha>0$. It can be shown [85, 86] that

$$\int_{-\infty}^{\infty}(G_b^{\alpha}f)(\omega)db = \hat{f}(\omega) \tag{2.165}$$

where $\hat{f}$ is the Fourier transform of f. Employing the notion of standard deviation, or root mean square (RMS), defined by

$$\Delta_{g_\alpha} = \frac{1}{\|g_\alpha\|_2}\left\{\int_{-\infty}^{\infty} x^2 g_\alpha^2(x)dx\right\}^{\frac{1}{2}} \tag{2.166}$$

where

$$\|g_\alpha\|_2 = \left\{\int_{-\infty}^{\infty} g_\alpha^2(x)dx\right\}^{\frac{1}{2}},$$

it can be shown [85, 86] , that for each $\alpha>0$

$$\Delta_{g_\alpha} = \sqrt{\alpha},$$

and the width of the window function g_α is 2 $\Delta_{g\alpha}$. Further

$$\int_{-\infty}^{\infty}\left(e^{-i\omega t}f(t)\right)g_\alpha(t-b)dt = \left(\sqrt{\frac{\pi}{\alpha}}e^{-ib\omega}\right)\frac{1}{2\pi}\int_{-\infty}^{\infty}\left(e^{i\omega\eta}\hat{f}(\eta)\right)g_{\frac{1}{4}\alpha}(\eta-\omega)d\eta, \tag{2.167}$$

which says that, with the exception of the term $\left(\sqrt{\frac{\pi}{\alpha}}e^{-ib\omega}\right)$, the "window Fourier transform" of f with window function g_α at t=b agrees with the "window inverse Fourier transform" of with window function $g_{1/4\alpha}$. Also

$$(2\Delta_{g\alpha})\,(2\Delta_{g\frac{1}{4}\alpha}) = 2\,. \tag{2.168}$$

The last equation represents a formulation of the uncertainty principle, expressing the fundamental fact that increasing the precision with which we determine the frequency decreases the precision in the time determination and vice versa.

The Cartesian product

$$\left[b-\sqrt{\alpha},b+\sqrt{\alpha}\right]x\left[\omega-\frac{1}{2\sqrt{\alpha}},\omega+\frac{1}{2\sqrt{\alpha}}\right] \tag{2.169}$$

of these windows is called a rectangular time-frequency window. The width of $2\sqrt{\alpha}$ of the time window is called the "width of the time-frequency window", and $\frac{1}{\sqrt{\alpha}}$ is the "height " of that window. Generalizing the discussion above, the Gabor transform can be determined as a particular case of Short Time Fourier Transform (STFT) with any Gaussian function g_α as the window function. In fact, it can be proven [86] that the Gabor transform is the STFT with the smallest time-frequency window* It can be proven that the inverse Gabor STFT is given by

$$f(x)=\frac{1}{2\pi}\int_{-\infty}^{\infty}\int_{-\infty}^{\infty}\left[e^{i\omega x}\left(G_b^a f\right)(\omega)\right]g_\alpha(x-b)\,d\omega db\,. \tag{2.170}$$

The width of the time-frequency window is fixed along the entire frequency spectrum. Since it takes a narrow time window to locate high-frequency phenomena more precisely

---

* This is expressed by the equal sign in eq. (2.168).

and a wide time window to analyze low frequency behaviors more thoroughly, STFT is not suitable for analyzing signals with both very high and very low frequencies. That is why the integral wavelet transform (IWT) has been developed [86,88,89], which provides a flexible time-frequency window which automatically narrows when observing high-frequency phenomena and widens when studying low-frequency environment. IWT is defined by

$$\left(W_{\psi}f\right)(b,a) = |a|^{-\frac{1}{2}} \int_{-\infty}^{\infty} f(t)\overline{\psi\left(\frac{t-b}{a}\right)}dt \tag{2.171}$$

a, b real and $a \neq 0$. The functions f and ψ satisfy the conditions

$$\int_{-\infty}^{\infty} |f(t)|^2 dt < \infty ; \quad \int_{-\infty}^{\infty} |\psi(t)|^2 dt < \infty \tag{2.172}$$

and, in addition

$$\int_{-\infty}^{\infty} \frac{|\hat{\psi}(\omega)|^2}{|\omega|} d\omega < \infty , \tag{2.173}$$

where as before $\hat{\psi}$ is the Fourier transform of ψ.

Any function ψ satisfying (2.171) and (2.173) is called a 'basic wavelet". In addition, if ψ and $\hat{\psi}$ are such that

$$\int_{-\infty}^{\infty} t^2 |\psi(t)|^2 dt < \infty ; \quad \int_{-\infty}^{\infty} t^2 |\hat{\psi}(t)|^2 dt < \infty , \tag{2.174}$$

then it follows, under this additional assumption, that $\hat{\psi}$ is a continuous function and from the finitness of the integral in (2.173) it follows that $\hat{\psi}(0) = 0$, or , equivalently

$$\int_{-\infty}^{\infty} \psi(t)dt = 0;$$

- a property not possessed by the Gabor STFT. Using the "admissibility condition" (2.172), the inverse IWT can be proven to be given by

$$f(x) = \frac{1}{C_\psi} \int_{-\infty}^{\infty} \int_{-\infty}^{\infty} \left[\left(W_\psi f\right)(b,a) \right] |a|^{\frac{1}{2}} \psi\left(\frac{x-b}{a}\right) \frac{da}{a^2} db, \tag{2.175}$$

where C_ψ is defined by the identity

$$\int_{-\infty}^{\infty} \int_{-\infty}^{\infty} \left[\left(W_\psi f\right)(b,a) \overline{\left(W_\psi g\right)(b,a)} \right] \frac{da}{a^2} db = C_\psi < f,g >, \; < f,g >= \int_{-\infty}^{\infty} f(x)\overline{g(x)}dx,$$

and $\overline{g(x)}$ denotes the complex conjugate.

An example of a 'basic" wavelet widely used in [87] for applications is the sombrero ("mexican hat"), given by

$$\psi(t) \cong (1-t^2)e^{-\frac{t^2}{2}} \tag{2.176}$$

It satisfies the conditions (2.172) and (2.173) and therefore has a zero mean value.

An example of application of Gabor STFT and CWT, borrowed from [87], is discussed here. Figure 2-6 shows a STFT of a white Gaussian noise. In figure 2-7 it is shown the CWT of the same noise. It is seen that while the STFT spreads the noise characteristics over all time and frequency domain, the CWT localize the noise at the shortest scales. This clearly illustrates the advantage of CWT over STFT and Fourier Transform, in particular for analyses of noisy signals where the noise may be considered as a white Gaussian noise.

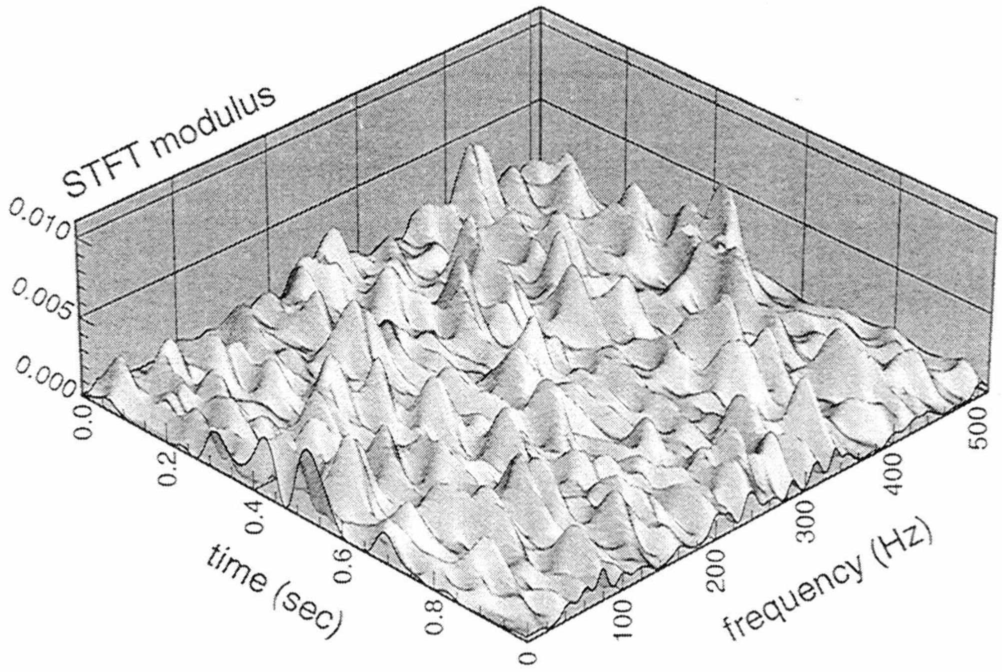

Figure 2-6. The Gabor Short Time Fourier Transform (STFT) of white noise.

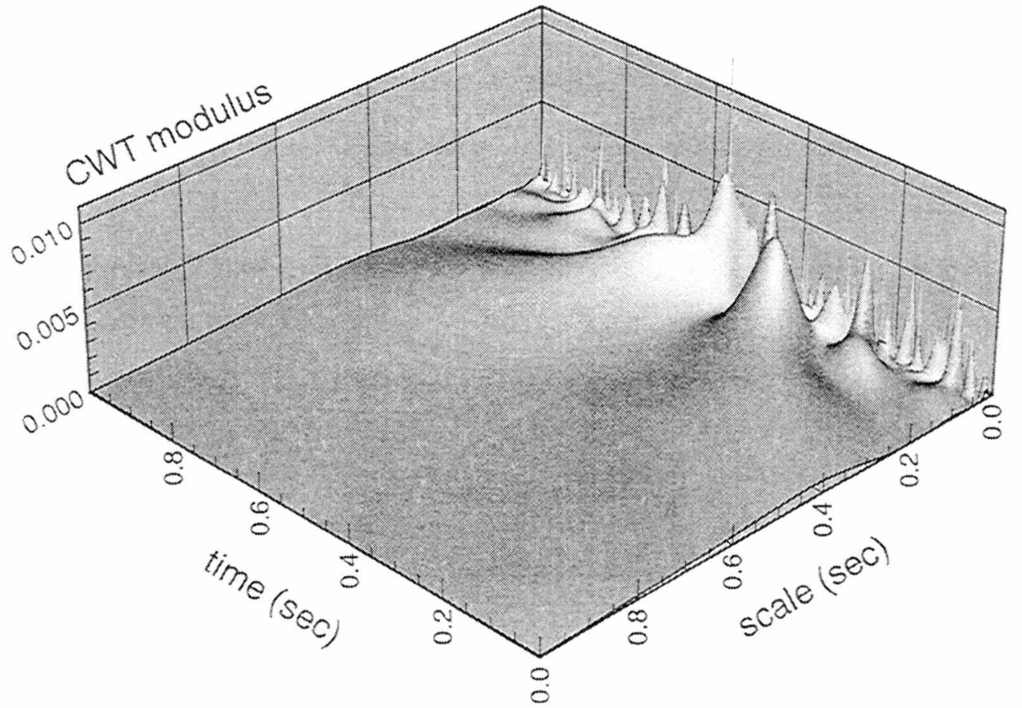

Figure 2-7. The Continuous Wavelet Transform (CWT) of white noise.

CHAPTER 3

Finite Difference Formulation of the Wave Equations

In this chapter we concentrate on development of a finite-difference formulation of the wave equation in two dimensions, as well as the formulation of boundary and interface conditions in a consistent manner using the finite-difference approximations.

The basic idea of the finite-difference method is very simple. The differential form of the wave equation for a continuum is replaced by a discrete set of equations in which the values of the field quantities (displacements in the present case) are defined only on the points of intersection of a grid. The partial derivatives in the wave equation are approximated, to a given accuracy, by combining Taylor expansions of functions defined over the grid. The present method works with the wave equation in its second order form. It is also possible [90] to express the problem in terms of coupled first order equations, using velocity and stress as the field quantities. Duncan [91] has used such a scheme for elastic wave scattering calculations. Bayliss [92] also used velocity and stress fields, to produce a scheme which is accurate to second order in time and fourth order in space.

3.1. Finite-Difference Wave Equations for Homogeneous Media

We start with the wave equation for homogeneous, isotropic media, in terms of the displacements $\vec{U}(\vec{r},t)$

$$s^2\vec{\nabla}^2\vec{U}+(p^2-s^2)\vec{\nabla}\vec{\nabla}.\vec{U}=\frac{\partial^2\vec{U}}{\partial t^2}, \tag{2.43}$$

where we assume that there are no body forces. If we consider a plane strain situation, in which the displacements are zero in the Z-directions, so that $\vec{U}(\vec{r},t) = \vec{U}(x,y,0,t)$, and there is no dependence on z, we obtain the system

$$\begin{vmatrix} (p^2 - s^2)(u_{xx} + v_{xy}) + s^2(u_{xx} + u_{yy}) + f_1 = u_{tt} \\ (p^2 - s^2)(u_{xy} + v_{yy}) + s^2(v_{xx} + v_{yy}) + f_2 = v_{tt} \end{vmatrix}, \tag{2.50}$$

where we use the notation introduced in Chapter 2, section 2.1.7. If we define the variables u and v on a uniform Cartesian mesh, of spacing h in both X- and Y- directions, and at time intervals Δt, we may write

$$\vec{U}(m,n,l) = \vec{U}(mh,nh,l\Delta t), \tag{3.1}$$

where m, m, l are positive integer numbers. The same notation is used for both components u and v of the displacement vector with respect to X- and Y- axes. Using the expression for the second derivatives with respect to x, y and t, given in Appendix A, we obtain for the finite difference approximation of the wave equations the following expressions:

$$\begin{vmatrix} u(m,n,l+1) = 2(1 - \beta^2 p^2 - \beta^2 s^2)u(m,n,l) - u(m,n,l-1) + p^2\beta^2[u(m+1,n,l) \\ +u(m-1,n,l)] + \beta^2 s^2[u(m,n+1,l) + u(m,n-1,l) + \frac{1}{4}\beta^2(p^2 - s^2) \\ x[v(m+1,n+1,l) - v(m+1,n-1,l) - v(m-1,n+1,l) + v(m-1,n-1,l)], \end{vmatrix}$$

$$
\begin{aligned}
&v(m,n,l+1) = 2(1-\beta^2 p^2 - \beta^2 s^2)v(m,n,l) - v(m,n,l-1) + \beta^2 p^2[v(m,n+1,l) \\
&+v(m,n-1,l)] + \beta^2 s^2[v(m+1,n,l) + v(m-1,n,l)] + \frac{1}{4}\beta^2(p^2 - s^2) \\
&x[u(m+1,n+1,l) - u(m+1,n-1,l) - u(m-1,n+1,l) + u(m-1,n-1,l)].
\end{aligned}
, \qquad (3.2)
$$

$$\beta = \frac{\Delta t}{h}$$

where p denotes the compression speed and s - the shear wave speed.

3.1.1. Stability of finite difference method

The stability of the finite difference method is a property of the entire problem: that is, it depends of the finite difference representation both of the bulk medium and the boundary and interface conditions. Commonly, however, a method of stability analysis is used which ignores the boundary or interface conditions. Such a method was applied to the elastic wave system by Alterman and Loewental [93]. The method involves studying the propagation of a plane wave through an infinite grid: as it is single frequency wave the method is known as the Fourier method [94], although it appears to have been suggested for the first time by von Neumann during the second world war [95,96].

Consider the plane wave

$$\vec{U}(m,n,l) = \vec{A}\, e^{i(k_x m + k_y n)h} \gamma^l, \qquad (3.3)$$

where the time dependence is contained within the factor γ, and the condition for stability is that $1 \geq |\gamma|$. To simplify the equations, we define

$$\alpha = \frac{p\Delta t}{h}, \quad \beta = \frac{s\Delta t}{h}, \tag{3.4}$$

and substituting equation (3.3) into (3.2). After removing the exponential factor we obtain

$$\begin{aligned} u\gamma &= 2(1-\alpha^2-\beta^2)u\gamma^{-1} + 2\alpha^2 u\cos(kh\cos\theta) + 2\beta^2 u\cos(kh\sin\theta) \\ &+ \frac{1}{4}(\alpha^2-\beta^2)v(\cos(kh(\cos\theta+\sin\theta)) - \cos(kh(\cos\theta-\sin\theta))) \end{aligned} \tag{3.5}$$

and similar for v. By evaluating the determinant of the coefficients of u and v for the worst case ($kh\sin\theta = .25\pi$ and $kh\cos\theta = .25\pi$) (this case corresponds to the extreme value of the parameter γ) in [93] was shown that, for stability, one must have

$$\frac{\Delta t}{h} \le (p^2+s^2)^{-\frac{1}{2}}. \tag{3.6}$$

This is, roughly speaking, a requirement that a signal shall not be able to propagate across one mesh spacing in less than one time step. In one-dimensional case this requirement was formulated by Courant, Friedrich and Lewy [97] and is known as Courant - Friedrich - Lewy criterion [96].

Ilan and Loewenthal [98] studied the effects of boundary conditions on the stability of finite difference schemes. Their approach was two-fold: empirical, using trial calculations with the chosen finite difference method, and theoretical, using a modification of the matrix method. The basic idea is: first, arrange all the displacement points at time $l\Delta t$ as a vector $\vec{U}^l$, which has dimension 2MN for the two displacement directions, M points in the X- direction and N points in Y- direction:

$$\vec{\mathbf{U}}^{l} = \begin{pmatrix} u(1,1,l) \\ v(1,1,l) \\ \cdot \\ \cdot \\ u(M,N,l) \\ v(M,N,l) \end{pmatrix}. \qquad (3.7)$$

Then the finite difference scheme may be written as

$$\vec{\mathbf{U}}^{l+1} = \mathbf{O}\vec{\mathbf{U}}^{l} - 1\vec{\mathbf{U}}^{l-1}, \qquad (3.8)$$

where **1** is the unit matrix of dimension 2MNx2MN and **O** is a matrix with the same dimensions which represents the coefficients of *u(m,n,l)* and *v(m,n,l)* in (3.2). We can modify the equations to make them resemble two-level rather than three-level schemes by defining the vector $\vec{\mathbf{V}}^{l}$:

$$\vec{\mathbf{V}}^{l} = \begin{pmatrix} \vec{\mathbf{U}}^{l} \\ \vec{\mathbf{U}}^{l-1} \end{pmatrix}, \qquad (3.9)$$

when we may write

$$\vec{\mathbf{V}}^{l+1} = \mathrm{P}\vec{\mathbf{V}}^{l} \qquad (3.10)$$

with

$$\mathrm{P} = \begin{pmatrix} \mathbf{O} & \mathbf{1} \\ \mathbf{1} & 0 \end{pmatrix}. \qquad (3.11)$$

The operation of the finite difference scheme is equivalent to rising the matrix P to a high power, and in the limit P^l will be dominated by the highest eigenvalue of P, p_{max} say. If the scheme is to be stable, p_{max} must be smaller than unity. This condition is most easily achieved by considering the eigenvalues and eigenvectors of P. If the eigenvectors are $\mathbf{X}^{(n)}$ with eigenvalues ε_n, we may expand $\vec{\mathbf{V}}^l$ as

$$\vec{\mathbf{V}}^l = \sum_n \chi_n \mathbf{X}^{(\mathbf{n})} \tag{3.12}$$

and then, as

$$\mathrm{P}\mathbf{X}^{(\mathbf{n})} = \varepsilon_n \mathbf{X}^{(\mathbf{n})}, \tag{3.13}$$

we have

$$\vec{\mathbf{V}}^{l+1} = \sum_n \chi_n \varepsilon_n^l \mathbf{X}^{(\mathbf{n})}. \tag{3.14}$$

From this expression it is clear that if all the eigenvectors of P have absolute values less than or equal to unity, no initial vector $\vec{\mathbf{V}}^l$, and in particular no error vector, will grow without limit.

If boundary conditions are neglected, the matrix P is easily analyzed [99] by taking advantage of the diagonally banded structure of the matrix. The result is the same stability as (3.6). When the boundary conditions are included, in [99] it was necessary to make use of the Gershgorin's theorems[20] to analyze the stability. The first theorem states that the eigenvalue of largest absolute magnitude of a square matrix cannot exceed the moduli of the elements in any row or column. The second theorem states that if S_s is the sum of the moduli of the elements along row *i* of the matrix, excluding the diagonal element *ii*, then each eigenvalue of the matrix lies inside or on the boundary of at least one of the circles centered on the diagonal element and of radius S_s. Their analysis was particularly useful in identifying regions of instability when their original finite difference scheme was applied to materials of low shear constants. Such considerations might be important for finite difference models which treated the coupling of solids with polymeric materials or viscous fluids, but should not arise for most engineering materials.

In addition to the discussion above, it should be noted that the stability of the finite difference calculations depends on the particular scheme used and the geometry setup as well. It is seen from (3.2) that the scheme chosen involves displacement values at three subsequent neighboring mesh points in each spatial direction. This fact rises the requirement that between two neighboring boundaries (or interfaces) it is necessary to have at least three mesh points inside the medium in order to calculate properly the displacements between the boundaries. The numerical experiments made even showed that the minimum number of mesh points must be actually twice the number mentioned above - in our case it is six, in order to keep the solution stable.

3.1.2. Accuracy of the Finite Difference Method

As it is well known, the stability criterion given in (3.6) does not offer guidance as to the grid spacing that is required if the solution is to be accurate rather than simply stable. What we actually need is to obtain convergence of the numerical solution to the true one for each particular case. That is why additional considerations for the accuracy (or consistency) of the solution is necessary.

Consider a plane compression wave traveling through a grid. From the difference equations (3.2), writing $\gamma = e^{i\omega\Delta t}$, where ω will be real if the stability criterion is satisfied, and taking $(k_x, k_y, 0) = k(\cos\theta, \sin\theta, 0)$, we find

$$\sin^2\frac{\omega\Delta t}{2} = \alpha^2\sin^2\left(\frac{kh\cos\theta}{2}\right) + \beta^2\sin^2\left(\frac{kh\sin\theta}{2}\right) + \frac{1}{4}(\alpha^2 - \beta^2)\tan\theta\sin(kh\cos\theta)\sin(kh\sin\theta), \tag{3.15}$$

and from this we can extract the phase velocity, $v = \frac{\omega}{k}$. For simplicity, consider the case $\theta=0$, i.e. the wave propagating in X-direction. Then

$$\frac{v}{p} = \frac{\omega}{kp} = \frac{2}{kp\Delta t}\sin^{-1}(\alpha\sin\frac{kh}{2}), \tag{3.16}$$

where α and β are defined in (3.4) and p denotes the compression phase velocity. If we define N to be the number of points taken per wavelength, then

$$\frac{v}{p} = \frac{N}{\pi}\frac{h}{p\Delta t}\sin^{-1}\left(\frac{\Delta t}{h}p\sin\frac{\pi}{N}\right). \tag{3.17}$$

From this expression it is immediately apparent that as $N \to \infty$ the phase velocity in the finite difference model approaches the exact value.

In practical calculations [20,99], it is advisable to take rather more than ten mesh points per wavelength to represent the wavelength of the dominant frequency, so that the higher frequencies which will be included in any pulse are adequately represented.

3.2. Zero Stress Boundary Conditions Formulation in Terms of Finite Difference Approximation

Rigid boundaries are trivial, as they only require the setting of displacements to zero at each time step. For stress-free boundaries, the situation is rather more complicated. One way of achieving a stable scheme requires the introduction of a row of artificial points just outside the boundary. The displacements of these points are then determined at each time step so as to give zero stress on the boundary.

Consider [80] the boundary at a plane perpendicular to y-axis at $y=n_o h$ and let introduce pseudo-nodes at $y=(n_o-1)h$ (fig.3-1). The body is assumed to occupy he plane $y \geq n_o h$. We introduce the fictitious displacements at these nodes in such a way that the corresponding stress-tensor components to be zero at the actual boundary. For the zero-stress conditions on a plane perpendicular to the y-axis we have:

$$\begin{aligned} \sigma_{yy} &= \lambda(u_x + v_y) + 2\mu v_y = 0, \\ \sigma_{xy} &= \mu(u_y + v_x) = 0. \end{aligned} \tag{3.18}$$

Rearranging (3.18) and using the notation introduced before, these equations become

$$\begin{aligned} \frac{\sigma_{yy}}{\rho} &= (p^2 - 2s^2)u_x + p^2 v_y = 0 \\ \frac{\sigma_{xy}}{\rho} &= s^2(u_y + v_x) = 0. \end{aligned} \tag{3.19}$$

For stress-free boundaries, the finite difference equations are expressed in one-sided form for derivatives normal to the boundary and in centered form (A.7) for tangential derivatives. Thus, on the plane $y=n_o h$ we get (fig.3-1, a))

$$(p^2-2s^2)[u(m+1,n_0,l)-u(m-1,n_0,l)]+2p^2[v(m,n_0,l)-v(m,n_0-1,l)]=0$$
$$2[u(m,n_0,l)-u(m,n_0-1,l)]+v(m+1,n_0,l)-v(m-1,n_0,l)=0.$$

Solving the last equation for $u(m,n_o-1,l)$ and $v(m,n_o-1,l)$ we get for these components of the displacement at the pseudo-nodes

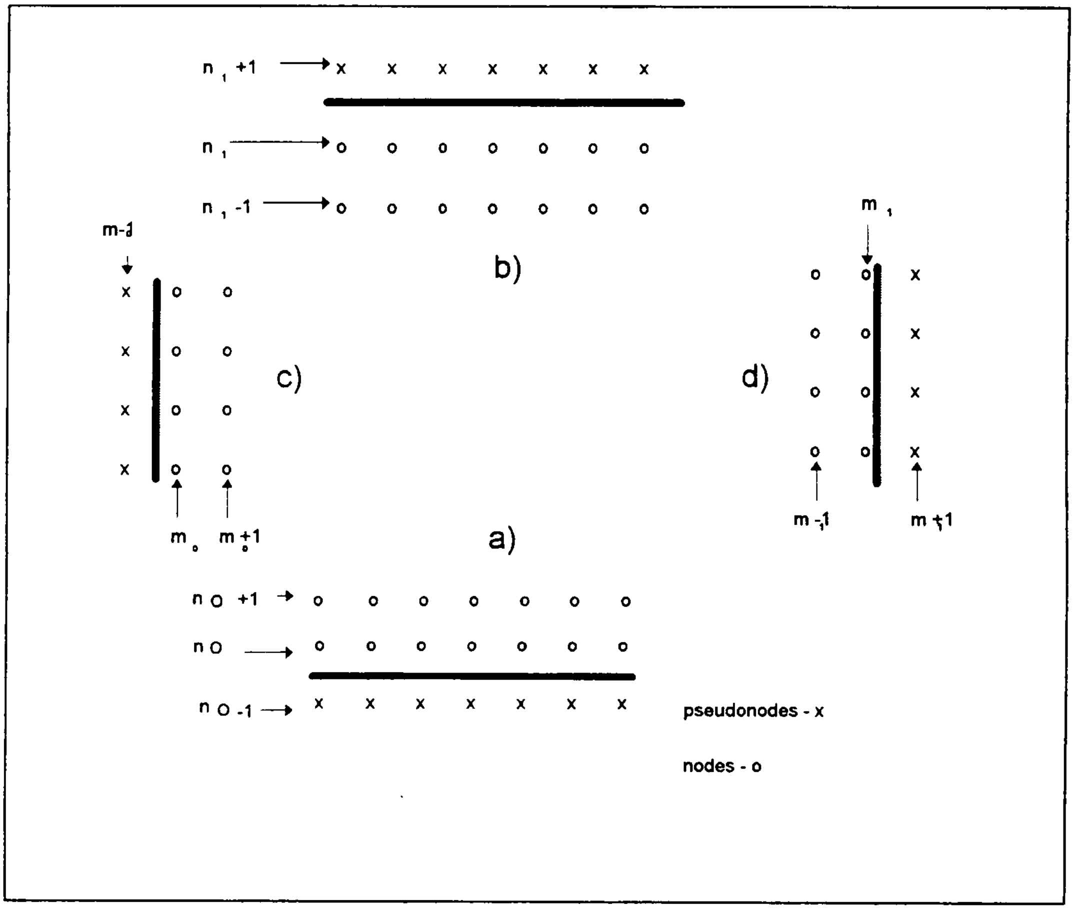

Figure 3-1. The geometry of the pseudonodes at the free boundaries.

$$v(m,n_0-1,l)=v(m,n_0,l)+\frac{p^2-2s^2}{2p^2}[u(m+1,n_0,l)-u(m-1,n_0,l)],$$
$$u(m,n_0-1,l)=u(m,n_0,l)+\frac{1}{2}[v(m+1,n_0,l)-v(m-1,n_0,l)]. \qquad (3.20)$$

Similarly, for the top boundary n_1 where the body occupies the space $y\leq n_1h$ (fig.3-1,b)) we obtain

$$v(m,n_1+1,l)=v(m,n_1,l)-\frac{p^2-2s^2}{2p^2}[u(m+1,n_1,l)-u(m-1,n_1,l)],$$
$$u(m,n_1+1,l)=u(m,n_1,l)-\frac{1}{2}[u(m+1,n_1,l)-v(m-1,n_1,l)]. \qquad (3.21)$$

For the left boundary where the body occupies the right half space $x\geq m_oh$ (fig.3-1, c)) we obtain using the same approach

$$u(m_0-1,n,l)=u(m_0,n,l)+\frac{p^2-2s^2}{2s^2}[v(m_0,n+1,l)-v(m_0,n-1,l)]$$
$$v(m_0-1,n,l)=v(m_0,n,l)+\frac{1}{2}[u(m_0,n+1,l)-u(m_0,n-1,l)] \qquad (3.22)$$

For the right boundary where the body occupies the half space $x\leq m_1h$ (fig.3-1, d)) we obtain

$$u(m_1+1,n,l)=u(m_1,n,l)-\frac{p^2-2s^2}{2p^2}[v(m_1,n+1,l)-v(m_1,n-1,l)],$$
$$v(m_1+1,n,l)=v(m_1,n,l)-\frac{1}{2}[u(m_1,n+1,l)-u(m_1,n-1,l)] \qquad (3.23)$$

The above difference scheme will not define the displacements if corners are introduced. Let consider the corner at $(x, y)=(m_3,n_3)$ as shown in fig.3-2. The difference equations for the bulk (3.2) fix the values at (m_3-1,n_3), (m_3,n_3), (m_3,n_3-1) and (m_3-1,n_3-1), and the ordinary boundary equations (3.21) fix the values at (m_3-1,n_3+1) and (m_3+1,n_3-1). To get the values at (m_3, n_3+1) and (m_3+1,n_3), the equations for the boundary planes are solved simultaneously. This gives

$$v(m_3+1,n_3,l)=\frac{4}{3}[v(m_3,n_3,l)-\frac{1}{4}v(m_3-1,n_3,l)-\frac{1}{2}(u(m_3,n_3,l)-u(m_3,n_3-1,l))],$$

$$u(m_3+1,n_3,l)=\frac{1}{1-q^2}[u(m_3,n_3,l)-q^2u(m_3-1,n_3,l)-q(v(m_3,n_3,l)-v(m_3,n_3-1,l))],$$

$$v(m_3,n_3+1,l)=\frac{1}{1-q^2}[v(m_3,n_3,l)-q^2v(m_3,n_3-1,l)-q(u(m_3,n_3,l)-u(m_3-1,n_3,l))],$$

$$u(m_3,n_3+1,l)=\frac{4}{3}[u(m_3,n_3,l)-\frac{1}{4}u(m_3,n_3-1,l)-\frac{1}{2}(v(m_3,n_3,l)-v(m_3-1,n_3,l))] \quad (3.24)$$

where $q=(p^2-2s^2)/2p^2$. This leaves the values at $(m_3+1, {}_n3+1)$ undetermined. In order to determine the displacement components at these points, we need additional two equations for the two displacement components. One possible approach is used in [100], which we apply here. Consider the upper right corner as shown in fig. 3-2. We may consider the corner edge as it is shown in fig. 3-3, that is, we may assume that the corner can be represented as an ark [100], and the zero-traction boundary conditions should be expressed in terms of tangential and normal stresses $\sigma_{\tau n}$ and σ_{nn}. The zero-stress

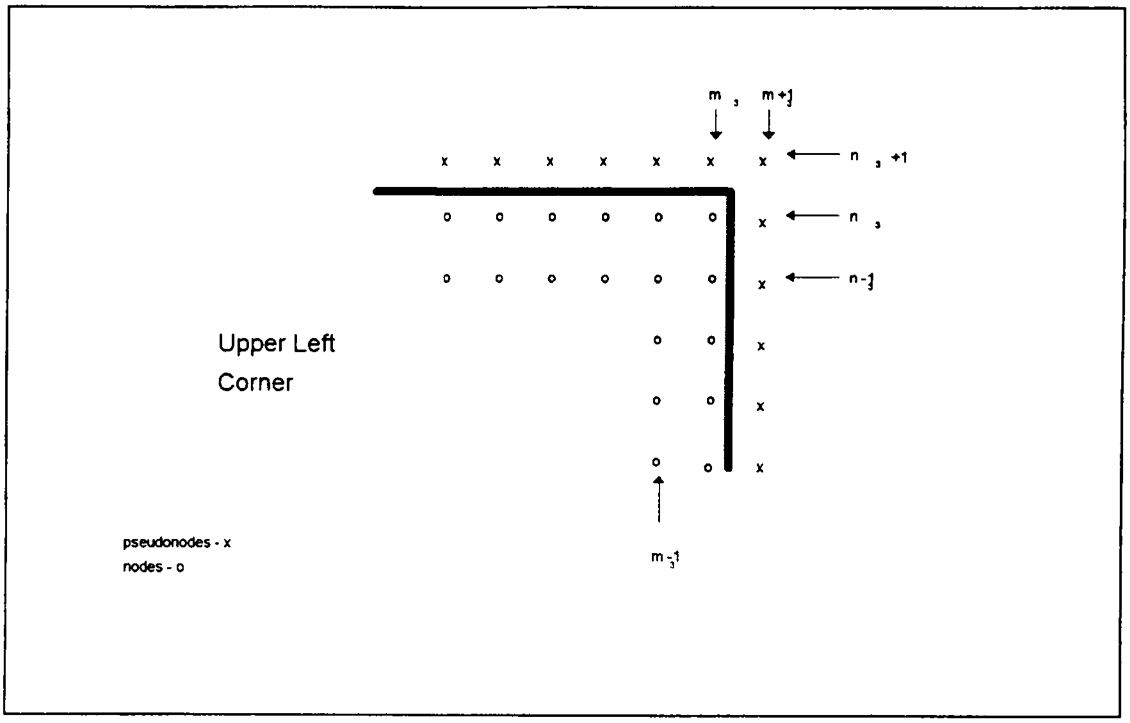

Figure 3-2. The geometry of the pseudonodes at a corner.

boundary conditions at the corner then may be written as:

$$\begin{aligned} \sigma_{nn} &= \lambda\left[u_{n,n} + u_{\tau,\tau}\right] + 2\mu u_{n,n} \\ \sigma_{n\tau} &= \mu\left[u_{n,\tau} + u_{\tau,n}\right] \end{aligned}, \tag{3.25}$$

where u_n and u_τ are the normal and tangential displacement component, and the notation $_{,n}$ and $_{,\tau}$ denotes the derivatives with respect to the normal and tangential coordinate in the coordinate system connected to the corner. This coordinate system can be considered as a rotated around Z-axis on angle θ.

Further, assuming that $\theta = 45°$ [100], we obtain the following relation between u_n, u_τ and u and v

$$u_\tau = \frac{1}{\sqrt{2}}(v - u)$$
$$u_n = \frac{1}{\sqrt{2}}(v + u) \qquad (3.26)$$

For the infinitesimal increments dn and dτ we obtain

$$dn = \frac{1}{\sqrt{2}}(dx + dy)$$
$$d\tau = \frac{1}{\sqrt{2}}(dy - dx) \qquad (3.27)$$

Utilizing (3.26) and (3.27) in (3.25), we obtain

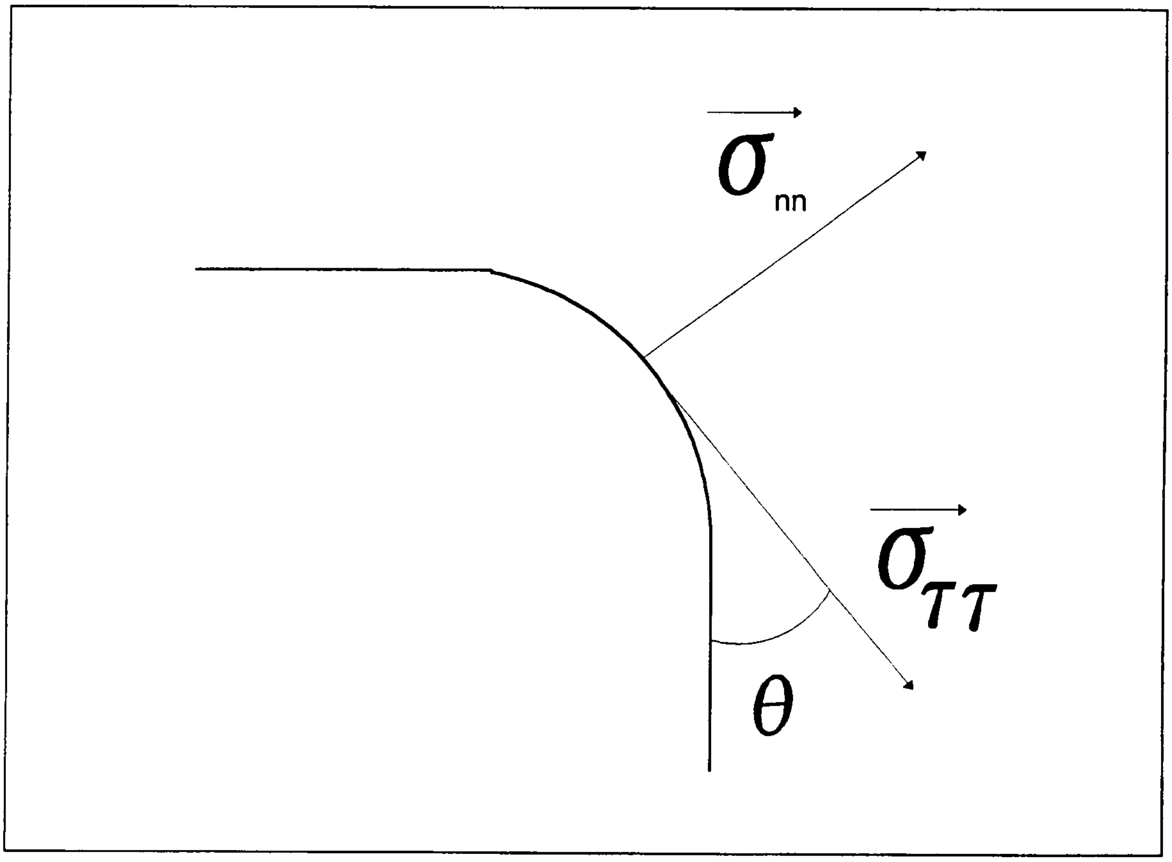

Figure 3-3. Stress-tensor components at the upper right corner.

$$\sigma_{nn} = \frac{1}{2}\sigma_{xx} + \sigma_{xy} + \frac{1}{2}\sigma_{yy}, \tag{3.28}$$

$$\sigma_{n\tau} = \frac{1}{2}(\sigma_{yy} - \sigma_{xx}). \tag{3.29}$$

Vanishing the stresses σ_{nn} and $\sigma_{n\tau}$, we obtain in terms of the derivatives of u and v and compression and shear velocities

$$\left|\begin{array}{l}(p^2 - s^2)(u_x + v_y) + s^2(u_y + v_x) = 0, \\ v_y - u_x = 0.\end{array}\right. \tag{3.30}$$

Applying the finite difference schemes (A.21-A.22), we obtain

$$\begin{aligned}
&u(m_3+1, n_3+1, l) = u(m_3-1, n_3-1, l) + \left(1 - \frac{s^2}{p^2}\right)[u(m_3-1, n_3+1, l) - u(m_3+1, n_3-1, l)] \\
&- \frac{s^2}{p^2}[v(m_3+1, n_3-1) - v(m_3-1, n_3+1)], \\
&v(m_3+1, n_3+1) = v(m_3-1, n_3-1) - \frac{s^2}{p^2}[u(m_3-1, n_3+1) - u(m_3+1, n_3-1)] \\
&-v(m_3-1, n_3+1)\left[1 - \frac{s^2}{p^2}\right] + v(m_3+1, n_3-1)\left[1 - \frac{s^2}{p^2}\right].
\end{aligned} \tag{3.31}$$

Using similar approach for the other three corners, we obtain: for the left upper corner, denoted as (m_2, n_2)

$$\begin{aligned}
&v(m_2, n_2+1, l) = \frac{1}{1-q^2}\left\{v(m_2, n_2, l) - q^2 v(m_2, n_2-1, l)\right. \\
&\left.-q\left[u((m_2+1, n_2, l) - u(m_2, n_2, l)\right]\right\}
\end{aligned}, \tag{3.32}$$

$$u(m_2-1,n_2,l)=\frac{1}{1-q^2}\Big\{u(m_2,n_2,l)-q^2u(m_2+1,n_2,l)$$
$$-q\left[v(m_2,n_2-1,l)-v(m_2,n_2,l)\right]\Big\} \quad , \qquad (3.33)$$

$$u(m_2,n_2+1,l)=\frac{4}{3}\Big\{u(m_2,n_2,l)-\frac{1}{4}u(m_2,n_2-1,l)$$
$$-\frac{1}{2}\left[v(m_2+1,n_2,l)-v(m_2,n_2,l)\right]\Big\} \quad , \qquad (3.34)$$

$$v(m_2-1,n_2,l)=\frac{4}{3}\Big\{v(m_2,n_2,l)-\frac{1}{4}v(m_2+1,n_2,l)$$
$$-\frac{1}{2}\left[v(m_2,n_2-1,l)-v(m_2,n_2,l)\right]\Big\} \quad . \qquad (3.35)$$

Using similar considerations as in the case for right upper corner, we have for the tangential and normal stresses at the corner

$$\sigma_{nn}=\frac{1}{2}\sigma_{xx}-\sigma_{xy}+\frac{1}{2}\sigma_{yy},$$
$$\sigma_{n\tau}=\frac{1}{2}\left[\sigma_{xx}-\sigma_{yy}\right] \quad . \qquad (3.36)$$

Expressing the corresponding stresses in terms of u and v and applying finite difference approximations to the involved derivatives, we obtain for the point above the corner:

$$u(m_2+1,n_2-1,l)=u(m_2-1,n_2+1,l)+\left[1-\frac{s^2}{p^2}\right][u(m_2-1,n_2-1,l)$$

$$-u(m_2+1,n_2+1,l)]+\frac{s^2}{p^2}[v(m_2+1,n_2+1,l)-v(m_2-1,n_2-1,l)]$$

$$. \tag{3.37}$$

$$v(m_2+1,n_2-1,l)=v(m_2-1,n_2+1,l)-\frac{s^2}{p^2}[u(m_2+1,n_2+1,l)$$

$$-u(m_2-1,n_2-1,l)]\ +\left[1-\frac{s^2}{p^2}\right][v(m_2+1,n_2+1,l)-v(m_2-1,n_2-1,l)]$$

For the lower left corner (where is the origin of the coordinate system) denoted as (m_1, n_1), we have

$$u(m_1-1,n_1,l)=\frac{1}{1-q^2}\Big\{u(m_1,n_1,l)-q^2u(m_1+1,n_1,l)$$
$$-q\big[v(m_1,n_1,l)-v(m_1,n_1+1,l)\big]\Big\} \quad , \tag{3.38}$$

$$v(m_1,n_1-1,l)=\frac{1}{1-q^2}\Big\{v(m_1,n_1,l)-q^2v(m_1,n_1+1,l)$$
$$-q\big[u(m_1,n_1,l)-v(m_1+1,n_1+1,l)\big]\Big\} \quad , \tag{3.39}$$

$$u(m_1,n_1-1,l)=\frac{4}{3}\Big\{u(m_1,n_1,l)-\frac{1}{4}u(m_1,n_1+1,l)$$
$$-\frac{1}{2}\big[v(m_1,n_1,l)-v(m_1+1,n_1,l)\big]\Big\} \quad , \tag{3.40}$$

$$v(m_1-1,n_1,l)=\frac{4}{3}\Big\{v(m_1,n_1,l)-\frac{1}{4}u(m_1+1,n_1,l)-\frac{1}{2}\big[u(m_1,n_1,l)-v(m_1,n_1+1,l)\big]\Big\}. \tag{3.41}$$

For the point below the corner the same expressions as in the case of upper right corner are held. Therefore, we obtain

$$u(m_1-1,n_1-1,l)=u(m_1+1,n_1+1,l)-\left[1-\frac{s^2}{p^2}\right][u(m_1-1,n_1+1,l)-u(m_1+1,n_1-1,l)]$$
$$+\frac{s^2}{p^2}[v(m_1+1,n_1-1,l)-v(m_1-1,n_1+1,l)] \quad ,(3.42)$$

$$v(m_1-1,n_1-1,l)=v(m_1+1,n_1+1,l)+\frac{s^2}{p^2}[u(m_1-1,n_1+1,l)-u(m_1+1,n_1-1,l)]$$
$$+\left[1-\frac{s^2}{p^2}\right][v(m_1-1,n_1+1,l)-v(m_1+1,n_1-1,l)] \quad . \quad (3.43)$$

Finally, for the right bottom corner, denoted as (m_4, n_4) we obtain

$$v(m_4+1,n_4,l)=\frac{4}{3}\left\{v(m_4,n_4,l)-\frac{1}{4}v(m_4-1,n_4,l)\right.$$
$$\left.-\frac{1}{2}\left[u(m_4,n_4+1,l)-u(m_4,n_4,l)\right]\right\} \quad , \quad (3.44)$$

$$u(m_4,n_4-1,l)=\frac{4}{3}\left\{u(m_4,n_4,l)-\frac{1}{4}u(m_4,n_4+1,l)\right.$$
$$\left.-\frac{1}{2}\left[v(m_4-1,n_4,l)-v(m_4,n_4,l)\right]\right\} \quad , \quad (3.45)$$

$$u(m_4+1,n_4,l)=\frac{1}{1-q^2}\left\{u(m_4,n_4,l)-q^2u(m_4-1,n_4,l)\right.$$
$$\left.-q\left[v(m_4,n_4+1,l)-v(m_4,n_4,l)\right]\right\} \quad , \quad (3.46)$$

$$v(m_4, n_4 - 1, l) = \frac{1}{1-q^2}\Big\{v(m_4, n_4, l) - q^2 v(m_4, n_4 + 1, l)$$

$$-q\big[u(m_4 - 1, n_4, l) - u(m_4, n_4, l)\big]\Big\} \qquad (3.47)$$

For the point below the corner, making the same considerations as above, we obtain the same expressions for the tangential and normal stress components as in the case of upper left corner above. Thus, we obtain

$$u(m_4 - 1, n_4 + 1, l) = u(m_4 + 1, n_4 - 1, l) + \left[1 - \frac{s^2}{p^2}\right][u(m_4 + 1, n_4 + 1, l)$$

$$-u(m_4 - 1, n_4 - 1, l)] - \frac{s^2}{p^2}[v(m_4 + 1, n_4 + 1, l) - v(m_4 - 1, n_4 - 1, l)], \qquad (3.48)$$

$$v(m_4 - 1, n_4 + 1, l) = v(m_4 + 1, n_4 - 1, l) + \frac{s^2}{p^2}[u(m_4 + 1, n_4 + 1, l)$$

$$-u(m_4 - 1, n_4 - 1, l)] - \left[1 - \frac{s^2}{p^2}\right][v(m_4 + 1, n_4 + 1, l) - v(m_4 - 1, n_4 - 1, l)] \qquad (3.49)$$

Two important notes may be emphasized : the boundary conditions' relations given above are accurate up to O(h) and they relate the displacement's components of the pseudonodes which belong to the same time interval (level).

3.3. Interface Conditions Formulation in Terms of Finite Difference Approximation

One way of achieving a stable scheme for interface conditions implementation, consistent with the already introduced boundary conditions, requires the introduction of a row of artificial points just outside the interface. The displacements of these points are then determined at each step so as to provide the continuity of the stresses on the interface. That means also to "extend" one of the media along the interface within the other one. The row of artificial points along the interface between media (1) and (2) around the intersection of the interface parallel to X-axis with the free boundary is shown in fig. 3-4. We are using the expressions (2.56) and (2.58) to formulate the finite difference approximations to the boundary conditions. We proceed with an approach similar to that of Alterman and Karal [102]. Figure 3-4 shows the artificial points along the interface and away from the intersection with the free boundary (marked as D); points A and C denote the intersection of the interface with the free boundary; point B denotes the intersection of the artificial row along the interface with the free boundary.

Here we derive the finite difference approximations for the displacement components at points D (fig. 3-4). We start with the equations (2.56)

$$\lambda^{(1)}(u_x^{(1)} + v_y^{(1)}) + 2\mu^{(1)}v_y^{(1)} = \lambda^{(2)}(u_x^{(2)} + v_y^{(2)}) + 2\mu^{(2)}v_y^{(2)}, \tag{2.56}$$

$$\mu^{(1)}(u_y^{(1)} + v_x^{(1)}) = \mu^{(2)}(u_y^{(2)} + v_x^{(2)}).$$

Let assume that the interface is at $y = n_0\,h$. Here and further all variables and parameters of medium 1 will be denoted with superscripts (1) and the same for medium 2 and the superscript (2). To distinguish the displacements at the artificial nodes along the interface we denote them with uf(m,n,l) and vf(m,n,l) for the X- and Y- displacement component, respectively. Using (A.10) for the derivatives with respect to Y and (A.24) for the derivatives with respect to X, we obtain, approximating the equations (2.56)

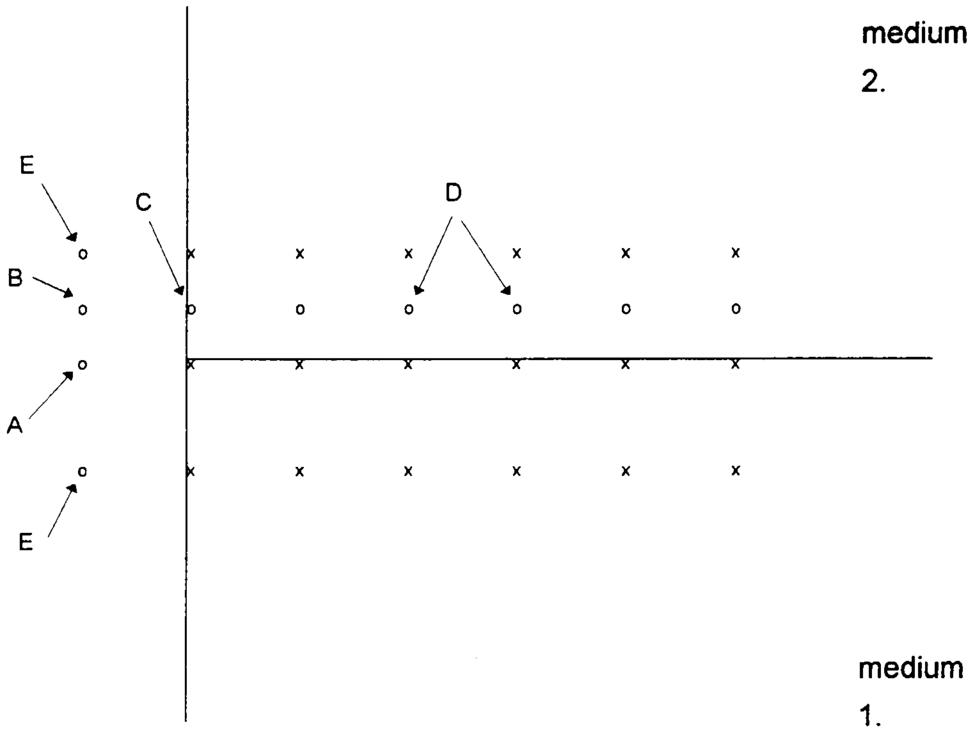

Figure 3-4. The artificial points along the interface between media (1) and (2).

$$uf(m,n_0,l)=\frac{1}{2}\left(1-\frac{s_2^2}{s_1^2}\frac{\rho_1}{\rho_2}\right)\left[v^{(1)}(m+1,n_0,l)-v^{(1)}(m-1,n_0,l)\right]+\frac{s_2^2}{s_1^2}\frac{\rho_1}{\rho_2}u^{(2)}(m,n_0+1,l)$$
$$+\left(1-\frac{s_2^2}{s_1^2}\frac{\rho_1}{\rho_2}\right)u^{(1)}(m,n_0,l)$$

, (3.50)

$$vf(m,n_0,l) = \left(1-\frac{p_2^2}{p_1^2}\frac{\rho_1}{\rho_2}\right)v^{(1)}(m,n_0,l)+\frac{1}{2}\left(\frac{\rho_1}{\rho_2}\frac{p_2^2-2s_2^2}{p_1^2}-\frac{p_1^2-2s_1^2}{p_1^2}\right)$$
$$x\left[u^{(1)}(m+1,n_0,l)-u^{(1)}(m-1,n_0,l)\right]+\frac{p_2^2}{p_1^2}\frac{\rho_1}{\rho_2}v^{(2)}(m,n_0+1,l) \quad . \tag{3.51}$$

In the case when the medium 2 is extended, we obtain similarly

$$uf(m,n_0,l) = \left(1-\frac{\rho_1}{\rho_2}\frac{s_1^2}{s_2^2}\right)\left[v^{(2)}(m+1,n_0,l)-v^{(2)}(m-1,n_0,l)\right]$$
$$+\left(1-\frac{\rho_1}{\rho_2}\frac{s_1^2}{s_2^2}\right)u^{(2)}(m,n_0,l)+\frac{\rho_1}{\rho_2}\frac{s_1^2}{s_2^2}u^{(1)}(m,n_0-1,l) \quad , \tag{3.52}$$

$$vf(m,n_0,l) = \frac{1}{2}\left(\frac{p_2^2-2s_2^2}{p_2^2}-\frac{\rho_1}{\rho_2}\frac{p_1^2-2s_1^2}{p_2^2}\right)$$
$$x\left[u^{(2)}(m+1,n_0,l)-u^{(2)}(m-1,n_0,l)\right] \quad . \tag{3.53}$$
$$+\left(1-\frac{\rho_1}{\rho_2}\frac{p_1^2}{p_2^2}\right)v^{(2)}(m,n_0,l)+\frac{\rho_1}{\rho_2}\frac{p_1^2}{p_2^2}v^{(1)}(m,n_0-1,l)$$

There is an obvious similarity between the expressions for both cases when medium 1 is extended and vise versa. The equations (3.35)-(3.38) contain the ratios of the shear velocities of the two media as well as their compression velocities and density ratios. If the constants characterizing the two media are quite different, then these ratios may be large. The effect of these large ratios is to introduce serious errors and (sometimes) instabilities in the calculations. The reason this occurs is because the one-sided derivative in y introduces an asymmetry in the interface conditions. If we had used a two-sided or centered derivative in y, the finite difference equations for the interface conditions would be symmetrical. However, the calculational scheme across the interface would no longer be explicit. That is why we considered above and below both cases when medium 1 is extended and vice versa. The reason is that this provide the opportunity to consider the opposite extension when the ratios mentioned above are large. From (3.35)-(3.37) it is seen that the expressions in both cases are similar, but depend on the opposite ratios of the characteristic parameters of the two media.

3.4. Cracks and Laminations Representation by Finite Difference Method

Planar defects may be treated by a simple extension of the equations for the boundary conditions given above. Again the rigid defects are trivial. A free surface defect is treated as two coincident planes, each with zero stress. This gives the defect of negligible width. However, this method assumes that the crack faces are non-interacting, i.e. the crack remains open under the influence of the incident wave. This is realistic for a smooth defect, according to Ogilvi and Temple [103], provided the defect width w obeys the condition: $d < w << \lambda$, where d is the displacement amplitude of the wave and λ is the ultrasonic wavelength.

Two different defects are considered: ones that are entirely inside the medium, and ones that break the free surface of the medium. Figure 3-5 shows a crack entirely inside the body. Two rows of pseudonodes are inserted along the crack position, and the equations for the zero-stress surfaces are used to compute the displacements at the pseudonodes. These are not real points and care must be taken to establish the rigid connectivity of the perfect solid beyond the crack tip. Similar approach is used to model a surface breaking crack, as shown in fig. 3-6. In this case we must consider the conditions at the crack edges on the surface. The same equations used for evaluation of the displacements at the free surface corner are used to evaluate the displacements at points A and B in figure 3-6. Again, at the ends of defects in the bulk, the fictitious points introduced have to have their displacements set equal to those of points in the bulk adjacent to the defect, to establish the correct connectivity and end the defect smoothly. It should be noted that this scheme models a crack with zero width, as it is in [20, 84], whereas most formulations treat a crack as a slot a few mesh spacing wide.

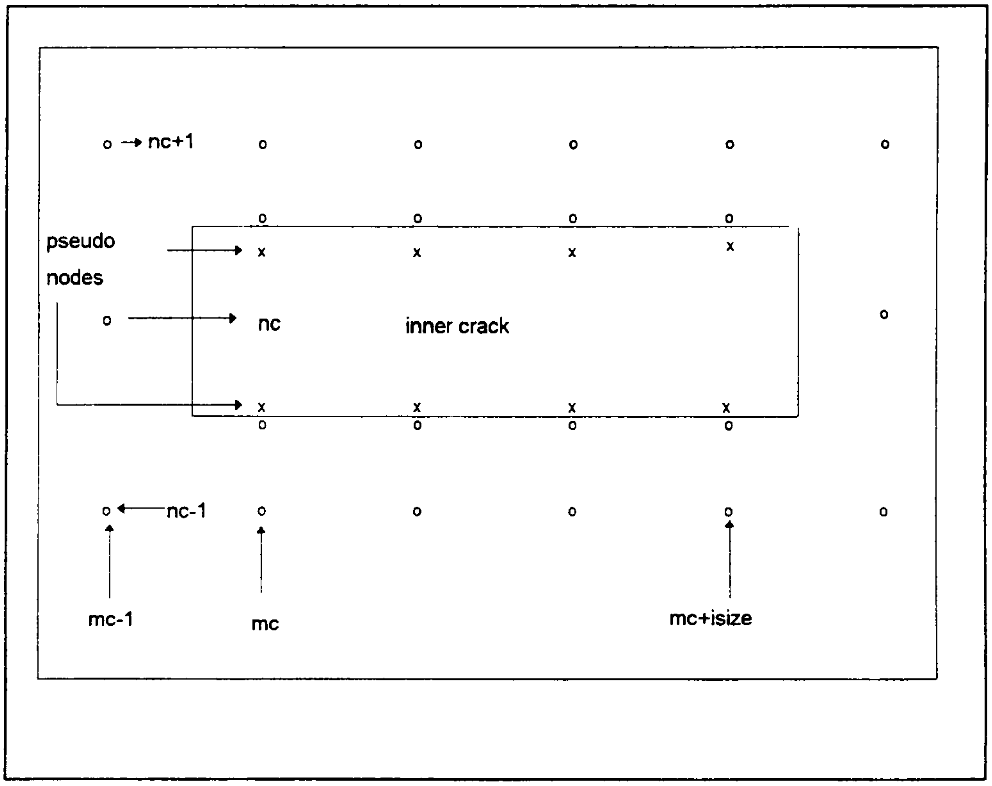

Figure 3-5. The pseudonodes at an inner crack.

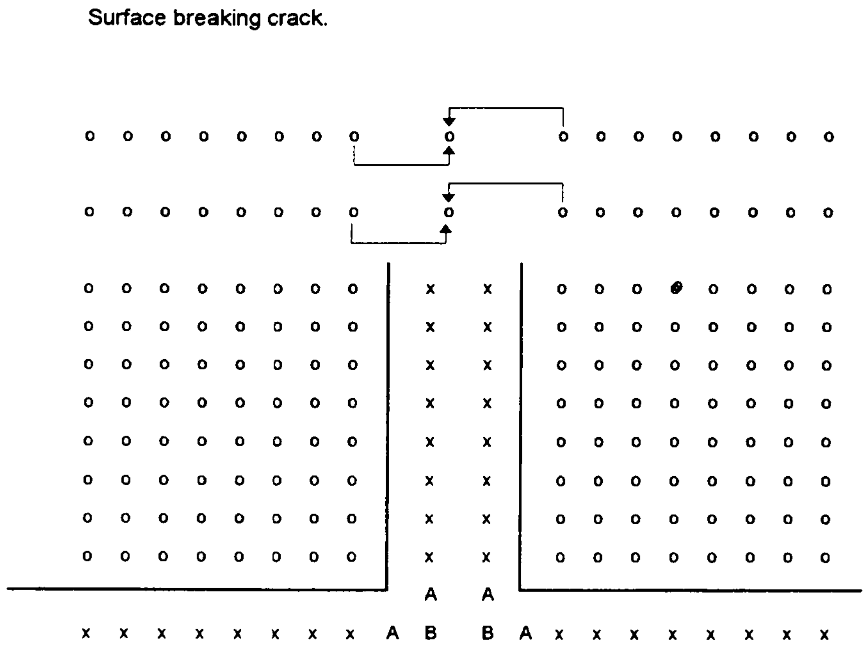

Figure 3-6. Pseudonodes at a surface breaking crack.

3.5. Dimensionless Variables

There are two sources of errors in the numerical computation. When the finite difference methods are concerned, one of the sources is the truncation error. The truncation error in our case, when the center-difference approximation is applied, is given by

$$\frac{\Delta t^2}{6}\left\{\begin{pmatrix}1 & 0\\ 0 & 1\end{pmatrix}\left[\frac{\Delta t^2}{2}\vec{U}_{tttt}-\frac{h^2}{2}\left(p^2\vec{U}_{xxxx}+s^2\vec{U}_{yyyy}\right)\right]-\frac{h^2}{2}(p^2-s^2)\begin{pmatrix}0 & 1\\ 1 & 0\end{pmatrix}\left[\vec{U}_{xxxy}+\vec{U}_{yyyx}\right]\right\}+\ldots$$

(3.54)

This error can be denoted with $O(\Delta t^2 + h^2)$ [104,105], where $O(h)$ is defined in Appendix A. From the equation (3.54) immediately follows that the smaller the steps Δt or h, the smaller the truncation error, provided that both steps satisfy the stability condition (3.6). However, because of the roundoff error, a purely computational effect due to the fact that each real number has a finite length in machine representation, decreasing further the spatial and time steps does not always lead to smaller error. In fact, decreasing the steps Δt and h indeed decreases the truncation error, but necessarily increase the roundoff error, and as a result, the error in the obtained results. As our computations showed, the roundoff error may significantly aggravate the final error. To make the effect of the roundoff error as small as possible, we introduce in the actual code the dimensionless variables, defined as follows

$$\tau=\frac{t}{t_a},\ \xi=\frac{x}{L_1},\ \varsigma=\frac{y}{L_2} \tag{3.55}$$

where L_1, L_2, are the sizes of the system with respect to X and Y directions, $t_a=\sqrt{\dfrac{L_1^2+L_2^2}{p^2-s^2}}$ is the "natural" time interval of the system, where p and s are the compression and shear speeds, respectively. With these variables, equations (2.50) become

$$\left|\begin{aligned}&(1+\kappa^2)\frac{\partial^2\hat{u}}{\partial\xi^2}+\frac{s}{p}\left(\kappa+\frac{1}{\kappa}\right)\frac{\partial^2\hat{v}}{\partial\varsigma\partial\xi}+\frac{s^2}{p^2-s^2}\left[(1+\kappa^2)\frac{\partial^2\hat{u}}{\partial\xi^2}+\left(1+\frac{1}{\kappa^2}\right)\frac{\partial^2\hat{u}}{\partial\varsigma^2}\right]=\frac{\partial^2\hat{u}}{\partial\tau^2}\\&\left(1+\frac{1}{\kappa^2}\right)\frac{\partial^2\hat{v}}{\partial\varsigma^2}+\frac{p}{s}\left(\kappa+\frac{1}{\kappa}\right)\frac{\partial^2\hat{u}}{\partial\varsigma\partial\xi}+\frac{s^2}{p^2-s^2}\left[(1+\kappa^2)\frac{\partial^2\hat{v}}{\partial\xi^2}+\left(1+\frac{1}{\kappa^2}\right)\frac{\partial^2\hat{v}}{\partial\varsigma^2}\right]=\frac{\partial^2\hat{v}}{\partial\tau^2}\end{aligned}\right., \tag{3.56}$$

where $\hat{u}=\frac{u}{p\Delta t}$, $\hat{v}=\frac{v}{s\Delta t}$, and $\kappa=\frac{L_2}{L_1}$. In equation (3.56) all variables and coefficients are dimensionless, and this is the system we actually solve by the finite difference approximation described above. The introduced set of dimensionless variables in fact keeps all values during computation at the same order of magnitude, and this fact prevents the increasing of the roundoff error effect in the final result even when the step sizes with respect to time and space are small.

3.6. Finite Difference Formulation for Cylindrical Geometry

To derive the finite difference approximation to the wave equations in cylindrical geometry, we start with the system (2.68)

$$\left|\begin{aligned}&p^2\left(\frac{\partial^2 u}{\partial r^2}+\frac{1}{r}\frac{\partial u}{\partial r}+\frac{\partial^2 w}{\partial r\partial z}-\frac{u}{r^2}\right)+s^2\left(\frac{\partial^2 u}{\partial z^2}-\frac{\partial^2 w}{\partial r\partial z}\right)=\frac{\partial^2 u}{\partial t^2}\\&p^2\left(\frac{\partial^2 w}{\partial z^2}+\frac{1}{r}\frac{\partial u}{\partial z}+\frac{\partial^2 u}{\partial r\partial z}\right)+s^2\left(\frac{\partial^2 w}{\partial r^2}+\frac{1}{r}\frac{\partial w}{\partial r}-\frac{1}{r}\frac{\partial u}{\partial z}-\frac{\partial^2 u}{\partial r\partial z}\right)=\frac{\partial^2 w}{\partial t^2}\end{aligned}\right.. \tag{2.68}$$

Using the approximations (A.7), (A.8), (A.11) and (A.18), we obtain

$$w(m,n,l) = 2w(m,n,l)\left[1-\frac{p^2\Delta t^2}{\Delta z^2}-\frac{s^2\Delta t^2}{\Delta r^2}\right]-w(m,n,l-1)+\frac{p^2\Delta t^2}{\Delta z^2}\left[w(m,n+1,l+w(m,n-1,l)\right]$$
$$+\frac{p^2\Delta t^2}{\Delta z^2}\frac{\Delta z}{2m\Delta r}\left[u(m,n+1,l)-u(m,n-1,l)\right]+$$
$$\frac{s^2\Delta t^2}{\Delta r^2}\left[w(m+1,n,l)+w(m-1,n,l)\right]+\left(\frac{p^2\Delta t^2}{\Delta z^2}\frac{\Delta z}{4\Delta r}-\frac{s^2\Delta t^2}{\Delta r^2}\frac{\Delta z}{4\Delta r}\right) \quad , \qquad (3.57)$$
$$x\left[u(m+1,n+1,l)-u(m-1,n+1,l)-u(m+1,n-1,l)+u(m-1,n-1,l)\right]$$
$$-\frac{s^2\Delta t^2}{\Delta r^2}\frac{1}{2m}\left[w(m+1,n,l)-w(m-1,n,l)\right]$$

$$u(m,n,l+1) = 2u(m,n,l)\left[1-\frac{p^2\Delta t^2}{\Delta r^2}-\frac{s^2\Delta t^2}{\Delta z^2}\right]-u(m,n,l-1)+$$
$$\frac{p^2\Delta t^2}{\Delta r^2}\left[u(m+1,n,l)+u(m-1,n,l)\right]+\frac{1}{2m}\frac{p^2\Delta t^2}{\Delta r^2}\left[u(m+1,n,l)-u(m-1,n,l)\right]$$
$$-\frac{1}{m^2}\frac{p^2\Delta t^2}{\Delta r^2}u(m,n,l)+\left(\frac{p^2\Delta t^2}{4\Delta r\Delta z}-\frac{s^2\Delta t^2}{4\Delta r\Delta z}\right) \quad , \qquad (3.58)$$
$$x\left[w(m+1,n+1,l)-w(m-1,n+1,l)-w(m+1,n-1,l)+w(m-1,n-1,l)\right]$$
$$+\frac{s^2\Delta t^2}{\Delta z^2}\left[u(m,n+1,l)-u(m,n-1,l)\right]$$

where we use the same notation as in the other subsections of this chapter, u is the displacement along R-axis, w is the displacement along Z-axis.

One can note that when $r = 0$ is included in the solution domain, the equations (3.57)-(3.58) contain undefined terms, and therefore cannot be used when $r = 0$. Valid equations along the axis of symmetry are easily derived, however, by using independent arguments. Due to continuity of the elastic media, along the axis of symmetry, the following conditions for the radial and axial displacement components are held [102,106]

$$u(0,z,t) = 0, \tag{3.59}$$

$$\left.\frac{\partial w}{\partial r}\right|_{r=0} = 0. \tag{3.60}$$

The terms causing trouble in (3.58) are $\frac{1}{r}\frac{\partial u}{\partial z}$ and $\frac{1}{r}\frac{\partial w}{\partial r}$. By using L'Hopital's rule at $r = 0$ these terms can be replaced by $\frac{\partial^2 u}{\partial r \partial z}$ and $\frac{\partial^2 w}{\partial r^2}$, respectively. These, in turn, can be replaced by their finite difference approximations. Due to their regularity near $r = 0$, they can be continued to $r < 0$ by using the asymmetry conditions

$$\begin{aligned} u(-1,n,l) &= -u(1,n,l) \\ w(-1,n,l) &= w(1,n,l) \end{aligned} \tag{3.61}$$

Making these new substitutions in the equation of motion for w, we obtain an additional equation

$$\begin{aligned} w(0,n,l+1) &= 2w(0,n,l)\left(1-\frac{p^2\Delta t^2}{\Delta z^2}-\frac{2s^2\Delta t^2}{\Delta r^2}\right)-w(0,n,l-1) \\ &+\frac{p^2\Delta t^2}{\Delta z^2}\left[w(0,n+1,l)+w(0,n-1,l)\right]+\frac{(2p^2-s^2)\Delta t^2}{2\Delta r\Delta z} \\ &x\left[u(1,n+1,l)-u(1,n-1,l)\right]+4\frac{s^2\Delta t^2}{\Delta r^2}w(1,n,l) \\ &-2\frac{s^2\Delta t^2}{\Delta r^2}u(0,n,l) \end{aligned} \tag{3.62}$$

Equations (3.57)-(3.58), together with the equations (3.59) and (3.60), are the foundation of the finite difference model in RZ cylindrical geometry.

3.6.1. Stability Conditions

Applying the same approach as in [102], for the stability we find the following approximate criterion

$$\frac{p\Delta t}{\Delta r} < \left[1 + \left(\frac{s}{p}\right)^2\right]^{-\frac{1}{2}},$$

when $\Delta r = \Delta z$. The stability criterion is approximate because we assumed, for simplicity, that the value of m is sufficiently large so that terms involving $1/r$ were small. Under this restriction the stability difference equation possesses constant coefficients and is easily solved.

3.6.2. Boundary conditions

To obtain the boundary conditions we use the same procedure, established for Cartesian geometry.

Introducing again artificial points along the free surface $r = r_0$, when the body occupies the half space $r < m_0 \Delta r$, we have the conditions

$$\begin{aligned} \sigma_{rr} &= p^2 u_r + (p^2 - 2s^2) w_z + (p^2 - 2s^2)\frac{u}{r} = 0 \\ \sigma_{rz} &= u_z + w_r = 0 \end{aligned} \qquad (3.63)$$

From these conditions we derive expressions for the displacements at the artificial points

$$u(m_0+1,n,l) = u(m_0,n,l) - \frac{p^2-2s^2}{p^2}\left[w(m_0,n+1,l) - w(m_0,n-1,l)\right]$$
$$-\frac{p^2-2s^2}{m_0 p^2}u(m_0,n,l) \quad , \qquad (3.64)$$

$$w(m_0+1,n,l) = w(m_0,n,l) - \frac{\Delta r}{2\Delta z}\left[u(m_0,n+1,l) - u(m_0,n-1,l)\right]. \qquad (3.65)$$

For the free boundary at $z = n_0\,\Delta z$, when the body occupies the half space $z < n_0\,\Delta z$, we have the conditions

$$\sigma_{zz} = p^2 w_z + (p^2-2s^2)u_r + (p^2-2s^2)\frac{u}{r} = 0$$
$$\sigma_{rz} = u_z + w_r = 0 \qquad (3.66)$$

Using the one sided finite differences for z-derivatives and centered differences for r-derivatives, we obtain

$$w(m,n_0+1,l) = w(m,n_0,l) - \frac{p^2-2s^2}{p^2}\frac{\Delta z}{2\Delta r}\left[u(m+1,n_0,l) - u(m-1,n_0,l)\right]$$
$$-\frac{1}{m}\frac{p^2-2s^2}{p^2}u(m,n_0,l) \quad , \qquad (3.67)$$

$$u(m,n_0+1,l) = u(m,n_0,l) - \frac{\Delta z}{2\Delta r}\left[w(m+1,n_0,l) - w(m-1,n_0,l)\right]. \qquad (3.68)$$

Using the same approach, for the case of a free surface at $r = r_1$, where the body occupies the half space $r > m_1\,\Delta r$, and $r_1 \neq 0$, we obtain

$$u(m_1-1,n,l)=u(m_1,n,l)+\frac{p^2-2s^2}{p^2}\frac{\Delta r}{2\Delta z}\left[w(m_1,n+1,l)-w(m_1,n-1,l)\right]$$
$$+\frac{p^2-2s^2}{m_1p^2}u(m_1,n,l) \qquad , \tag{3.69}$$

$$w(m_1+1,n,l)=w(m_1,n,l)+\frac{\Delta r}{2\Delta z}\left[u(m_1,n+1,l)-u(m_1,n-1,l)\right]. \tag{3.70}$$

When $r_1 = 0$, we use the condition $u(0, n, l+1) = 0$ and equation (3.62).

For the last remaining case, when the free surface is along $z = 0$, we have the conditions

$$w(m,-1,l)=w(m,0,l)+\frac{p^2-2s^2}{p^2}\frac{\Delta z}{2\Delta r}\left[u(m+1,0,l)-u(m-1,0,l\right]$$
$$+\frac{p^2-2s^2}{p^2}\frac{\Delta z}{m\Delta r}u(m,0,l) \qquad , \tag{3.71}$$

$$u(m,-1,l)=u(m,0,l)+\frac{\Delta z}{2\Delta r}\left[w(m+1,0,l)-w(m-1,0,l)\right]. \tag{3.72}$$

3.6.3. Conditions at the Corners

We use similar approach as in the case of Cartesian geometry. For the case of an upper right corner (m_0 ,n_0) we obtain the following expressions

$$w(m_0+1,n_0,l)=\frac{4}{3}\Big\{w(m_0,n_0,l)-\frac{1}{4}w(m_0-1,n_0,l)$$
$$-\frac{\Delta r}{2\Delta z}\left[u(m_0,n_0,l)-u(m_0,n_0-1,l)\right]\Big\} \qquad , \tag{3.73}$$

$$u(m_0,n_0+1,l)=\frac{4}{3}\left\{u(m_0,n_0,l)-\frac{1}{4}(m_0,n_0-1,l)\right.$$
$$\left.-\frac{\Delta z}{2\Delta r}\left[w(m_0,n_0,l)-w(m_0-1,n_0,l)\right]\right\} \qquad ,\qquad (3.74)$$

$$u(m_0+1,n_0,l)=\frac{1}{1-q^2}\left\{u(m_0,n_0,l)-q^2u(m_0-1,n_0,l)\right.$$
$$\left.-\frac{\Delta r}{\Delta z}\left[w(m_0,n_0,l)-w(m_0,n_0-1,l)\right]+\frac{2}{m}q(q-1)u(m_0,n_0,l)\right\} \qquad ,\qquad (3.75)$$

$$w(m_0,n_0+1,l)=\frac{1}{1-q^2}\left\{w(m_0,n_0,l)-q^2w(m_0,n_0-1,l)\right.$$
$$\left.+q\frac{\Delta z}{\Delta r}\left[u(m_0-1,n_0,l)-u(m_0,n_0,l)\right]+\frac{2}{m}\frac{\Delta z}{\Delta r}q(q-1)u(m_0,n_0,l)\right\} \qquad .\qquad (3.76)$$

In the above equations we use again the notation $q=\dfrac{p^2-2s^2}{2p^2}$, as it is in the case of Cartesian geometry.

To obtain conditions for the artificial point above the corner, we use the same considerations as in the case of Cartesian geometry. The result is

$$w(m_0+1,n_0+1,l)=w(m_0-1,n_0-1,l)+$$
$$\left(1-\frac{s^2}{p^2}\right)\left[w(m_0+1,n_0-1,l)-w(m_0-1,n_0+1,l)\right] \qquad ,\qquad (3.77)$$
$$+\frac{s^2}{p^2}\frac{\Delta z}{\Delta r}\left[u(m_0+1,n_0-1,l)-u(m_0-1,n_0+1,l)\right]-\frac{2}{m_0}\frac{\Delta z}{\Delta r}\frac{p^2-2s^2}{p^2}u((m_0,n_0,l)$$

$$u(m_0+1,n_0+1,l) = u(m_0-1,n_0-1,l)$$
$$-\left(1-\frac{s^2}{p^2}\right)\left[u(m_0+1,n_0-1,l) - w(m_0-1,n_0+1,l)\right] \quad . \tag{3.78}$$
$$-\frac{s^2}{p^2}\frac{\Delta r}{\Delta z}\left[w(m_0+1,n_0-1,l) - w(m_0-1,n_0+1,l)\right] - \frac{2}{m_0}\frac{p^2-2s^2}{p^2}u((m_0,n_0,l)$$

For the rest three corners we obtain similarly:

Upper left corner at (m_0 ,n_0):

$$w(m_0-1,n_0,l) = \frac{4}{3}\Big\{w(m_0,n_0,l) - \frac{1}{4}w(m_0-1,n_0,l)$$
$$-\frac{\Delta r}{2\Delta z}\left[u(m_0,n_0-1,l) - u(m_0,n_0,l)\right]\Big\} \quad , \tag{3.79}$$

$$u(m_0,n_0+1,l) = \frac{4}{3}\Big\{u(m_0,n_0,l) - \frac{1}{4}(m_0,n_0-1,l)$$
$$-\frac{\Delta z}{2\Delta r}\left[w(m_0+1,n_0,l) - w(m_0,n_0,l)\right]\Big\} \quad , \tag{3.80}$$

$$u(m_0-1,n_0,l) = \frac{1}{1-q^2}\Big\{u(m_0,n_0,l) - q^2 u(m_0-1,n_0,l)$$
$$+q\frac{\Delta r}{\Delta z}\left[w(m_0,n_0,l) - w(m_0,n_0-1,l)\right] - \frac{2}{m}q(q-1)u(m_0,n_0,l)\Big\} \quad , \tag{3.81}$$

$$w(m_0,n_0+1,l) = \frac{1}{1-q^2}\Big\{w(m_0,n_0,l) - q^2 w(m_0,n_0-1,l)$$
$$-q\frac{\Delta z}{\Delta r}\left[u(m_0-1,n_0,l) - u(m_0,n_0,l)\right] + \frac{2}{m}\frac{\Delta z}{\Delta r}q(q-1)u(m_0,n_0,l)\Big\} \quad . \tag{3.82}$$

$$w(m_0+1,n_0-1,l) = w(m_0-1,n_0+1,l)$$
$$+\left(1-\frac{s^2}{p^2}\right)\left[w(m_0+1,n_0+1,l)-w(m_0-1,n_0-1,l)\right] \quad , \quad (3.83)$$
$$-\frac{s^2}{p^2}\frac{\Delta z}{\Delta r}\left[u(m_0+1,n_0+1,l)-u(m_0-1,n_0-1,l)\right]+\frac{2}{m_0}\frac{\Delta z}{\Delta r}\frac{p^2-2s^2}{p^2}u((m_0,n_0,l)$$

$$u(m_0+1,n_0-1,l) = u(m_0-1,n_0+1,l)$$
$$-\left(1-\frac{s^2}{p^2}\right)\left[u(m_0+1,n_0-1,l)-u(m_0-1,n_0+1,l)\right] \quad . \quad (3.84)$$
$$+\frac{s^2}{p^2}\frac{\Delta r}{\Delta z}\left[w(m_0+1,n_0-1,l)-w(m_0-1,n_0-1,l)\right]-\frac{2}{m_0}\frac{p^2-2s^2}{p^2}u(m_0,n_0,l)$$

Bottom left corner at (m_0, n_0):

$$w(m_0-1,n_0,l) = \frac{4}{3}\left\{w(m_0,n_0,l)-\frac{1}{4}w(m_0+1,n_0,l)\right. \quad , \quad (3.85)$$
$$\left.+\frac{\Delta r}{2\Delta z}\left[u(m_0,n_0-1,l)-u(m_0,n_0,l)\right]\right\}$$

$$u(m_0,n_0-1,l) = \frac{4}{3}\left\{u(m_0,n_0,l)-\frac{1}{4}(m_0,n_0+1,l)\right. \quad , \quad (3.86)$$
$$\left.+\frac{\Delta z}{2\Delta r}\left[w(m_0+1,n_0,l)-w(m_0,n_0,l)\right]\right\}$$

$$u(m_0-1,n_0,l) = \frac{1}{1-q^2}\left\{u(m_0,n_0,l)-q^2u(m_0+1,n_0,l)\right. \quad , \quad (3.87)$$
$$\left.-q\frac{\Delta r}{\Delta z}\left[w(m_0,n_0,l)-w(m_0,n_0+1,l)\right]-\frac{2}{m}q(q-1)u(m_0,n_0,l)\right\}$$

$$w(m_0,n_0-1,l)=\frac{1}{1-q^2}\{w(m_0,n_0,l)-q^2w(m_0,n_0+1,l)$$

$$+q\frac{\Delta z}{\Delta r}\left[u(m_0+1,n_0,l)-u(m_0,n_0,l)\right]-\frac{2}{m}\frac{\Delta z}{\Delta r}q(q-1)u(m_0,n_0,l)\Big\} \tag{3.88}$$

$$w(m_0+1,n_0-1,l)=w(m_0-1,n_0+1,l)$$

$$+\left(1-\frac{s^2}{p^2}\right)\left[w(m_0+1,n_0+1,l)-w(m_0-1,n_0-1,l)\right] \quad , \tag{3.89}$$

$$-\frac{s^2}{p^2}\frac{\Delta z}{\Delta r}\left[u(m_0+1,n_0+1,l)-u(m_0-1,n_0-1,l)\right]+\frac{2}{m_0}\frac{\Delta z}{\Delta r}\frac{p^2-2s^2}{p^2}u((m_0,n_0,l)$$

$$u(m_0-1,n_0-1,l)=u(m_0+1,n_0+1,l)$$

$$+\left(1-\frac{s^2}{p^2}\right)\left[u(m_0+1,n_0-1,l)-u(m_0-1,n_0+1,l)\right] \quad . \tag{3.90}$$

$$+\frac{s^2}{p^2}\frac{\Delta r}{\Delta z}\left[w(m_0+1,n_0-1,l)-w(m_0-1,n_0+1,l)\right]+\frac{2}{m_0}\frac{p^2-2s^2}{p^2}u(m_0,n_0,l)$$

For the bottom right corner at (m_0 ,n_0) we have

$$w(m_0+1,n_0,l)=\frac{4}{3}\{w(m_0,n_0,l)-\frac{1}{4}w(m_0-1,n_0,l)$$

$$-\frac{\Delta r}{2\Delta z}\left[u(m_0,n_0+1,l)-u(m_0,n_0,l)\right]\Big\} \quad , \tag{3.91}$$

$$u(m_0,n_0-1,l)=\frac{4}{3}\{u(m_0,n_0,l)-\frac{1}{4}(m_0,n_0+1,l)$$

$$-\frac{\Delta z}{2\Delta r}\left[w(m_0-1,n_0,l)-w(m_0,n_0,l)\right]\Big\} \quad , \tag{3.92}$$

$$u(m_0+1,n_0,l)=\frac{1}{1-q^2}\{u(m_0,n_0,l)-q^2u(m_0-1,n_0,l)$$
$$\left.-q\frac{\Delta r}{\Delta z}\left[w(m_0+1,n_0,l)-w(m_0,n_0,l)\right]+\frac{2}{m}q(q-1)u(m_0,n_0,l)\right\}, \tag{3.93}$$

$$w(m_0,n_0-1,l)=\frac{1}{1-q^2}\{w(m_0,n_0,l)-q^2w(m_0,n_0+1,l)$$
$$\left.+q\frac{\Delta z}{\Delta r}\left[u(m_0,n_0,l)-u(m_0-1,n_0,l)\right]+\frac{2}{m}\frac{\Delta z}{\Delta r}q(q-1)u(m_0,n_0,l)\right\}. \tag{3.94}$$

$$w(m_0-1,n_0+1,l)=w(m_0+1,n_0-1,l)$$
$$-\left(1-\frac{s^2}{p^2}\right)\left[w(m_0+1,n_0+1,l)-w(m_0-1,n_0-1,l)\right] \quad , \tag{3.95}$$
$$-\frac{s^2}{p^2}\frac{\Delta z}{\Delta r}\left[u(m_0+1,n_0+1,l)-u(m_0-1,n_0-1,l)\right]-\frac{2}{m_0}\frac{\Delta z}{\Delta r}\frac{p^2-2s^2}{p^2}u((m_0,n_0,l)$$

$$u(m_0-1,n_0+1,l)=u(m_0+1,n_0-1,l)$$
$$+\left(1-\frac{s^2}{p^2}\right)\left[u(m_0+1,n_0+1,l)-u(m_0-1,n_0-1,l)\right] \quad . \tag{3.96}$$
$$-\frac{s^2}{p^2}\frac{\Delta r}{\Delta z}\left[w(m_0+1,n_0+1,l)-w(m_0-1,n_0-1,l)\right]+\frac{2}{m_0}\frac{p^2-2s^2}{p^2}u(m_0,n_0,l)$$

The equations above are very similar to those obtained in the case of Cartesian geometry. The theoretical analysis [1, 3, 7-10, 13, 20] shows that in the limit of cylinders whose radii are large compared with the wavelength, all the modes of the cylinder may be equated with corresponding modes of a plane surface. An analysis of the asymptotic forms of the Bessel functions (which are the eigenfunctions of the involved differential operators with respect to r in this case) for large values of the order n and argument kr shows that the error made in treating the surfaces as plane are of order $1/(kr)^2$ times the terms which are kept. For a typical ultrasonic experiment, with a wavelength of the order of millimeter (that is, for compression mode velocity at about 6,000 m/s, the frequency should be at about 3 MHz), the modes propagating in a pipe may be treated as a bulk waves, Rayleigh surface waves and lateral waves, provided that the pipe radius is 5 cm or more. The resonance analysis given in [107] of the modes of an elastic cylinder shows the convergence of the poles onto those for a plane surface, and confirms that the plane surface approximation is accurate for $(kr) > 100\pi$.

CHAPTER 4

Finite Difference Model Applications and Analyses of the Results by Using STFT and CWT Tools

In this chapter we consider practical some applications of the finite difference model for elastic wave propagation and scattering which has been developed in this work by a variety of flaws in Cartesian geometry in two dimensions. The methods for excitation of elastic waves are discussed in detail and an analysis of the angular distribution of a surface source is included. We apply STFT and CWT to the results obtained by the model for crack determination and Lamb waves analysis as well as to a set of data from experimental ultrasonic transmission measurements.

4.1. Excitation of Elastic Waves

The analytical results presented in Chapter 2 showed the main features of the generation of elastic waves in solids by surface and buried sources. The analysis is limited to sources of simple geometries, and to the limiting cases of step functions, delta functions or continuous wave sources. In practice transducers are only a few wavelengths across, and are excited by pulses of significant length, although the laser sources [112, 113] provide an elegant exception to this generalization. The finite difference method allows calculations with arbitrary sources and pulse shapes [20]. For analyses of pulses of arbitrary shape and duration, Riker [114] proposed a true wavelet pulse shape with respect to time for applications in analyses in seismology. For the purposes of the present work, we adopt similar concept, based, however, on pulses shaped in the form of the "sombrero" wavelet, equation (2.176). We constructed a three dimensional "sombrero" in the following manner

$$\psi_\theta(x,y,t) = A\left[1-\frac{(x\cos\theta + y\sin\theta - ct)^2}{a^2}\right]e^{-\frac{1}{2}\frac{(x\cos\theta+y\sin\theta-ct)^2}{a^2}}. \tag{4.1}$$

It is readily seen that the function above represents a solution of the wave equation (2.32) in the absence of external forces, the pulse will propagate with a velocity c, and in addition it satisfies the conditions (2.172)-(2.174). Moreover, we have

$$\int_{-\infty}^{\infty}\int_{-\infty}^{\infty}\int_{-\infty}^{\infty}\psi_\theta(x,y,t)dxdydt = 0. \tag{4.2}$$

The shape and time duration of the pulse (that is, its frequency characteristics), can be easily modified via changes of the constant amplitude A, parameter a and the angle θ. In

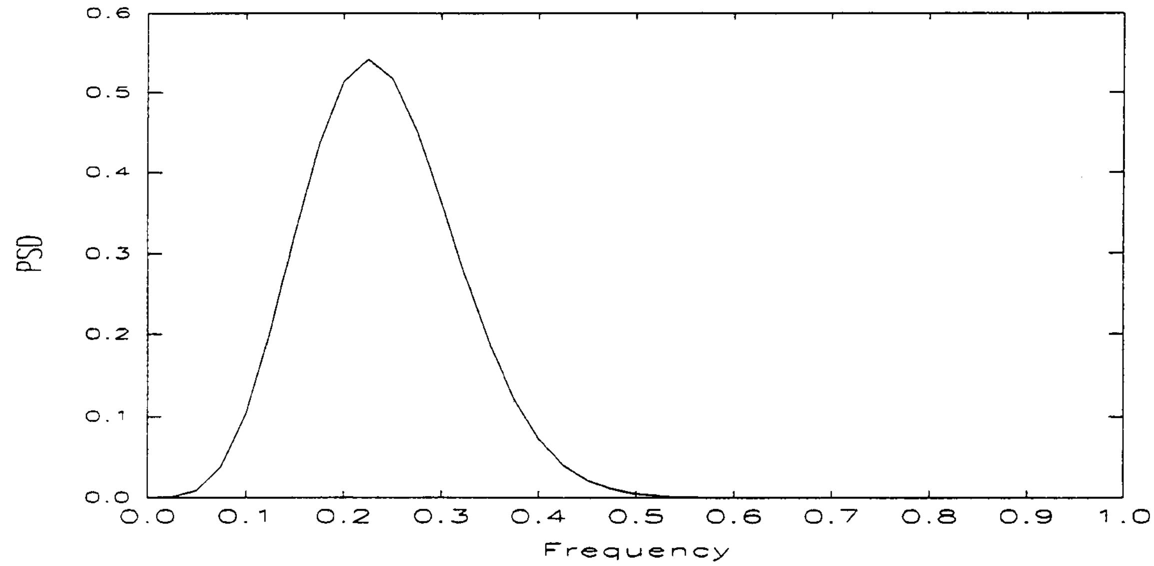

Figure 4-1. The Power Spectrum Density (PSD) of the function (4.1)

the following sections we will see how this formulation is used to generate longitudinal and transverse pulses with arbitrary duration and amplitude, according to the required analysis. The Fourier transform of the function is shown in figure 4-1. It is seen, as it was expected, that the pulse has a finite frequency range and well defined center frequency, both defined by the three parameters in (4.1) - A, a, and c.

4.1.1. Excitation via Initial Conditions

The general form of the wave equations (Chapter 2) as well as their finite difference realization (3.2) implies that we need to determine the displacements at two subsequent time instants (at time moments 0 and 1 in terms of finite time steps) in order to determine the initial conditions, providing a unique solution of the equations. Similarly one must also define the initial displacements and the first displacements' time derivative at time instant zero. In general, two different types of waves are considered - longitudinal and transverse. As shown in Chapter 2, they have different velocities and must be inserted separately. We use the potential approach as it is stated in Chapter 2. Let Φ be the scalar potential, defined in (2.38). It has to satisfy equations (2.40), (2.44), and, as it is shown in section 2.1.7, it represents the longitudinal elastic wave.

Consider the equation

$$\Phi(x,y,t) = A(x\cos\theta + y\sin\theta - pt)e^{-\frac{1}{2}\frac{(x\cos\theta + y\sin\theta - pt)^2}{a^2}}, \tag{4.3}$$

where p is the longitudinal speed as defined in (2.42).

It is readily seen that (4.3) satisfies the equation (2.44) and therefore represents a longitudinal plane wave with the particular form (4.3), propagating with a velocity p, and having a normal at angle θ with respect to the X-axis. Using the definition (2.38) and assuming that the vector potential $\vec{H} = 0$, for the corresponding displacements we obtain

$$u(x,y,t) = \frac{\partial\Phi}{\partial x} = A\cos\theta\left[1 - \frac{(x\cos\theta + y\sin\theta - pt)^2}{a^2}\right] e^{-\frac{1}{2}\frac{(x\cos\theta + y\sin\theta - pt)^2}{a^2}}, \tag{4.4}$$

$$v(x,y,t) = \frac{\partial\Phi}{\partial y} = A\sin\theta\left[1 - \frac{(x\cos\theta + y\sin\theta - pt)^2}{a^2}\right] e^{-\frac{1}{2}\frac{(x\cos\theta + y\sin\theta - pt)^2}{a^2}}. \tag{4.5}$$

At time instant $t = 0$ we therefore obtain

$$u(x,y,0) = A\cos\theta\left[1 - \frac{(x\cos\theta + y\sin\theta)^2}{a^2}\right] e^{-\frac{1}{2}\frac{(x\cos\theta + y\sin\theta)^2}{a^2}}, \tag{4.6}$$

$$v(x,y,0) = A\sin\theta\left[1 - \frac{(x\cos\theta + y\sin\theta)^2}{a^2}\right] e^{-\frac{1}{2}\frac{(x\cos\theta + y\sin\theta)^2}{a^2}}. \tag{4.7}$$

To start calculations, along with the expressions (4.6) and (4.7) we need to define the first time derivatives of the displacement components at instant 0. Differentiating (4.4) and (4.5) with respect to time, we obtain

$$\frac{\partial u(x,y,0)}{\partial t} = \frac{Ap\cos\theta}{a^2}(x\cos\theta + y\sin\theta)\left[3 - \frac{(x\cos\theta + y\sin\theta)^2}{a^2}\right]\exp\left\{-\frac{1}{2}\frac{(x\cos\theta + y\sin\theta)^2}{a^2}\right\}, \tag{4.8}$$

$$\frac{\partial v(x,y,0)}{\partial t}$$

$$= \frac{Ap\sin\theta}{a^2}(x\cos\theta + y\sin\theta)\left[3 - \frac{(x\cos\theta + y\sin\theta)^2}{a^2}\right]\exp\left\{-\frac{1}{2}\frac{(x\cos\theta + y\sin\theta)^2}{a^2}\right\}. \quad (4.9)$$

The displacements at time instant 0 are readily substituted from (4.6) and (4.7). The displacements at time instant Δt are computed as follows: from the Taylor series we have

$$u(x,y,\Delta t) = u(x,y,0) + \frac{\partial u(x,y,0)}{\partial t}\Delta t + \frac{\Delta t^2}{2}\frac{\partial^2 u(x,y,0)}{\partial t^2} + O(\Delta t^2). \quad (4.10)$$

Taking into account that u(x,y,0) satisfies the wave equations, we express the second time derivative in terms of spatial derivatives of the displacements' components from the wave equation. Finally, we obtain

$$u(x,y,\Delta t) = u(x,y,0) + \frac{\partial u(x,y,0)}{\partial t}\Delta t$$
$$+\frac{\Delta t^2}{2}\left[(p^2 - s^2)(u_{xx}(x,y,0) + v_{xy}(x,y,0)) + s^2(u_{xx}(x,y,0) + u_{yy}(x,y,0)\right] + O(\Delta t^2) \quad .(4.11)$$

In (4.11) we have used the notation introduced in (2.42), (2.50). The expression for $v(x,y,\Delta t)$ is

$$v(x,y,\Delta t) = v(x,y,0) + \frac{\partial v(x,y,0)}{\partial t}\Delta t$$
$$+\frac{\Delta t^2}{2}\left[(p^2 - s^2)(u_{xy}(x,y,0) + v_{yy}(x,y,0)) + s^2(v_{xx}(x,y,0) + v_{yy}(x,y,0)\right] + O(\Delta t^2) \quad .(4.12)$$

In (4.11), (4.12) all terms are known or readily calculated from (4.6) and (4.7). The parameter a in (4.6), (4.7) defines the spatial spread of the pulse at moment 0, A is the amplitude of the initial wave, and both a and A together determine the frequency spectrum of the propagating pulse. This procedure leads to the generation of longitudinal waves.

Figures 4-2a,b and 4-3a,b show the u and v displacements initiated in an aluminum plate, for two values of $\theta = 0, 30^0$, correspondingly. Figures 4-4a,b and 4-5a,b show the displacements of the waves initiated as shown in fig. 4-2a,b and 4-3a,b at $t = 6$ μs. The displacements at $t = 20$ μs are shown in fig. 4-6a,b and 4-7a,b correspondingly. Figure 4-2 clearly demonstrates the physical nature of the compression wave - the displacement is non zero only along the direction of the wave velocity. It is seen from the figures that since expressions (4.6)-(4.12) represent a solution of the wave equations for a compression wave with the particular shape defined by (4.4), (4.5), the wave preserves its shape and the conversion to a shear mode is made only at the free surfaces via the appearance of shock waves. The Rayleigh waves propagating along the surface are also clearly visible. Note that the shock ,or head waves, as we see later, appear only at the critical angle $\theta = \arcsin(s/p)$. Figures 4-4 through 4-7 show the process of the longitudinal wave propagation and reflection in aluminum plate 8 cm x 6 cm.

Figure 4-8 shows a "history" at a detector point $x = y = 29.76$ cm, resulting from a longitudinal pulse propagating at $\theta = 90^0$ in a rectangular block with infinite length in Z-direction, 65.88 cm in Y-direction and 83.88 cm in X-direction. Zero-stress boundary conditions are employed along X- and Y- axes. The stepsize along X- and Y- direction is taken the same and is $h = 1.2$ mm, the time step is $\Delta t = 0.08$ μs, the sampling rate is 3.125 MHz. The computation has been carried up to 4,096 time steps (328 μs). The medium is steel with Poisson ratio $\nu = 0.29$, Young modulus $E = 200$ GPa, and a density

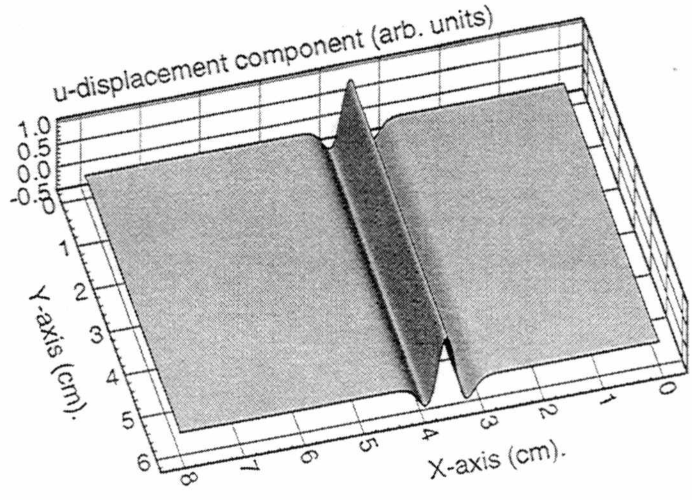

a)

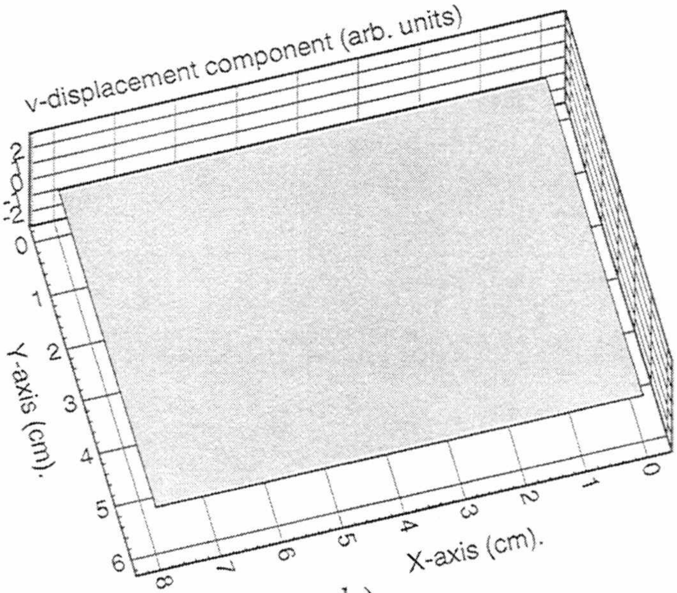

b)

Figure 4-2. Initial compression pulse at θ=0°, Δt=0.02 μs, h=0.2 mm, at t=0 s. Aluminum plate.
a) u-displacement component; b) v-displacement component.

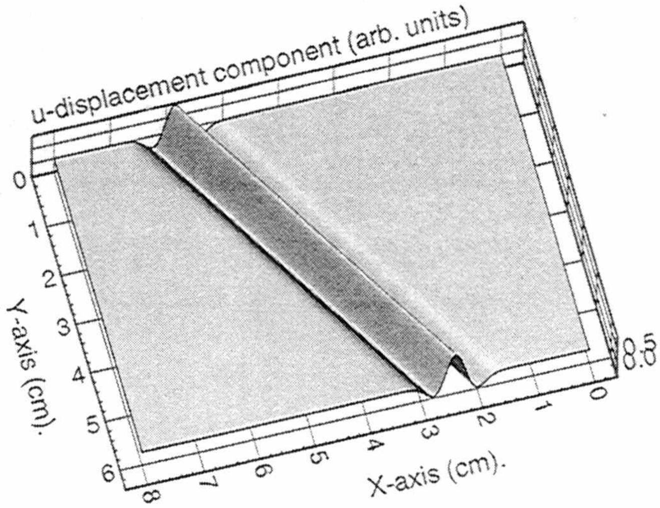

a)

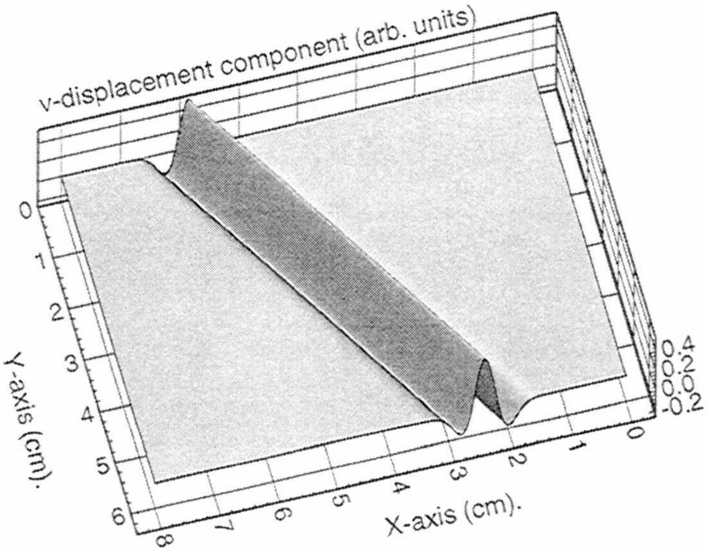

b)

Figure 4-3. Initial compression pulse at $\theta=30^{\circ}$;$\Delta t=0.02\mu s$, h=0.02 mm at t=0s. Aluminum plate.
a) u-displacement component; b) v-displacement component.

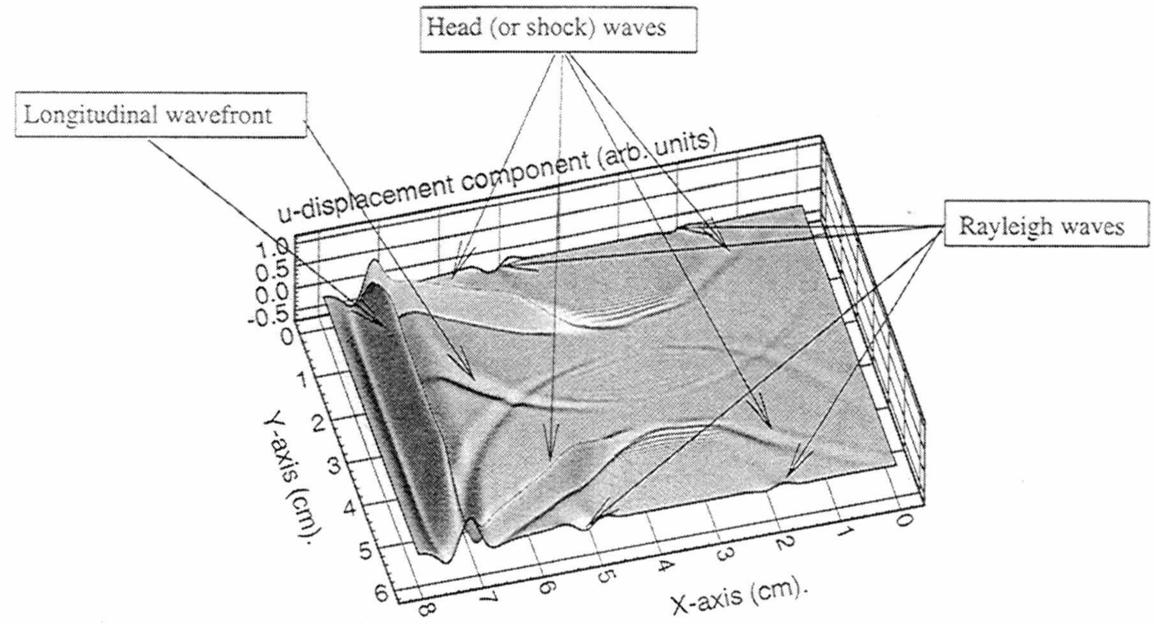

a)

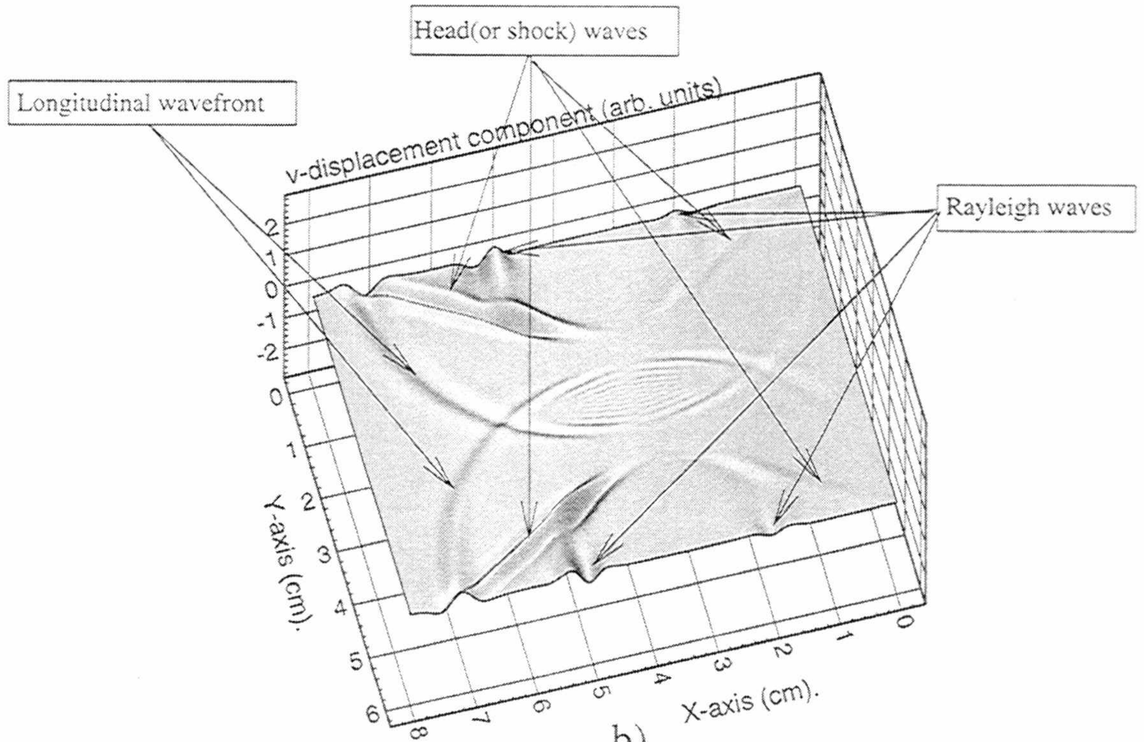

b)

Figure 4-4. Same as in figure 4-2 at t=6μs.

a) u-displacement component; b) v-displacement component.

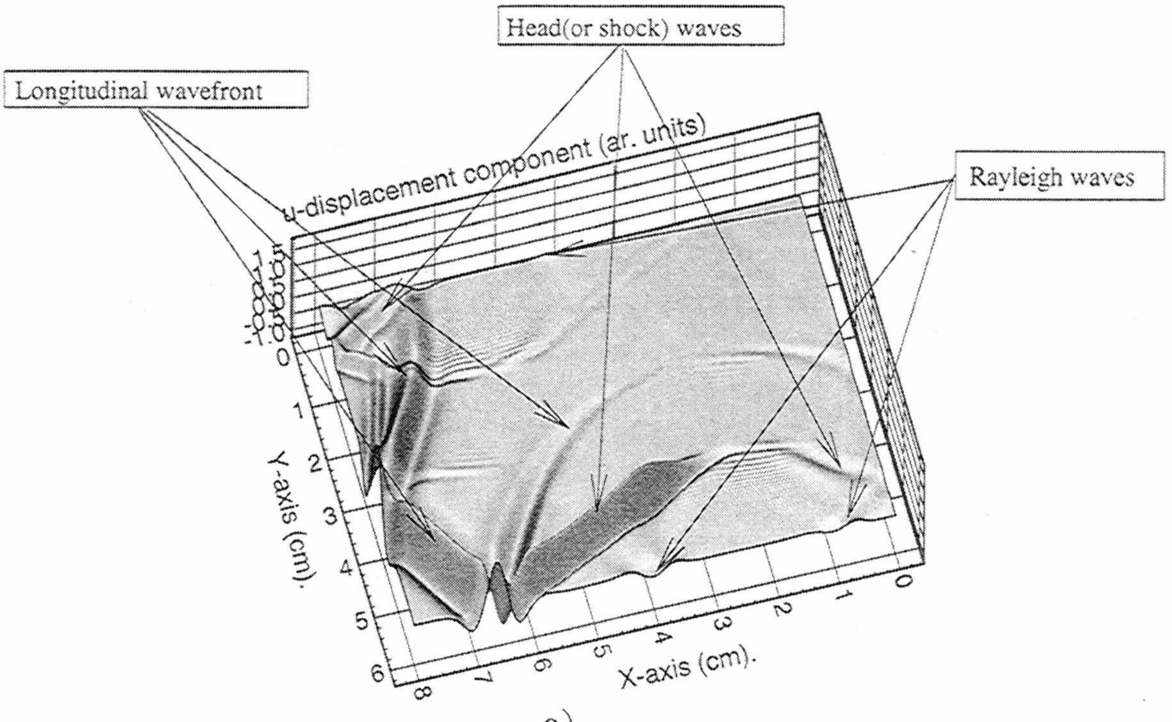

a)

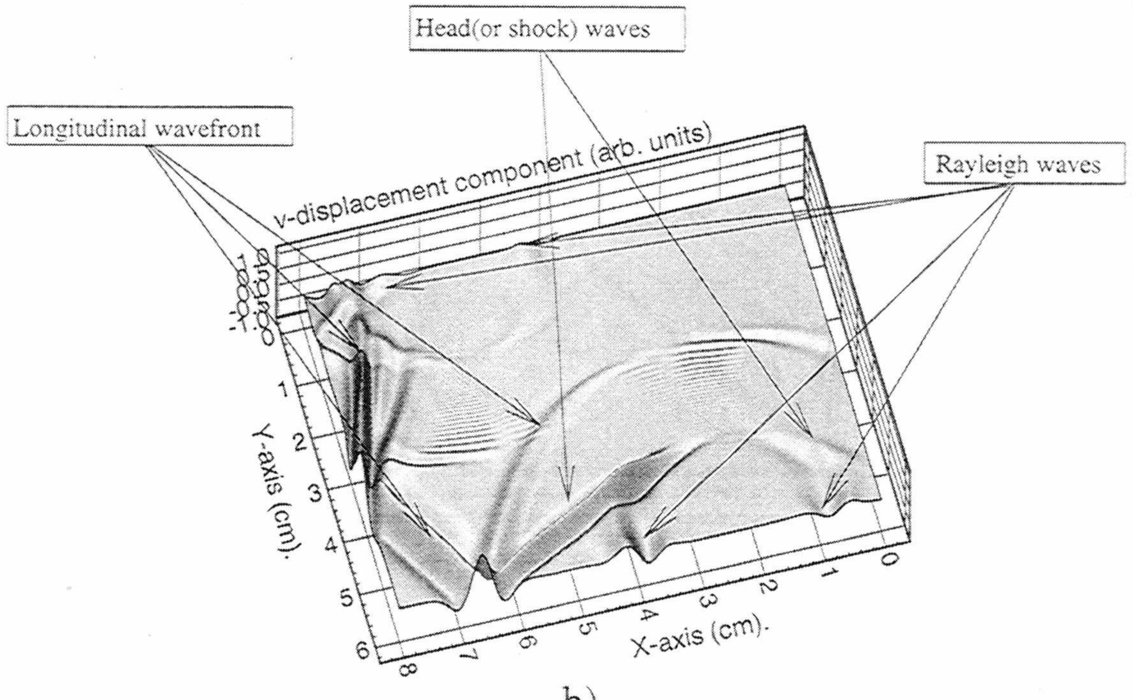

b)

Figure 4-5. Same as in figure 4-3 at t=6μs.

a) u-displacement component; b) v-displacement component.

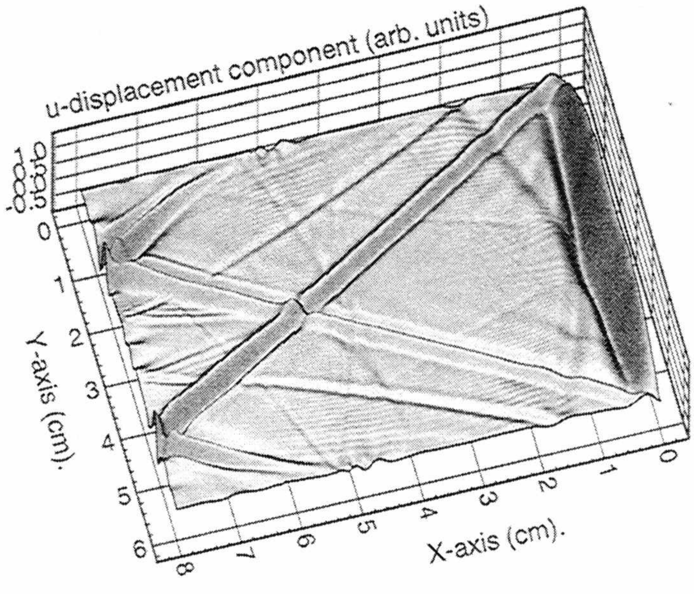

a)

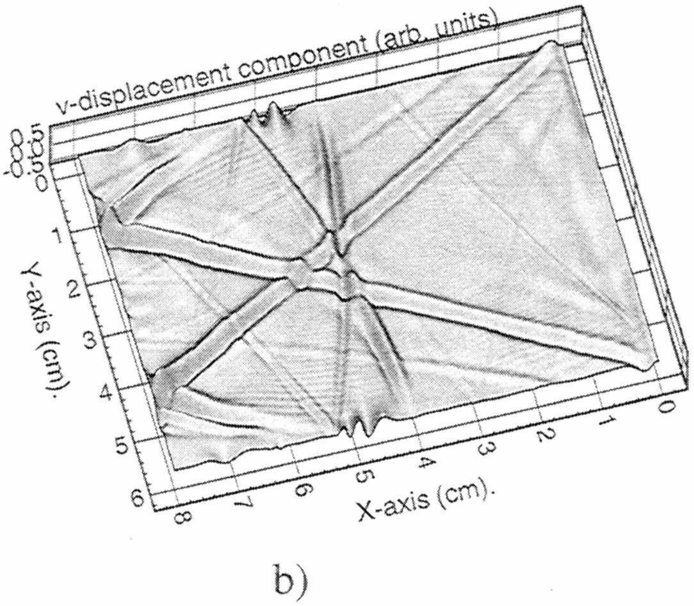

b)

Figure 4-6. Same as in figure 4-2 at t=20μs.

a) u-displacement component; b) v-displacement component.

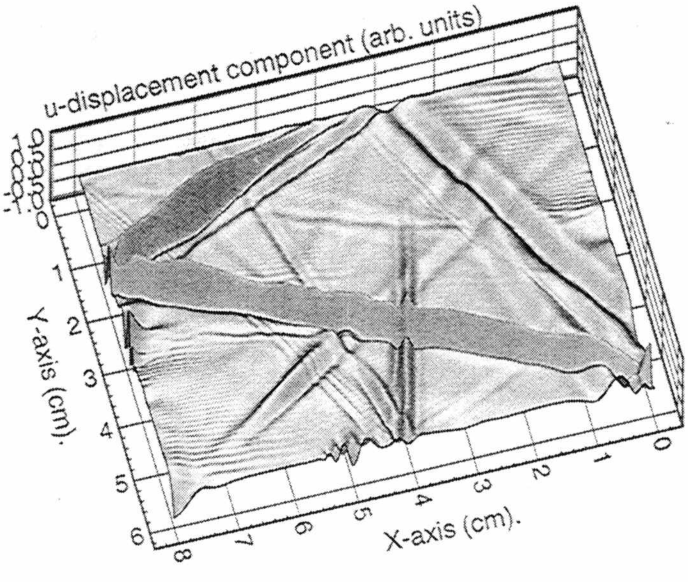

a)

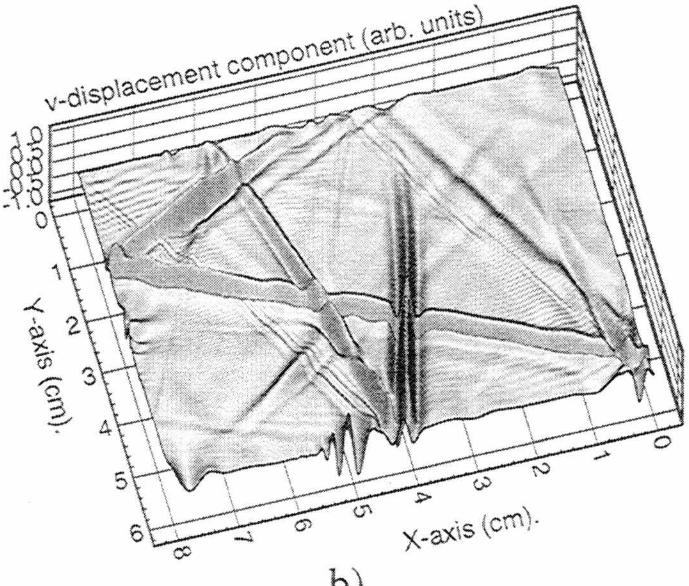

b)

Figure 4-7. Same as in figure 4-3 at t=20μs.

a) u-displacement component; b) v-displacement component.

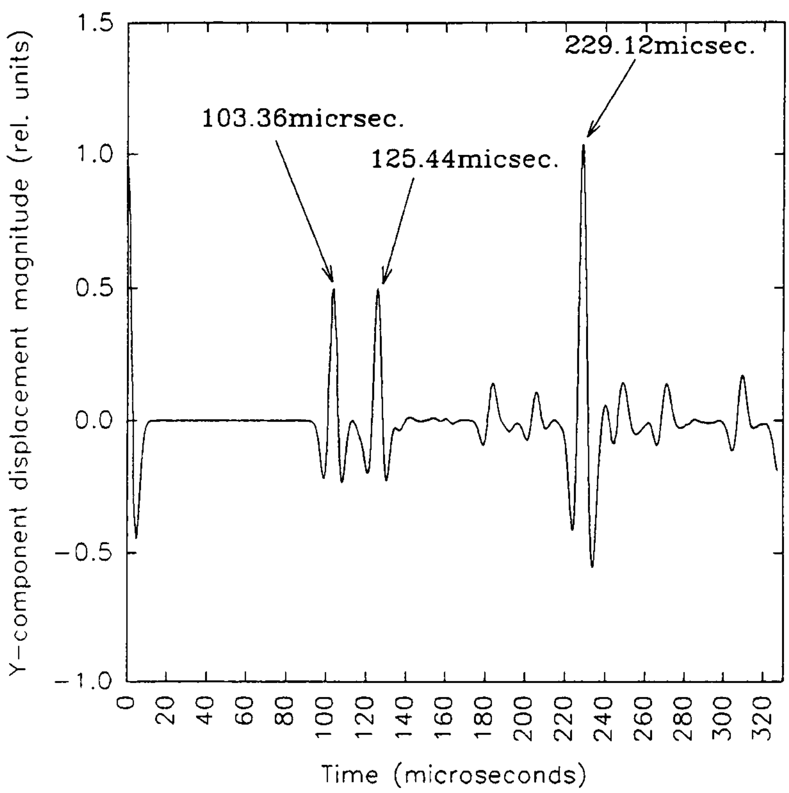

Figure 4-8. A "history" at a point.

ρ = 7,800 kg/m^3 . The longitudinal velocity in this case is p = 5,774.49 m/s. It is seen that:

- After the first peak at t=0 sec the peak at 103.36μs represents the pulse reflected from the boundary at X=0 cm and the next peak at t=125.44μs represents the reflected pulse from the boundary at X=83.88 cm. Both peaks have one half of the amplitude of the initial signal. The peak at t=229.12 μs represents the interference between two pulses propagating in opposite directions when they arrived at the "detector" point after their second reflection from the corresponding boundary. In fact, both pulses arrive at the "detector" point simultaneously. It is readily calculated that both pulses propagate with the longitudinal wave speed p=5,774.49 m/s and preserve their shape and phase.

Similar approach was used to represent a shear wave. However, in this case we assume that $\Phi = 0$. Since we consider a two dimensional case, the only component of the vector potential $\vec{H}$ which is non trivial in this case and must be considered, is the Z-component. We denote this component with $\psi(x,y,t)$ and consider the following particular expression for ψ

$$\psi_\theta(x,y,t) = A(x\cos\theta + y\sin\theta - st)e^{-\frac{1}{2}\frac{(x\cos\theta + y\sin\theta - st)^2}{a^2}}. \tag{4.13}$$

It is readily seen that (4.13) satisfies the equation (2.45) and therefore represents a transverse plane wave it the particular form (4.13), propagating with a velocity s, and having a normal at angle θ with respect to the X-axis. Using the relation (2.37), we have

$$u(x,y,t) = \frac{\partial\psi(x,y,t)}{\partial y},\ v(x,y,t) = -\frac{\partial\psi(x,y,t)}{\partial x}. \tag{4.14}$$

Further, following essentially the same procedure as in the case of the compression wave above, we obtain for the zeroth and first time instants the following expressions

$$u(x,y,0) = A\sin\theta\left[1 - \frac{(x\cos\theta + y\sin\theta)^2}{a^2}\right]e^{-\frac{1}{2}\frac{(x\cos\theta + y\sin\theta)^2}{a^2}}, \tag{4.15}$$

$$v(x,y,0) = A\cos\theta\left[1 - \frac{(x\cos\theta + y\sin\theta)^2}{a^2}\right]e^{-\frac{1}{2}\frac{(x\cos\theta + y\sin\theta)^2}{a^2}}. \tag{4.16}$$

For the time derivatives we use

$$\frac{\partial u(x,y,0)}{\partial t}$$

$$= \frac{Ap\sin\theta}{a^2}(x\cos\theta + y\sin\theta)\left[3 - \frac{(x\cos\theta + y\sin\theta)^2}{a^2}\right]\exp\left\{-\frac{1}{2}\frac{(x\cos\theta + y\sin\theta)^2}{a^2}\right\}, \quad (4.17)$$

$$\frac{\partial v(x,y,0)}{\partial t}$$

$$= \frac{Ap\cos\theta}{a^2}(x\cos\theta + y\sin\theta)\left[3 - \frac{(x\cos\theta + y\sin\theta)^2}{a^2}\right]\exp\left\{-\frac{1}{2}\frac{(x\cos\theta + y\sin\theta)^2}{a^2}\right\}. \quad (4.18)$$

These are the expressions, substituted in (4.11)-(4.12) to obtain the displacements at time instant Δt.

The practical aspects of the elastic wave excitation via initial conditions will be discussed later.

4.1.2. Surface Source Modeling

In order to introduce a more realistic way to model actual practical situations we consider surface sources of limited size, able to be excited somewhere on the free boundaries of the modeled medium and having finite time duration. For this purpose we employ equations (4.4) and (4.5) for compression pulse excitation or derivatives (4.14) of (4.13) in case of shear wave excitation. The constant, *a*, in this case is proportional to the time duration of the pulse and the corresponding longitudinal or shear velocity. The longer the pulse duration, the larger the constant, *a*, and the smaller the center frequency of the resulting signal PSD. Along the area of the source the displacements are set according to the analytical formulae stated above, and the free boundary conditions are applied on the rest of the surface.

Figure 4-9 shows the wavefronts arising from a point surface source when a normal stress is applied. When this situation was modeled using the finite difference method, the displacements were calculated according to (4.4) and (4.5), the pulse time duration was 1 μs. The velocity of the compression wave in Al is $p = 6{,}224.58$ m/s, the shear wave velocity is $s = 3{,}112.29$ m/s, and the Rayleigh wave velocity is $c_R = 2{,}902.29$ m/s. The resulting displacements along X- and Y- axes are shown in figure 4-10a,b, respectively. The head wave only occurs above the critical angle $\theta_C = \arcsin(s/p)$.

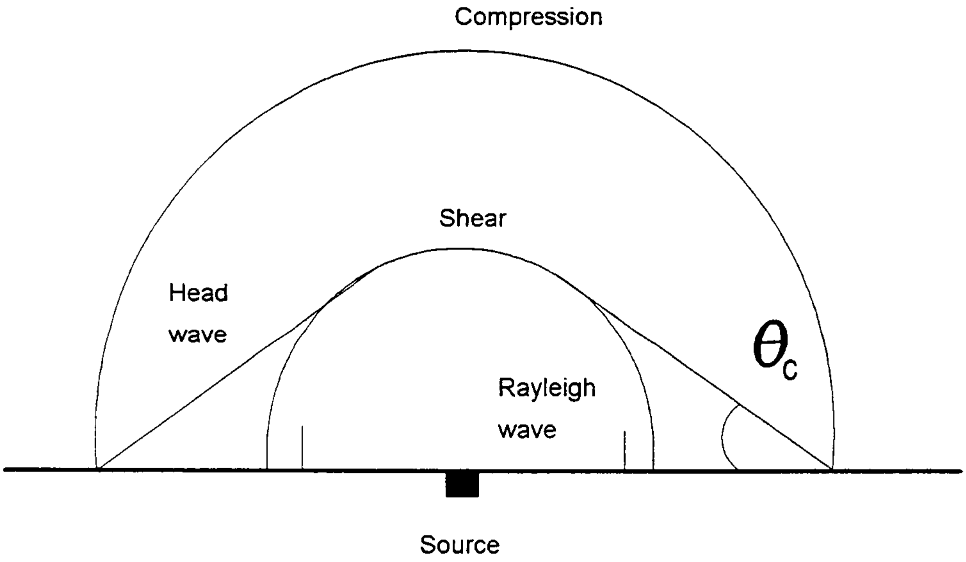

Figure 4-9. The pattern of wavefronts arising from a surface source.

In figures 4-10a,b the propagating compression, shear and Rayleigh waves* are clearly visible. Also the head wave is clearly visible at the critical angle $\theta_C = 30^0$. A careful study of figures 4-10a,b reveals the angular anisotropy of the waves emitted from the source. While a detail discussion of the angular anisotropy will be made in section 4.1.3, we note here that the results are in excellent qualitative agreement with the calculations of Harker [20] and Miller and Pursey [115].

Figures 4-11a,b, 4-12a,b show the displacement components along X- (parts a) and Y- (parts b) axes of the resulting wavefronts arising from a surface source 1.5 cm in length, in an aluminum block, 4 μs after the pulse initiation. One feature of the transducer behavior is illustrated: an attempt to set up a plane compression wave of finite width has resulted in a small amount of shear wave at the edges of the beam. The same effect is observed when a plane shear wave with finite width is set up; in this case a small amount of compression wave results at the edges of the beam. This has been noted in many visualization studies [116, 117]. These are the so-called edge waves, which play an important part in any accurate model of transducer characteristics [118].

From the results presented here it is clear that the present finite difference model does decsribe correctly the important features of the sources used in practice for the implementation of NDE procedures. In subsequent sections we will use the methods of elastic wave excitation for study of the wave propagation and scattering in a variety of cases, which include verification of the modeling features of the present code as well as to

---

* Details for Rayleigh waves and other guided surface waves are given in Appendix B.

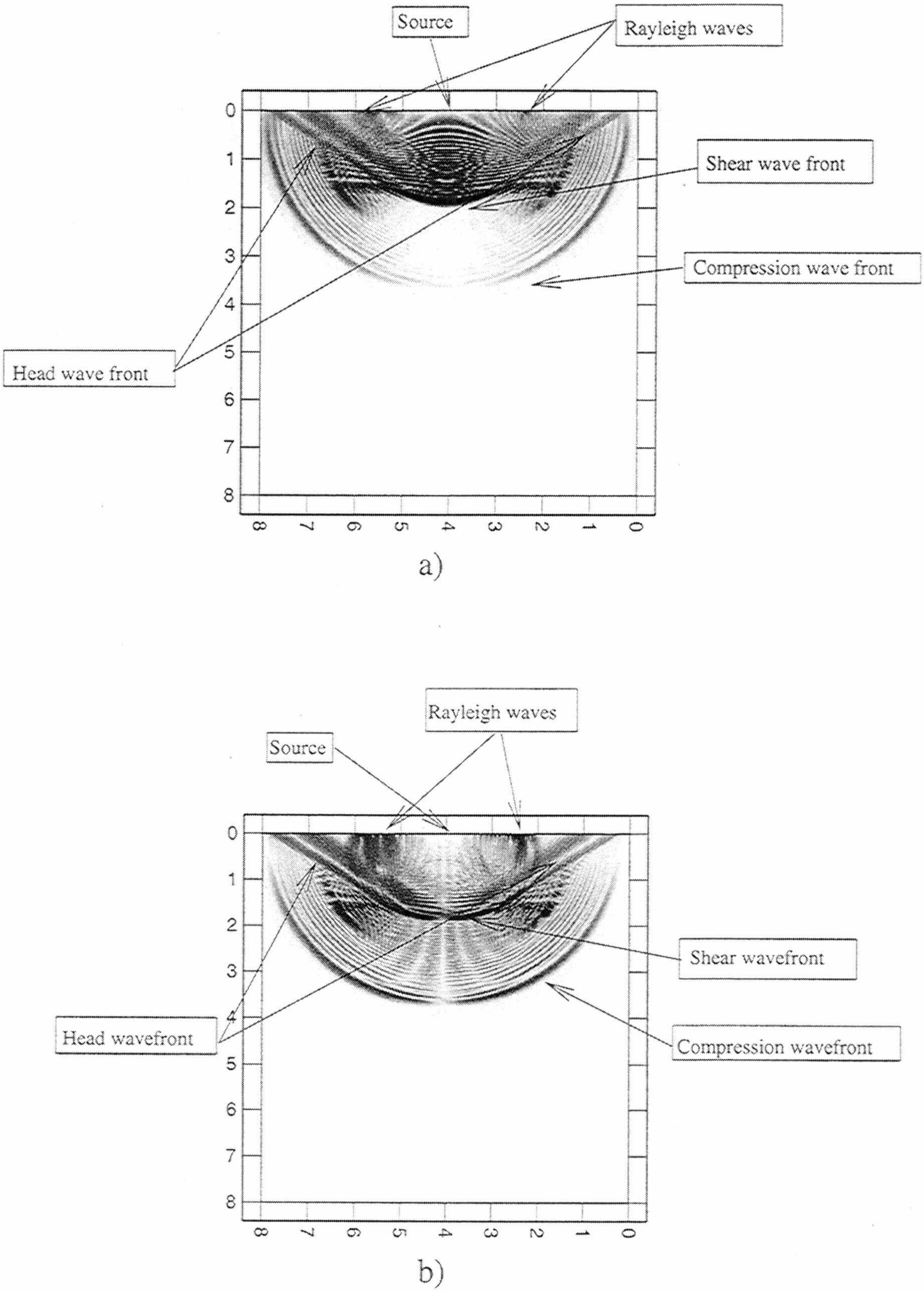

Figure 4-10. Compression pulse from a surface point source at t=6μs;Δt=0.02μs;h=0.2mm. Aluminum plate.
a) u-displacement component; b) v-displacement component.

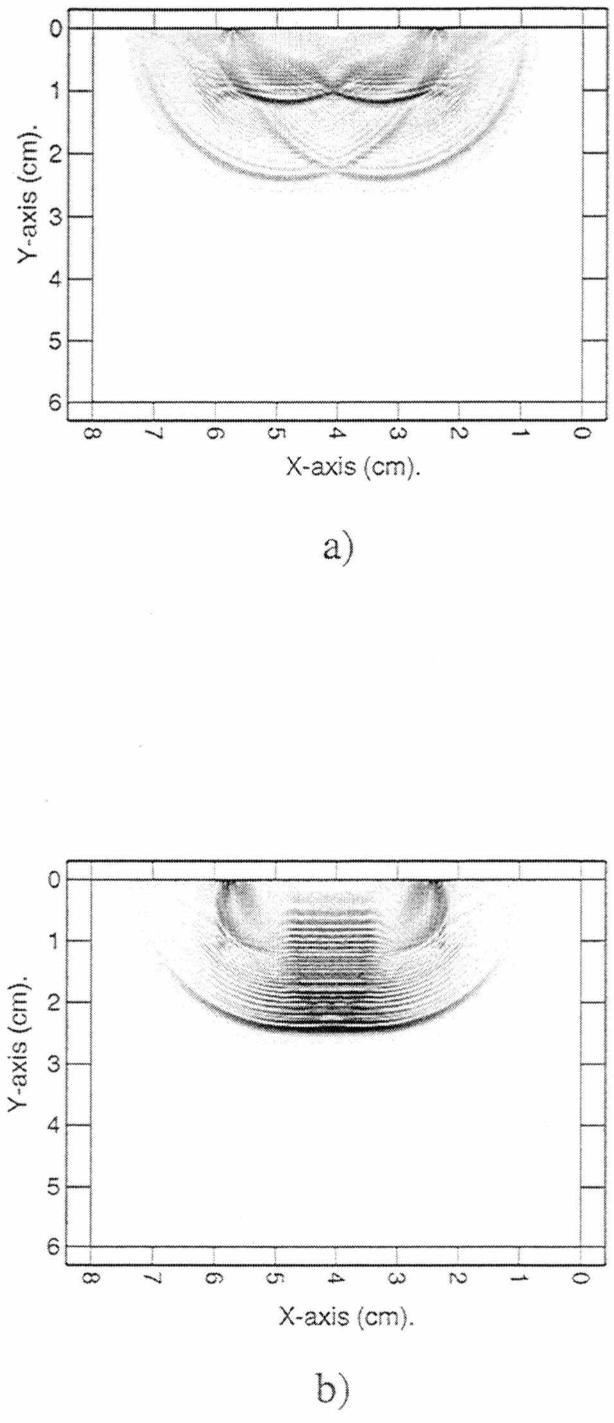

Figure 4-11. Compression wave excitation via surface source 1.5 cm wide at t=4 μs, aluminum plate. a) u-displacement component; b) v-displacement component.

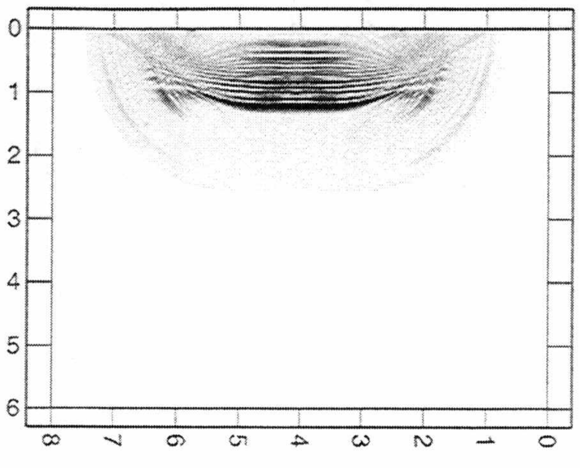

a)

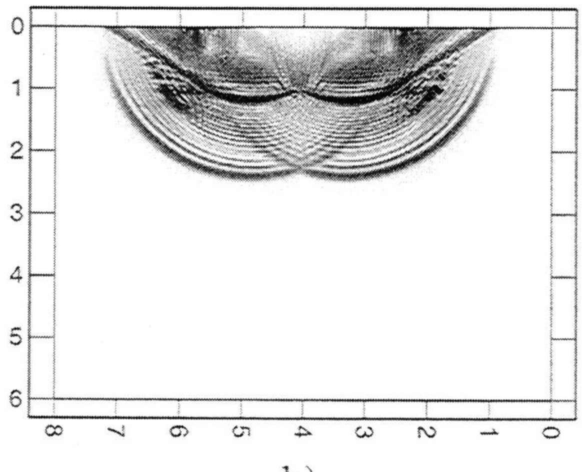

b)

Figure 4-12. Shear wave excitation by a surface source 1.5 cm wide at t=4 μs, aluminum plate. a) u-displacement component; b) v-displacement component.

interpret some complicated cases of wave scattering.

Figures 4-13a,b show the Gabor STFT of the v-displacement (Y-axis) component at a detector point as given by the numerical modeling (fig. 4-13a) and as given by the analytical solution (fig. 4-13b). The consistency between the two signals is obvious. The number of mesh points per wavelength is about 18 in the numerical solution. As the figures show, dispersion of the numerical solution cannot be observed, in agreement with the results in Chapter 3.

The analysis of these results leads to the same conclusion as in the previous works (see for example [20]), that the present numerical algorithm reproduces a stable and consistent, and therefore convergent, numerical solution of the wave equation.

4.1.3. Angular Anisotropy of the Surface Source

Further study of the angular anisotropy exhibited by extended surface sources, provides some details of the angular distribution of the displacement amplitudes at different angles surrounding the source. For this purpose a numerical experiment was carried out in an aluminum plate with the point source shown in figures 4-10a,b and 4-11a,b. For the purpose of this calculation the time-of-flight technique, described in [119], was used. The geometry setup is shown in figure 4-14. The detectors were distributed along the perimeter of a circle of radius 3 cm, centered at the source. As it was noted in previous section, the compression velocity in Al is $p = 6224.579$ m/s, which gives a time-of-flight of 4.82 μs for the compression wave from the source to the detectors at the circle perimeter.

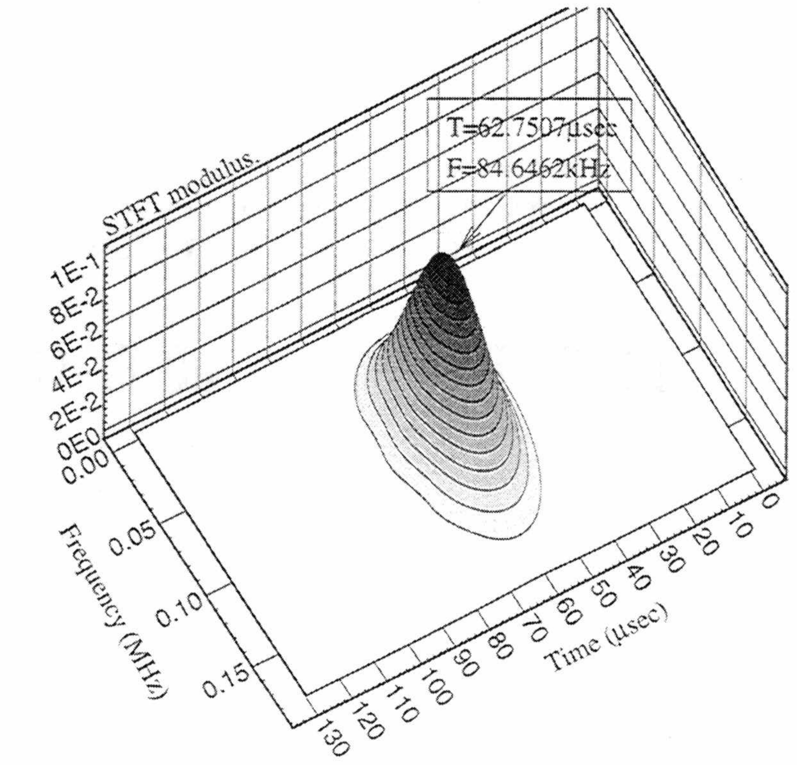

a)

b)

Figure 4-13. The Gabor STFT for the v-displacement component, pulse width 1.56 cm, longitudinal wave. a) numerical solution with Δt=0.08 μs, h=1.2 mm; b) analytical solution.

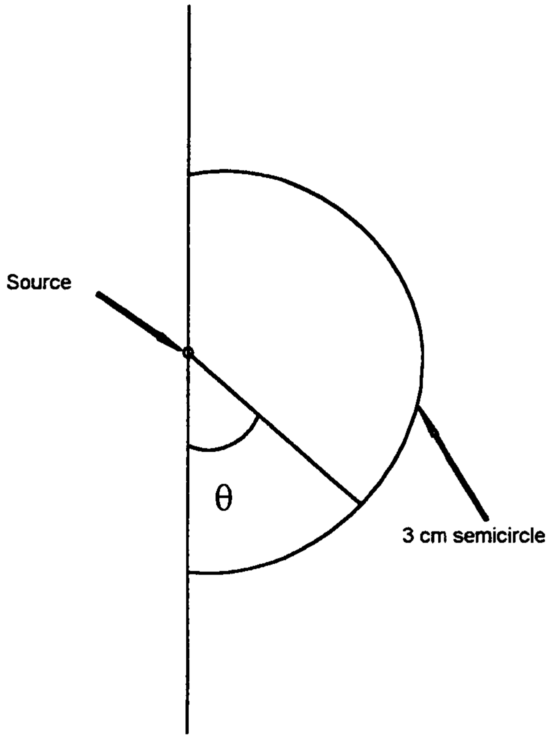

Figure 4-14. The geometry setup for angular distribution calculations.

For the shear wave we have a velocity s = 3112.29 m/s, and this gives a time-of-flight of 9.63 μs. It is readily seen that the arrival time provides an efficient method for the separation of the two wave modes, which is the basis of the time-of-flight technique.

Figure 4-15 shows the total displacement magnitude $|\bar{U}| = \sqrt{u^2 + v^2}$ as a function of the angle for the case of compression wave in the angular range $20° - 144°$. It is readily seen that the displacement is symmetric around the direction $\theta = 90°$. The angular distribution in the range $20° - 90°$ is in excellent agreement with the results reported by Harker [20]. The symmetry of the total displacement, however, does not mean symmetry

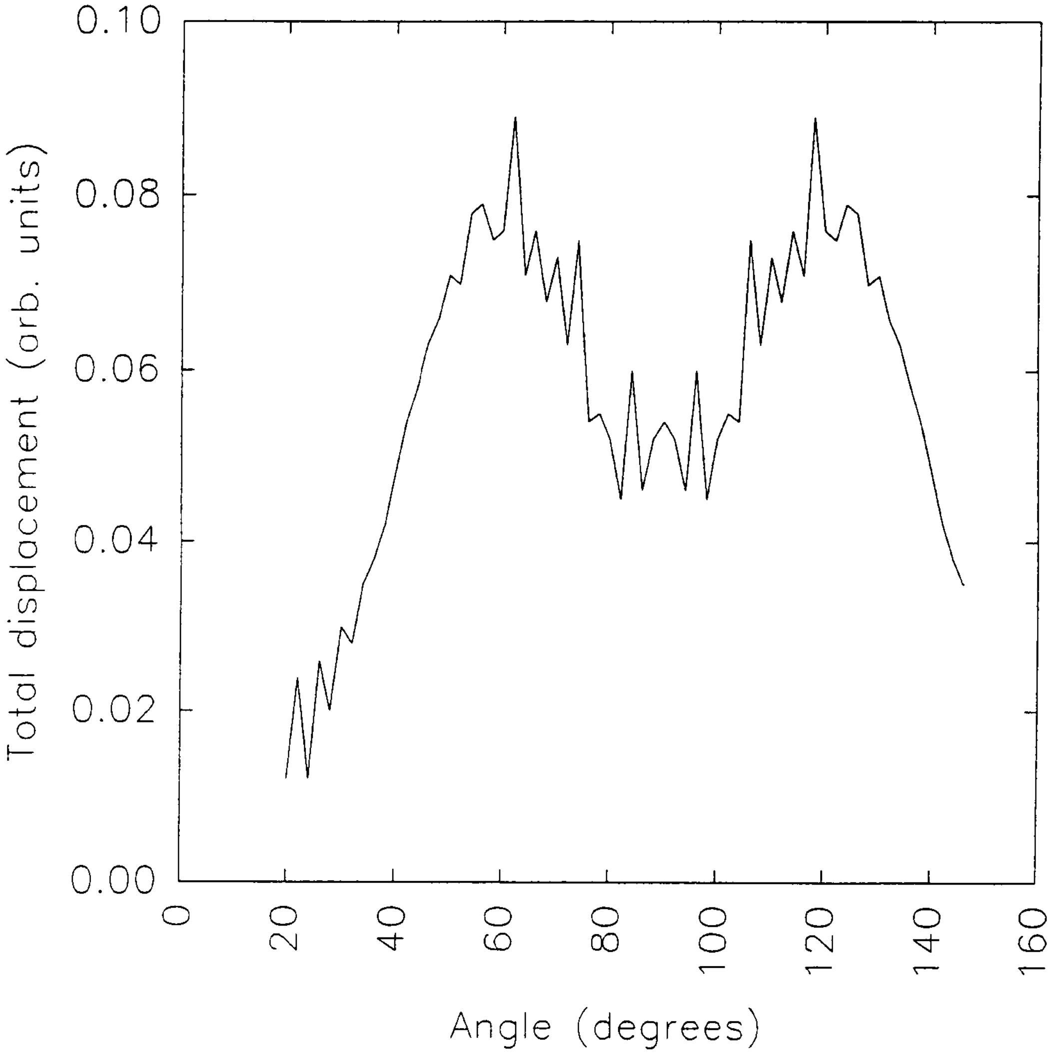

Figure 4-15. Angular distribution of the displacement magnitude for compression wave.

of the displacement components by themselves. Figures 4-16a,b,c,d show the u-displacement component at 60°, 70° and at their symmetric with respect to 90° angles 110° and 120°, respectively. It is seen that indeed the X-component of the displacement is symmetric with respect to the normal direction 90°. Figures 17a,b,c,d

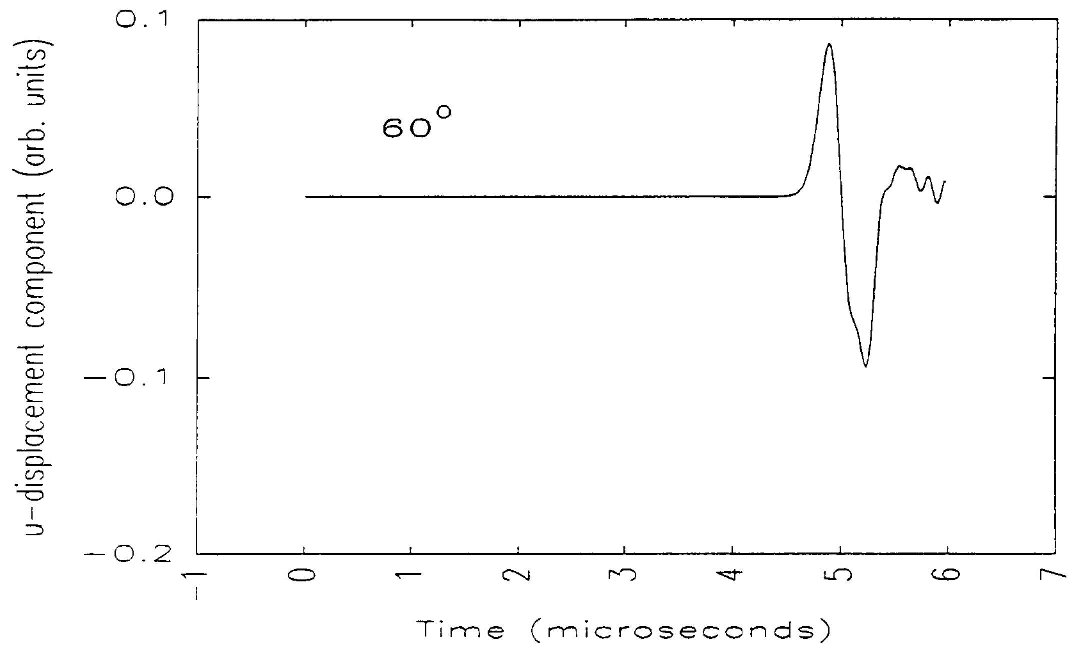

a)

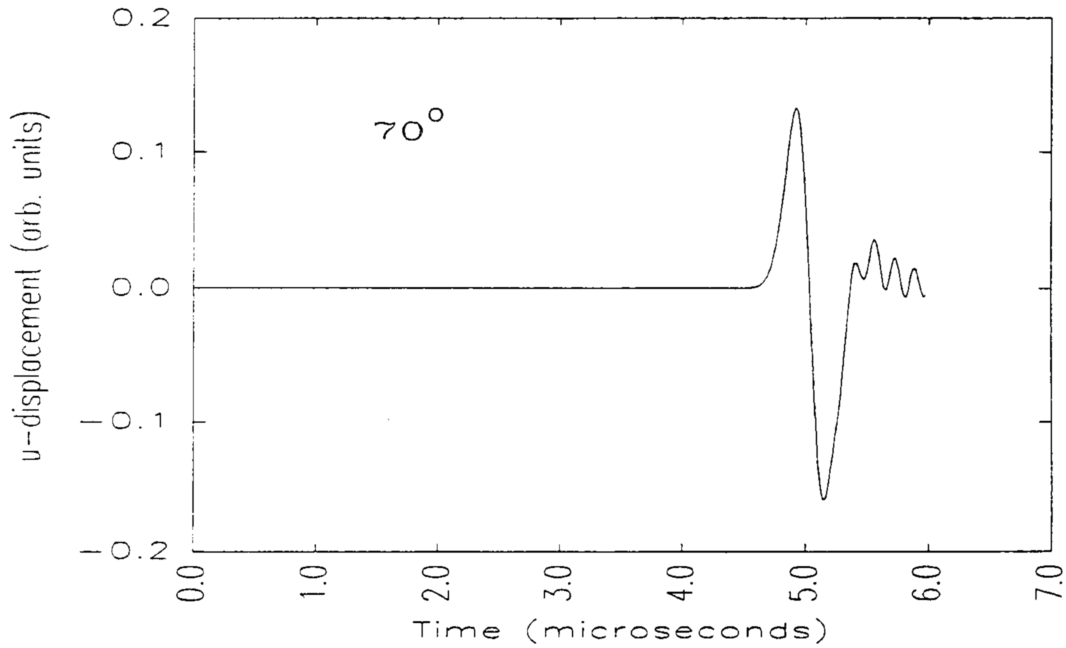

b)

Figure 4-16. The u-displacement component, compression wave. a) for angle 60° ; b) for angle 70° ; c) for angle 110° ; d) for angle 120°.

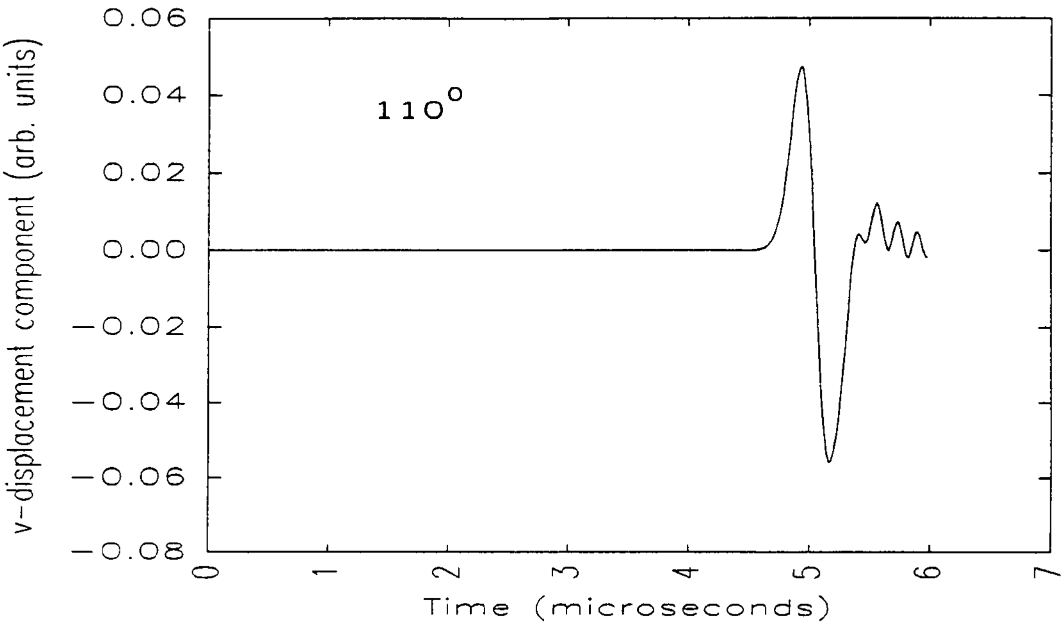

c)

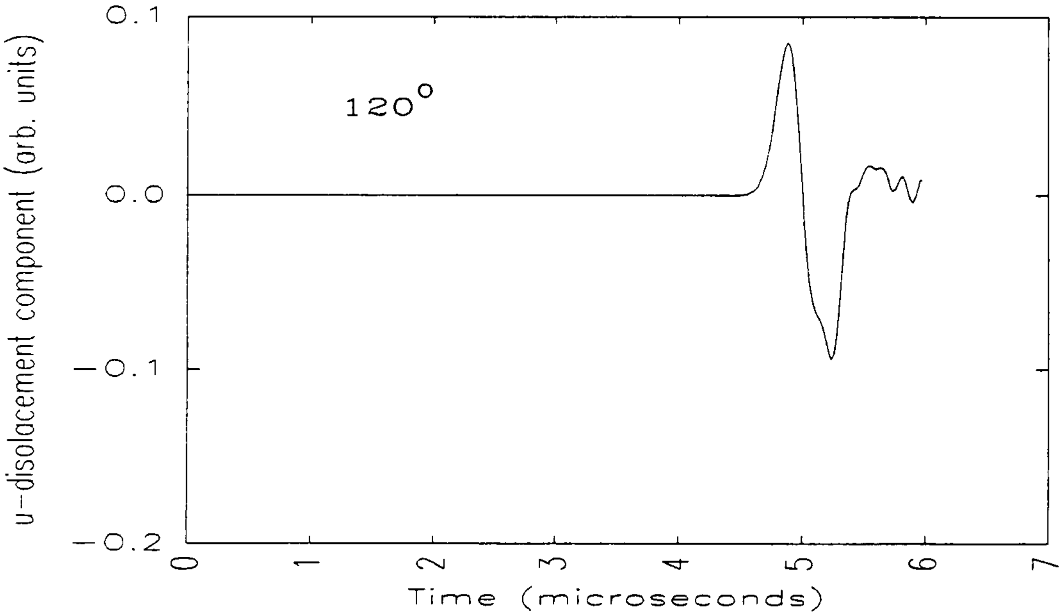

d)

Figure 4-16. Continued.

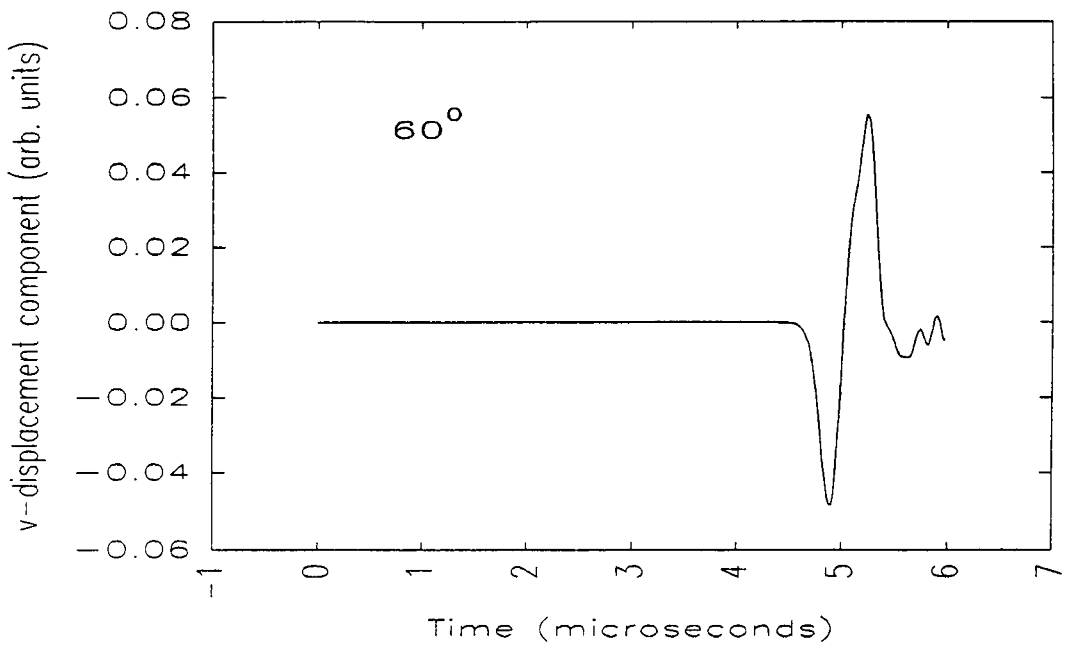

a)

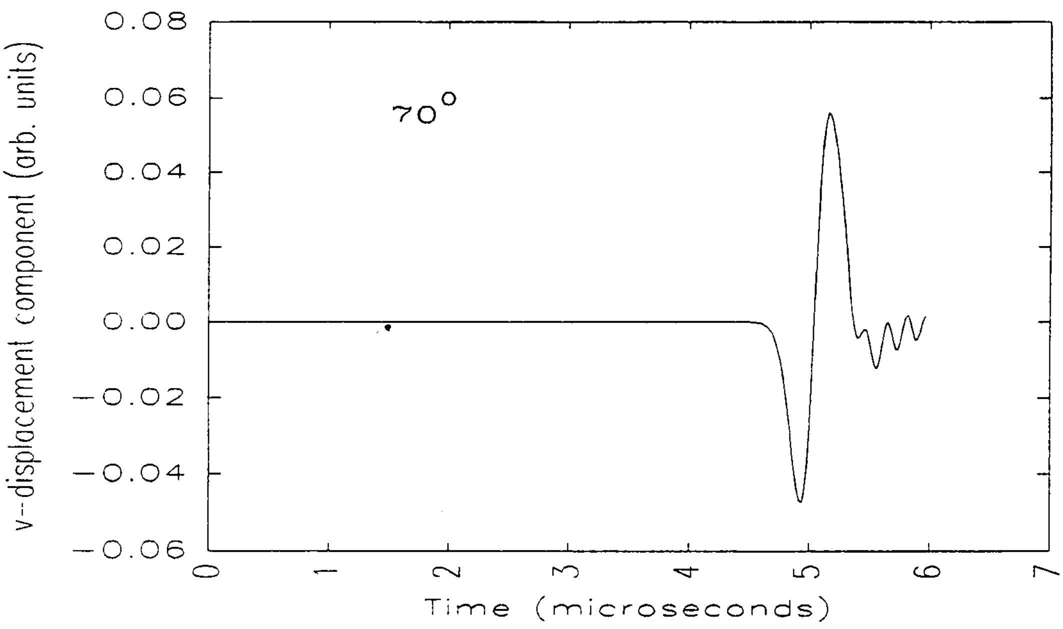

b)

Figure 4-17. The v-displacement component, compression wave. a) for angle 60° ; b) for angle 70° ; c) for angle 110° ; d) for angle 120° .

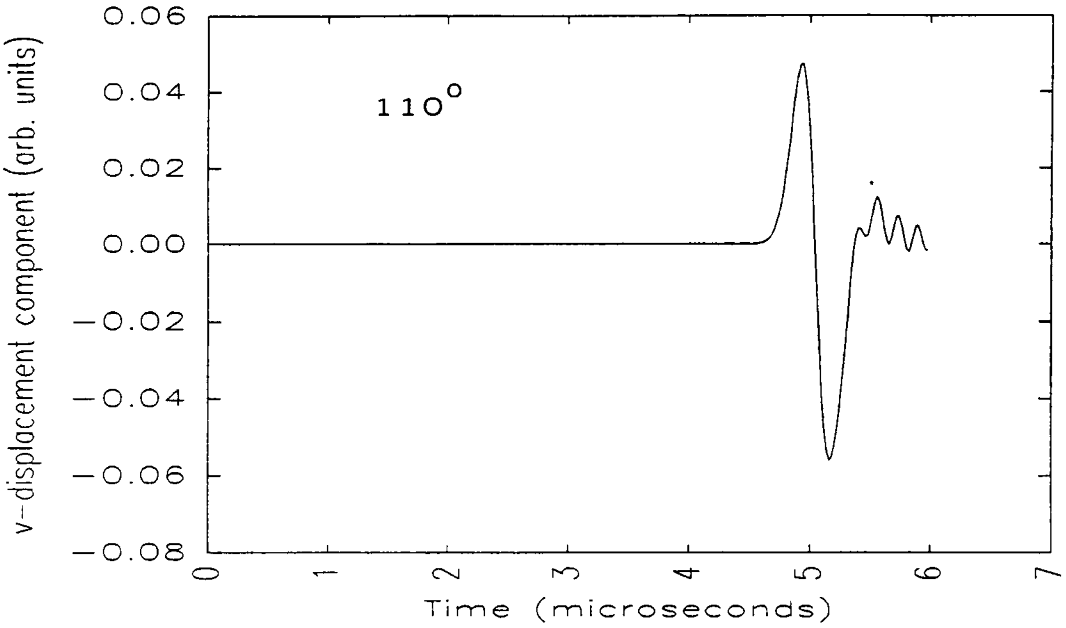

c)

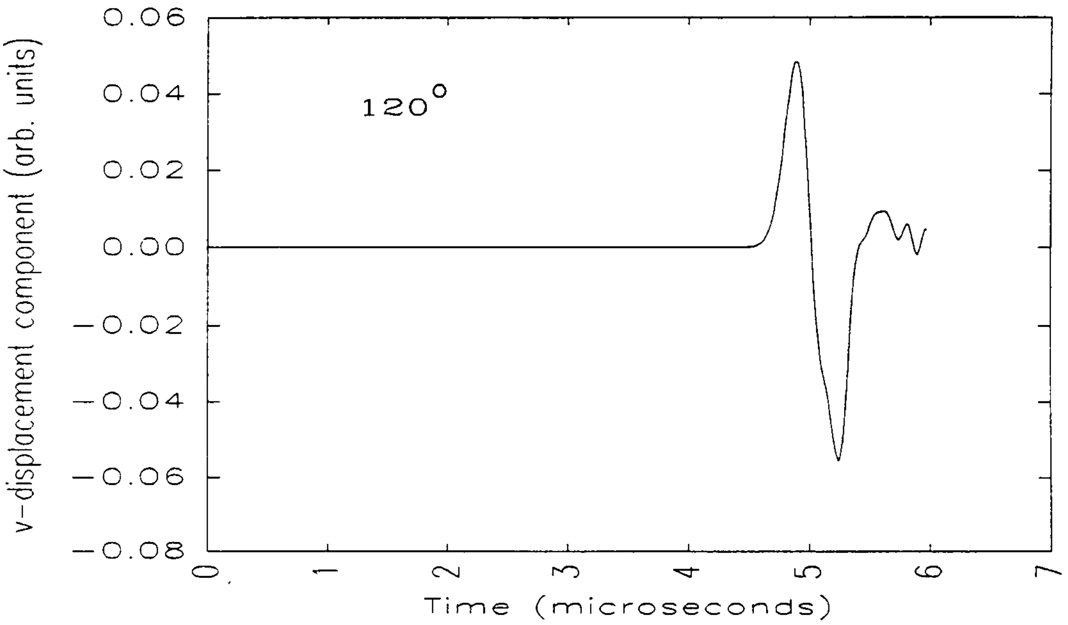

d)

Figure 4-17. Continued.

show the same features, this time for the v-displacement component. Note that the Y-component of the displacement is antisymmetric with respect to the direction 90°. In addition these figures show that the modeled wave coincides with the particular shape of a wavelet pulse as it is described by Ricker in [114]. Ricker also showed that the asymmetry of the pulse shape is specific for the true wavelet pulses when detected in the area near the source. In the far field the shape becomes symmetric as it is defined in the previous section and was used for surface source excitation.

Figure 4-18 shows the total displacement magnitude along the same circle shown in fig. 4-14 but for the case of shear wave excitation. It is readily seen that the wave displacement is symmetric with respect to the direction 90°. There is a difference, however, concerning not only the velocity of the propagating wave, but its displacement components as well. Figures 14-19a,b show the time dependence of u-displacement

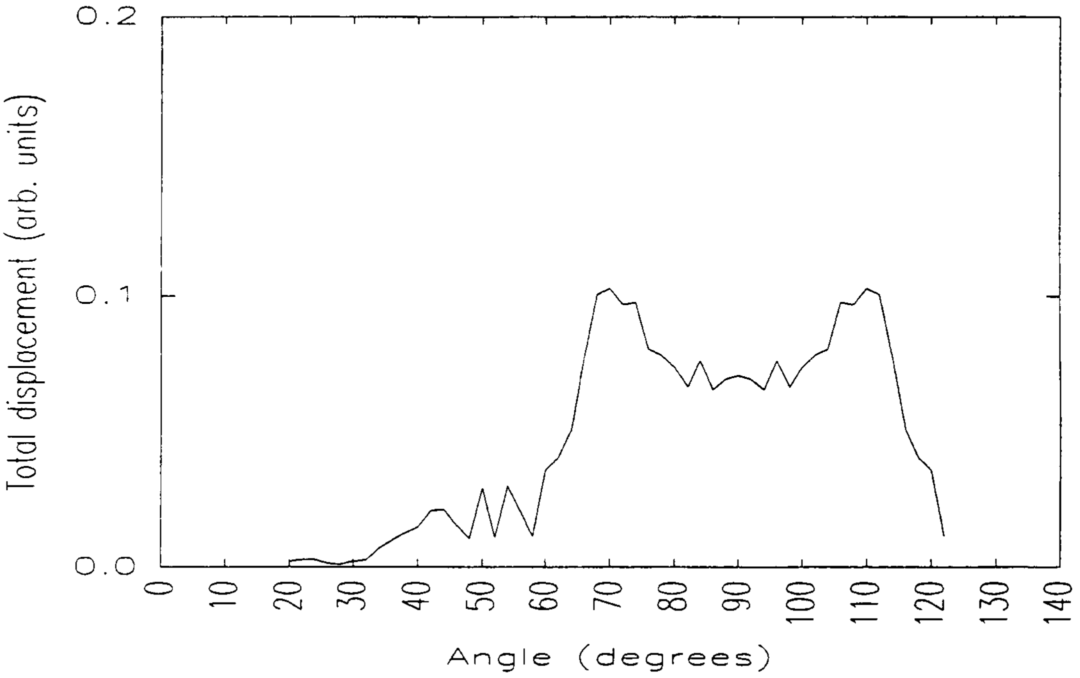

Figure 4-18. Angular distribution of the total displacement in the case of shear wave.

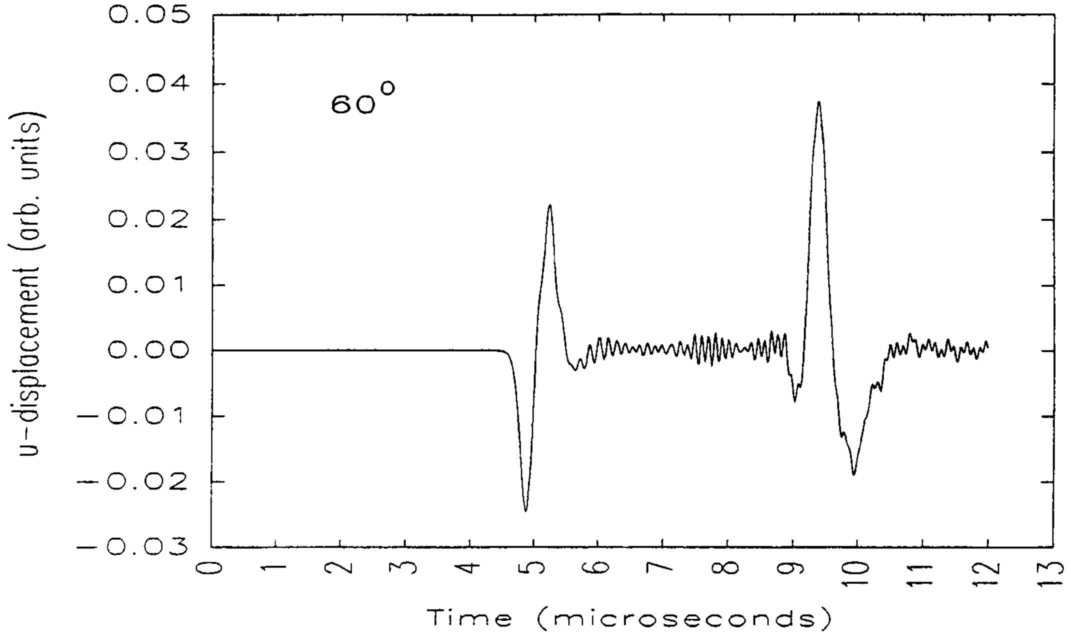

a)

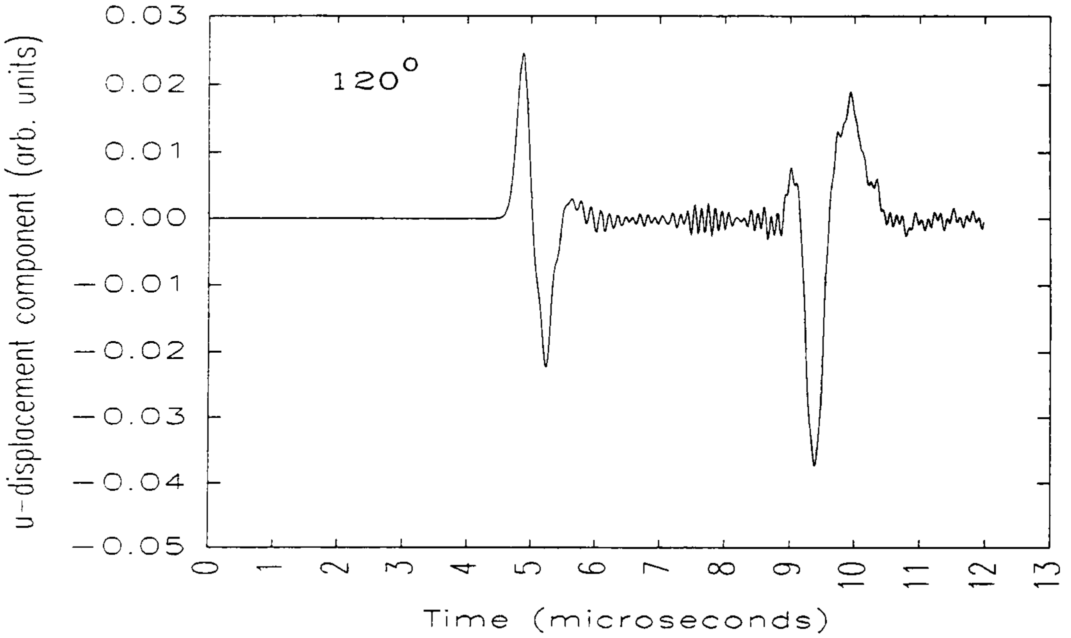

b)

Figure 4-19. The u-displacement component for shear wave, 366 kHz peak frequency. a) for angle 60° ; b) for angle 120° .

component at 60° and 120°, symmetric with respect to the direction 90°. The same, but for the v-displacement components, is shown in figures 4-20a,b. From the figures it is seen that in this case the v-displacement is symmetric with respect to the 90° angle, and the u-component is antisymmetric. The angular distribution is in excellent agreement with the results reported in [20, 115].

Using the terminology introduced in [114], we note that the surface source is an excellent option for modeling near the transducer area, which is mostly the case in practice, while the initial value excitation may be used to represent the wave field for areas far from the source. The analysis above also shows that the symmetry of the displacement components is in fact determined by the way we are applying the stress on the surface: in the case of a normal stress (longitudinal wave) the normal displacement component is symmetric with respect to the direction of the surface normal ; in the case of tangential stress (shear wave) the tangential component is symmetric. This is a general theoretical fact and as it is seen above, the developed model is representing it in a very general case of pulse excitation.

4.2. Scattering by Near-Surface Parallel Cracks

As the method of crack modeling described in Chapter 3 implies, it is assumed that the crack faces are non-interacting, i.e. the crack remains open under the influence of the incident wave. This is realistic for a smooth defect, according to Ogilvy and Temple [103], provided the defect width w obeys the condition $d < w << \lambda$, where d is the displacement amplitude of the wave and λ is the ultrasonic wavelength. It is also assumed that the crack

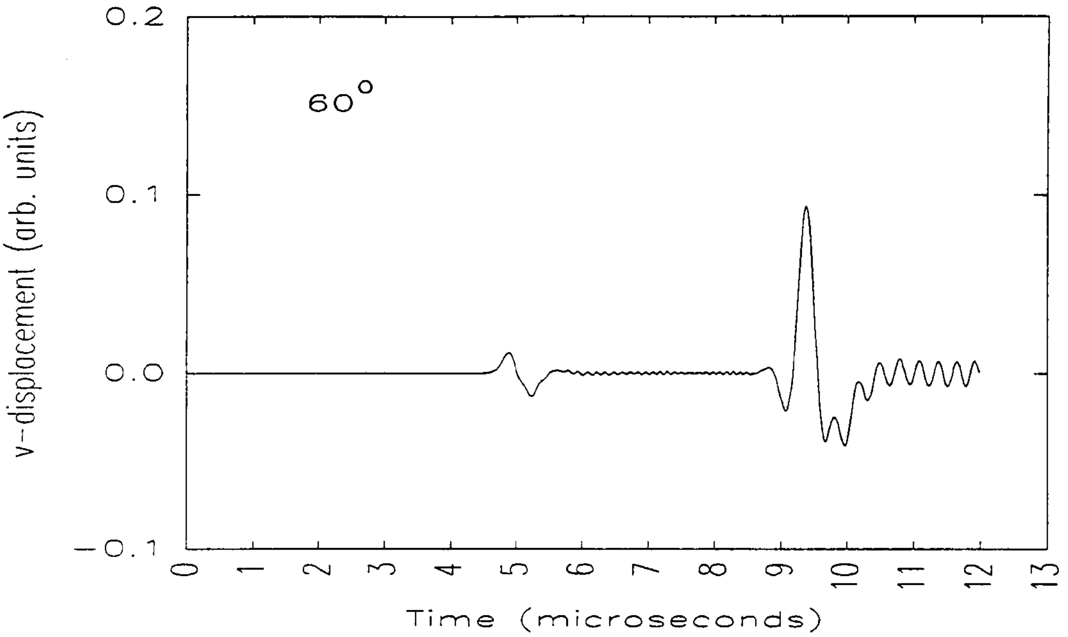

a)

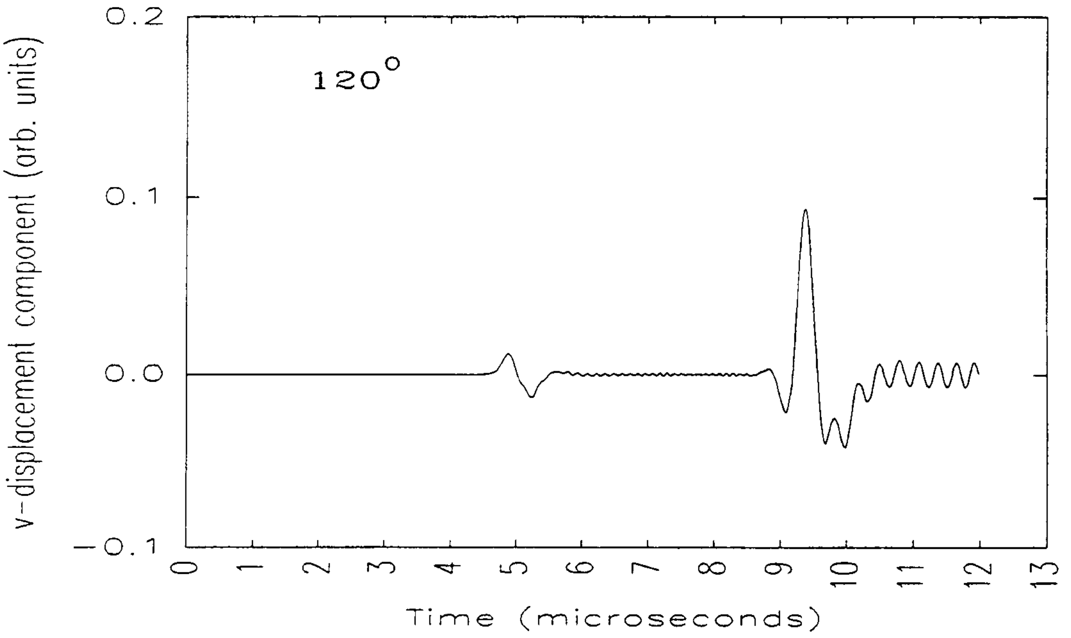

b)

Figure 4-20 The v-component of shear wave. a) for angle 60° ; b) for angle 120° .

faces act as stress-free boundaries.

Further analysis and comparison of the numerical results with analytical ones was made for the case of a near-surface parallel crack. The analytical results used are those obtained by J. Achenbach et al. [32, 120], where they use the diffraction ray theory [32, 61] approximations for analysis of the elastic wave scattering for a near-surface parallel crack. The basic assumptions in [120] are as follows: **(i)** a plane time harmonic longitudinal wave propagates along the Y-axis, normal to the crack surface in an infinite half-space; **(ii)** the crack length is a and the crack is parallel to the free surface of the infinite half-space, as shown in figure 4-21; **(iii)** the propagation takes place in a homogeneous linearly elastic solid. The theoretical model developed in [120] predicts a distinctive peak of the horizontal surface displacement (X- axis) or u-displacement component at a given dimensionless frequency $\omega d/c_R$, due to the scattered surface wave generated by the crack face. The total fields generated by the interaction of incident waves and the crack can be expressed as

$$u_i^t = u_i^{in} + u_i, \tag{4.19}$$

$$\sigma_{ij}^t = \sigma_{ij}^{in} + \sigma_{ij}, \tag{4.20}$$

where u_i^{in} and σ_{ij}^{in} are the displacement and stress components for the incident field, while u_i and σ_{ij} correspond to the scattered field. For the incident wave generated at the surface we have

$$u_y^{in} = v^{in} = A_L \exp i(k_L y - \omega t), \tag{4.21}$$

where A_L is the wave amplitude. The zero-stress boundary conditions implies that at y = d

$$\begin{aligned} \sigma_{yy}^{in} &= ik_L(\lambda+2\mu)A_L \exp i(k_L d - \omega t), \\ \sigma_{xy}^{in} &= 0 \end{aligned} \tag{4.22}$$

For a wave generated in the interior the displacement field incident on the crack includes the reflection from the free surface, and is taken in the form

$$u_y^{in} = v^{in} = A_L\left[\exp i(k_L y - \omega t) + \exp\{-i(k_L y + \omega t)\}\right]. \tag{4.23}$$

The relevant stresses at y = d are

$$\begin{aligned} \sigma_{yy}^{in} &= -2k_L(\lambda+2\mu)A_L \sin(k_L d)\exp(-i\omega t), \\ \sigma_{xy}^{in} &= 0 \end{aligned} \tag{4.24}$$

Scattered surface waves generated by normal incidence of a longitudinal wave on the crack are symmetrical relative to the plane $x = a/2$. For an incident longitudinal wave generated at the free surface, in [120] it is shown that the scattered surface wave is generated by the crack face condition

$$\sigma_{yy}^{(1)} = -ik_L(\lambda+2\mu)A_L \exp\{i(k_L d - \omega t)\}. \tag{4.25}$$

Denoting the corresponding horizontal displacement component by $u_S^{(1)}$, in [120] it is shown that

$$U_L^{(1)} = \frac{\mu}{\lambda+2\mu}\frac{2}{k_L a}\left|\frac{u_S^{(1)}}{A_L}\right|, \tag{4.26}$$

where $U_L^{(1)}$ is the corresponding dimensionless displacement component as defined in [120]. For an incident wave generated in the interior of the half-space, the crack-face condition is obtained to be [120]

$$\sigma_{yy}^{(2)} = 2k_L(\lambda + 2\mu)A_L \sin(k_L d). \tag{4.27}$$

In [120] it is noted that the term $2\sin(k_L d)$ enters in (4.27) because of the reflection from the free surface of the half-space. Denoting the horizontal (or X-axis) component by $u_s^{(2)}$, in [120] one obtains:

$$U_L^{(2)} = \left|\frac{u_s^{(2)}}{A_L}\right| = \frac{\lambda + 2\mu}{\mu}\frac{a}{d}(k_L d)\sin(k_L d)U_L^{(1)}. \tag{4.28}$$

In [120] it is concluded that with the assumptions made: **(i)** the waves perpendicularly incident on a crack which is parallel to the free surface, generate scattered surface waves whose amplitude-spectra show distinct resonance peaks; **(ii)** the peaks appear at frequencies corresponding to the ratio d/a; **(iii)** the peaks become less distinct as the ratio d/a increases. Analyzing the equations (4.26) and (4.28) and using the equations (2.42) and results in Table 2-4, it is seen that the dimensionless amplitudes (4.26) and (4.28) are proportional (or inverse proportional) to the ratio

$$\frac{\mu}{\lambda + 2\mu} = \frac{s^2}{p^2} = \frac{(1 - 2\nu)}{2(1 - \nu)}, \tag{4.29}$$

and therefore the peaks observed are function of the Poisson ratio ν. Table 4-1 shows the approximate values of the dimensionless variable $\omega d/c_R$ for the value of $\nu = 0.3$.

For comparison with these results we use a pulse of the particular shape (4.4) and (4.5) instead of plane harmonic waves for the following reasons: **(a)** such a pulse contains a well defined range of frequencies (see fig. 4-1) and can be shaped in such a manner to contain those frequencies required for the comparison; **(b)** the pulse provides the opportunity to localize the peak in only one computation for each *d* and *d/a*. The A-scan data has been collected with a sampling rate 3.125 MHz at a point situated on the crack surface, as shown in figure 4-21. The crack has

Table 4-1. Analytical predictions for $\nu = 0.3$.

d/a	$\omega d/c_R$ $\nu = 0.3$
0.2	**~0.26**
0.4	**~0.63**

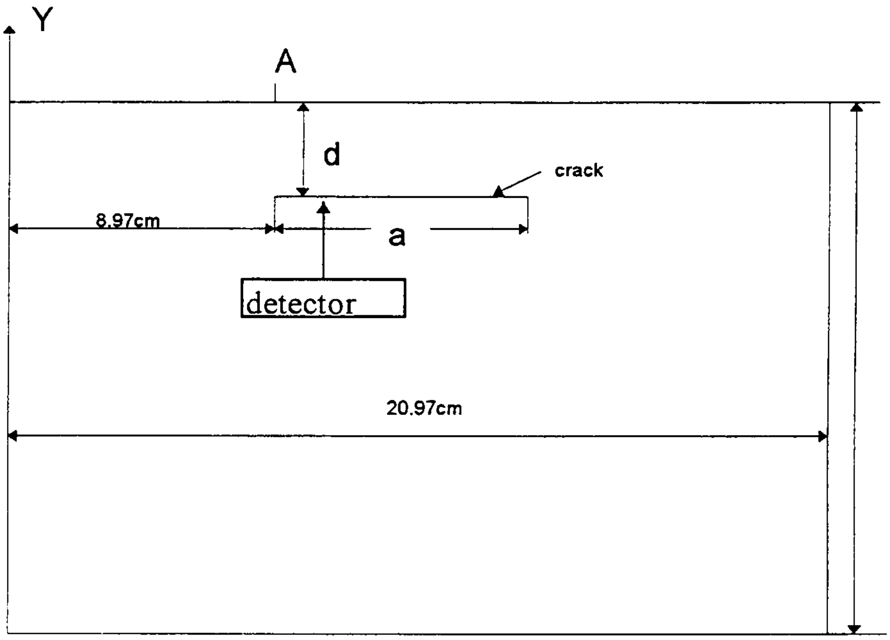

Figure 4-21. Geometry of the problem with near-surface parallel crack.

been modeled as shown in Chapter 3 in different materials with $\nu = 0.29$ and 0.3. The comparison has been carried out with a stepsizes h = 1.2 mm and 0.6 mm and time stepsizes Δt = 0.08 μs and 0.04 μs, respectively, for the cases listed in table 4-1. For d/a = 0.4 a plane longitudinal wave with an exponential width 1.56 cm has been selected for the comparison. The power spectrum density (PSD) of the pulse Y-component (as it is shown in section 4.1, in this case X-component is zero) for the case of steel with $\nu = 0.29$, $\rho = 7.86\text{x}10^3$ kg/m^3 and p = 5774 m/s is shown in figure 4-22. The corresponding Gabor STFT, obtained with the tools developed in [87] in their PC's version is shown in figure 4-13a. Figure 4-23 shows "history" at the detector point for the case d = 3.6 cm,

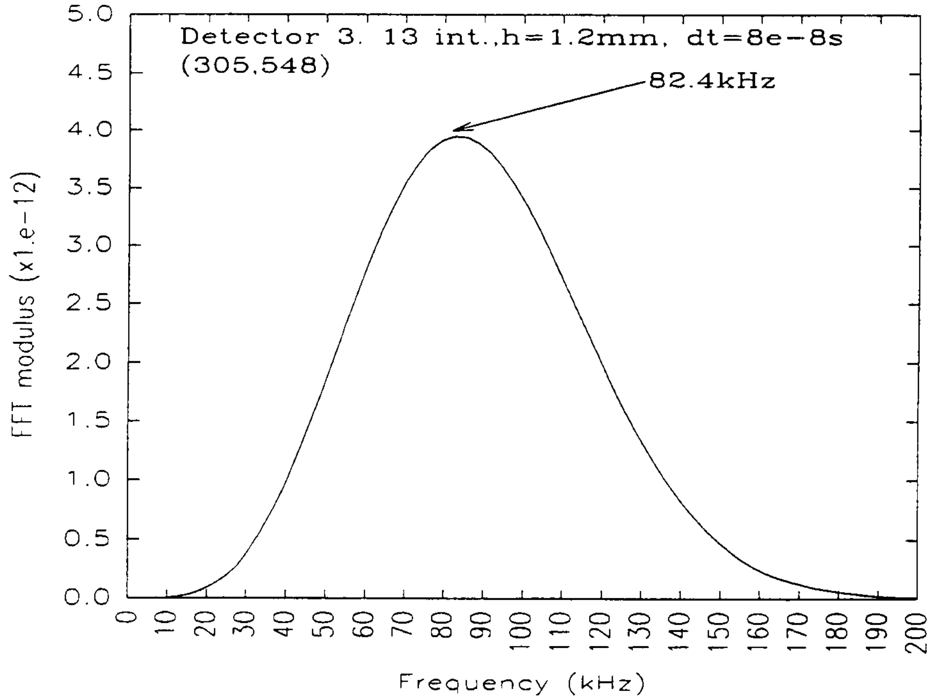

Figure 4-22. Power spectrum density of the initial value analytical solution, pulse width 1.56 cm in steel with $\nu = 0.29$.

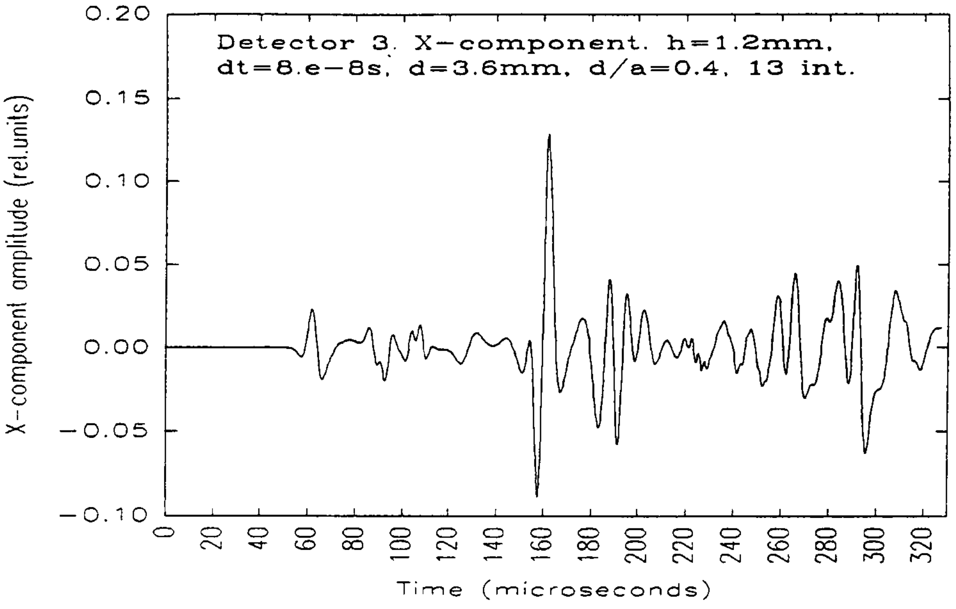

Figure 4-23. The "history" at the detector point for d = 3.6 mm, d/a = 0.4.

d/a = 0.4 as given by the numerical solution for the displacement X-component. Figures 4-24, 4-25 show the fast Fourier transform (FFT) PSD of the displacement X-component for d = 3.6 mm and d = 4.8 mm respectively, when d/a = 0.4, and the data has been collected over 327 μs (4096 time steps). The analysis of these PSD's does not provide the necessary information to confirm the analytical results as they are shown in Table 4-1. The frequency peaks at frequencies close to the expected values might or might not result from the displacements generated at the other surfaces and corners of the system. Therefore, it is obvious that the Fourier transform is not capable to reveal the effect since it is strongly influenced by the various reflected signals appeared due to the finite size of the modeled system.

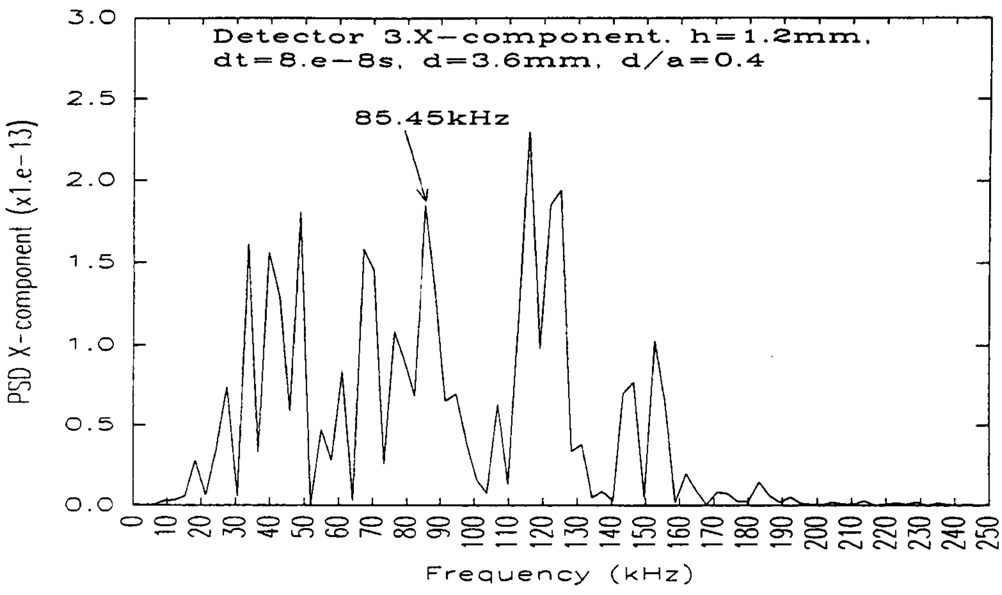

Figure 4-24. FFT of the u-displacement component, d = 3.6 mm, d/a = 0.4.

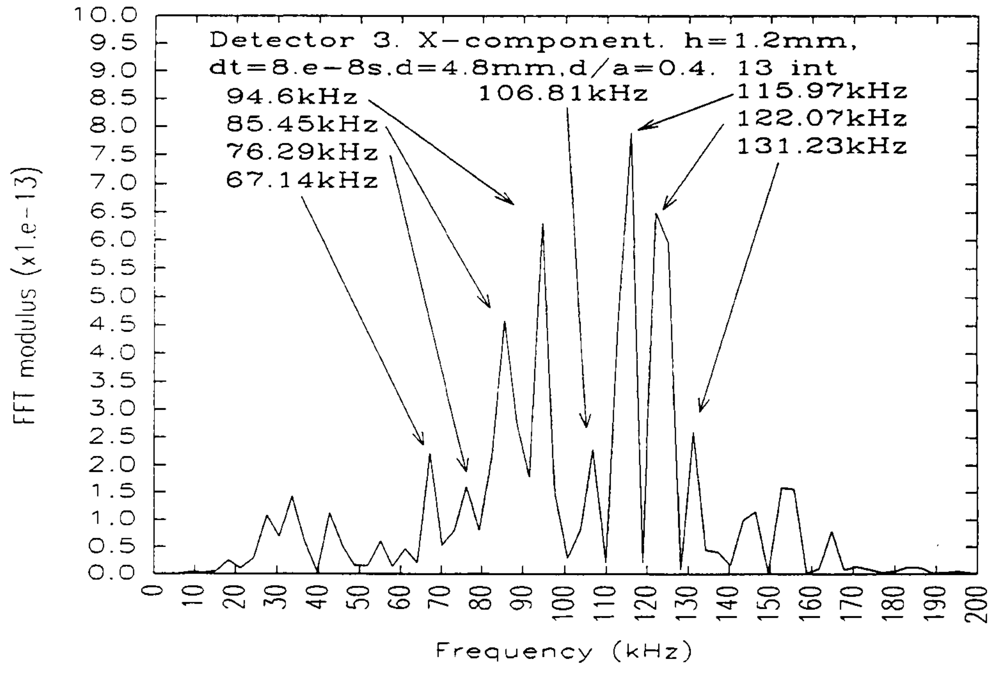

Figure 4-25. Same as in figure 4-24 for d = 4.8 mm.

Figures 4-26a,b show the STFTs' of the X- (or u-) displacement component in the case $d = 3.6$ mm, $d/a = 0.4$ (fig. 4-26a) and without a crack present (fig. 4-26b) as given by the numerical solution during the first 130 μs after the initiation of the process. The analysis of these figures shows that: **(a)** - the peak at 81.84 kHz is due to the presence of the crack; **(b)** - the peak appears at the time the pulse reaches the crack surface and spans over a magnitude range 1.5 times smaller than the case when the crack is missing. These observations lead to the conclusion that the peak at 81.84 kHz results from u-displacement component generated by the crack surface stresses defined by (4.25) and (4.27) and is in excellent agreement with the result from table 4-1. In figure 4-27 is shown the Gabor STFT of u-displacement component when $d = 4.8$ mm and $d/a = 0.4$ for the first 130 μs after the process initiation. Again, the comparison with fig. 4-26b leads to the conclusion that the peak at 72.64 kHz is caused by the crack surface stresses. Also the comparison between figures 4-26a and 4-27 shows that the frequency shift is due to the increased depth and size of the crack. Indeed, the ratio $\frac{\omega d}{c_R}$ gives 0.63 when d = 3.6 mm and 0.74 when d = 4.8 mm, taking into account that the Rayleigh wave velocity in this case is 2908 m/s. It is seen that the result for d = 4.8 mm differs by 16%. The discrepancy can be caused by three reasons: **(i)** - the theoretically predicted peak for $d/a = 0.4$ is relatively wider and less distinct than the one at 0.2, as it will be seen below; **(ii)** - we analyze a pulse scattering with a finite range of frequencies instead of a single frequency as in the theoretical analysis; **(iii)** - the material has Poisson ratio $\nu = 0.29$ instead of 0.3, as it is in the theoretical results. Also the numerical results are undoubtedly affected by the a)

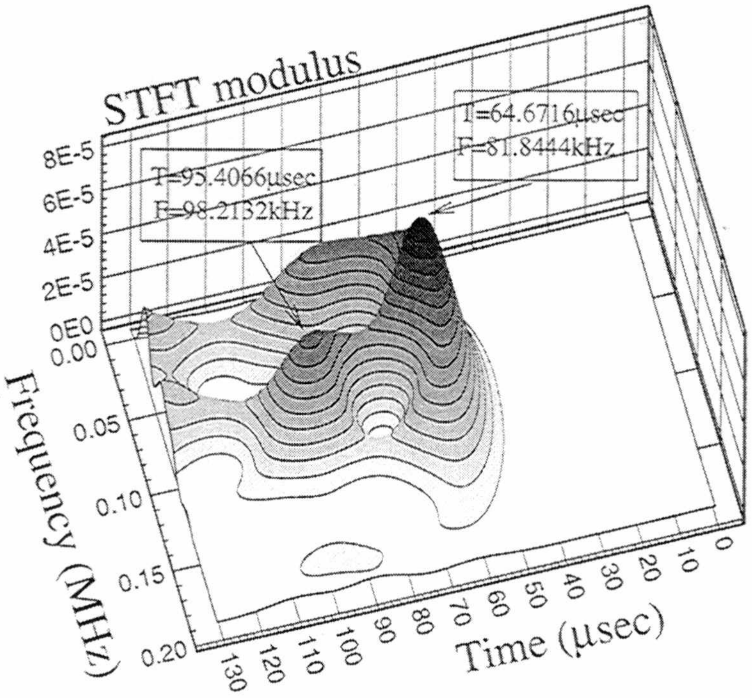

b)

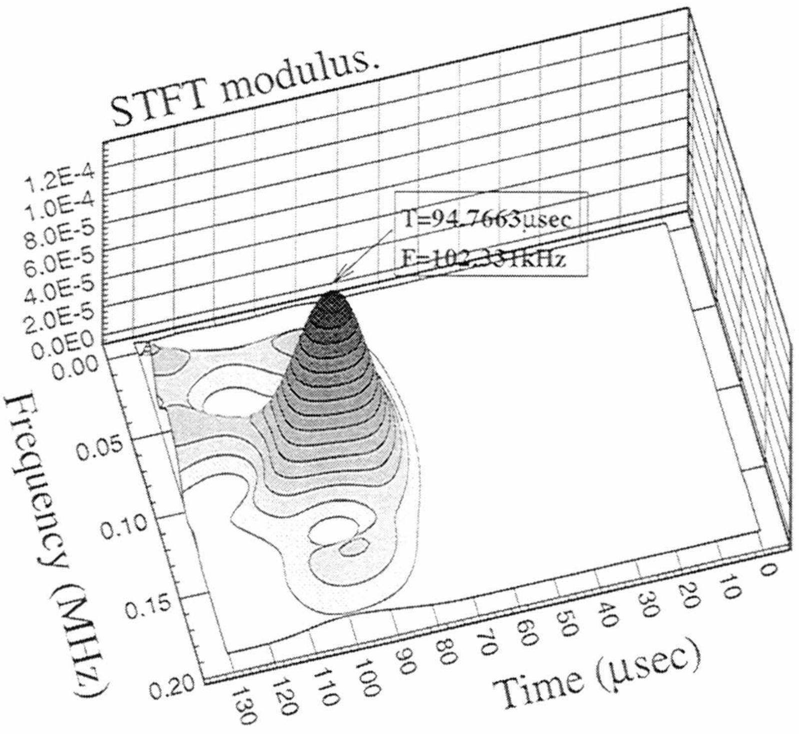

Figure 4-26. The Gabor STFT of the u-component, h=1.2 mm, Δt=0.08 μs, ν=0.29.
a) crack with d=3.6 mm, d/a=0.4; b) no crack presented.

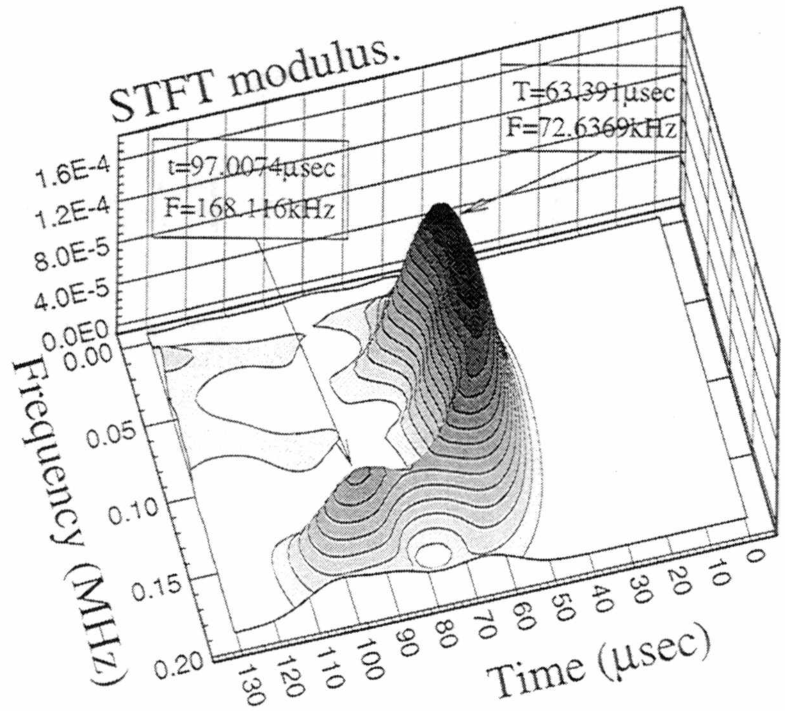

Figure 4-27. Gabor STFT of the X-component. $h=1.2$mm, $\Delta t=0.08\mu$sec, $d=4.8$mm, $d/a=0.4$, pulse width 1.56cm. $\nu=0.29$.

truncation error. The most important causes for the discrepancy seems to be the pulse range of frequencies and the less distinct peak for $d/a = 0.4$. However, as a whole the numerical results are in an excellent qualitative agreement with the theoretical predictions for the case $d/a = 0.4$

To clarify the conclusions above and to compare results for $d/a = 0.2$ we used different time and spatial step sizes, $\Delta t = 0.04$ µs and h = 0.6 mm in order to use the same values of d and a and to obtain a stable scheme. Since the expected peak frequencies are about 30 kHz, we used wider pulses with exponential width 6 cm for the case of $\nu = 0.29$

and 4.5 cm for the case $\nu = 0.3$. Figures 4-28a,b show the Gabor STFT of the v-component of the pulse at the line on which the pulse is initiated for the cases of pulses with width 6 cm and 4.5 cm, respectively. Figures 4-29 and 4-30 show the Gabor STFT for $d = 3.6$ mm and 4.8 mm, respectively, when $\nu = 0.29$. Taking into account that $c_R = 2908$ m/s for this case, it is seen that the ratio $\frac{\omega d}{c_R}$ gives 0.18 for $d = 3.6$ mm and 0.187 when $d = 4.8$ mm. It is seen that this results is in excellent qualitative agreement with the theoretical predictions. The better consistency, in comparison with the previous case, is also due to the fact that the expected peak is much sharper and easier to distinct than above. The different value of the ratio can be explained with the different Poisson ratio ν. To verify this assumption, we calculated the STFT of the u-component for a material with $\nu = 0.3$ and $c_R = 2901$ m/s on a crack at $d = 4.8$ mm and $d/a = 0.2$. The spatial stepsize was $h = 0.6$ mm and $\Delta t = 0.04$ μs, and the pulse shown in fig.4-28b was used. Figure 4-31 shows this STFT. It is seen that is we calculate the ratio $\frac{\omega d}{c_R}$ for $f = 25.2$ kHz, where the absolute peak of the STFT modulus is observed, we obtain 0.26, which is in excellent agreement with the theoretically predicted value.

The results presented in this section lead to the following conclusions:

1. The present computer model reproduces the expected physical phenomena and leads to a consistent and stable numerical solution of the wave equations;

2. The first order approximation for the boundaries used in the numerical model is sufficient to represent the zero stress boundary conditions at the system boundaries and at

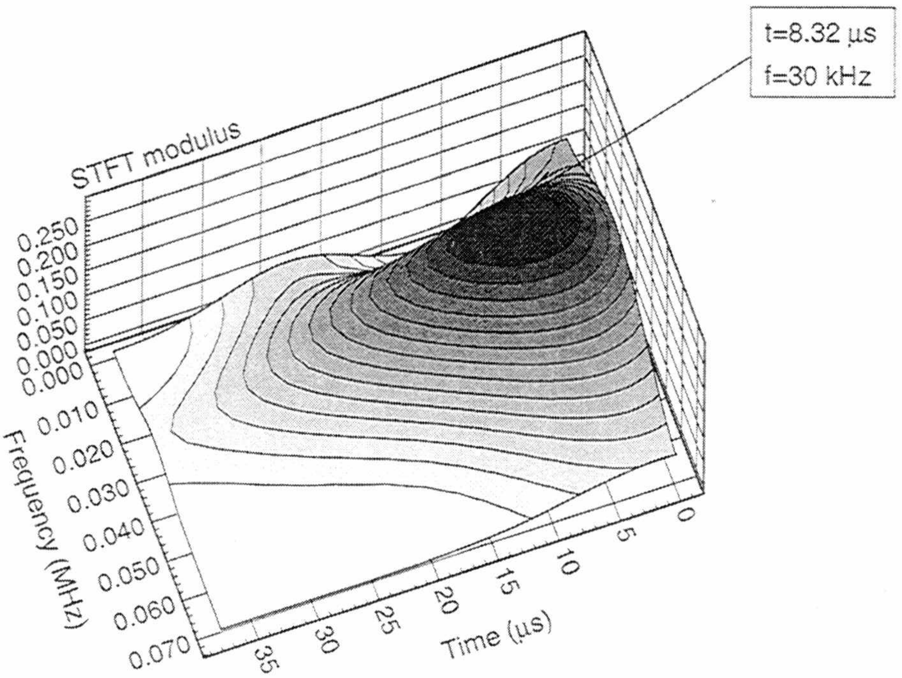

a)

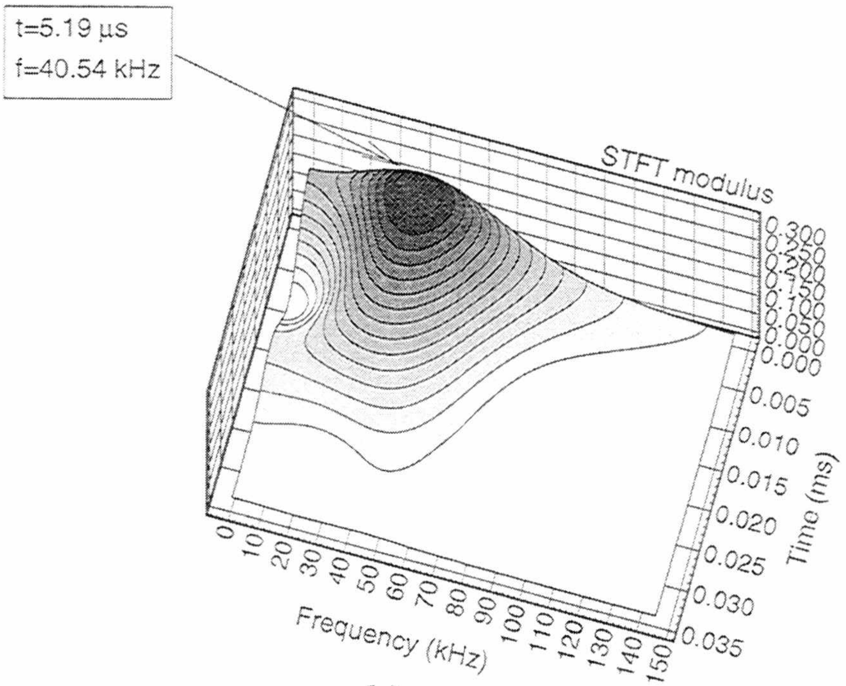

b)

Figure 4-28. The Gabor STFT for v-component of a pulse. a) pulse width 6 cm, ν=0.29; b) pulse width 4.5 cm, ν=0.3.

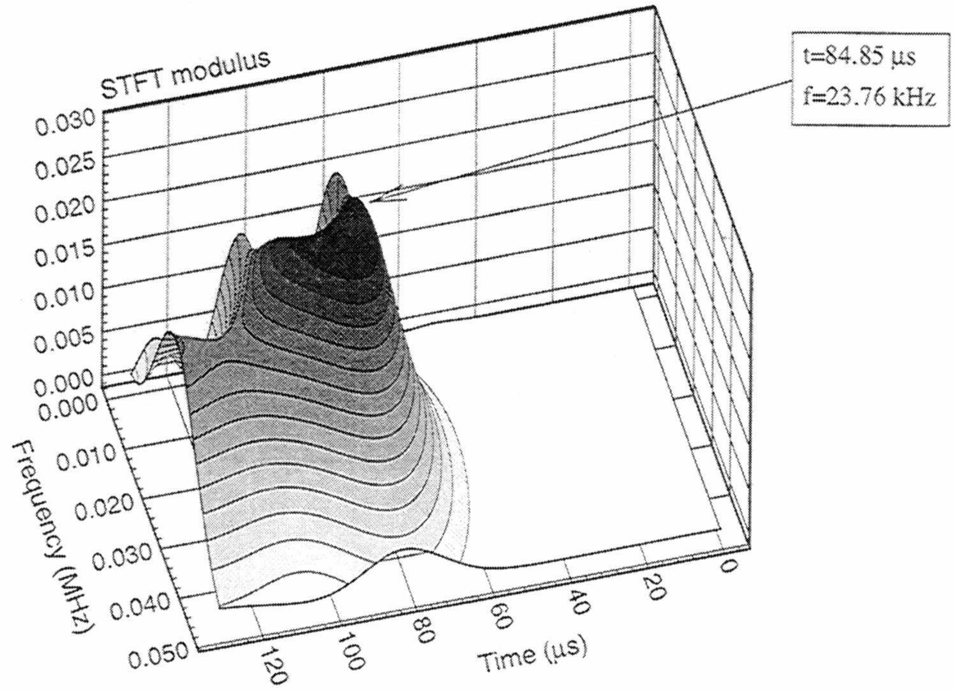

Figure 4-29. The Gabor STFT for u-component on a crack at d=3.6 mm, d/a=0.2, Δt=0.04 µs, h=0.6 mm, ν=0.29.

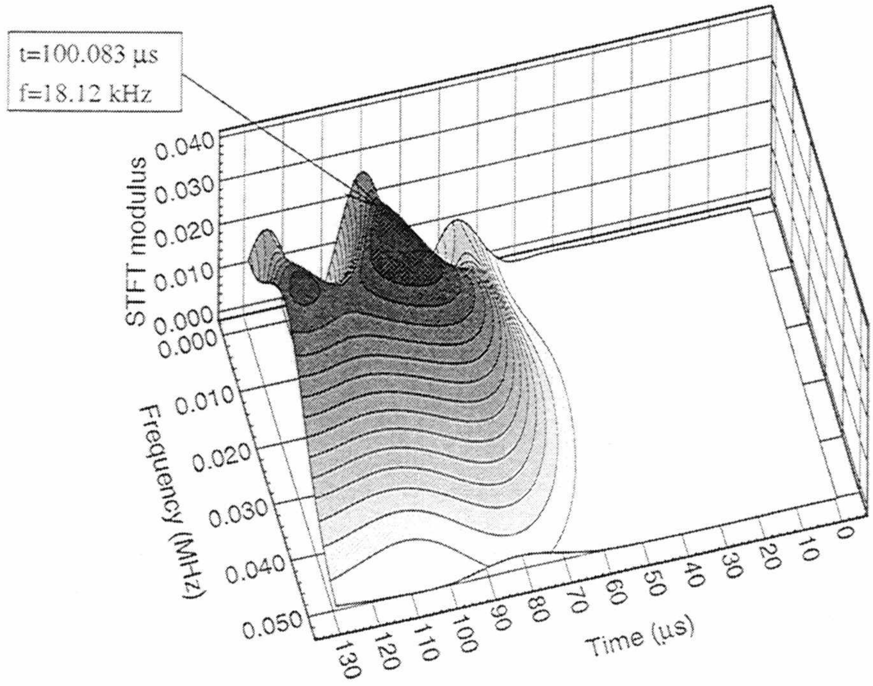

Figure 4-30. Same as in figure 4-29 for d=4.8 mm.

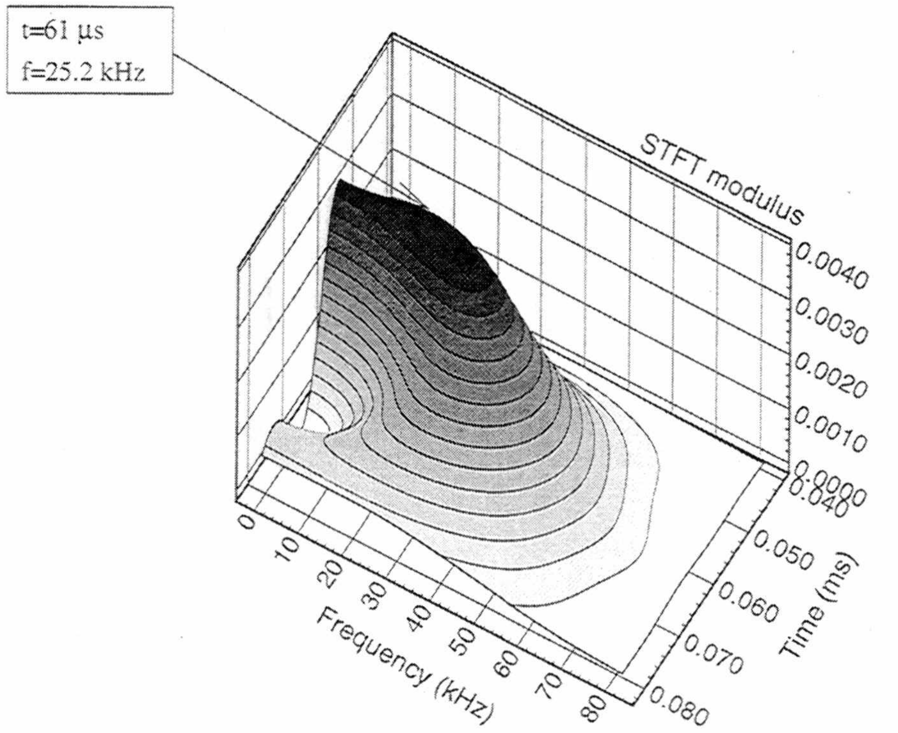

Figure 4-31 . The Gabor STFT of u-component, d=4.8mm, d/a=0.2, h=0.6mm,Δt=0.04μs, pulse width 4.5cm, ν=0.3.

the crack surfaces provided that the truncation error is kept small by using appropriate time and space step sizes;

3. The numerical algorithm contains a correct representation of the effect of material flaws in the case of non-surface breaking crack;

4. The analysis of a pulse scattering does not differ from the theoretical predictions in the particular cases of infinitely thin cracks and are in excellent consistency with the theoretical predictions especially when the expected frequency peak is sharp and easily to distinct, which decreases the influence of the finite range of frequencies carried by the pulse. However, when the effect is not that distinct, the results may differ from the theoretical predictions due to the effect of the pulse finite frequency range.

5. The results also show that when the expected effect is highly non-stationary, the Gabor STFT is able to provide a reliable and easy-to-interpret time-frequency distributed information. As a whole, the Gabor STFT with its time localization capabilities vastly improves the quality of the analysis.

Finally, the numerical analysis revealed some of the difficulties inherent to the process of ultrasonic measurements and result analysis.

4.3 Diffraction of Elastic Waves from a Crack Tip

In this section we consider the effects of scattering of the elastic waves from a crack tip. It is usefull to use experimental visualisations [20] to illustrate the process. Several groups have used schlieren or photoelastic methods to obtain snapshots of the wavefield in elastic wave generation [116] or scattering [121]. Some progress is being made towards making such techniques quantitative, and eventually there may be close links between visualization and computation as is the coming practice in stress analysis [20], but for our purpose the qualitative results will suffice.

Results of interpretation of a photoelastic method for visualization to study the scattering of compression waves by a surface breaking slit are shown in figure 4-32 for three different times after the injection of a compression pulse. The interpretation is as follows [20] in terms of wavefronts: C_1 is the injected pulse. Part of it is transmitted past the tip of the crack, part forms the reflected front C_2. The reflected front is continuous

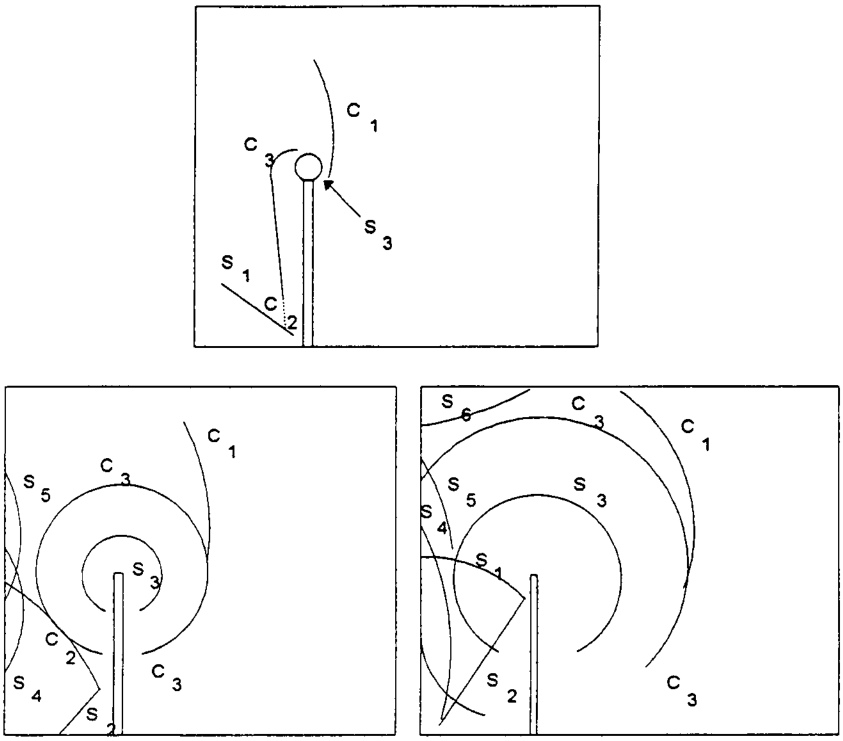

Figure 4-32. Interpretation of a photoelastic study of a compression wave scattering by a slit in terms of wavefront.

with the diffracted compression wave C_3, and a diffracted shear wave S_3 is also formed. As the incident compression wave interacts with the surfaces of the block head waves S_1 and S_6 are formed, and a similar wave S_2 is formed by the reflected compression wave. The two remaining shear waves, S_4 and S_5 were formed at the edges of the transducer which generated the main compression wave C_1. Figures 4-33a,b,c,d show the calculated wave fronts for a compression wave scattering on a slit at 4.8 μs, 5 μs, 6 μs and 8 μs, respectively. It is readily seen that the calculated wavefront picture is consistent with to the experimental results sketched in figure 4-32. These results show the excellent qualitative agreement of the numerical model with the physical phenomena of elastic wave

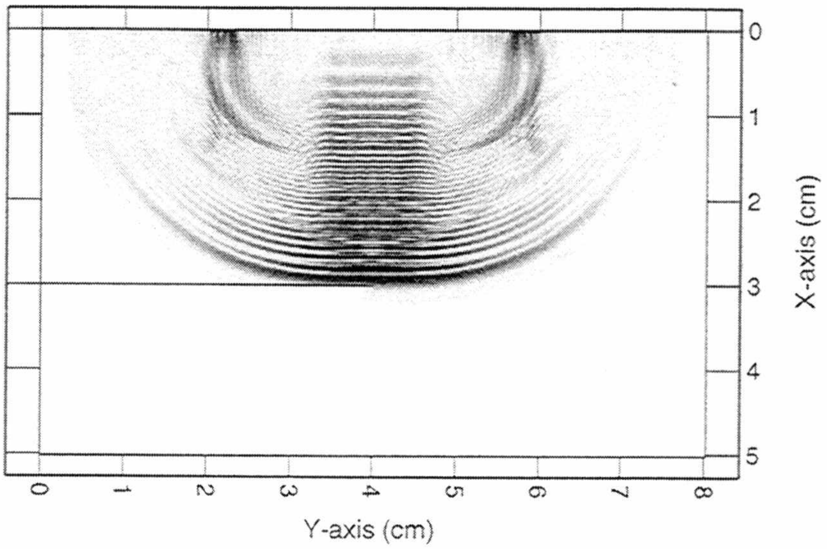

a)

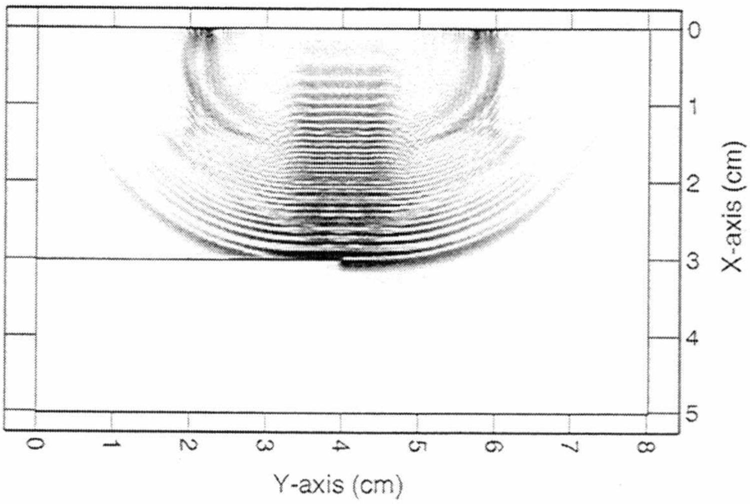

b)

Figure 4-33. Compression pulse incident on a slit. a) at t=4.8 μs; b) at t=5 μs; c) at t=6 μs; d) at t=8 μs.

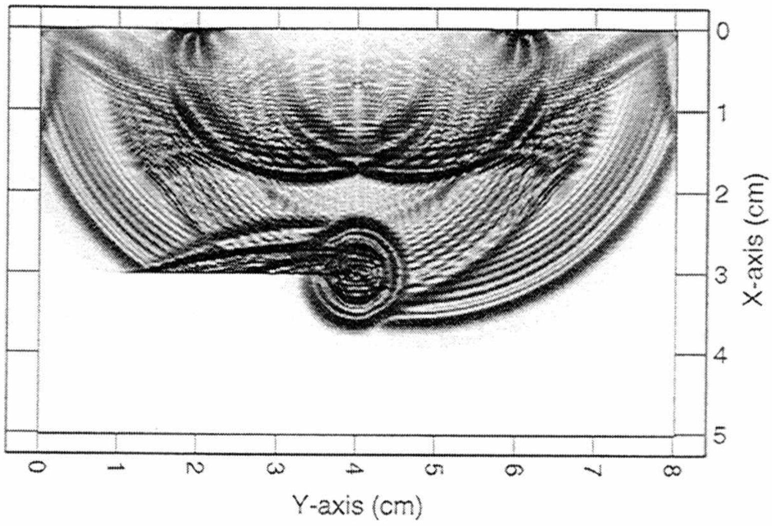

c)

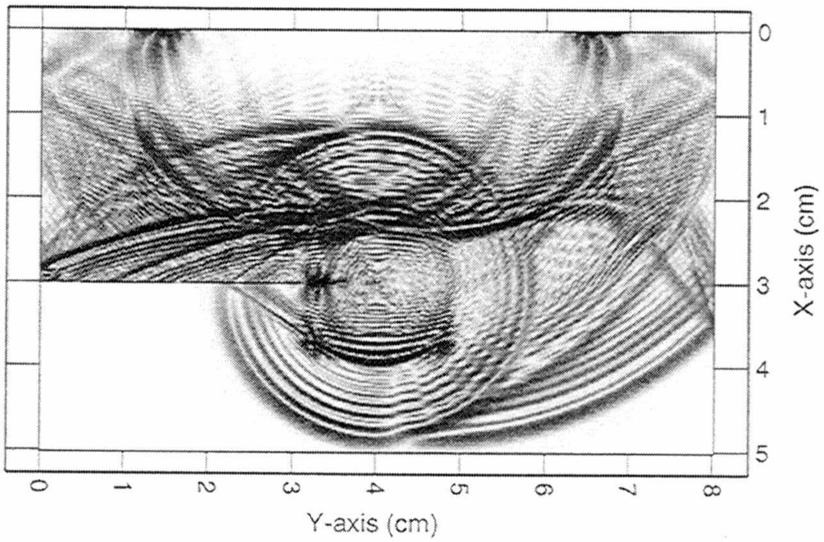

d)

Figure 4-33. Continued.

scattering from a crack tip. This results also show that the way the crack tip is modeled in the code represents properly the actual physical phenomena. Figures 4-34a,b show the scattering from the same crack tip, but of a transverse pulse, at time instants 11 μs and 12 μs, respectively. It is seen that despite of some similarities such as the presence of a transmitted and reflected waves, the picture of the wave fronts is very different and the diffracted wave somehow is whirling around the crack tip. The obvious difference of the scattering of the two elastic wave modes is due to their different physical nature - the particles' oscillations in the case of compression wave are along the velocity vector and in the same plane as the direction of propagation, and this is the reason for the compression wave to be called longitudinal. However, in the case of a shear pulse the particles' oscillations are perpendicular to the direction of propagation and for this reason the shear mode is called transverse.

4.3.1. Angular Distribution of the Amplitude of the Diffracted by a Crack Tip Compression Wave

Once established the qualitative agreement of the numerical results with the experiment, it is time to obtain some quantitative information. Harker [20] considered the reflection of an elastic wave from a surface breaking crack and calculated the reflection coefficients for cracks with different sizes and different incident angles of the elastic waves. More challenging problem, however, seemed to be the calculation of the angular distribution of the diffracted wave amplitude and comparison with the theoretical results, given in [113]. The basic assumptions in the theoretical study are as follows: **(i)** the incident ultrasonic waves are infinite plane waves; **(ii)** the crack is a semi-infinite plane;

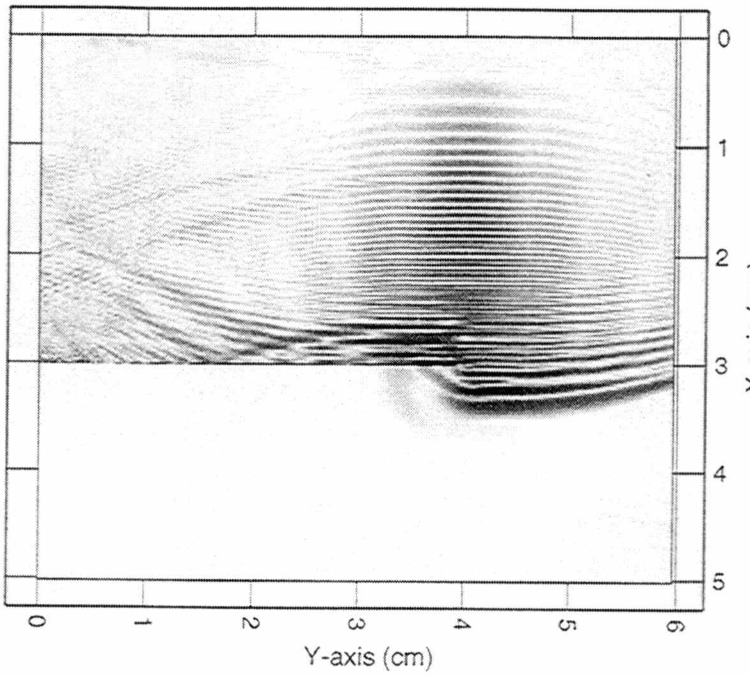

a)

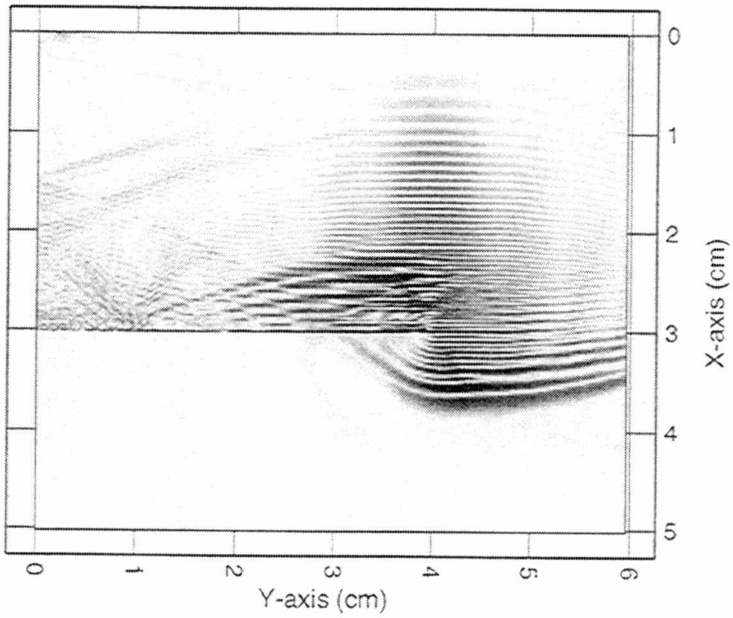

b)

Figure 4-34. Shear pulse incident to a slit. a) at t=11 μs; b) at t=12 μs.

and **(iii)** the crack faces are non-interacting, i.e. the crack remains open under the influence of the incident wave. As it was noted before, this is realistic for a smooth defect, provided that the defect width w obeys the condition: $d < w << \lambda$, where d is the displacement amplitude of the wave and λ is the ultrasonic wavelength. It is also assumed that the crack faces act as stress-free boundaries.

For incident compression waves diffracted as compression waves, the diffraction potential Φ is given by the equation

$$\Phi = G(\alpha,\beta)\sqrt{\frac{\lambda_p}{R}}e^{ik_pR}, \tag{4.30}$$

where R is the distance from the crack edge to the receiver; λ_p is the wavelength of the compression waves; k_p is the wavenumber of the compression wave; β is the angle of incidence; α is the angle of the diffracted wave (in a counterclockwise direction from the crack face) and

$$G(\alpha,\beta) = \frac{\psi_1 + \psi_2}{D}\exp\left\{\frac{i\pi}{4}\right\}\sin\left(\frac{\beta}{2}\right), \tag{4.31}$$

where

$$\psi_1 = \sin\left(\frac{\alpha}{2}\right)\left(2k_p^2\cos^2\beta - k_s^2\right)\left(2k_p^2\cos^2\alpha - k_s^2\right), \tag{4.32}$$

$$\psi_2 = 2k_p^3\cos\left(\frac{\beta}{2}\right)\cos(\beta)\sin(2\alpha)\sqrt{\left(k_s - k_p\cos\alpha\right)\left(k_s - k_p\cos\beta\right)} \tag{4.33}$$

$$D = 2\pi\left(k_s^2 - k_p^2\right)\left(\cos\alpha + \cos\beta\right)\left(k_R - k_p\cos\alpha\right)\left(k_R - k_p\cos\alpha\right)K^+(-k_p\cos\beta). \tag{4.34}$$

The in the above expressions k_R is the Rayleigh wavenumber, and the function K^+ is defined as

$$K^+(\sigma) = \exp\left\{-\frac{1}{\pi}\int_{k_p}^{k_s} \tan^{-1}\left[\frac{\sqrt{4x^2(x^2 - k_p^2)}\sqrt{4x^2(x^2 - k_s^2)}}{(2x^2 - k_s^2)^2}\right]\frac{dx}{x+\sigma}\right\}. \tag{4.35}$$

In [113] two cases are considered: one when $\alpha = \beta$ (symmetric case) and one when α varies and β is fixed (asymmetric case). For the asymmetric case, the expressions above show that the displacement amplitude falls to zero at angle $\alpha = 54^0$ when β is fixed and equal to 20^0. In 1991, in reference [122] this theoretical fact was verified by using the time-of-flight technique. In [122] the experimental measurements were carried out on an assembly as shown in figure 4-35. A steel block was machined so as to provide eighteen facets at different angles. A slit was spark eroded in the specimen with a length of 75 mm. The experiment uses 10 mm diameter 5 MHz compression wave probes as well as laser generated ultrasounds.

We attempted to verify the above theoretical result numerically, using the setup shown in figure 4-36. We modeled a steel material with Young modulus 200 GPa, Poisson ratio 0.3 and density $7.86\text{x}10^3$ kg/m^3. We used a step size 0.1 mm and time step size $\Delta t = 0.01$ μs. The slit had a length $d = 7$ cm. We used pulse with center frequency 5 MHz for this calculation and initiated a compression pulse as shown in figure 4-37 at an angle of 70 degrees. The detectors were situated along a circle with a radius 2 cm. Figure

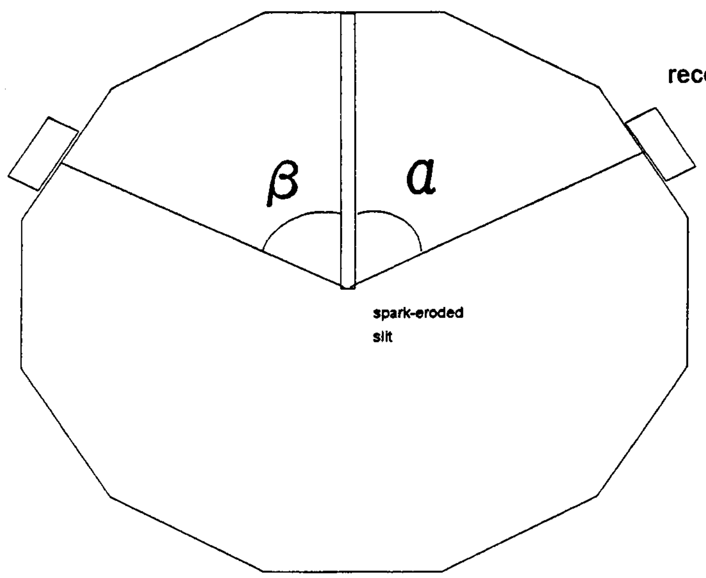

Figure 4-35. The experimental assembly for crack tip diffraction measurements by time-of-flight technique.

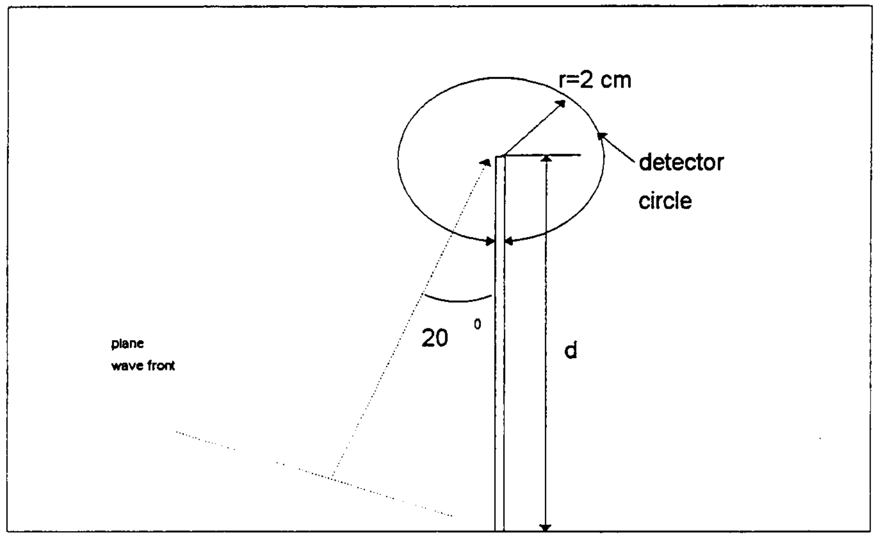

Figure 4-36. The geometry setup for numerical calculations of the crack tip diffraction.

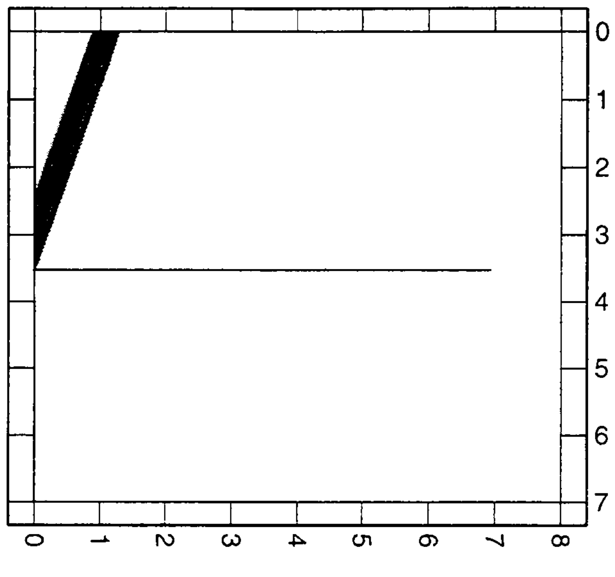

Figure 4-37. Initial wave at t=0 s for study of the amplitude angular distribution.

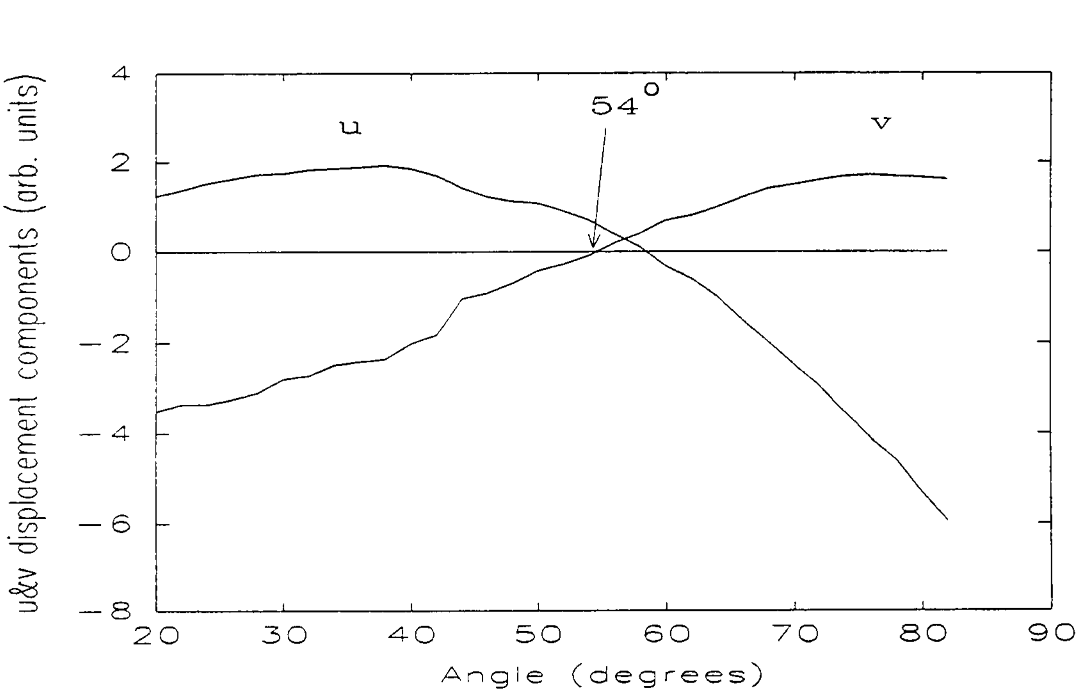

Figure 4-38. The u- and v-displacement components as a function of the diffraction angle.

4-38 shows the u- and v-displacement components as a function of the angle for the range from 20^0 to 82^0. The data were collected at t = 15.03 μs. It is seen that while the v-component goes to zero at the required angle of 54 degrees, the u-component goes to zero at angle 58 degrees. The reason for that is in the way we initiate the wave, which gives a small distortion in the generated signal for angles different than 0, 90 and 45 degrees. The same effect has been observed in [122]. However, the differences which arise in the finite difference calculations are much smaller than in the actual experiment due to the infinitesimal width of the modeled crack. The corresponding results for the magnitude of the total displacement are shown in figure 4-39. It is seen that the finite difference calculations are in very good agreement with the theoretical results. The amplitude at 54^0 is not zero due to the distortion described above, but this is in complete agreement with the finite difference calculations made earlier [20].

The results in this section show that there are distinct optimal angles for crack sizing with the time-of-flight technique. As multiprobe arrays of transmitters and receivers are often used with this method, it is generally possible to take advantage of these angles to increase the reliability of the inspection.

4.4. Modeling of Lamb Waves Propagation and STFT and CWT Application for Lamb modes Detection

Lamb waves are the fundamental propagating modes in plates. The establishment and the solution of the transcendental equations which describe the normal modes are discussed in Appendix B.

One of the advantages of Lamb waves for nondestructive testing work is that they

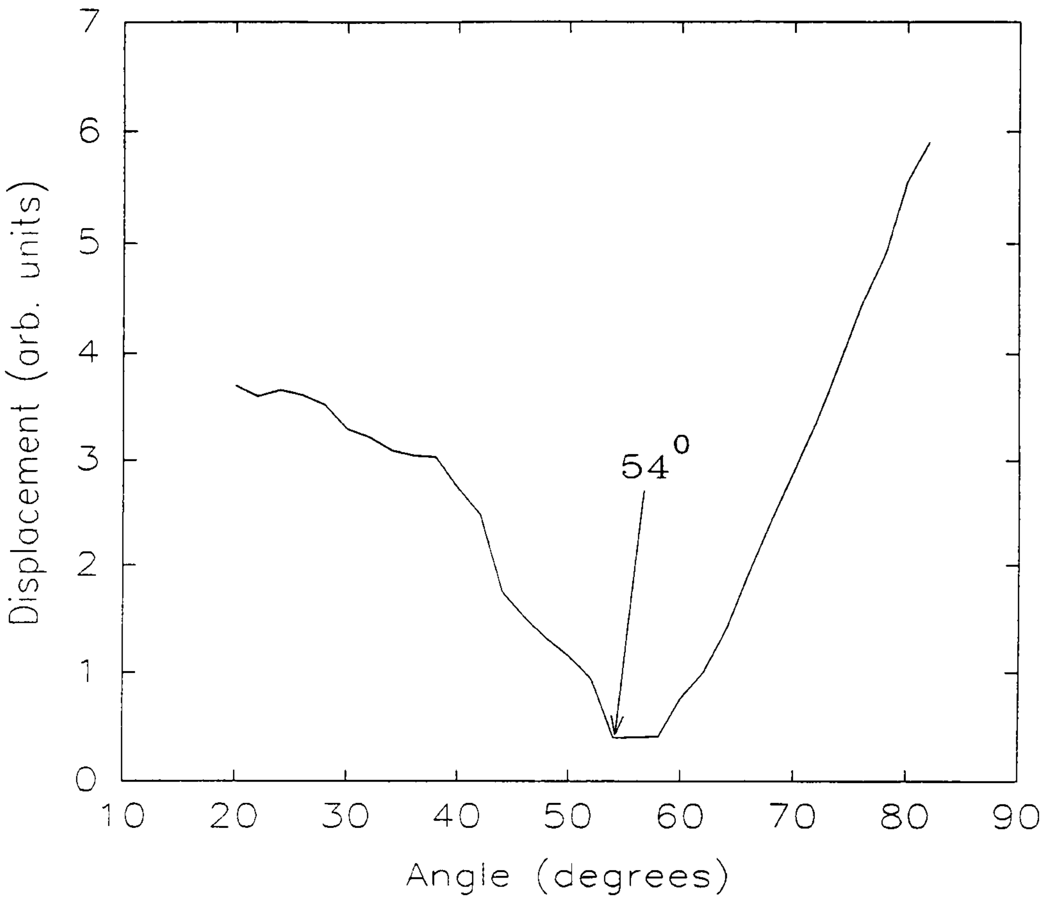

Figure 4-39. Angular distribution of the amplitude of the diffracted from a crack tip compression wave.

can conveniently be generated in metals by noncontacting electromagnetic transducers. By using coils to induce eddy currents in the presence of strong magnetic fields perpendicular or parallel to the metal surface, stresses are generated normal or tangential to the metal.

The different Lamb wave modes are highly dispersive which makes them difficult for analysis. That makes the modeling study an important feature for application of the Lamb waves for nondestructive study.

Finite difference methods have been applied for the study of Lamb wave propagation and scattering by Harker [84]. However, he used a wide sinusoidal signals with well developed frequencies, which gave him the opportunity to separate the different Lamb modes.

We attempted to simulate the Lamb waves propagation by using the pulse excitation technique developed in this work in order to apply the STFT and CWT technique for the analysis of the dispersion and separability of the different Lamb wave modes and to verify the ability of these transforms to achieve these goals. The computational setup is shown in figure 4-40. The coupled detectors from the top and the

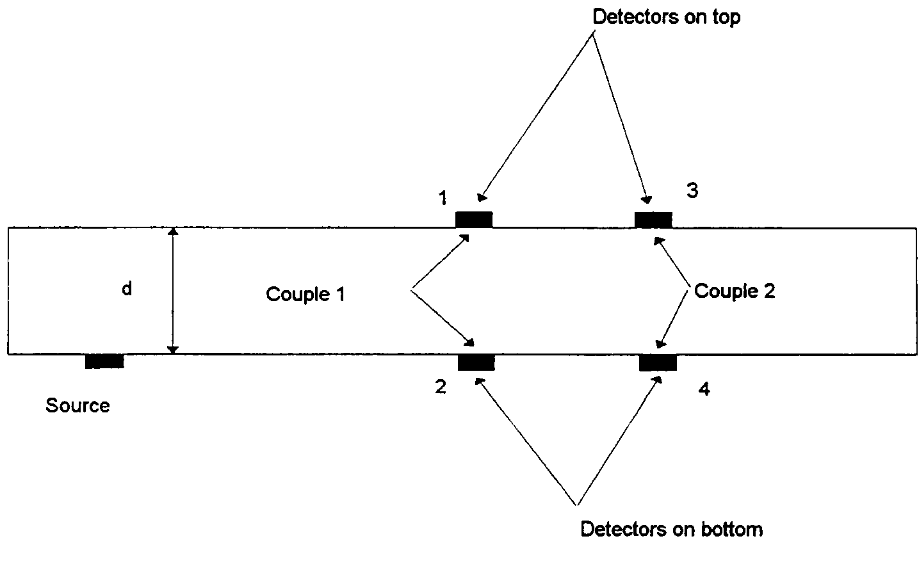

Figure 4-40. The computational setup for the Lamb waves calculations.

bottom facilitate the separation between the symmetric and antisymmetric Lamb modes. In fact, using the fundamental properties of the two independently existing modes, one can establish the relation

$$u_s = \frac{u_1 + u_2}{2}; \; u_a = \frac{u_1 - u_2}{2}; \; v_s = \frac{v_1 - v_2}{2}; \; v_a = \frac{v_1 + v_2}{2}, \tag{4.36}$$

where u_s ,v_s stand for the symmetric u- and v- displacement components at the position of the detector couple 1, respectively, and u_a and v_a stand for the antisymmetric components at the same position, u_i , v_i are the displacement components at detector 1 and 2 . Similar expressions hold for the position of the detector couple 2. For the computations we use steel material with Young modulus E = 200 GPa, Poisson ratio $\nu = 0.34$, and density

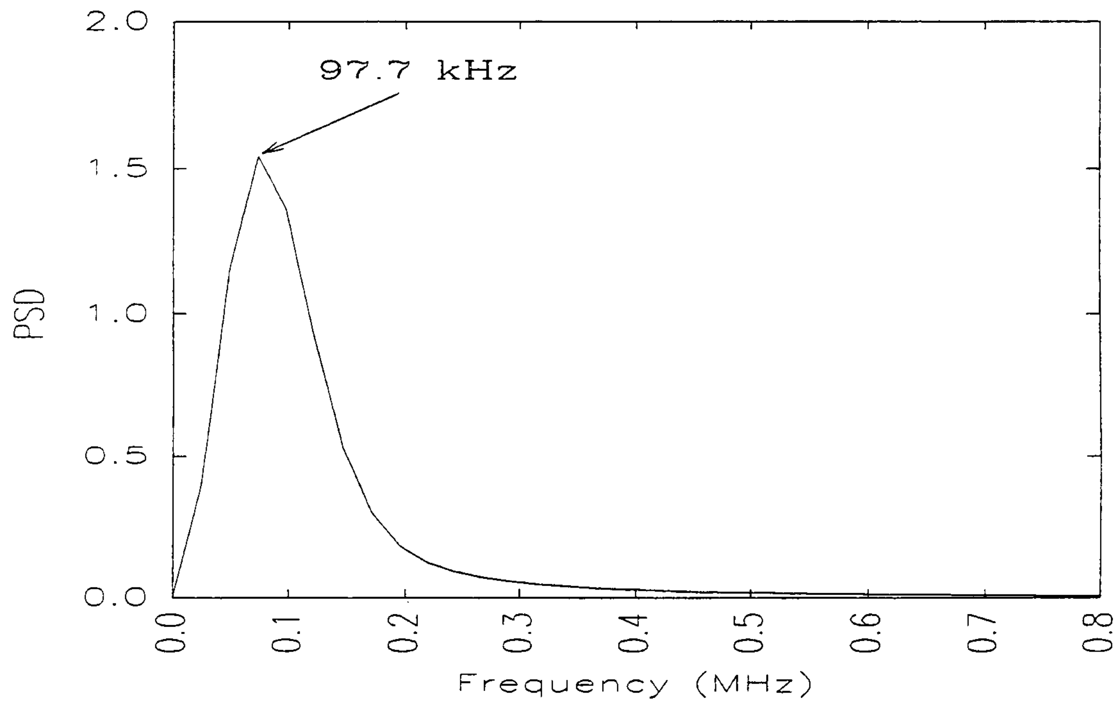

Figure 4-41. The PSD of the source for the Lamb waves calculations.

$\rho = 7.86 \times 10^3$ kg/m^3. The thickness of the plate is d = 8 mm, and the PSD of the source signal is shown in figure 4-41 with a peak frequency at about 100 kHz. The applied stresses are tangential and therefore the resulting signal represents a shear wave. The distance from the source to the first couple of detectors is 5 cm, a distance that is expected to be enough for the Lamb waves to be formed. The distance between the two detector couples is 1 cm.

Figures 4-42a,b show the snapshots of developing Lamb waves at 2 μs and 8 μs after the initiation of the pulse. Note the waves reflecting from the right boundary as it is shown in figure 4-42b. Figure 4-43 shows the displacement detected at the position of the detector 1 before the separation of the symmetric from antisymmetric modes. Figures 4-44 and 4-45 show the symmetric and antisymmetric displacements at the position of the detector couple 1. Figures 4-46, 4-47 show the corresponding PSD's for the symmetric and antisymmetric displacement signals from figures 4-44 and 4-45, respectively. As it is seen in fig. 4-46, the frequency spectrum of the symmetric modes is divided into two parts. The first part, according to the results given in Appendix B, corresponds to a frequency range where only zeroth Lamb modes exist. The second part corresponds to the range where first and higher symmetric Lamb modes exist. Figure 4-47 shows that he PSD of the antisymmetric modes and it is seen that the spectrum is concentrated in one part only, which spans exactly over the range where there is a "gap" in the spectrum of the symmetric modes. A comparison with the results in Appendix B shows that in this frequency range the zeroth and the first antisymmetric Lamb modes exist. The two frequency areas from figure 4-46 are clearly visible in figures 4-48a,b, where it is shown

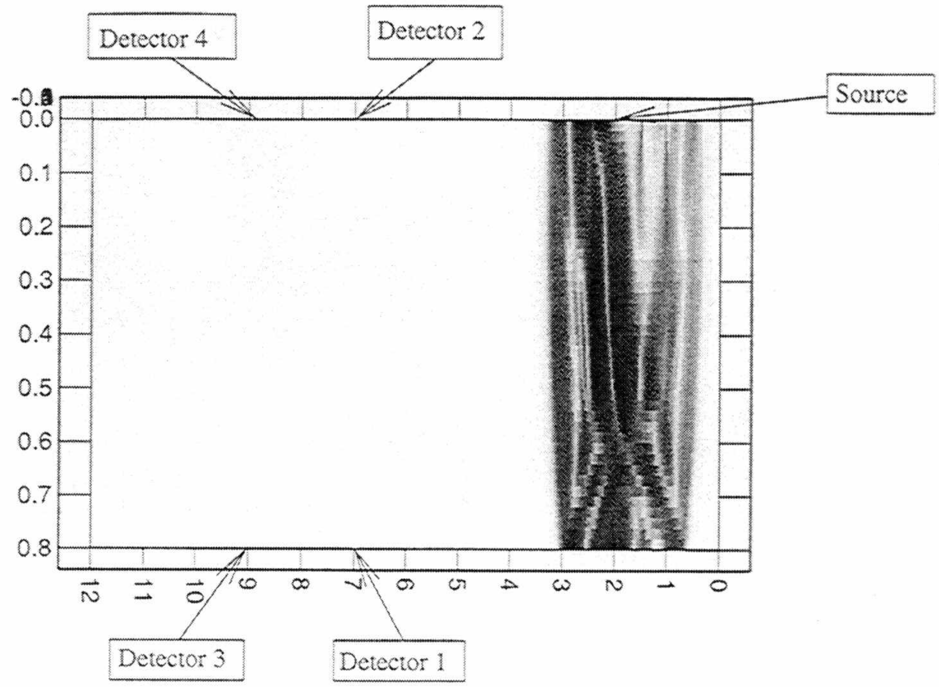

a)

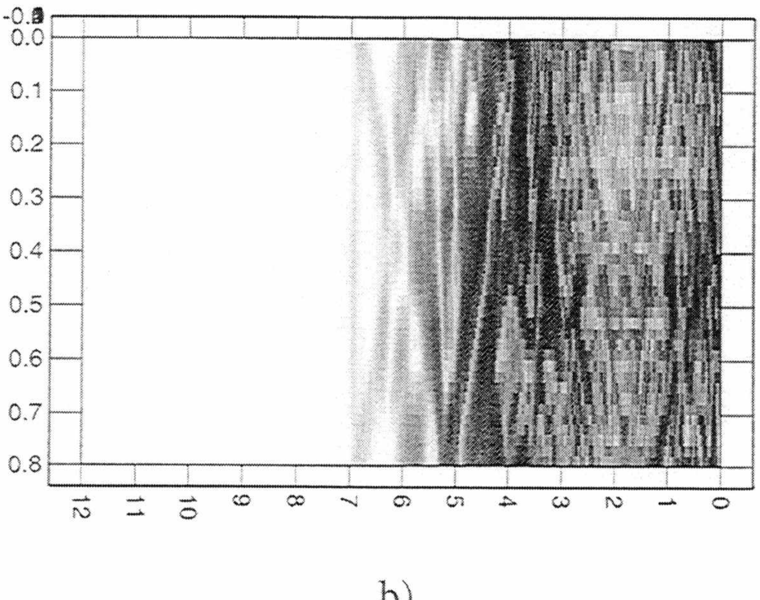

b)

Figure 4-42. A snapshot of the developing Lamb waves. a) at t=3 μs; b) at t=8 μs.

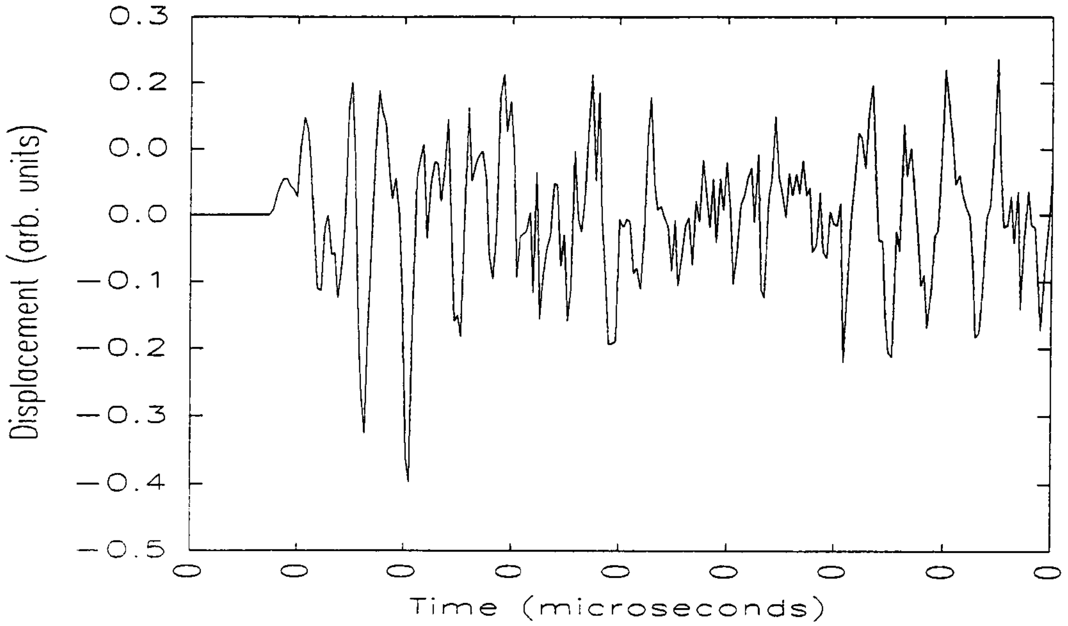

Figure 4-43. The displacement at the position of detector 1.

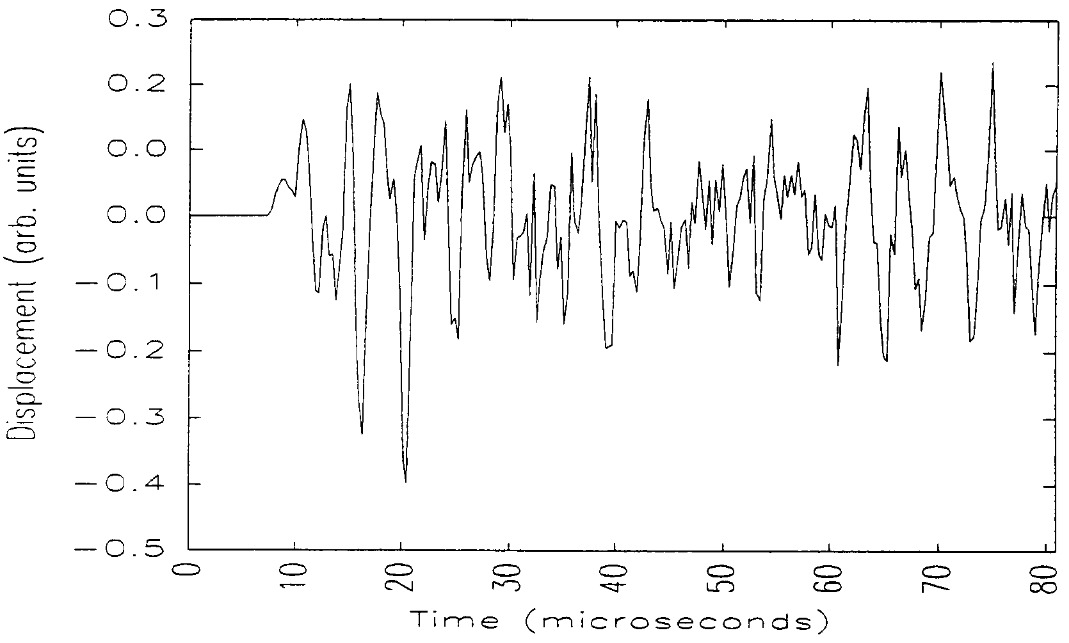

Figure 4-44. The symmetric Lamb modes' signal detected at detector 1.

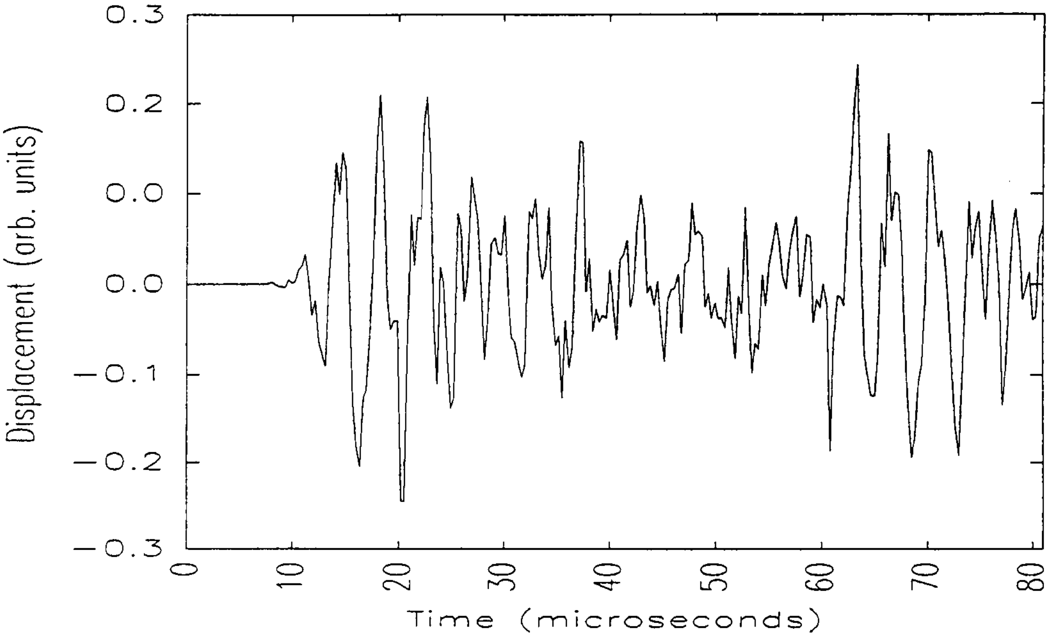

Figure 4-45. The antisymmetric lamb modes' signal detected at detector 1.

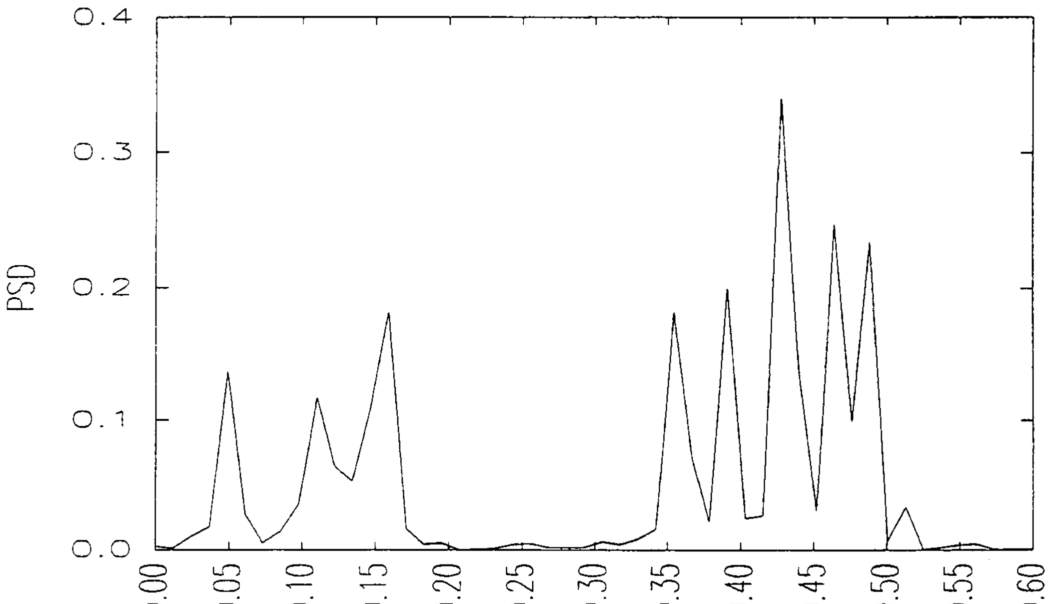

Figure 4-46. The PSD of the symmetric modes' signal at detector 1.

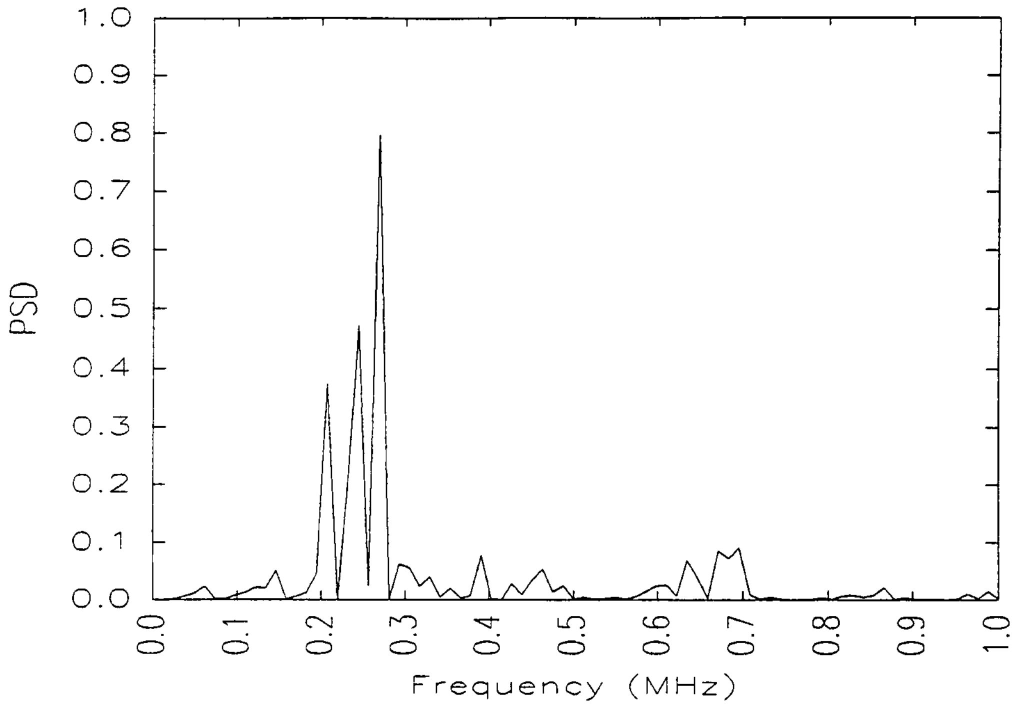

Figure 4-47. The PSD of the antisymmetric modes' signal at detector 1.

the Gabor STFT of the symmetric signal at the positions of detector couples 1 and 2, respectively. The idea of the dispersion analysis is to compare the time of appearance of the corresponding frequency peaks in both STFT, and knowing the distance between the detectors, to obtain the corresponding velocities. Knowing the theoretical curves of the Lamb modes' dispersion (for this material, when $\nu = 0.34$, they are given in [123]) we can attempt to recognize the dispersion law of each mode (symmetric, in this case). Unfortunately, this simple procedure was not possible to be completed entirely. The two frequency areas, as shown in figures 4-48a,b, correspond to values of the dimensionless parameter $\alpha = \dfrac{2\pi fd}{2c_S}$ (where c_s denotes the shear velocity) in the range from 0.35 to 1.31

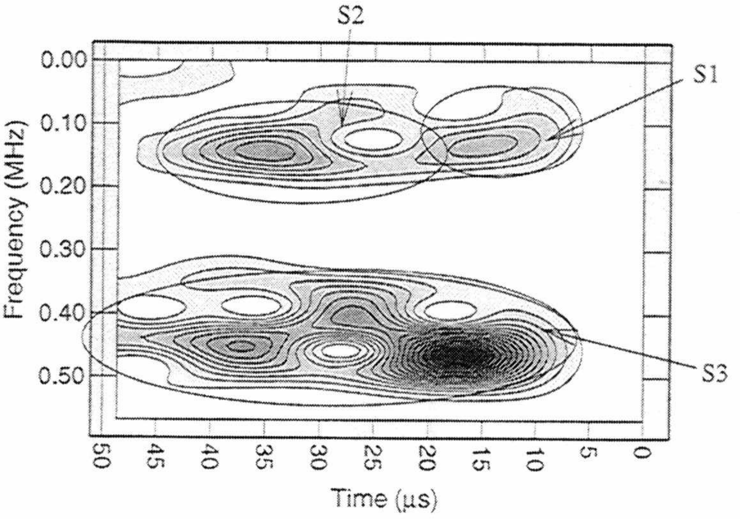

a)

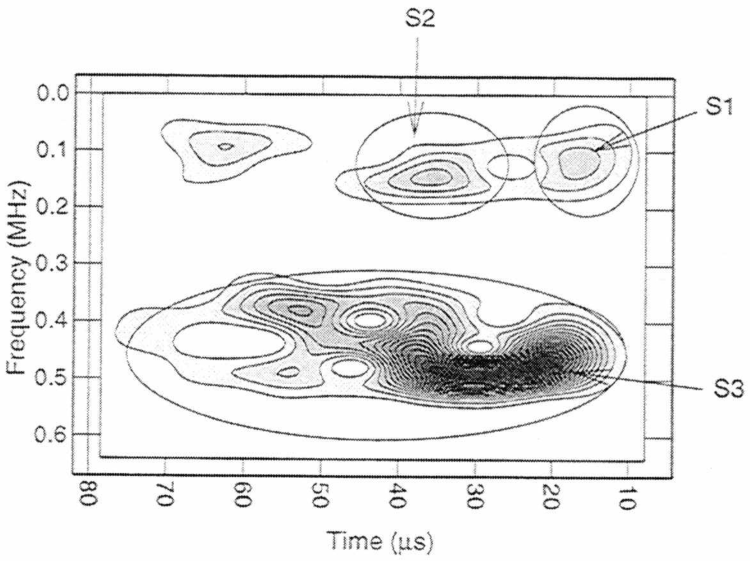

b)

Figure 4-48. The Gabor STFT for the symmetric modes. a) at detector 1; b) at detector 3.

(the lower frequency area), and between 3.72 and 4.53 (for the higher frequency area). As noted above, the first area corresponds to the range of values for α where only zeroth symmetric and antisymmetric modes exist, and is marked as S1 + S2 in figures 4-48a,b, while the second area, marked as S3 in figures 4-48a,b, corresponds to a frequency range where one finds up to the second symmetric Lamb modes. The two marked fields S1 and S2 correspond to the two zeroth symmetric Lamb modes, one of which (the field S2) arises from a signal reflected from the boundary. For the field S3 the analysis of the numerical data corresponding to figures 4-48a,b shows that there is a number of peaks which indicates the superposition of several higher symmetric modes and their reflections from the boundaries. From the analysis above, it is concluded that the STFT is able to distinguish two separate frequency regions. In the low frequency region it is able to separate the zeroth mode from its reflections. However, in the high frequency region one cannot distinguish between the higher modes and their reflections. The comparison between STFTs' at the position of detectors couple 1 and 2 shows the complicated dispersion going on in the system with a very high speed since there is apparent deformation in the observed frequency peaks. Similar conclusion is true for the antisymmetric Lamb modes.

The action of the CWT is to classify the signal into a set of scales at each time frame. Figure 4-49a corresponds to a situation where there are wide peaks (which show at intermediate and large scales) exhibiting highly fluctuating components at their tips, which are represented by the high transform densities at short scales. Upon propagation of the signal to the detector 3, one can determine the filtering of the signal in two scale regions,

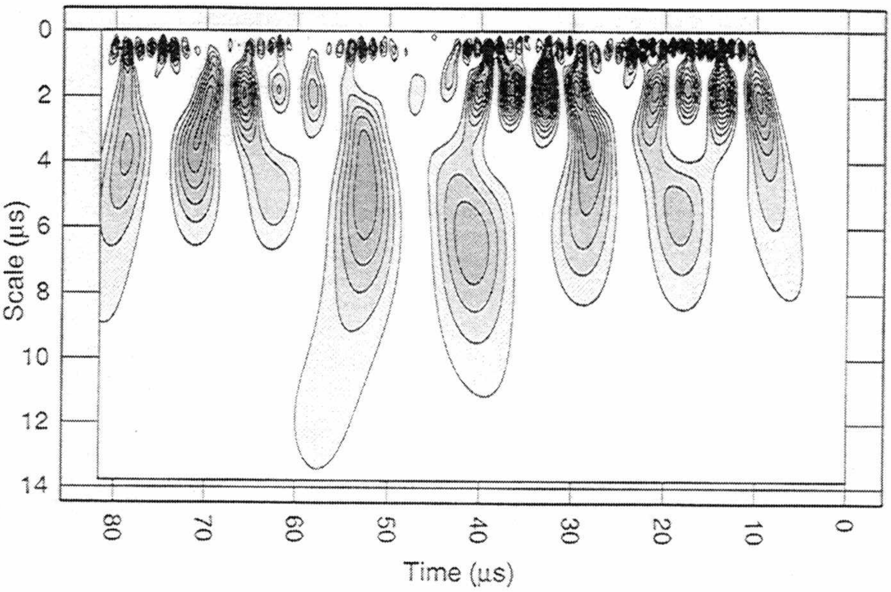

a)

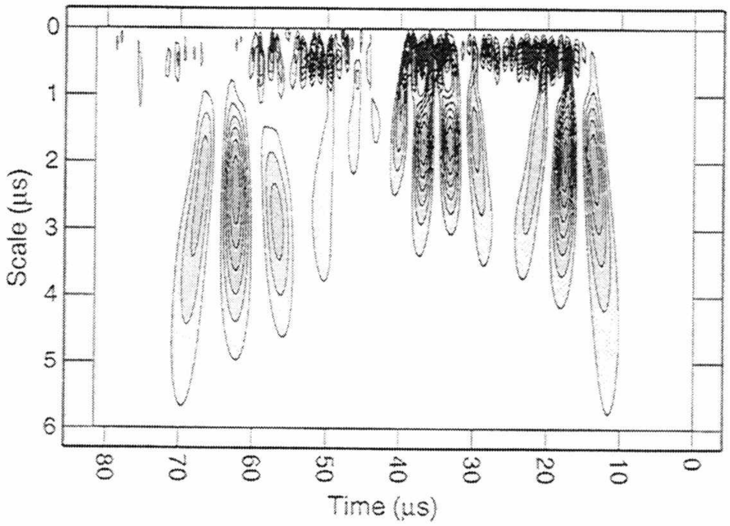

b)

Figure 4-49. The CWT of the symmetric modes. a) at detector 1; b) at detector 3.

the low and the high scale regions. This finding is in agreement with the known fact that waveguides act as band-pass filters.

Similar conclusions are held in the case of the antisymmetric Lamb modes in this case.

The results in this section show that:

1). The model is able to simulate the propagation of Lamb waves in conditions which are physically necessary for the appearance of Lamb waves, that is, in layers (or plates) with free boundaries with thickness comparable with the wavelength. The generation of Lamb waves is made in a very natural manner with surface sources developed in part 4.1. With the application of this pulse source a set of symmetric and antisymmetric Lamb modes are generated, including the reflection of these modes from the free boundaries.

2). The application of STFT and CWT to the generated by the model signals shows that both transforms are suitable tools for signal analysis in this case.

4.5. Characterization of Anisotropic Elastic Constants with Application of Ultrasonic Measurements

Ultrasonic techniques have been used recently as a nondestructive evaluation tool for quality control of Al/SiC composites during manufacturing processes [124, 125], and for measuring anisotropic elastic properties of these composites [110, 126-130]. The elastic constants may be determined either by a series of mechanical tests or by ultrasonic wave propagation characteristics. Ultrasonic methods offer some advantage because they can be used nondestructively with small samples. The magnitude of the velocity of an ultrasonic wave propagating in a material is related to the density and one or more stiffness components c_{IJ} * of the material. Therefore, measurements of wave velocity along a sufficient number of directions will enable all the stiffness components to be determined.

In [110] is provided a detailed description of the ultrasonic method for measurements of the anisotropic elastic stiffness constants of SiC_P reinforced aluminum (Al/SiC_P) composites and the results are compared with mechanical tests' measurements and microstructural analysis. It is assumed that the composite material is orthotropic and all nine stiffness components are determined using through-transmission, immersion testing techniques, where the elastic wave propagation in anisotropic materials is used to measure the effective stiffness constants in the long wavelength limit of these materials. The propagation characteristics of plane waves in an anisotropic solid can be found by rewriting the Christoffel equation (2.26) as

$$\left[k^2\Gamma_{ik} - \rho\omega^2\delta_{ik}\right]\left[V_k\right] = 0, \tag{4.36}$$

where $\Gamma_{ik} = c_{ijkl}n_j n_l$ are the Christoffel stiffnesses, ρ is the density, and $\vec{n}$ is the unit vector normal to the plane wave. A dispersion relation is then obtained by setting the characteristic determinant of (4.36) equal to zero

$$\det\left|k^2\Gamma_{ik} - \rho\omega^2\delta_{ik}\right| = 0. \tag{4.37}$$

---

* Here and below we use the abbreviated subscripts as they have been introduced in Chapter 2 (see Table 2-3).

At fixed ω, (4.37) defines a surface in k-space that gives k as a function of its direction $\vec{n}$, which is called the *wave vector surface*. Assuming that $k \neq 0$ and dividing (4.37) by k^2, we obtain

$$\det\left|\Gamma_{ik} - \rho V^2 \delta_{ik}\right| = 0, \qquad (4.38)$$

where $V = \frac{\omega}{k}$ is the phase wave velocity. The equation (4.38) is employed in [110] to relate the elastic stiffness constants to the ultrasonic speed subject to the measurement. For this purpose, using the abbreviated subscripts (Table 2-3, Chapter 2) we have

$$\Gamma_{11} = n_1^2 c_{11} + n_2^2 c_{66} + n_3^2 c_{55}, \qquad (4.39)$$

$$\Gamma_{22} = n_1^2 c_{66} + n_2^2 c_{22} + n_3^2 c_{44}, \qquad (4.40)$$

$$\Gamma_{33} = n_1^2 c_{55} + n_2^2 c_{44} + n_3^2 c_{33}, \qquad (4.41)$$

$$\Gamma_{12} = n_1 n_2 (c_{12} + c_{66}), \qquad (4.42)$$

$$\Gamma_{13} = n_1 n_3 (c_{13} + c_{55}), \qquad (4.43)$$

$$\Gamma_{23} = n_2 n_3 (c_{23} + c_{44}). \qquad (4.44)$$

Equation (4.38) is a cubic in ρV^2, it has three roots, giving rise to three different velocities of propagation. Therefore, for a given direction of propagation defined by n_i, there will be three waves with mutually perpendicular displacement vectors propagating with different phase velocities. In general, these waves will not be pure longitudinal or pure transverse, as in the case of an isotropic medium, but one will be quasilongitudinal (QL), and the other two will be quasitransverse (QT). However, for certain special directions of propagation (usually directions of symmetry), one is pure longitudinal (L), and the other two are pure transverse (T). Since three distinct wave modes can propagate in anisotropic media, a single incident wave of the L type may cause transmission of three different modes.

Another aspect of wave propagation, which is of great importance in anisotropic materials, is the propagation of energy. Because the energy flux vector usually does not coincide with the wave normal, $\vec{n}$, the magnitude and direction of the phase velocity and energy (or group) velocity are generally different [1, 7-10]. The energy velocity, V_g, is greater than or equal to the phase velocity, V, and they are related by the following equation [1, 7-10]

$$V_g \cos\varphi = V, \tag{4.45}$$

where φ is the angle between the energy velocity and $\vec{n}$. This phenomenon of the deviation of energy from the direction of wave propagation in anisotropic solids has many important consequences that must be taken into account in the experimental studies of ultrasonic wave speed for material characterization purposes [110].

Orthotropic materials have three mutually perpendicular symmetry directions. The three symmetry axes were defined for metal matrix composites as follows [110]: x_1 as the extrusion direction, x_2 as the in-plane transverse direction, and x_3 as the out-of-plane direction. The x_1 - x_2 plane was designated as the extrusion plane. The elastic stiffness matrix is given than by

$$C = \begin{bmatrix} c_{11} & c_{12} & c_{13} & 0 & 0 & 0 \\ c_{12} & c_{22} & c_{23} & 0 & 0 & 0 \\ c_{13} & c_{23} & c_{33} & 0 & 0 & 0 \\ 0 & 0 & 0 & c_{44} & 0 & 0 \\ 0 & 0 & 0 & 0 & c_{55} & 0 \\ 0 & 0 & 0 & 0 & 0 & c_{66} \end{bmatrix}. \tag{4.46}$$

One may note that (4.46) has the same non-zero components as in the case of isotropic material (2.34). However, the isotropy condition $c_{12} = c_{11} - 2c_{44}$ is not satisfied for orthotropy material, as it is stated in Chapter 2.

In order to determine the elastic stiffness constants, in [110] it was necessary to make at least nine independent velocities (especially phase velocity) measurements. It can be shown [110] that the diagonal stiffness components c_{ii} can be determined by measuring velocities of appropriate waves propagating along symmetry directions. The off-diagonal components c_{ij}, $i \neq j$, however, have to be determined from the velocities of either QL or QT waves propagating at an angle against the symmetry axes in the planes of symmetry. The through transmission, immersion method used in [110] is shown in figure 4-50, and is similar to those used in other works [110].

In [110] it is noted, that when the elastic stiffness constants of a composite material are determined by the ultrasonic velocities, one is concerned with wave dispersion effects, although in many measurements they can be neglected. To test the validity of wave dispersion effects, a new method for the measurement of the frequency dependence of the wave velocity is presented in next subsection.

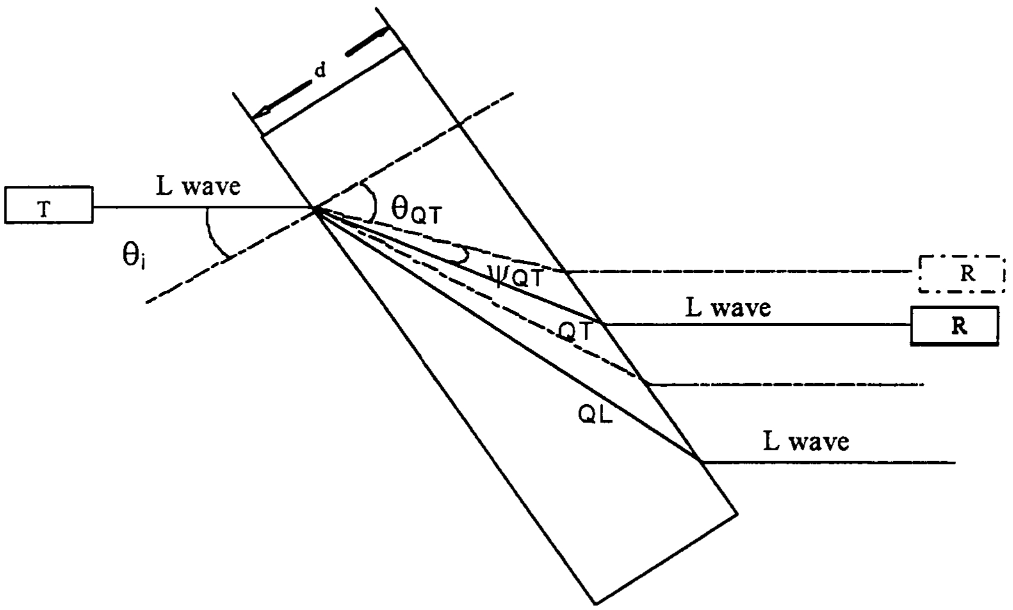

Figure 4-50. Oblique incidence of longitudinal wave in an orthotropic plate submerged in water.

4.5.1. Time-Frequency Measurements of the Dispersion Law

In this section we describe a time-frequency technique for the measurement of the dispersion law. This method based on the Gabor STFT was applied to a data set provided by Dr. D. Hsu fro Iowa State University [131]. The measurement has been carried out with the experimental assembly in fig. 4-50 with $\theta_i = 0°$ and distance between the transmitter T and receiver R equal to 6.2 cm. The sample is SiC/SiC composite material with thickness 3.9 mm . The sampling rate was 100 MHz. The data set contained 512 data points, measured in units volts. The data time series of the signal through water without a sample is shown in figure 4-51. The transducer used has 0.25" diameter and center frequency 5 MHz. The gate length* was equal to 5.11 μsec. The time series of the signal with the sample immersed is shown in figure 4-52. For the calculations of the longitudinal velocity through the sample we use the equation [110]

$$V = \frac{1}{\frac{1}{V_W} - \frac{\Delta t}{d}}, \tag{4.47}$$

where V_W is the velocity of the wave through the water. It is assumed that $V_W = 1490$ m/s. Figures 4-53 and 4-54 show FFT of the signal without and with a sample immersed, respectively. It is seen that the PSD of the through-sample signal has change significantly. The same picture is observed in figures 4-55 and 4-56, which show the Gabor STFT of the signal without and with the sample, respectively. To obtain the dispersion we use the time-frequency data available from the STFT modulus, when the moment of the arrival of the signal is assumed to be the peak in the STFT modulus along each line parallel to the time axis with constant frequency. To minimize the roundoff error produced by the numerical procedure of STFT, we assume that the elastic wave velocity magnitude in water given above is true for the center frequency where the signal through water only has absolute maximum. Figure 4-57 shows the ratio of the obtained velocity to the reference point ($V_0 = 1490$ m/s) as a function of frequency for the signal through water only. We use further the obtained values for the water velocity together with equation (4.47) to calculate the through-sample wave velocity for each frequency. The

* i.e. the time interval during which the data has been recorded.

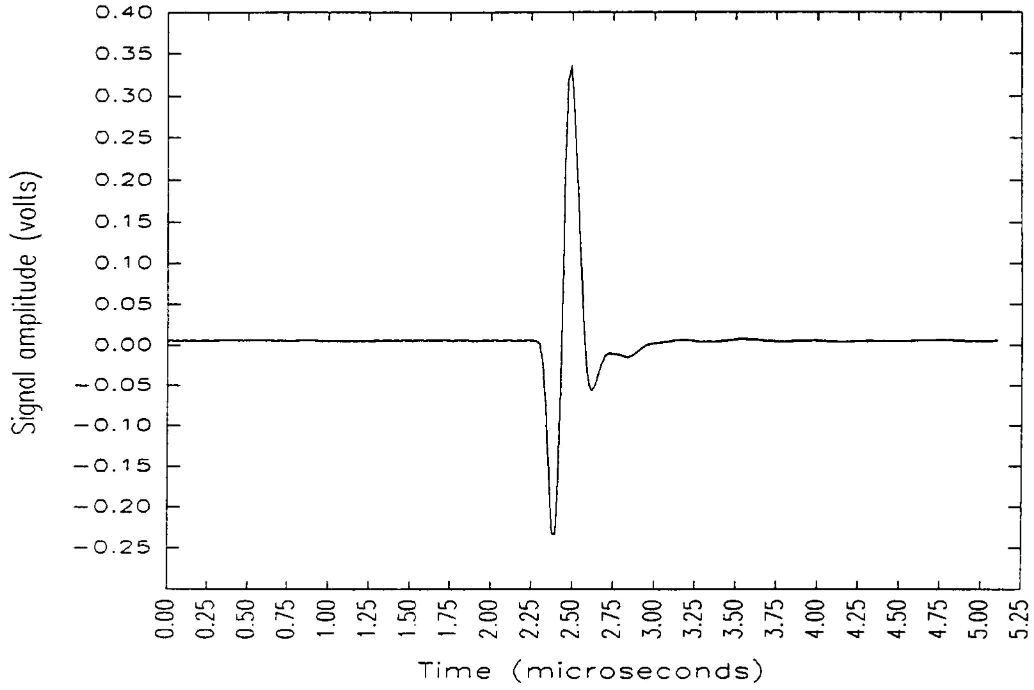

Figure 4-51. Time domain of the transmitted signal through 6.2 cm of water.

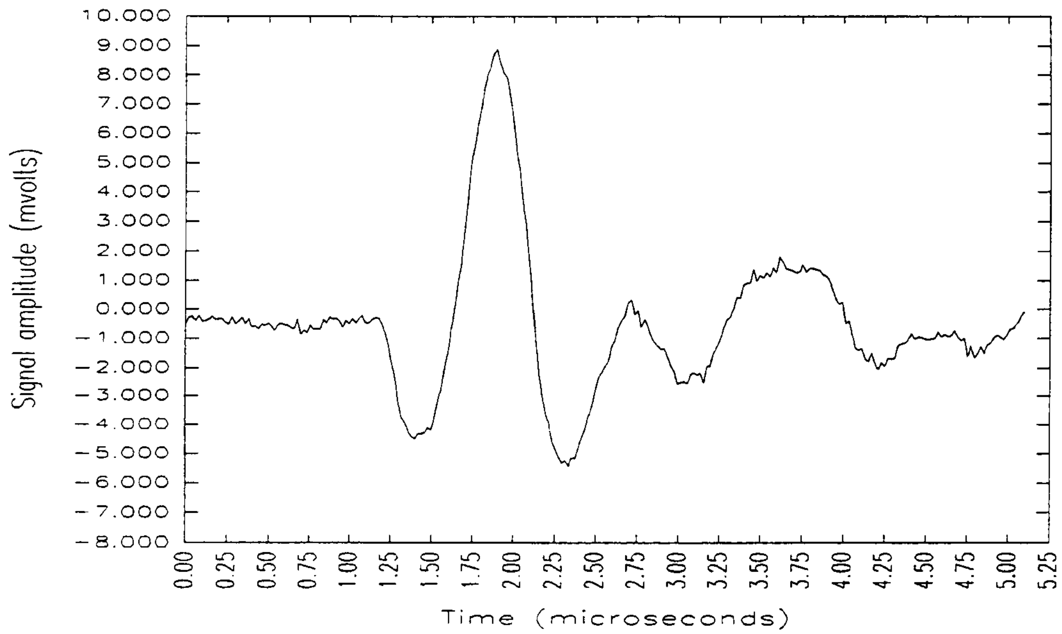

Figure 4-52. Time domain of the transmitted through SiC/SiC, 3.9 mm thick sample immersed in water.

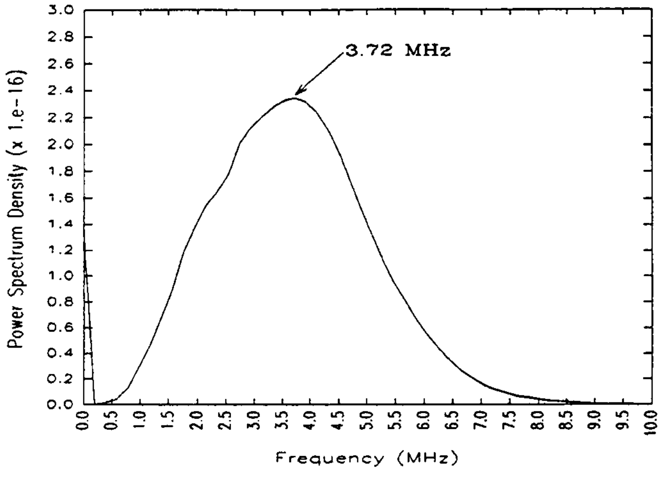

Figure 4-53. Power Spectrum Density of the transmitted signal through water.

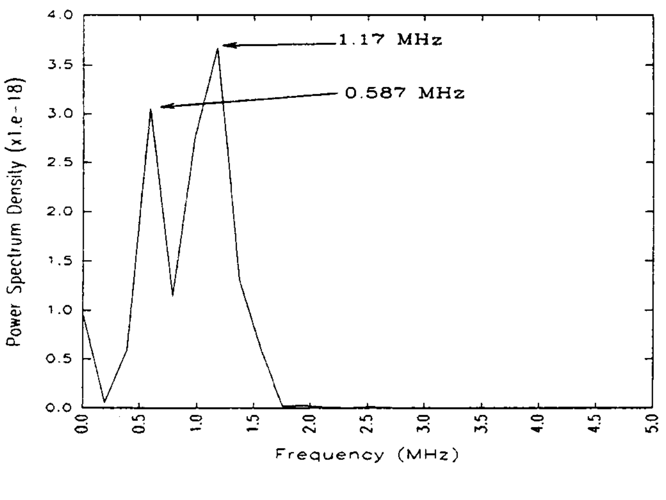

Figure 4-54. PSD of the transmitted through SiC/SiC, 3.9 mm thick sample immersed in water.

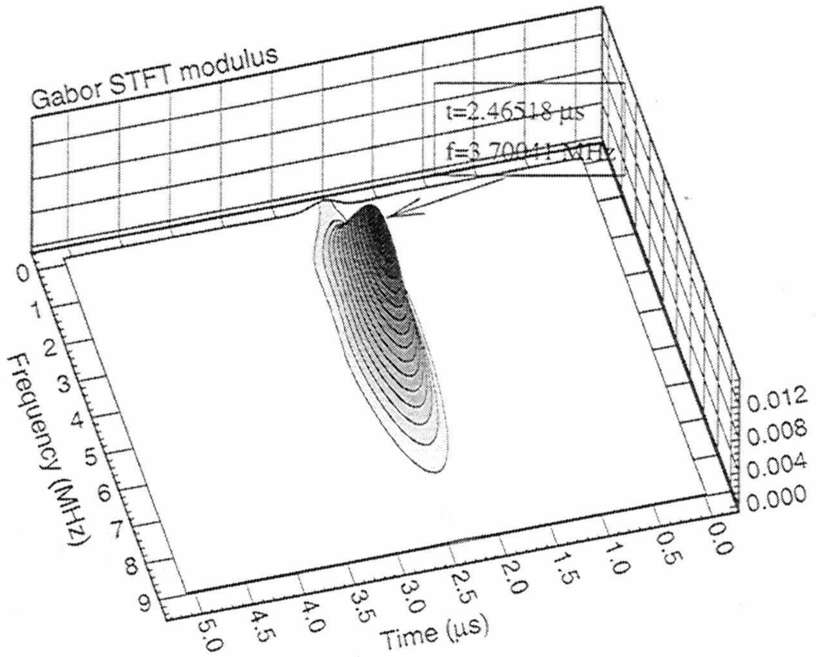

Figure 4-55. The Gabor STFT of the signal through water without sample.

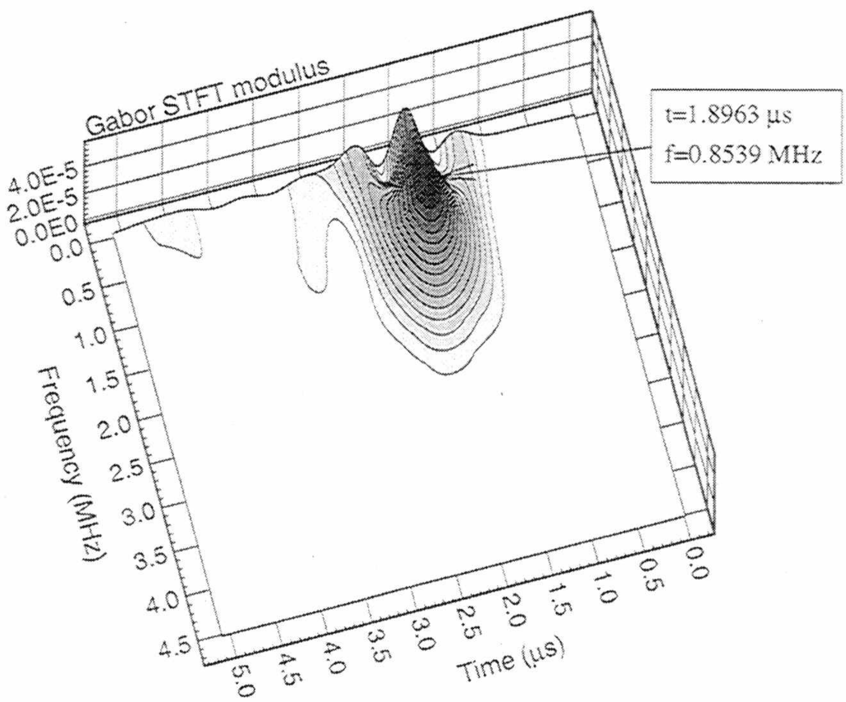

Figure 4-56. The Gabor STFT of the signal through the sample.

ratio of the obtained speeds to the reference speed in water as a function of time are shown in figure 4-58. It is seen in figure 4-57 that the assumption made in the previous section, about the lack of dispersion of the longitudinal wave in water is confirmed. The small variance of the velocity (under 3%) shown in the figure is partly due to the roundoff error of the numerical realization of the STFT since the sampling rate is very high, compared with the range of frequencies to be analyzed, and can be ignored. Figure 4-58 shows that the dispersion of the longitudinal wave through the sample is within the range of 14%. However, for the frequency range below 2.6 MHz the dispersion is about 3% and can be ignored for the same reason as in the water. When the frequency increases (above 3 MHz), the wave velocity in the sample decreases. The dispersion law can provide an important information for the structure of the material and as it is seen above STFT can provide the dispersion information simultaneously with the velocity magnitude data and for the same frequency range covered by the analysis, which is in particular very important when elastic wave velocity is measured for the purpose to evaluate the mechanical properties of the material [110].

Figures 4-59 and 4-60 show the CWT of the signal through-water only and when the sample is immersed in the water, respectively. It is seen that CWT of the signal is subdivided in three parts, separated from one another. A comparison with the signal in the time domain (figures 4-51, 4-52) show that the three peaks in CWT correspond to the three extrema of the signal in time domain. Therefore, CWT provides an ability to look "inside" the structure of the signal corresponding to each signal peak (either negative or positive) in time domain. It is seen that each part of CWT is shifted to the longer scale

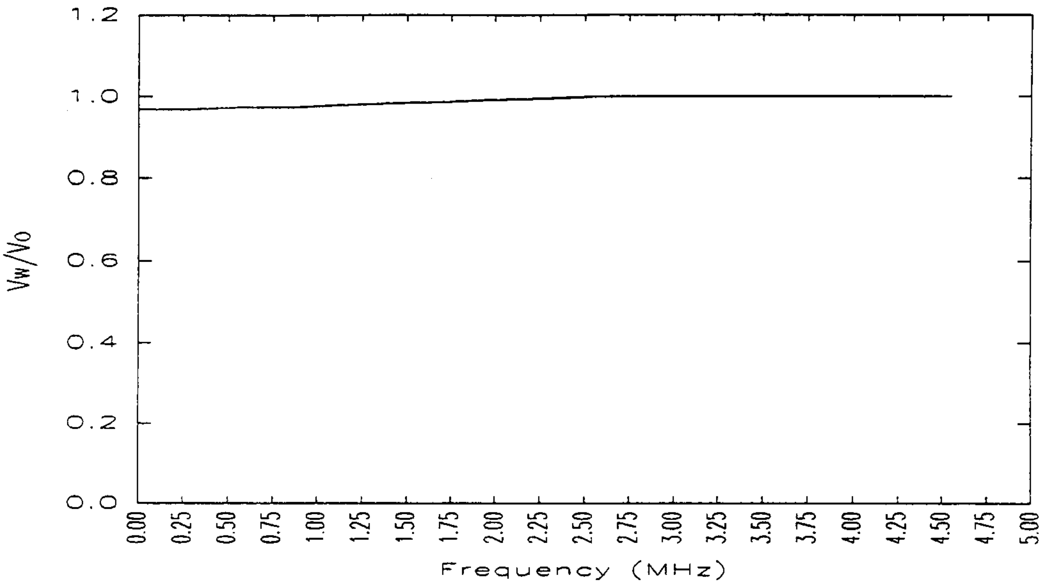

Figure 4-57. The dispersion curve of the longitudinal wave through water only.

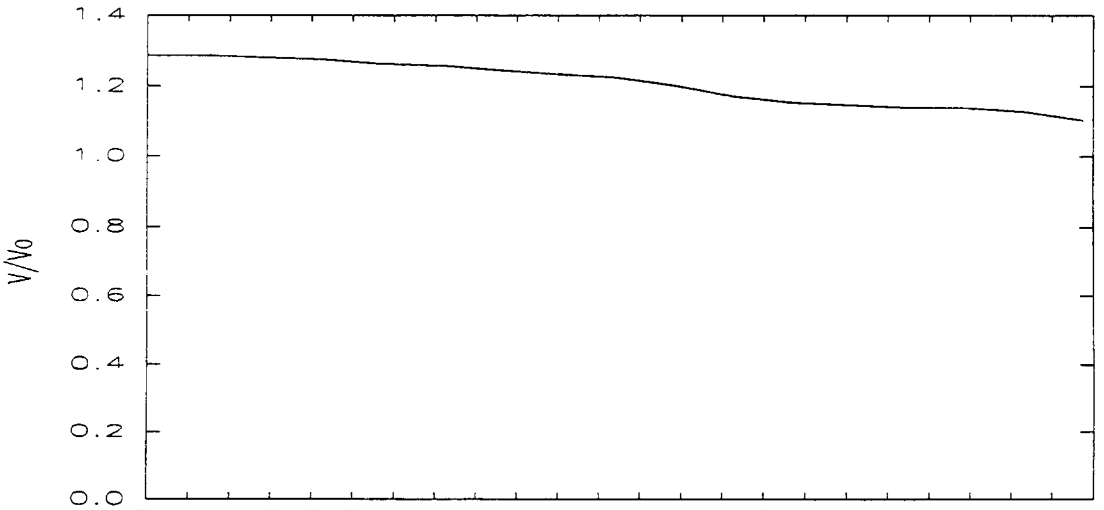

Figure 4-58. The dispersion curve for the through-sample velocity.

(scale is marked as a in the figures) when the sample is immersed in comparison with the through-water-only case. This fact apparently corresponds to a shift of the signal to lower frequencies, as it is seen from the Gabor STFT in figures 4-55, 4-56, respectively. Also, similarly to the STFT modulus, the magnitude of CWT decreases significantly when the sample is immersed. The decrement is about 381 times in the highest magnitudes, which corresponds to the decrement in the signal magnitude in time domain. Further, the three peaks in CWT appear equidistantly in time in water with a distance 0.12 μs, while when the sample is immersed, the distance between the three peaks increases in length (0.45 μs). This indicates the widening of the signal through-sample itself, which is an indication for the appearance of a slight dispersion in the through-sample signal. Indeed, using the expression (4.47) and the times provided from CWT for the different peaks, we obtain the same magnitude of dispersion (~15%) for the range of the entire signal. However, while it is clear that longer scales correspond to lower frequencies, the quantitative frequency estimate is not that straight forward and apparently requires further study. These interpretation problems appear to be partly because CWT decomposes the signal itself and in principle differs from the mathematical concept of frequency and Fourier transform. However, since CWT preserves the instantaneous power and as it is shown in Chapter 2, is able to almost eliminate the possible white noise in the signal, one can use these features for filtering white noises in signals and for study of the signal attenuation, an important feature that STFT due to the fact it does not preserves the instantaneous signal power, does not possesses.

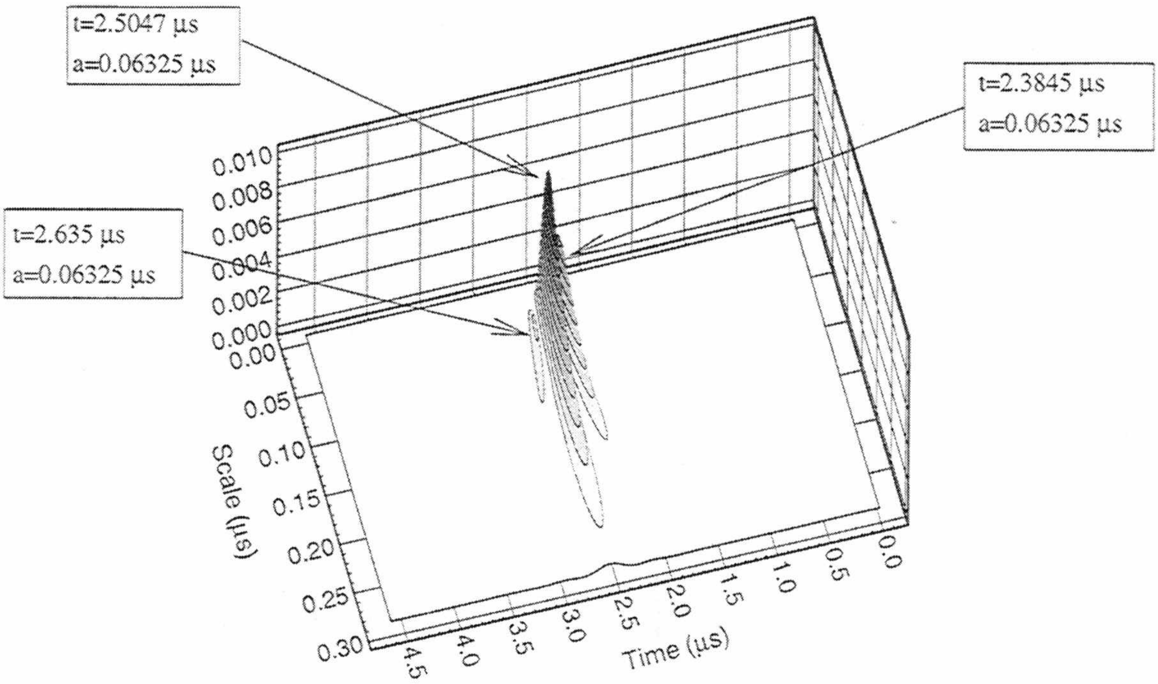

Figure 4-59. CWT of the through-water signal without sample.

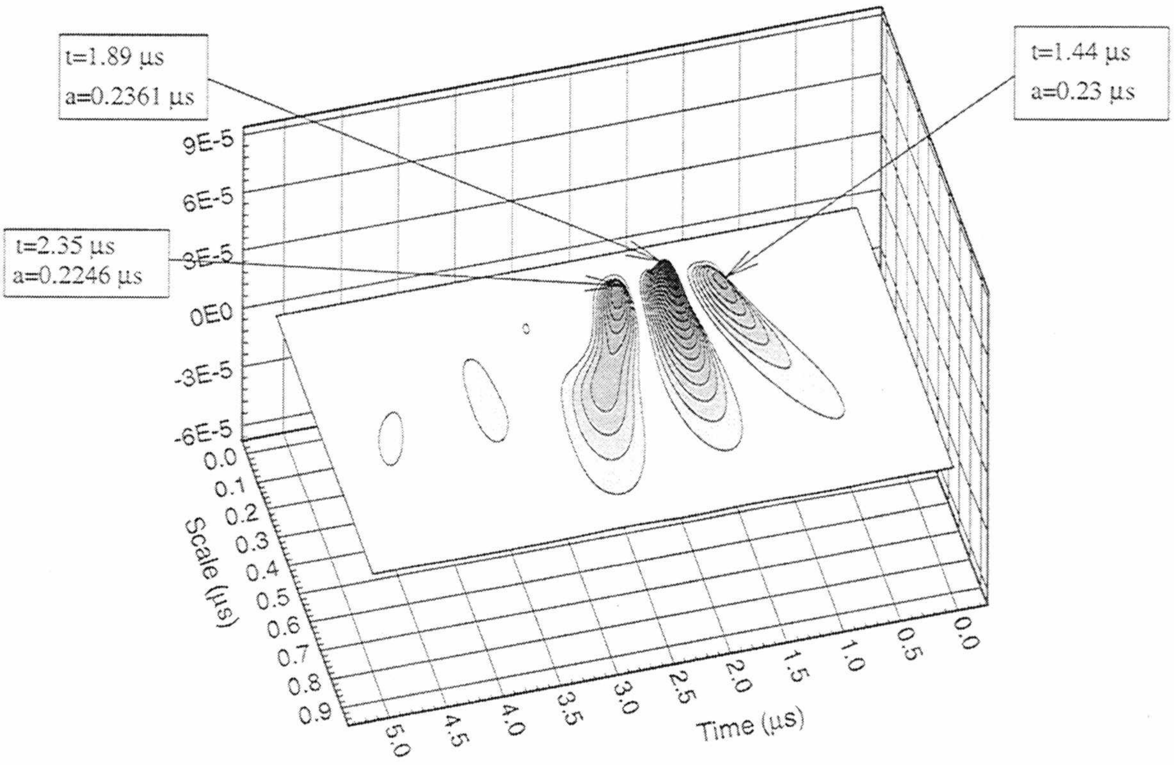

Figure 4-60. CWT of the through-sample signal.

CHAPTER 5

Originality of the Present Work, Conclusions and Future Developments

In this chapter we enlist the original developments in the present work, make conclusions based on the presented results, and give some ideas for a future research on the topics of these dissertation.

5.1. Originality of the Present Work

The following original developments have been made in the present dissertation:

1. Based on the finite difference approach, an algorithm was developed for solution of the wave equations in two dimensional Cartesian geometry. Based on that algorithm, a computer code **JUNA** was developed for computation of the solution, representing propagating waves in the medium. Artificial nodes were employed in the model in order to implement a first order approximation of the traction free boundary conditions, which represent the free of stress body surfaces. The stability of the calculations was controlled by a stability test, presented in Chapter 3. The present numerical scheme was tested up to 30,000 time steps and does not give rise to any instability.

2. A model for representing infinitesimally thin cracks and delaminations in the medium, described in Chapter 3, was developed and implemented in the code **JUNA**. This model consists of insertion of free boundaries at the position of the flaw, which are infinitesimally close to each other. In particular, a scheme was developed for coupling the edges of the modeled flaws to keep the body solid based on the geometrical splitting of the amplitudes in the nodes prior to the flaw edges. This scheme was also checked during the process of obtaining the results in Chapter 4, and does not cause any instability.

3. Analytical expressions for three-dimensional wavelet pulse, representing an exact analytical solution of the wave equations, were developed. Based on these expressions, two algorithms for elastic wave excitations in the medium were developed and implemented in the code **JUNA**. Both plane wave excitation and surface source waves excitation of compression and shear wave modes developed in the code **JUNA**, were analyzed in detail. In particular the surface source amplitude angular distributions for compression and shear modes excitation were analyzed, and the results were shown to be in excellent agreement with the theoretical predictions and independent calculations by another authors.

4. A set of dimensionless variables was introduced in the model in an effort to keep the roundoff error small and to provide an opportunity for computation in a wide range of parameter values.

5. The Gabor STFT was applied for analysis of the signal generated due to tangential stresses on the face parallel to the free surface of a solid crack and allowed us to verify the analytically predicted peaks in the frequency distribution of the displacement component tangential to the crack face, which were found to be a function of the ratio d/a, where d is the crack depth and a is the length of the crack.

6. The angular distribution of the amplitudes of a compression elastic wave diffracted from a crack tip was calculated and compared with the analytical predictions and experimental measurements of this angular distribution, and an excellent agreement of the calculated results with the analytical predictions and calculated by other authors results was shown.

7. A method was developed based on the Gabor STFT and CWT for calculations of the dependence of the elastic wave velocity by the frequency and wave mode characterization in two cases: on the generated by **JUNA** Lamb waves and on experimental data from through-sample transmission ultrasonic measurements, when the sample is a SiC/SiC composite material. The results show the feasibility of the application of these transforms for dispersion law characterization.

5.2. Conclusions

The results presented in this work lead us to the following conclusions:

1. The developed computer code **JUNA** represents an accurate numerical treatment of the ultrasonic wave propagation in flawed medium with finite sizes. The algorithm used in **JUNA** is stable and provides a quantitative analysis of different elastic wave modes and their scattering by material flaws. The first order approximation for the boundaries and material flaws used in the numerical model is sufficient to represent the zero stress truncation error is kept small by using appropriate time and space step sizes.

2. The methods developed in this dissertation for elastic wave excitation represent realistic pulses used in practice and provide an opportunity for analysis of complicated practical cases where ultrasonic waves are employed.

3. The set of dimensionless variables, implemented in **JUNA** allows for computations in a wide range of values of system parameters, which significantly extends the applicability of the code.

4. The algorithm for parallel-to-the-surface crack represents adequately material flaws inside the body.

5. The analysis of the results obtained for the diffraction of compression waves from a crack is in very good quantitative and qualitative agreement with the theoretically predicted results and the ones calculated by other authors [20].

6. The application of the method based on the Gabor STFT for dispersion law characterization by using ultrasonic data from transmission measurements, shows that the Gabor STFT can provide the dispersion information simultaneously with the velocity magnitude data and for the same frequency range covered by the analysis, which is of interest in the interpretation of ultrasonic measurements of the mechanical properties of materials.

7. Both the application of the Gabor STFT and CWT, appear to be appropriate tools for the analysis of propagation of Lamb waves in thin plates as well as for flaw detection.

5.3. Recommendations for Future Research

Three main general features are open for a future research - **(i)** - an implementation of interface conditions in the code, **(ii)** - implementation of modeling in cylindrical geometry and **(iii)** - an extension of the code to anisotropic materials and three dimensional geometries. In regard to the first mentioned desired development, we used the formulas in part 3.3 for modeling the interface conditions, and also attempted to model the intersection of the interface with the free boundary in order to model a system, with a finite size and in particular to develop a model to study Rayleigh and Lamb waves propagation through an interface. For this purpose we used first order approximations to calculate the displacements at points A, B, and C as they are shown in figure 3-4. Unfortunately, the scheme used was unstable, which indicates that most likely the first order approximation used is not enough and should be increased. What exactly should be done is a matter of additional research. Regarding the implementation of wave propagation in cylindrical structures we already have developed the necessary mathematical background in section 3.6.

The extension of the code for anisotropy media seems to be straightforward and does not cause difficulties, since the difficulties that arise are mainly of a technical nature, in particular in programming the obtained expressions. The same is true for the extension of the code in three dimensions.

In conclusion, much of the efforts in underlying research in elastic wave scattering has, in recent years, been directed towards comparing very detailed experimental measurements of scattering from idealized (although not necessarily trivial) artificial defects with theoretical results on the same system. The emphasis is now shifting towards more general problems, especially in modeling of complete systems. A committee of the American Society of Mechanical Engineering surveyed the fields of elastic waves and quantitative nondestructive evaluation [132] and concluded that further progress depends critically on large-scale computations. Areas of particular interest include wave propagation in inhomogeneous and anisotropic media, scattering from rough and semi-transparent cracks, and the detection and identification of defects. I would like to think that the present work is a positive effort in this direction.

LIST OF REFERENCES

1. Auld B. A. Acoustic Fields and Waves in Solids. Vol. 1 and 2, R. E. Krieger Publ. Company, Malabar, Florida (1990).

2. Morse P. M., H. Feshbach. Methods of Theoretical Physics. McCraw-Hill (1953).

3. Graff K.F. Wave Motion in Elastic Solids. Ohio State University Press, (1975).

4. Tiersen H. F. *J. Math. Phys.* **6**, pp.779-787 (1965).

5. Brown W. F. Jr. *J. Appl. Phys.* **36**, pp. 994-1000 (1965).

6. Estman D. E. *Phys. Rev.*, **148**, pp. 530-542 (1966).

7. Landau L. D., E. M. Lifshitz. Theory of Elasticity. Pergamon Press, New York (1970).

8. Nye J. F. Physical Properties of Crystals. Oxford, England (1964).

9. Misgrave M. J. P. Crystal Acoustics. Holden-Day, San Francisko (1970).

10. Chou P. C., N. J. Pagano. Elastic Tensors, Dyadics and Engineering Approaches. van Nostrand, New York (1967).

11. Nadeau G. Introduction of Elasticity. Pergamon Press, New York (1970).

12. Bond W. L. "The Mathematics of the Physical Properties of Crystals". BSTJ, **22** (1943).

13. Achenbach J.D. Wave Propagation in Elastic Solids. Elsevier Pub.Co., NY, 1975.

14. Sternberg E. *Archs ration Mech. Analysis.* **6**, (1960).

15. Sternberg E. *Archs ration Mech. Analysis.* **34**, (1960).

16. Sternberg E. Gintin. *Proc. 4th U.S. Congress of Applied Mechanics.* p. 793 (1962).

17. Sokolnokoff I.S. Mathematical Theory of Elasticity. New York, McGraw-Hill Book Co., Inc. (1968).

18. Wheeler L. T., E. Sternberg. *Arch. ration. Mech. and Analysis*, **31**, p. 51 (1968).

19. Brekhovsikh L. M. Waves in Layered Media. Academic Press (1980).

20. Harker A.H. Elastic Waves in Solids with Applications to Nondestructive Testing of Pipelines. Adam Hilger (1988).

21. Kupradze V.D. in "*Dynamical Problems in Elasticity, Progress in Solid Mechanics*", v. III, I.N. Sneddon and R. Hill, edts., North-Holland (1963).

22. Pao Y-H., V. Varatharajulu. *J. Acoust. Soc. Am.* **59**, p.1361 (1976).

23. Rayleigh, Lord. *Proc. London Math. Soc.*, **4**, p.357 (1873).

24. Tan T.H. *Appl. Sci. Res.* , **31**, p. 363 (1975).

25. Becker M. The Principles and Applications of Variational Methods, MIT Press, Cambridge, MA 1964.

26. Pao Y-H., C. C. Mow. Diffraction of Elastic Waves and Dynamic Stress Concentration., Adam Hilger/Crane Russak (1973).

27. Neubauer W.G. *J. Acoust. Soc. Am.*, **35**, p.279 (1963).

28. Johnson J. *J. Acoust. Soc. Am.*, **59**, p. 1319 (1976).

29. Haines N.F., D.B. Laugston. *J. Acoust. Soc. Am.*, **67**, p. 1443 (1980).

30. Beckmann P., A. Spizzichino. The Scattering of Electromagnetic Waves from Rough Surfaces., Macmillan (1963).

31. Trorey A.W. *Geophysics*, **35**, p. 762 (1970).

32. Achenbach J.D., A.K. Gautesen, H. McMacken. Ray Methods for Waves in Elastic Solids - with Applications to Scattering by Cracks, Pitman, London (1982).

33. Coffey J.M., R.K. Chapman. *Nucl. Energy*, **22**, p. 319 (1983).

34. Chapman R.K., J.M. Coffey. in "*Review of Progress in Quantitative NDE*", v. 3, D.O. Thompson and D.E. Chimenti, edts., Plenum Press (1984).

35. Banaugh R.P., W. Goldsmith. *J. Acoust. Soc. Am.*, **35**, p. 159 (1963).

36. Burton A.J., G.F. Miller. *Proc. Roy. Soc. London,* **A323**, p. 201 (1971).

37. Reut Z. *J. Sound and Vibr.*, **103**, p. 297 (1985).

38. Tan T.H. *Appl. Sci. Res.* , **32**, p. 97 (1976).

39. Tan T.H. *Appl. Sci. Res.* , **33**, p. 75 (1977).

40. Tan T.H. *Appl. Sci. Res.* , **33**, p. 89 (1977).

41. Martin P.A., G.R. Wickman. *Proc. Toy. Soc.,* **A390**, p.91 (1983).

42. Schenk H.A. *J. Acoust. Soc. Am.* **44**, p. 41 (1968).

43. Gubernatis J.E., E. Domany, J.A. Krumhausl. *J. Appl. Phys.* **48**, p. 2804 (1977).

44. de Hoop A.T. *Wave Motion,* 7, p. 569 (1985).

45. Waterman P.C. *J. Acoust. Soc. Am.* **45**, p. 1417 (1969).

46. Waterman P.C. *J. Acoust. Soc. Am.* **60**, p. 567 (1976).

47. Varathajulu V., Y-H. Pao. *J. Acoust. Soc. Am.*, **60**, p. 556 (1976).

48. Millar R.F. *Radio Sci.* **8**, p.785 (1973).

49. Bates R.H.T, D.J.N. Wall. *Philos. Trans. R. Soc. London,* **45**, p. 287 (1977).

50. Pao Y-H. in "*Modern Problems in Elastic Wave Propagation*", J. Miklowitz and J.D. Achenbach, edts., Wiley-Interscience (1978).

51. Visscher W.M. *J. Appl. Phys.*, **51**, p.825 (1980).

52. Visscher W.M. *J. Appl. Phys.*, **51**, p.835 (1980).

53. Waterman P.C. in "*Acoustics, Ferromagnetic and Elastic Wave Scattering - Focus on the T-matrix Approach*", V.K. Varadan and V.V. Varadan, edts., Pergamon Press (1980).

54. Kraut E.A. *IEEE Trans. Sonics and Utrason.*, **SU-23**, p. 162 (1976).

55. Friedlander F.G. Sound Pulses, Cambridge Univ. Press (1958).

56. Keller J.B. in "*Proc. Symposium on Microwave Optics*", McGill Univ. (1953).

57. Karal F.C., J.B. Keller. *J. Acoust. Soc. Am.*, **31**, p. 694 (1959).

58. Achenbach J.D., A.K. Gautesen. *J. Acoust. Soc. Am.*, **61**, p. 413 (1977).

59. Gautesen A.K., J.D. Achenbach, H. McMacken. *J. Acoust. Soc. Am.*, **63**, p. 1824 (1978).

60. Achenbach J.D., A.K. Gautesen, D.A. Mendelson. *IEEE Trans. Sonics and Ultras.*, **SU-27**, p. 124 (1980).

61. Mendelson D.A., J.D. Achenbach, L.M. Keer. *Wave Motion,* **2**, p. 277 (1980).

62. Bond L.J. *Ultrasonics,* **17**, p.71 (1979).

63. Scandreff G.L., G.A. Kriegsmann, J.D. Achenbach. *J. Comp. Phys.*, **65**, p. 410 (1986).

64. Scandreff G.L., G.A. Kriegsmann, J.D. Achenbach. *SIAM J. Sci. Comput.*, **7**, p. 571 (1986).

65. Scandreff G.L., G.A. Kriegsmann, J.D. Achenbach. *Wave Motion*, **9**, p. 171 (1987).

66. Morton K.W. *Comput. Phys. Commun.*, **12**, p. 99 (1976).

67. Euler L. Instructiones Calculi Integrali, St. Petersburg (1768).

68. Runge C.Z. *Math. Phys.*, **56**, p. 225 (1908).

69. Clough R.W. *Proc. 2nd Conf. Electronic Computation,* ASCE, Pittsburg (1960).

70. Turner M.J., R.W. Clough, H.C. Martin, L.J. Top. *J. Aeronaut. Sci.*, **23**, p. 805, p. 854 (1956).

71. Argyris J.H. Energy Theorems and Structural Analysis, Butterworths (1960).

72. Alterman Z. *J. Phys. Earth,* **16**, p. 113 (1968).

73. Bertholf I.D. *J. Appl. Mech.*, **34**, p. 725 (1967).

74. Harumi K., F. Suzuki, T. Saito. *J. Acoust. Soc. Am.*, **53**, p. 600 (1973).

75. Rose J.L., P.A. Meyer. *J. Acoust. Soc. Am.*, **57**, p. 598 (1975).

76. Harumi K., T. Saito, T. Fujimori. in "*Proc. 9th World Conf. on NDT*", Melbourne, Australia (1979).

77. Saito T., T. Fujimori, K. Harumi, H. Okada. in " *Proc. 10th World Conf. on NDT*", Moscow (1982).

78. Blake R.J., L.J. Bond, A.L. Downie. in "*Review of Progress in Quantitative NDT*", v.1, D.O. Thompson and D.E. Chimenti, edts., Plenum Press (1982).

79. Bond L.J., R.J. Blake. in "*Proc. Ultrason. International '83*", Butterworths (1983).

80. Harker A.H. *Journal of Nondestructive Evaluation*, **4**, No.2, p. 89 (1984).

81. Harker A.H., J.A. Ogilvy, J.A.G. Temple. *Journal of Nondestructive Evaluation,* **9**, No.2/3, (1990).

82. Belyshko T., R. Mulen. In "*Modern Problems in Elastic Wave Propagation*", J. Miclowitz and J. Achenbach eds., p. 67 (1978).

83. Ludwig R., W. Lord. *IEEE Trans. of Ultrasonics, Ferroelectrics, and Frequency Control,* **35**, 6 (1988).

84. Lord W., R. Ludwig, Z. You. *J. Nondestructive Eval.*, **9**, No. 213, p. 129 (1990).

85. Gabor D. *J. IEE (london)*. **93**, pp. 429-457 (1946).

86. Chui Charles K. Wavelet Analysis and Its Applications. vol.1, Academic Press (1992).

87. Mattingly J. K. M. S. Thesis. University of Tennessee - Knoxville, Nuclear Engineering Department (1995).

88. Daubechies I. *Comm. Pure and Appl. Math.* **46**, p. 909 (1988).

89. Daubechies I. *IEEE Trans. Inf. Theory.* **36**, p. 961 (1990).

90. Clifton R.J. *Quart. Appl. Math.* **25**, p. 97 (1967).

91. Duncan D.B. in "Proc. 5th Canadian Conf. Nondestr. Test.", (1985).

92. Bayliss A. *Bull. Seism. Soc. Am.*, **76**, p.1115 (1966).

93. Alterman Z., D. Loewenthal. *Geophys. J. R. astr. Soc.*, **20**, p.101 (1970).

94. Ames W.F. Numerical Methods for Partial Differential Equations, Academic Press (1977).

95. O'Brien C.G., M.A. Hyman, S. Kaplan. *J. Math. Phys.*, **29**, p.223 (1951).

96. Mitchell A.R., D.F. Griffiths. The Finite Difference Method in Partial Differential Equations. John Wiley & Sons Ltd., (1980).

97. Courant R., K. Friedrichs, H. Lewy. *Mathenatische Annalen,* **100**, p.32 (1928).

98. Ilan A. D. Loewenthal. *Geophys. Prospect.*, **24**, p.431 (1976).

99. Boore D.M. in "*Methods in Computational Physics*", **11**, B.A. Bolt, edt., Academic Press (1972).

100. Alterman Z., D. Loewenthal. *Geophys. J. R. astr. Soc.*, **43**, p. 727 (1975).

102. Alterman Z., F. C. Karal Jr. *Bull. Seism. Soc. Am.*, **58**, p. 367 (1968).

103. Ogilvi J. A., J.A.G. Temple. *Ultrasonics*, **21**, p.259 (1983).

104. Lax P.D., B. Wendroff. *Comm. Pure and Appl. Math.*, **13**, p.217 (1960).

105. Lax P.D., B. Wendroff. *Comm. Pure and Appl. Math.*, **17**, p.381 (1964).

106. Xue T., W. Lord, S. Udpa. *Res. Nondestr. Eval.*, **7**, p.31 (1995).

107. Dickey J.W., G.V. Frisk, H. Überall. *J. Acoust. Soc. Am.*, **59**, p.1339 (1976).

108. Kinra D. *Experimental Mechanics*, **28**, No.3, p.288 (1988).

109. Kinra D., S.E. Hannemann. *Experimental Mechanics*, **32**, No.4, p.323 (1992).

110. Jeong H., D. Hsu, R.E. Shannon, P.K. Liaw. *Metallurgical and Materials Transactions A*, **25A**, p. 799 (1994).

111. Jeong H., D. Hsu, R.E. Shannon, P.K. Liaw. *Metallurgical and Materials Transactions A*, **25A**, p. 811 (1994).

112. Scruby C.B., H.N.G. Wadley, R.J. Dewhurst, D.A. Hutchins, S.B. Palmer. *Mat. Eval.*, **39**, p.1250 (1981).

113. Wagner J.W. *Proc. of IEEE Ultrason. Symposium*, p.791 (1992).

114. Ricker N. *Geophysics*, **10**, p.207 (1945).

115. Miller G.F., H. Pursey. *Proc. R. Soc. London*, **A223**, p.521 (1954).

116. Hall K.G. *Ultrasonics*, **15**, p.245 (1977).

117. Ying C.F., M.X. Li, H.L. Zhang. *Ultrasonics*, **19**, p.155 (1981).

118. Weight J.P. *J. Acoust. Soc. Am.*, **81**, p.815 (1987).

119. Temple J.A.G. *Nucl. Energy*, **22**, p.335 (1983).

120. Achenbach J.D.,et al. *IEEE Trans. Of Sonics and Ultrasonics*, **SU-30**, 4 (1980).

121. Baborovsky V.M., E.A. Slater, D.M. Marsh. *Proc. Ultrasonics International Conf.*, **46**, p. 157 (1975).

122. Ravenscroft F.A., K. Newton, C.B. Scruby. *Ultrasonics*, **29**, p.29 (1991).

123. Victorov I. A. Rayleigh and Lamb Waves. Plenum Press, New York (1967).

124. P.L. Blue. in "Review of Progress in Quantitative Nondestructive Evaluation", D.O. Thompson and D.E. Chimenti, edts., Plenum Press, New York, NY, **8B**, p.1157 (1989).

125. Liaw P.K., R.E. Shannon, W.G. Clark, Jr., W.C. Harrigan: in "Morris E. Fine Symposium", P.K. Liaw, J.R. Weertman, H.L. Marcus, J.S. Santer, edts., TMS-AIME, Warrendale, PA, p. 193-208 (1990).

126. Jeong H., D.K.Hsu, R.E. Shannon, P.K. Liaw. in "Review of Progress in

Quantitative Nondestructive Evaluation", D.O. Thompson and D.E. Chimenti, edts., Plenum Press, New York, NY, **9B**, p.1395 (1990).

127. Spies M., K. Salama. *Res. Nondestr. Eval.*, **1**, p.99 (1989).

128. Grelsson B., K. Salama. *Res. Nondestr. Eval.*, **2**, p.83 (1990).

129. Blessing G.V., W.L. Elvan. *J. Appl. Mech.*, **48**, p.965 (1981).

130. Ledbetter H.M., S.K. Datta, R.D. Kriz. *Acta Metall.*, **32**, p.2225 (1984).

131. I am indepted to Dr. D. Hsu of the Center for Nondestructive Evaluation, Iowa State University, Ames, IA, for performing the ultrasonic measurement and providing me with a carefully documented data set (1995).

132. Clifton R.J. *Appl. Mech. Rev.*, **38**, p.1276 (1985).

133. Barnett D.M., J. Lothe, K. Nishioka, R.J. Asaro. *J. Phys. F: Metal Physics*, **3**, p.1083 (1973).

134. Chadwick P., G.D. Smith. *Adv. Appl. Mech.*, **17**, p.303 (1977).

135. Chadwick P., G.D. Smith. in "Mechanics of Solids" (Rodney Hill 60th Anniversary Volume), H.G. Hopkins, M.J. Sewell edts., Pergamon Press (1982).

136. Barnett D.M., J. Lothe. *J. Phys. F: Metal Physics*, **4**, p.671 (1974).

137. Barnett D.M., J. Lothe. *Proc. R. Soc. London*, **A402**, p.135 (1985).

138. Lothe J., D.M. Barnett. *J. Appl. Phys.*, **47**, p.428 (1976).

139. Love A.E.H. Some Problems in Geodynamics, Cambridge University Press (1911).

140. Stoneley R. *Proc. R. Soc. London*, **A106**, p.416 (1924).

141. Caignard L. Reflection and Refraction of Progressive Seismic Waves. transl. and revised by E.A. Flinn and C.H. Dix, McGraw-Hill (1962).

142. Lee D.A., D.M. Corby. *IEEE Trans. Sonics & Ultras.*, **SU-24**, p.206 (1977).

143. Rokhlin S.I., M. Hefets, M. Rosen. *J. Appl. Phys.*, **52**, p.3579 (1980).

144. Barnett D.M., J. Lothe, S.D. Gavazza, M.J.P. Misgrave. *Proc. R. Soc. London*, **A402**, p.153 (1985).

145. Lamb H. *Proc. R. Soc. London*, **A93**, p.114 (1917).

146. Abramovitz M., I.A. Stegun. Handbook of Mathematical Functions, Dover, New York (1965).

APPENDICES

Appendix A

Used Finite Difference Approximations to the Partial Derivatives in the Wave Equation

Many expressions for the finite difference approximations to various derivatives can be found in [146]. This Appendix describes the used in the present work finite difference approximations.

Let f(x,y,t) be a scalar function, which is continuous and differentiable at each point x, y, t of the phase space up to, at least, second oreder, and let us define a uniform Cartesian mesh, of spacing h in both X- and Y- direction, and at time intervals Δt. Then we may write

$$f(mh, nh, l\Delta t) = f(m, n, l). \tag{A.1}$$

A.1. Derivatives with Second Order Accuracy

The Taylor expansion in a forward sense is defined as

$$f(m+1, n, l) = f(m, n, l) + hf_x(m, n, l) + \frac{h^2}{2} f_{xx}(m, n, l) + O(h^2). \tag{A.2}$$

The backward Taylor expansion is defined as

$$f(m-1, n, l) = f(m, n, l) - hf_x(m, n, l) + \frac{h^2}{2} f_{xx}(m, n, l) + O(h^2). \tag{A.3}$$

In both expressions $O(h^2)$ means that

$$\lim_{h \to 0} \frac{O(h^2)}{h^2} \to 0. \tag{A.4}$$

Similarly

$$f(m, n+1, l) = f(m, n, l) + hf_y(m, n, l) + \frac{h^2}{2} f_{yy}(m, n, l) + O(h^2), \tag{A.5}$$

$$f(m, n-1, l) = f(m, n, l) - hf_y(m, n, l) + \frac{h^2}{2} f_{yy}(m, n, l) + O(h^2). \tag{A.6}$$

Adding (A.3) and (A.2) we obtain the center difference approximation for the second derivative with respect to x

$$f_{xx}(m, n, l) = \frac{1}{h^2}\left[f(m+1, n, l) - 2f(m, n, l) + f(m-1, n, l)\right] + O(h^2). \tag{A.7}$$

Similarly, adding (A.5) and (A.6), we obtain

$$f_{yy}(m, n, l) = \frac{1}{h^2}\left[f(m, n+1, l) - 2f(m, n, l) + f(m, n-1, l)\right] + O(h^2). \tag{A.8}$$

Subtracting (A.3) from (A.2), and (A.6) from (A.5), we obtain correspondingly for the first derivatives

$$f_x(m, n, l) = \frac{f(m+1, n, l) - f(m-1, n, l)}{2h} + O(h^2), \tag{A.9}$$

$$f_y(m, n, l) = \frac{f(m, n+1, l) - f(m, n-1, l)}{2h} + O(h^2). \tag{A.10}$$

Using similar expansions for the time derivative, we obtain

$$f_{tt}(m, n, l) = \frac{1}{\Delta t^2}\left[f(m, n, l+1) - 2f(m, n, l) + f(m, n, l-1)\right] + O(\Delta t^2). \quad \text{(A.11)}$$

For the mixed derivative we use

$$\begin{aligned} f(m+1, n+1, l) &= f(m, n, l) + h\left[f_x(m, n, l) + f_y(m, n, l)\right] \\ &+ \frac{h^2}{2}\left[f_{xx}(m, n, l) + f_{yy}(m, n, l) + 2f_{xy}(m, n, l)\right] + O(h^2) \end{aligned}, \quad \text{(A.12)}$$

$$\begin{aligned} f(m-1, n+1, l) &= f(m, n, l) + h\left[f_y(m, n, l) - f_x(m, n, l)\right] \\ &+ \frac{h^2}{2}\left[f_{xx}(m, n, l) + f_{yy}(m, n, l) - 2f_{xy}(m, n, l)\right] + O(h^2) \end{aligned}, \quad \text{(A.13)}$$

$$\begin{aligned} f(m+1, n-1, l) &= f(m, n, l) + h\left[f_x(m, n, l) - f_y(m, n, l)\right] \\ &+ \frac{h^2}{2}\left[f_{xx}(m, n, l) + f_{yy}(m, n, l) - 2f_{xy}(m, n, l)\right] + O(h^2) \end{aligned}, \quad \text{(A.14)}$$

$$\begin{aligned} f(m-1, n-1, l) &= f(m, n, l) - h\left[f_x(m, n, l) + f_y(m, n, l)\right] \\ &+ \frac{h^2}{2}\left[f_{xx}(m, n, l) + f_{yy}(m, n, l) + 2f_{xy}(m, n, l)\right] + O(h^2) \end{aligned}. \quad \text{(A.15)}$$

Adding (A.12) and (A.15) leads to

$$\begin{aligned} &f(m+1, n+1, l) + f(m-1, n-1, l) \\ &= 2f(m, n, l) + h^2\left[f_{xx}(m, n, l) + f_{yy}(m, n, l) + 2f_{xy}(m, n, l)\right] + O(h^2) \end{aligned} \quad \text{(A.16)}$$

Adding (A.13) and (A.14) gives

$$\begin{aligned} &f(m-1, n+1, l) + f(m+1, n-1, l) \\ &= 2f(m, n, l) + h^2\left[f_{xx}(m, n, l) + f_{yy}(m, n, l) - 2f_{xy}(m, n, l)\right] + O(h^2) \end{aligned} \quad \text{(A.17)}$$

Subtracting (A.17) from (A.16) gives

$$f_{xy}(m, n, l) = \frac{1}{4h^2}\left[f(m + 1, n + 1, l) - f(m - 1, n + 1, l)\right. \qquad \text{(A.18)}$$
$$\left.-f(m + 1, n - 1, l) + f(m - 1, n - 1, l)\right] + O(h^2)$$

When the step sizes along X- and Y- axes are different (say, Δx and Δy) (A.18) becomes:

$$f_{xy}(m,n,l) = \frac{1}{4\Delta x \Delta y}\left[f(m+1,n+1,l) - f(m-1,n+1,l)\right. \qquad \text{(A.18a)}$$
$$\left.-f(m+1,n-1,l) + f(m-1,n-1,l)\right] + O(h^2)$$

Subtracting (A.13) from (A.14) and (A.15) from (A.12) gives respectively

$$f(m+1,n-1,l) - f(m-1,n+1,l) \qquad \text{(A.19)}$$
$$= 2h\left[f_x(m,n,l) - f_y(m,n,l)\right] + O(h^2)$$

$$f(m+1,n+1,l) - f(m-1,n-1,l) \qquad \text{(A.20)}$$
$$= 2h\left[f_x(m,n,l) + f_y(m,n,l)\right] + O(h^2)$$

Adding the last two equations gives

$$f_x(m,n,l) = \frac{1}{4h}\left[f(m+1,n-1,l) - f(m-1,n+1,l)\right. \qquad \text{(A.21)}$$
$$\left.+f(m+1,n-1,l) - f(m-1,n-1,l)\right] + O(h^2)$$

Subtracting (A.19) from (A.20) gives

$$f_y(m,n,l) = \frac{1}{4h}\left[f(m+1,n-1,l) + f(m-1,n+1,l)\right. \qquad \text{(A.22)}$$
$$\left.-f(m+1,n-1,l) - f(m-1,n-1,l)\right] + O(h^2)$$

A.2. Derivatives with First Order Accuracy

The first order of accuracy approximations are used in the finite difference formulation of the stress tensor components when boundary and interface conditions are introduced. We use the forward and backward Taylor expansions (A.2) , (A.3), (A.4) and (A.5) and neglect all terms proportional to h^2 or higher powers of h. This gives the forward first order approximations

$$f_x(m, n, l) = \frac{f(m + 1, n, l) - f(m, n, l)}{h} + O(h), \tag{A.23}$$

$$f_y(m, n, l) = \frac{f(m, n + 1, l) - f(m, n, l)}{h} + O(h), \tag{A.24}$$

and the backward first order approximations

$$f_x(m, n, l) = \frac{f(m, n, l) - f(m - 1, n, l)}{h} + O(h), \tag{A.25}$$

$$f_y(m, n, l) = \frac{f(m, n, l) - f(m, n - 1, l)}{h} + O(h), \tag{A.26}$$

For the finite difference formulation of the intersections of the interfaces with the free boundaries we use the expressions

$$\begin{aligned} f_x(m, n, l) = {} & \frac{1}{2h}\Big[f(m, n - 1, l) - f(m - 1, n - 1, l) \\ & + f(m, n, l) - f(m - 1, n, l)\Big] + O(h) \end{aligned}, \tag{A.27}$$

$$f_y(m,n,l) = \frac{1}{2h}\left[f(m-1,n,l) - f(m-1,n-1,l)\right. \\ \left. +f(m,n,l) - f(m,n-1,l)\right] + O(h) . \tag{A.28}$$

Additional expressions, similar to the obtained above, are

$$f_x(m,n,l) = \frac{1}{2h}\left[f(m+1,n+1,l) + f(m+1,n,l)\right. \\ \left. -f(m,n,l) - f(m,n+1,l)\right] + O(h) , \tag{A.29}$$

$$f_y(m,n,l) = \frac{1}{2h}\left[f(m+1,n+1,l) + f(m,n+1,l)\right. \\ \left. -f(m,n,l) - f(m+1,n,l)\right] + O(h) , \tag{A.30}$$

$$f_x(m,n,l) = \frac{1}{2h}\left[f(m,n+1,l) - f(m-1,n+1,l)\right. \\ \left. +f(m,n,l) - f(m-1,n,l)\right] + O(h) , \tag{A.31}$$

$$f_y(m,n,l) = \frac{1}{2h}\left[f(m-1,n+1,l) + f(m,n+1,l)\right. \\ \left. -f(m,n,l) - f(m-1,n,l)\right] + O(h) , \tag{A.32}$$

$$f_x(m,n,l) = \frac{1}{2h}\left[f(m+1,n-1,l) + f(m+1,n,l)\right. \\ \left. -f(m,n,l) - f(m,n-1,l)\right] + O(h) , \tag{A.33}$$

$$f_y(m,n,l) = \frac{1}{2h}\left[f(m+1,n,l) + f(m,n,l)\right. \\ \left. -f(m+1,n-1,l) - f(m,n-1,l)\right] + O(h) . \tag{A.34}$$

APPENDIX B

Surface and Guided Waves

In this appendix three different kinds of waves will be considered: the so called Rayleigh, Lamb and Stoneley waves. All three kinds exist independently and are confined to an interface between two media with different elastic properties or to a free surface.

B.1. Rayleigh Waves

Rayleigh [23] studied the case of a traction-free surface: in effect he looked for solutions of the wave equation (2.50) with no incident waves. We restrict our consideration to two-dimensional Cartesian geometry. We use the scalar and vector potentials Φ and $\vec{H}$. In two dimensional geometry, due to the relation (2.37), it is seen that we may consider only the Z-component of $\vec{H}$, and we denote it with ψ.

The expressions linking these potentials with the displacement components and stresses are:

$$u = \frac{\partial \Phi}{\partial x} + \frac{\partial \psi}{\partial y}, \tag{B.1}$$

$$v = \frac{\partial \Phi}{\partial y} - \frac{\partial \psi}{\partial x}, \tag{B.2}$$

$$\sigma_{xx} = \lambda\left(\frac{\partial^2 \Phi}{\partial x^2} + \frac{\partial^2 \Phi}{\partial y^2}\right) + 2\mu\left(\frac{\partial^2 \Phi}{\partial x^2} + \frac{\partial^2 \psi}{\partial y\, \partial x}\right), \tag{B.3}$$

$$\sigma_{yy} = \lambda\left(\frac{\partial^2\Phi}{\partial x^2} + \frac{\partial^2\Phi}{\partial y^2}\right) + 2\mu\left(\frac{\partial^2\Phi}{\partial y^2} - \frac{\partial^2\psi}{\partial y\,\partial x}\right), \tag{B.4}$$

$$\sigma_{xy} = \mu\left(2\frac{\partial^2\Phi}{\partial y\,\partial x} - \frac{\partial^2\psi}{\partial x^2} + \frac{\partial^2\Psi}{\partial y^2}\right). \tag{B.5}$$

As it is shown in Chapter 2, the potentials Φ and ψ may be considered as potentials of longitudinal and shear waves, respectively, and satisfy (for harmonic processes) the following wave equations:

$$\frac{\partial^2\Phi}{\partial x^2} + \frac{\partial^2\Phi}{\partial y^2} + k_l^2\Phi = 0, \tag{B.6}$$

$$\frac{\partial^2\psi}{\partial x^2} + \frac{\partial^2\psi}{\partial y^2} + k_t^2\psi = 0, \tag{B.7}$$

where $k_l = \omega\sqrt{\frac{\rho}{(\lambda + 2\mu)}}$ and $k_t = \omega\sqrt{\frac{\rho}{\mu}}$ are the wave numbers for longitudinal and transverse modes, respectively, ω is the circular frequency, λ and μ are the elastic Lamè constants, ρ is the density of the medium.

We seek the solution of equations (B.6) and (B.7) corresponding to a plane harmonic wave propagating in the positive X- direction. For that we let

$$\Phi = F(y)e^{i(kx-\omega t)}, \quad \psi = G(y)e^{i(kx-\omega t)}. \tag{B.8}$$

Substituting (B.8) in (B.6) and (B.7), we obtain two differential equations for the functions F and G:

$$\frac{d^2F}{dy^2} - (k^2 - k_l^2)F(y) = 0, \tag{B.9}$$

$$\frac{d^2G}{dy^2} - (k^2 - k_t^2)G(y) = 0. \tag{B.10}$$

The two independent solutions of each of the above equations are the $\exp\left(\pm\sqrt{k^2 - k_t^2}\, y\right)$ and $\exp\left(\pm\sqrt{k^2 - k_l^2}\, y\right)$. We assume that $k^2 > k_t^2 > k_l^2$ (as we see below, this assumption is confirmed). Than the solution with positive radicals will correspond to motion increasing with depth, the solution with negative radicals will correspond to exponentially decaying motion, i.e. surface wave. Consequently, we consider the solution

$$\Phi = Ae^{-qy}e^{i(kx-\omega t)}, \tag{B.11}$$

$$\psi = Be^{-sy}e^{i(kx-\omega t)}, \tag{B.12}$$

where $q^2 = k^2 - k_l^2$; $s^2 = k^2 - k_t^2$; A and B are arbitrary constants.

The conditions of the problem demands also that the stresses σ_{yy} and σ_{xy} go to zero at the boundary of the half space (plane y=0). Substituting the expressions for Φ and ψ into these conditions, we obtain

$$\left| \begin{array}{l} -A2iqk + B(s^2 + k^2) = 0 \\ A[(\lambda + 2\mu)q^2 + \lambda k^2] + B2i\mu sk = 0 \end{array} \right. . \tag{B.13}$$

Nontrivial solution for A and B of this system exists only if the determinant of the coefficients vanishes, i.e.

$$\begin{vmatrix} -2iqk & (s^2+k^2) \\ (\lambda+2\mu)q^2+2\mu k^2 & 2i\mu sk \end{vmatrix} = 0, \tag{B.14}$$

which gives the characteristic equation for k:

$$4k^2qs-(s^2+k^2)^2 = 0. \tag{B.15}$$

This equation has, in general, four roots. However, the careful analysis of the solution [3, 7, 13, 23] shows that there is only one real root k_R and this root satisfies the condition $k_R > k_t$. Using this, we have for the potentials

$$\begin{aligned} \Phi &= -Ae^{i(k_R x-\omega t)-q_R y}, \\ \psi &= -iA\frac{2q_R k_R}{s_R^2+k_R^2}e^{i(k_R x-\omega t)-s_R y}. \end{aligned} \tag{B.16}$$

In (B.16) A is an arbitrary constant to be determined from the initial conditions, $q_R^2 = k_R^2 - k_l^2$; $s_R^2 = k_R^2 - k_t^2$. Substituting (B.16) in (B.1) and (B.2) and taking the real part of the obtained expressions, we have

$$u_R = Ak_R\left\{e^{-q_R y} - \frac{2q_R s_R}{s_R^2+k_R^2}\right\}\sin(k_R x-\omega t), \tag{B.17}$$

$$v_R = Aq_R\left\{e^{-q_R y} - \frac{2k_R^2}{s_R^2+k_R^2}\right\}\cos(k_R x-\omega t). \tag{B.18}$$

The equation (B.15) can be rewritten in terms of the velocities

$$\left(2-\frac{c_R^2}{c_s^2}\right)^2 - 4\left(2-\frac{c_R^2}{c_s^2}\right)^{\frac{1}{2}}\left(2-\frac{c_R^2}{c_p^2}\right)^{\frac{1}{2}} = 0, \tag{B.19}$$

where c_R denotes the Rayleigh wave velocity and c_s, c_p are the transverse and longitudinal velocities, respectively. Eq. (B.19) has been originally obtained by Rayleigh [23]. Its solution can be obtained by applying numerical techniques. However, the procedure can be simplified and approximate expressions for the Rayleigh velocities can be used. One good approximation to the Rayleigh wave velocity is given by Victorov [123]

$$\frac{c_R}{c_S} = \frac{0.87 + 1.12\nu}{1+\nu}, \tag{B.20}$$

where ν is the Poisson ratio. As ν varies from 0 to 0.5, the Rayleigh wave phase velocity varies monotonically from 0.87 c_t to 0.96 c_t. It is also readily seen that the Rayleigh wave does not exhibit phase velocity dispersion, since (B.19) does not depend on the frequency.

The expressions (B.16) describing the Rayleigh wave show that it consists of two inhomogeneous waves, one longitudinal and one transverse, which propagates along the boundary of the half-space with identical velocities and attenuate with depth according to exponential laws.

Since the displacement components u_R and v_R in the Rayleigh wave are shifted in phase by $\frac{\pi}{2}$, the trajectories of the particle motion in the wave are ellipses. For wave propagation in positive X-direction, given our assignment of the coordinate system, the ellipsoidal rotation of the particle at the surface proceeds clockwise; at a depth $y > 0.2\lambda_R$

the direction of rotation reverses and the displacement u_R changes its sign.

Along with the lack of dispersion Rayleigh waves poses other important properties, making them very useful tools for ultrasonic inspection. Since they do not penetrate into the depth of a solid, their amplitude decays with distance as $\frac{1}{\sqrt{k_R R}}$ (where R is the distance from the source) due to divergence of the wave beam emitted by the source. This decay is like that of cylindrical waves, i.e. it occurs more slowly than in the case of volume waves, where the analogous decay law is $1/(k_{l,t} R)^*$.

In inhomogeneous and anisotropic media, the structure and properties of Rayleigh waves are very complicated and there exist anisotropic media (for example, crystals of the triclinic system [123]) in which Rayleigh waves cannot exist in general. The existence and uniqueness of Rayleigh waves in anisotropic media has been studied by Barnett, Lothe, Nishioka and Asaro [133], Chadwick and Smith [134, 135], Barnett and Lothe [136, 137, 138]. In [137] it is used a method based on the impedance tensor to derive formulae which are particularly well suited to numerical computation.

B.2. Stoneley Waves

In nondestructive testing, one often encounters situations where the test piece is in contact with another material. Obvious cases include submerged or fluid-containing structures, with a solid - fluid interface, and buried or coated structures, where the second medium is a solid which may have rather ill-defined characteristics. One then asks whether

---

* This is precisely why Rayleigh waves are the principal type of waves recorded in earthquakes.

there are modes similar to Rayleigh waves on such interfaces. Love [139] and Stoneley [140] studied the problem: it is related to the solution of the solid-fluid interface problem with no incident waves in the same way as the Rayleigh problem was related to the solution of the wave equation.

For the solid-fluid case, there are two solutions, one complex and one real. As the density of the overlying fluid tends to zero, the complex solution tends to the Rayleigh wave velocity. It is complex because the Rayleigh wave is attenuated, and examination of the wave vector in the fluid shows that there is a real component normal to the surface. The Rayleigh wave on the surface of the solid is leaking into a bulk (compression) wave in the fluid. The real solution has a speed less than the wave speed in the fluid or the shear wave in a solid, whichever is smaller, and has imaginary components of wavevector on both sides of the interface [19,20]. This is an undamped interface wave, the Stoneley wave. If the density is much less than that of the solid, which is the usual case in nondestructive testing applications, most of the energy of the Stoneley wave propagates through the fluid and most of that in the leaky Rayleigh wave through the solid, and the Stoneley wave may be neglected in most applications.

When the interface is between two solids Caignard [141] has given a complete analysis. It turns out that Stoneley wave occurs only for a restricted range of ratios of the densities and shear moduli of the two media. In particular, the shear wave velocities have to be quite similar for a Stoneley wave to exist, and this condition is unlikely to hold for a metallic structure buried in soil or coated with a resinous material. Even in the Earth's crust, where material properties might be expected to be similar enough to allow Stoneley wave propagation, seismologists have not observed such waves. Nevertheless, it has been suggested [142, 143] that interface waves might prove useful for the examination of adhesive bounded joints. It is useful, then, to have an efficient procedure for calculating the properties of Stoneley waves when they exist, and such a method based on the impedance matrix has been developed in [144], which is suitable for anisotropic materials.

B.3. Lamb Waves

Lamb waves refer to elastic perturbation propagating in a solid plate (or layer) with free boundaries, for which displacements occur both in the direction of wave propagation and perpendicularly to the plane of the plate.

We consider, following [145], a plane harmonic Lamb wave propagating in a plate of thickness 2d in the positive x direction (figure B-1). As in section B.1, we use again the

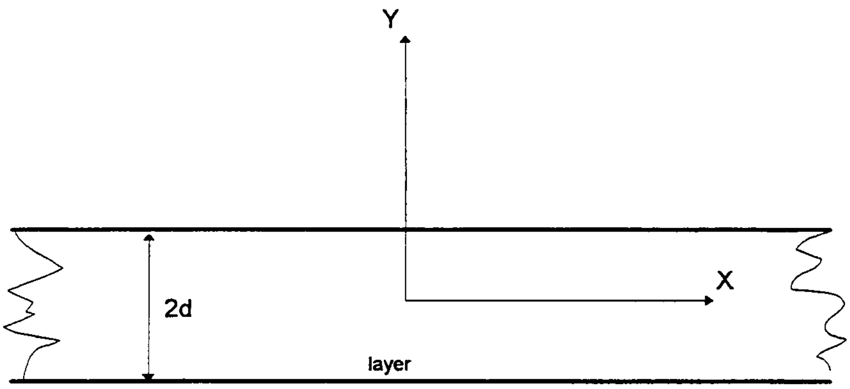

Figure B-1. A layer of thickness 2d and the corresponding 2D coordinate system.

potentials Φ and ψ. We represent them in the following manner:

$$\begin{aligned}\Phi &= A_s \mathrm{ch}qz e^{ikx} + B_a \mathrm{sh}qz e^{ikx},\\ \psi &= D_s \mathrm{sh}sz e^{ikx} + C_a \mathrm{ch}sz e^{ikx}\end{aligned}, \qquad (B.21)$$

where A_s, B_a, C_a, D_s are arbitrary constants, k is the Lamb wave number, and q and s are defined after (B.12). The factor $e^{-i\omega t}$ is dropped for brevity. It is readily seen that (B.21) satisfy the equations (B.6) - (B.7). Moreover, they must cause the stresses σ_{xy} and σ_{yy} to vanish on the planes $y=\pm d$. Substituting (B.21) in (B.4) and (B.5) and vanishing the stresses gives

$$\begin{aligned}&(k^2+s^2)\mathrm{ch}(qd)\,A_s + (k^2+s^2)\mathrm{sh}(qd)\,B_a + 2iks\,\mathrm{sh}(sd)\,C_a + 2iks\,\mathrm{ch}(sd)\,D_s = 0;\\ &(k^2+s^2)\mathrm{ch}(qd)\,A_s - (k^2+s^2)\mathrm{sh}(qd)\,B_a - 2iks\,\mathrm{sh}(sd)\,C_a + 2iks\,\mathrm{ch}(sd)\,D_s = 0;\\ &2ikq\,\mathrm{sh}(qd)\,A_s + 2ikq\,\mathrm{ch}(qd)\,B_a - (k^2+s^2)\mathrm{ch}(sd)\,C_a - (k^2+s^2)\mathrm{sh}(sd)\,D_s = 0;\\ &-2ikq\,\mathrm{sh}(qd)\,A_s + 2ikq\,\mathrm{ch}(qd)\,B_a - (k^2+s^2)\mathrm{ch}(sd)\,C_a + (k^2+s^2)\mathrm{sh}(sd)\,D_s = 0.\end{aligned} \qquad .(B.22)$$

It is seen that the above system is satisfied if the following two subsystems are satisfied:

$$\begin{aligned}&(k^2+s^2)\mathrm{ch}(qd)\,A_s + 2iks\,\mathrm{ch}(sd)\,D_s = 0;\\ &2ikq\,\mathrm{sh}(qd)\,A_s - (k^2+s^2)\mathrm{sh}(sd)\,D_s = 0;\end{aligned}, \qquad (B.23)$$

$$\begin{aligned}&(k^2+s^2)\mathrm{sh}(qd)\,B_a + 2iks\,\mathrm{sh}(sd)\,C_a = 0;\\ &2ikq\,\mathrm{ch}(qd)\,B_a - (k^2+s^2)\mathrm{ch}(sd)\,C_a = 0\end{aligned}. \qquad (B.24)$$

The subsystems have nontrivial solution only when their determinants are equal to zero. This leads to two characteristic equations, determining the eigenvalues of the wave number k:

$$(k^2+s^2)^2 ch(qd)sh(sd) - 4k^2 qs\, sh(qd)ch(sd) = 0, \tag{B.25}$$

$$(k^2+s^2)^2 sh(qd)ch(sd) - 4k^2 qs\, ch(qd)sh(sd) = 0. \tag{B.26}$$

With these equations we obtain from the subsystem (B.23) an expression for D_s in terms of A_s, and from the subsystem (B.24) an expression for C_a in terms of B_a. For the wave potentials we obtain then

$$\begin{aligned} \Phi &= A_s ch(q_s y) e^{ik_s x} + B_a sh(q_a y) e^{ik_a x}; \\ \psi &= \frac{2ik_s q_s\, sh(q_s d)}{(k_s^2+s_s^2) sh(s_s d)} A_s\, sh(s_s y) e^{ik_s x} + \frac{2ik_a q_a\, sh(q_a d)}{(k_a^2+s_a^2) sh(s_a d)} B_a ch(s_a y) e^{ik_a x}. \end{aligned} \tag{B.27}$$

Here, k_s are the values of k satisfying (B.25), k_a are the values satisfying (B.26); $q_{s,a} = \sqrt{k_{s,a}^2 - k_l^2}$; $s_{s,a} = \sqrt{k_{s,a}^2 - k_t^2}$. The displacement components u and v are calculated from (B.1) - (B.2) as

$$\begin{aligned} u &= u_s + u_a \\ v &= v_s + v_a \end{aligned}, \tag{B.28}$$

where

$$\begin{aligned} u_s &= Ak_s\left(\frac{ch(q_s y)}{sh(q_s d)} - \frac{2q_s s_s}{(k_s^2+s_s^2)}\cdot\frac{ch(s_s y)}{sh(s_s d)}\right) e^{i\left(k_s x - \omega t - \frac{\pi}{2}\right)}; \\ v_s &= -Aq_s\left(\frac{sh(q_s y)}{sh(q_s d)} - \frac{2k_s^2}{(k_s^2+s_s^2)}\cdot\frac{sh(s_s y)}{sh(s_s d)}\right) e^{i(k_s x - \omega t)} \end{aligned}, \tag{B.29}$$

$$u_a = Bk_a\left(\frac{sh(q_a y)}{ch(q_a d)} - \frac{2q_a s_a}{(k_a^2 + s_a^2)}\cdot\frac{sh(s_a y)}{ch(s_a d)}\right)e^{i\left(k_a x-\omega t-\frac{\pi}{2}\right)};$$

$$v_a = -Bq_a\left(\frac{ch(q_a y)}{ch(q_a d)} - \frac{2k_a^2}{(k_a^2 + s_a^2)}\cdot\frac{ch(s_a y)}{ch(s_a d)}\right)e^{i(k_a x-\omega t)} \tag{B.30}$$

Here A and B are new arbitrary constants.

The expressions (B.27) - (B.30) and equations (B.25) and (B.26) describe two groups of waves, each of which satisfies the wave equations of motions and boundary conditions, i.e. both can propagate in the plate independently of one another. Analyzing the expressions (B.29) and (B.30), we see that the first group of waves, indicated by a subscript s, describes waves in which the motion occurs symmetrically with respect to the plane $y = 0$ (i.e. the displacement u has the same sign, the displacement v opposite signs in the upper and lower halves of the plate). The second group, indicated by subscript a, describes waves in which the motion is antisymmetrical with respect to $y = 0$ (i.e., the displacement u has opposite signs, the displacement v the same signs in the upper and the lower halves of the plate). The waves of the first group are called symmetric Lamb waves, those of the second group are called antisymmetrical.

In a plate of thickness 2d at a frequency ω there can exist a finite number of symmetrical and antisymmetrical Lamb waves, differing from one another by their phase and group velocities and distribution of the displacements and stresses throughout the thickness of the plate. The number of symmetrical waves is determined by the number of real roots of eq. (B.25), the number of antisymmetrical waves by the real roots of (B.26). Every root defines a wave number $k_{s,a}$ or phase velocity $c_{s,a}$ of the corresponding wave. It can be shown[123] that, in addition to the finite number of real roots $k_{s,a}$, both of the indicated equations have for any ω and d an infinite set of purely imaginary roots, corresponding to in-phase motions of the plate which decay or grow exponentially along the x-axis. Since we are concerned with propagating waves, we will only deal with the real roots of the characteristic equations (B.25) and (B.26).

For $\omega d \to 0$, eq. (B.25) and (B.26) have only one root each. The root of (B.25) corresponds to the so-called zeroth symmetrical normal mode, which is usually designated as s_0, while the root of (B.26) represents the zeroth antisymmetrical mode a_0. As ωd increases, the roots k_{s_0} and k_{a_0} vary in magnitude, and for definite ratios between ω and d new roots appear, corresponding to the first, second, and higher symmetrical (s_1, s_2,.., s_n) and antisymmetrical (a_1, a_2,.., a_n) Lamb waves. The values of ω and d at which new roots appear are called "critical" thickness and frequency. The relation between the critical thicknesses and transverse and longitudinal wavelengths are as follows [123]:

$$\left.\begin{aligned} 2d &= \frac{\lambda_l}{2}, \frac{3\lambda_l}{2}, \frac{5\lambda_l}{2}, \ldots \\ 2d &= \lambda_t, 2\lambda_t, 3\lambda_t, \ldots \end{aligned}\right\} \text{ for symmetrical modes;} \tag{B.31}$$

$$\left.\begin{aligned} 2d &= \lambda_l, 2\lambda_l, 3\lambda_l, \ldots \\ 2d &= \frac{\lambda_t}{2}, \frac{3\lambda_t}{2}, \frac{5\lambda_t}{2}, \ldots \end{aligned}\right\} \text{ for antisymmetrical modes.} \tag{B.32}$$

At critical frequencies the wavenumbers $k_{s,a} \to 0$ (the phase velocity $c_{s,a} \to \infty$), and the new symmetrical and antisymmetrical mode represent a standing longitudinal [upper set of values in (B.31) and (B.32)] or transverse [lower set of values in (B.31) and (B.32)] wave in a plate.

The total number of symmetrical nodes N_s that are possible in a plate of given thickness 2d at the frequency ω is equal to [123]:

$$N_s = 1 + \left[\frac{2d}{\lambda_t}\right] + \left[\frac{2d}{\lambda_l} + \frac{1}{2}\right], \tag{B.33}$$

the total number of antisymmetrical modes N_a is

$$N_a = 1 + \left[\frac{2d}{\lambda_l}\right] + \left[\frac{2d}{\lambda_t} + \frac{1}{2}\right]. \tag{B.34}$$

The brackets in this case indicate the nearest integer part of the number that they enclose.

It is convenient to express the characteristic equations in terms of the phase velocity ν and the dimensionless frequency Ω by defining:

$$\vartheta \equiv \left(\frac{c_s}{\nu}\right)^2, \tag{B.35}$$

$$\kappa \equiv \left(\frac{c_s}{c_p}\right)^2, \tag{B.36}$$

$$\Omega \equiv \left(\frac{\omega t}{2c_s}\right). \tag{B.37}$$

Then the characteristic equations may be written as

$$\frac{\tan(1-\vartheta)^{\frac{1}{2}}\Omega}{\tan(\kappa-\vartheta)^{\frac{1}{2}}\Omega}=\left\{\frac{4\vartheta(1-\vartheta)^{\frac{1}{2}}(\kappa-\vartheta)^{\frac{1}{2}}}{(2\vartheta-1)^2}\right\}^{\pm 1} \tag{B.38}$$

where the positive sign is taken for symmetric modes.

The solutions ϑ of the above equation give the phase velocity of waves propagating without attenuation in plates. They consist of compression and shear waves propagating at angles θ_p and θ_s to the perpendicular of the plate surfaces [123], where

$$\sin\theta_p=\sqrt{\frac{\vartheta}{\kappa}}, \tag{B.39}$$

$$\sin\theta_s=\sqrt{\vartheta}\,. \tag{B.40}$$

There are regions where one or both of the compression and shear waves are evanescent [20, 123], giving rise of the modified characteristic equations

$$\frac{\tan(1-\vartheta)^{\frac{1}{2}}\Omega}{\tan(\vartheta-\kappa)^{\frac{1}{2}}\Omega}=\pm\left\{\frac{4\vartheta(1-\vartheta)^{\frac{1}{2}}(\vartheta-\kappa)^{\frac{1}{2}}}{(2\vartheta-1)^2}\right\}^{\pm 1} \tag{B.41}$$

in the region $\kappa<\vartheta<1$ and

$$\frac{\tan(\vartheta-1)^{\frac{1}{2}}\Omega}{\tan(\vartheta-\kappa)^{\frac{1}{2}}\Omega}=\left\{\frac{4\vartheta(\vartheta-1)^{\frac{1}{2}}(\vartheta-\kappa)^{\frac{1}{2}}}{(2\vartheta-1)^2}\right\}^{\pm 1} \tag{B.42}$$

when $\vartheta>1$. From this case we can recover the Rayleigh wave equation in the high-frequency limit (when the left hand-side of the equation is unity). That is, when the frequency is so high that the wavelength is very small compared with the plate thickness one can propagate surface waves along each surface and their exponential decay implies that they are independent. In the same region a solution also occurs for small Ω, and this is the flexural mode of a thin plate [20]. Apart from this, in the case of high frequency limit the phase velocity tends to c_s and the displacements consist of layers of shear waves traveling parallel to the surface, separated by a null planes of zero displacement. The number of null planes increases with the order of the mode, and is odd or even according to the symmetry.

The group velocity, as it is for the phase velocity, is also a function of frequency. It is related to the phase velocity

$$v = \frac{\omega}{k} \tag{B.43}$$

by

$$v_g = \frac{\partial \omega}{\partial k} \tag{B.44}$$

and may be calculated from the relationship between v and Ω by

$$v_g = \frac{v}{1 - \dfrac{\Omega}{v}\dfrac{\partial v}{\partial \Omega}}. \tag{B.45}$$

Curves of group velocity are shown in figure B-3, and curves of phase velocities are shown in figure B-2, borrowed from [20]. At $\Omega = 0$ the group velocities of s_n, a_n for $n > 0$ are all zero: this corresponds to the plate thickness modes, for which there is no energy flow along the plate. At the high frequency limit, the phase velocities approach c_s

with ever decreasing slopes, so that the group velocities approach c_s from below. There are regions of negative group velocity, which simply mean regions where the group and phase velocities are opposite. The dispersive properties of Lamb waves must satisfy the Kramer-Kronig relations, so that there must be regions of spectrum where there is attenuation. For practical purposes, however, only the modes propagating without attenuation are of interest.

For NDT purposes, the most important feature of the dispersion curves is the existence of minima and maxima in the group velocity. With the use of the method of stationary phase [2,123], one can conclude that at large distances the components which dominate the signal will be those corresponding to maxima or minima of the group velocity. If Lamb waves are to be used in NDT, then, it is sensible to select modes near such extrema, as these will allow fairly short pulses to be propagated without substantial losses in amplitude and time resolution arising from spreading.

When a Lamb wave propagates in a plate, it transfers energy parallel to the surface of the plate[20, 123]. The energy density is not spread uniformly throughout the plate. The energy density is the product of the stress and the particle velocity. Since u_y, σ_{xy} and σ_{yz} are all zero, there is no energy flow in Y-direction. The energy flow in Z-direction averages to zero over a whole cycle of the oscillating wave, as the product $\sigma_{xz} u_x$ and $\sigma_{zz} u_z$ both have a time dependence $\sin(2kx - \omega t)$. Only the energy flow in cX-direction has a non-zero average.

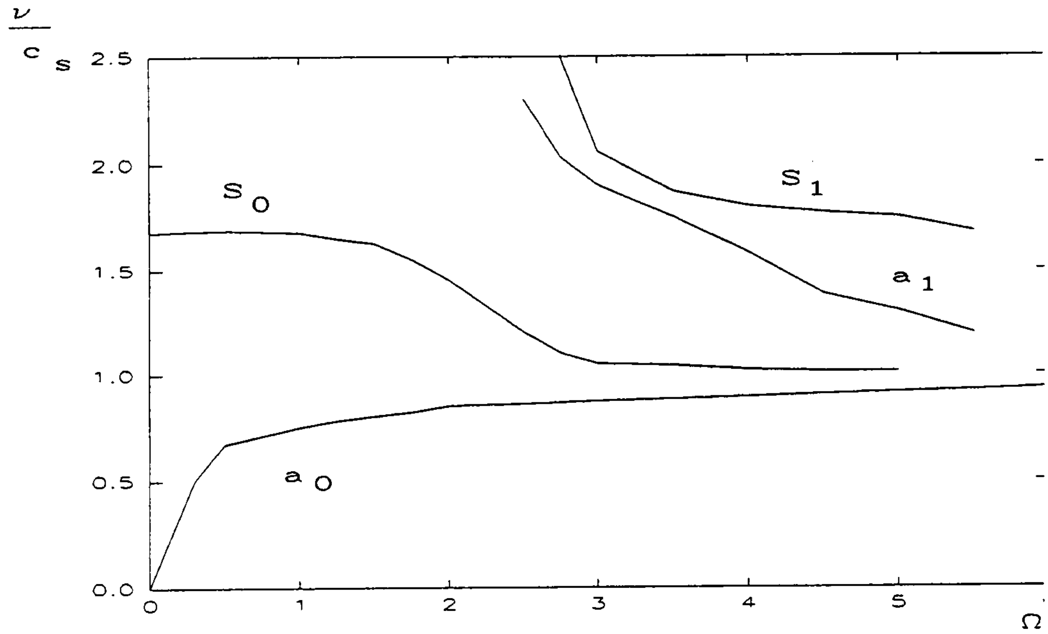

Figure B-2. Dispersion curves for the phase velocity for modes 0, 1.

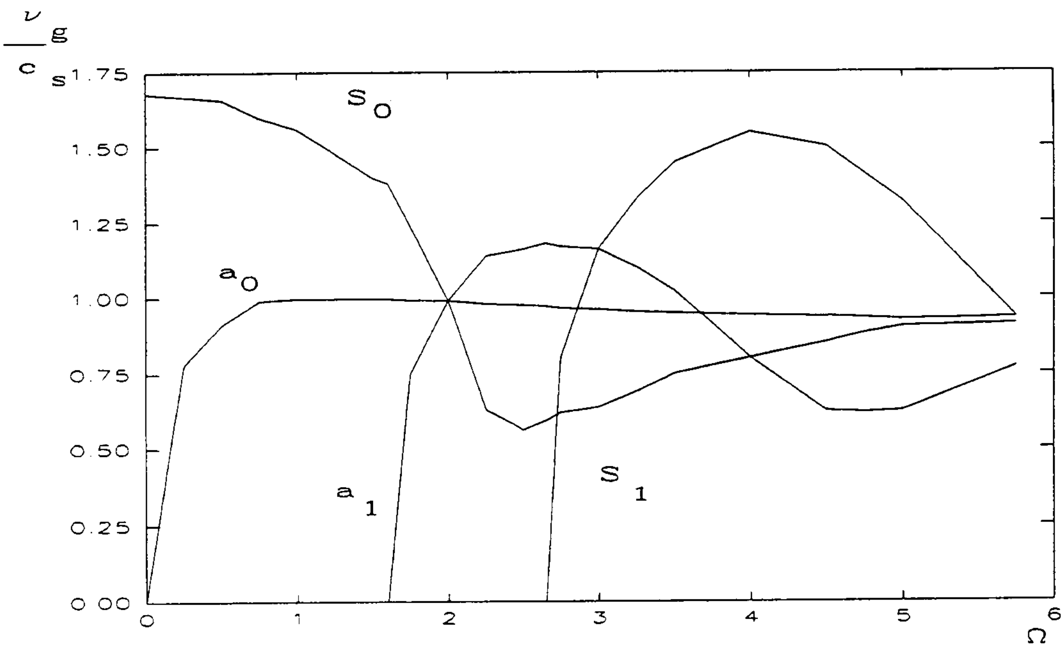

Figure B-3. Dispersion curves for the group velocity for modes 0, 1.

APPENDIX C

Input-Output Features of the Code JUNA

In this Appendix we provide a description of the input data for **JUNA** and the output which **JUNA** produces for further analysis.

C.1. Input Data for JUNA

An example of the input data for **JUNA** is given in figure C-1. The input data is read by the code in a free format form so only the number of the read parameters and their order is of importance. The input data is expected in the input file **juna.res** and is ordered as follows:

nx - number of X-axis intervals (since the numeration starts with 2 and spans through nx+2, the actual size of the system is calculated according to L1=(nx-1)*stepsize)

ny - number of Y-axis intervals (same as for nx)

ltmax - number of time steps to be computed.

iface - spare (set 0).

```
601 41 405 0 0 2.e-8 2.e-4 12 2 2 4 10
452 2 452 42 601 2 601 42
50 77 30 0.
0 0 0
2
101 401
0 0 0 0
0 0 0 0
200. .34 7.86e3 2902.29
```

Figure C-1. Sample input for **JUNA**. (juna.inp).

igeom - set 0

dt - time step size.

h - spatial step size.

nprint - number of time intervals (in units dt) between each output print from detectors

nsflag = 1 - compression wave mode;

2 - shear wave mode.

l1flag = 1 - plane wave;

2 - surface boundary source on the bottom boundary (ny = 2);

-2 - surface boundary source on the left boundary (nx = 2).

nd - number of detector point - if less or equal to 4 - in the output file **juna.res**, if 8 - from detector #5 through 8 - in a file **detector.1**, if 12 - additional file **detector.2**, if 16 - additional file **detector.3**. **JUNA** will open up to 7 additional files for detectors up to 32 (only exactly dividing by 4)

nerfl - 0 - nothing;

any number(#) - calculates the current error each # of steps and writes results in a file **errno.ou**.

The second record (or line in **juna.res**) contains 2*nd integers - first number of each pair is the X-coordinate of the detector point, the second - the Y-coordinate. Note that 2 or nx+1 or ny+1 means to put the detector on some of the surfaces. The count begins with 2.

Third record contains 4 numbers as follows

If **l1flag**.eq.1 - xw - pulse width (in stepsizes h);

nsx - x - position of a point of the pulse line;

nsy - y-position of the same point;

tit - angle between the wave normal and X-axis (degrees).

If **l1flag**.eq.2/-2 - **ntdur** - pulse duration (dt units);

itpos - source position (long X- or Y-boundary);

itlth - source length (in h units) - the surface source will span from itpos to itpos+itlth;

tit - angle of the theoretical normal with X-axis (degrees).

Fourth record contains three integers - the crack parameters

mc- X-coordinate of the crack edge (if 0, no crack in the system);

nc - Y-coordinate of the same crack edge (if 2 - then bottom (nx=2) surface breaking crack;

isize - crack length (h units); if nc+isize=ny+1 - surface breaking crack at the top (y=ny+1) surface;

The fifth record contain 1 integer

mt - number of time moments for snapshots (must be less than 10), if zero - omit the next three records - no snapshots allowed;

The sixth record - contains **mt** integers, omit it if **mt**=0. Subsequent time moments for snapshots (in dt units);

The seventh record - four integers - coordinates of the area for a snapshot of the source in a case of a plane wave: **ixb** - X-coordinate of the lower left corner of the area (if 0, set to 2);

ixn - X-coordinate of the top right corner (if 0, set to nx+1);

iyb - Y-component of the lower left corner (if 0, set to 2);

iyn - Y-component of the top right corner (if 0, set to ny+1).

The eighth record contain the same as the seventh record, but for the system during the calculations. Both seventh and eighth records must be omitted if **mt** = 0.

The ninth record - material properties - 4 real numbers

eyoung - Young modulus (in GPa);

pois - poison ratio;

rho - material density;

rayc = Rayleigh speed in this material.

End of Input data.

C2. Output Data from JUNA

JUNA creates a number of output files. figure C-2 lists the main output file **juna.res**. In section C.3 is listed the content of this file. After editing the input data and the system parameters (Lamé constants, compression and shear wave speeds, and system sizes l1 and l2), under detector # is shown two columns - first column lists X-displacement components, the second - Y-displacement components. The leftmost column list the time in μs. If **mt** not zero, the snapshots for the corresponding time instants are listed in file names provided by the operating system and with extension 2I and 6I, where I=1,2,..,mt, and are written in the point format as given by the PostScript standard. Files with extension 2I contain X-displacement component, these with extension 6I - Y-displacement components. Other output files are described in the input data section above.

C.3. Sample Output of the Code JUNA

Starting date: 17-Dec-95; Time: 22:18:51

nx = 601 number of x-axis intervals
ny = 41 number of y-axis intervals
ltmax = 4096 number of time intervals
iface = 0 number of interfaces
igeom = 0 1/2/3-XY/RZ/RTITA geometry
dt = 2.00000E-08 time step size (seconds)
h = 2.00000E-04 spatial step size (m)

srate = 3.12500E+00 sampling rate (MHz)
nsflag= 1 1/2/3-longitudinal/shear wave/Rayleigh
nd = 4 number of detector points

l1flag= 2 1/2-plane wave/BNDRY area
nerfl = 10 0/# - none/error calc. each # of steps
ntdur = 200 transducer pulse duration (dt units)
itpos = 7 transducer position (h units)
itlth = 30 transducer length (h units)
tit = 90.00000 normal direction (degrees)
on the left BNDRY (parallel to y-axis)
no crack presented at this time..
calculated data for material 1
eyoung= 2.00000E+11 Young modulus(Pa)
pois = 2.90000 Poison ratio (if 0.5 - liquid)
rho = 7.86000E+03 density (kg/m**3)
Calculated system parameters:
mu = 7.75194E+10 Lame mu (kg/(m*s**2)
lambda= 1.07051E+11 Lame lambda (kg/(m*s**2)
spedc2= 5.77449E+03 Compression speed squared (m/s)
speds2= 3.14046E+03 Shear speed squared (m/s)
l1 = 1.20000E-01 m
l2 = 8.00000E-03 m
dzeta = 2.50000E-02
dksi = 1.66667E-03
dtau = 8.05851E-04
kappa = 6.66667E-02
Performs test for stability..mat# 1
The Alterman&loewental stability test successful..
The Alterman&loewental stability test successful..
History output for 2 detector point(s):

	det.1		det.2	
	x= 351		x= 351	
time(s)	y= 2		y= 42	
0.00000E+00	-8.40779E-45	5.60519E-45	8.40779E-45	5.60519E-45
3.20000E-07	-1.15780E-36	6.05451E-37	1.14897E-36	6.00775E-37

6.40000E-07	-1.92651E-29	9.32865E-30	1.90820E-29	9.23842E-30
9.60000E-07	-4.47985E-23	2.03075E-23	4.42532E-23	2.00547E-23
1.28000E-06	-1.53907E-17	6.59482E-18	1.51404E-17	6.48447E-18
1.60000E-06	-7.79654E-13	3.18473E-13	7.61507E-13	3.10785E-13
1.92000E-06	-5.36843E-09	2.10403E-09	5.16683E-09	2.02109E-09
2.24000E-06	-4.00024E-06	1.50413E-06	3.69212E-06	1.37956E-06
2.56000E-06	-1.72421E-04	5.90379E-05	1.21430E-04	3.85218E-05
2.88000E-06	-3.33010E-04	8.04026E-05	-2.58240E-04	-1.55434E-04
3.20000E-06	4.73469E-05	-1.12489E-04	-1.06213E-03	-4.76145E-04
3.52000E-06	-1.43348E-04	5.49889E-05	-1.33257E-03	-4.38074E-04
3.84000E-06	-1.29098E-03	7.68663E-04	-1.47220E-03	-1.76275E-04
4.16000E-06	-3.17745E-03	1.60532E-03	-1.83636E-03	-1.06429E-04
4.48000E-06	-4.31995E-03	1.95985E-03	-3.18448E-03	-5.00729E-04

Ending date: 17-Dec-95; Time: 23:20:51
user time: 1394.41162sec.
system time: 0.97375sec
total exec.time: 0h. 23 min. 15.38538sec.

□

VITA

Georgi Metodiev Daskalov was born in the city of Sofia, Bulgaria, on January 6, 1960. He received the M.S. degree in Nuclear Physics from the University of Sofia in 1982. From 1984 to 1992 he was a researcher in the Institute for Nuclear Research and Nuclear Energy, Sofia, Bulgaria, where he worked on the problems of the radiation transport in three-dimensional heterogeneous systems. His collaboration with scientists in Russia led to his Ph.D. degree in nuclear physics, which he received in 1994.

In 1992 he won a Fulbright grant for work in nuclear engineering, and in June 1993 became a graduate research assistant in the Nuclear Engineering Department of the University of Tennessee in Knoxville.